AN INVESTIGATION OF POLYMERIC ADSORPTION ON ALUMINIUM OXIDE BY INELASTIC ELECTRON TUNNELLING SPECTROSCOPY

by

Robert Ronnan Mallik

January 1985

A thesis presented in partial fulfilment of the requirements for the degree of Doctor of Philosophy of the Council for National Academic Awards.

Sponsoring Establishment:
School of Applied Physics,
Leicester Polytechnic,
P.O.Box 143,
Leicester LE1 9BH,
U.K.

Collaborating Establishment:
Royal Aircraft Establishment,
Farnborough,
Hants,
U.K.

ACKNOWLEDGEMENTS

I would like to thank the following:

My first supervisor Dr.R.G.Pritchard who has given freely of his time. His assistance, and coherent guidance concerning the direction of this work has proved invaluable.

My second supervisors Dr.J.Comyn, and Dr.C.C.Horley for their counsel, and several useful suggestions. Additionally, John Comyn has provided sound advice regarding matters of polymer chemistry.

Professor D.P.Oxley for his encouragement and numerous informal discussions which have enhanced my understanding.

The technical staff in the Schools of Applied Physics and Chemistry and in particular Mr.N.Bevan and Mr.D.W.Bazeley. Their (for the most parts) unflinching assistance in tunnel junction fabrication cannot go unmentioned.

My fellow research students for rousing discussions, and anecdotes on various subjects.

Dr.P.Poole of The Royal Aircraft Establishment, Farnborough, for a continuing interest in the project.

Mrs.M.C.Ward for her rapid and precise typing of this thesis, and patience under harassment.

The Directors and Governors of the Polytechnic for provision of laboratory resources and the SERC for funding of the work.

Finally, I am grateful for the help and support of my wife and family - especially over the last few years.

ABSTRACT

Inelastic electron tunnelling spectroscopy (IETS) has been used to investigate the adsorption of several synthetic polymers on Aℓ-oxide. The polymers studied included polyvinylacetate (PVA), polymethylmethacrylate (PMMA), and polyvinylalcohol (PVOH). All of these are of importance in the field of adhesion, and were incorporated into Aℓ/Aℓ-oxide/Pb IET junctions for the first time by the technique of liquid-phase doping. Assigned IET spectra are presented and discussed. Evidence from these, and corresponding bulk IR spectra suggest that cleavage of the ester side-groups of the former two polymers, catalysed by the hydrated Aℓ-oxide, leads to their adsorption. It is believed that PVA is hydrolysed to PVOH and then adsorbed by hydrogen bonding between alcohol side groups and surface hydroxyls on the oxide; acetic acid is produced as a by-product which is also adsorbed. For PMMA, ester cleavage generates carboxylate anions on the polymer side-groups. Strong spectral evidence suggests that PMMA is subsequently adsorbed by the formation of a bidentate symmetrical bridging complex between the carboxylate anions, and Aℓ cations in the oxide. Tentative evidence also exists to suggest that PVOH is adsorbed through the formation of an Aℓ-O-C monodentate bridge between the polymer and the oxide surface.

Corresponding IET spectra of these, and other polymers have been obtained by the technique of glow-discharge polymerization (GDP); the spectra are in good agreement with their liquid-phase doped counterparts. GDP has proved to be a valuable complementary technique to liquid-phase doping since spectra are obtained without the use of solvents. An apparatus has been developed which allows glow-discharge polymerized films to be incorporated routinely into IET junctions under controlled atmospheres.

Infusion doping, whereby dopant molecules are introduced into completed, undoped IET junctions through the top Pb electrode has been used to study certain monomers, and related solvents. Problems associated with formic acid contamination have been effectively eliminated by the implementation of a simple apparatus. Monomers investigated to date do not appear to adsorb when doped in this manner. Results from infusion doped solvents have allowed a model to be proposed which to a first approximation predicts the behaviour of IET junction conductance during infusion.

IET junctions having hydrocarbon-free, and relatively anhydrous Aℓ-oxides have been prepared and doped in situ under controlled conditions. Suitable modifications to the vacuum evaporation system have been made to facilitate the above. Preliminary work to vapour-phase dope these oxides with D_2O, and the monomer ethylacrylate has been successful. Doping of the oxides with glow-discharge formed polymers is now feasible.

CONTENTS

CHAPTER 1

INTRODUCTION

1.1 Aims of the Present Work

Polymeric adsorption on metal oxide surfaces has aroused considerable attention both in academic, and industrial spheres. Polymer films have been applied to metallic substrates by a variety of techniques, for example from dispersion, solution, or the melt (1,2), and by glow-discharge polymerization of monomers at the substrate (3,4) to name a few. Generally speaking the films range in thickness from several μm's (or more for bulk films) down to a few tenths of nm's. Such films have several important technological applications including extrusion coating (5), electrodeposition of paints (6), corrosion inhibition (7), and adhesion (1,2). The present work pertains to the latter of these, and is addressed to the adsorption of some polymers of interest in the field of adhesion on Aℓ-oxide at a molecular level. On a larger scale, the physical aspects of polymeric adhesion on metal oxides are fairly well understood; effects such as mechanical keying due to irregularities in surface topographies (of the order a few μm's magnitude) come into play (1,2). In contrast, relatively little is known about the Aℓ-oxide/polymer interface at a molecular level whose structure and composition will also influence polymeric adhesion.

Great interest has already stemmed from studies of the adsorption of thin polymer films on Aℓ-oxide - a substrate which is widely used, and commercially important in the field of adhesion. A good example where considerable interest has been shown is the aircraft industry which (despite the introduction of carbon fibre composites) still relies strongly upon bonded Aℓ as one of the primary materials for air frame construction (13); epoxide adhesives are also used almost extensively in this context (14).

Techniques such as FTIR (8,9,10), TEM (11), AES, and XPS (12) amongst others are currently employed to characterize the polymer-metal oxide interfacial systems. The primary aim of the present work was to explore some Aℓ-oxide synthetic polymer interfacial systems by the novel application of inelastic electron tunnelling spectroscopy (IETS); hitherto, such systems had not been studied in this way. IETS is an extremely sensitive technique which reveals the vibrational spectrum of molecular species adsorbed on a metal oxide surface. An adsorbed monolayer offers optimal spectral sensitivity. Fundamental aspects of the technique will be briefly discussed in the next section.

IET spectra of several ester-based polymers adsorbed on Aℓ-oxide have been recorded which has led to an enhanced understanding of their respective surface chemistries. Some results from these studies have been published (15), and presented in conference (16,17). Supplementary IETS work has also been undertaken to investigate the behaviour of the respective monomers, and associated solvents on Aℓ-oxide. Levels of impurities on the surfaces of the oxides employed have also been checked. The general approaches adopted for the above investigations will be outlined

1.2 BRIEF OVERVIEW OF IETS

IETS was discovered in 1966 by Jaklevic and Lambe (18,19). Following earlier work due to Giaver (20), Fisher and Giaver (21), and Simmons (22), they were investigating band structures of metal electrodes in thin film metal-insulator-metal (MIM) tunnel junctions, so called because electrons may be transferred from one metal to the other through the classically forbidden insulating layer by the quantum mechanical phenomenon of tunnelling. The insulating layer in such a device is usually the hydrated oxide of the base electrode metal. Jaklevic and Lambe applied a small dc bias across an Aℓ/Aℓ-oxide/Pb tunnel junction, and then employed an ac modulation technique to obtain a plot of the second derivative of the junction's I-V characteristic as a function of applied bias - an IET spectrum. A typical spectrum obtained from a "clean" junction is shown in Fig.1.1, and shows structure due to the Aℓ metal, and Aℓ-oxide phonons, and the surface hydroxyl layer on the oxide. They then noticed that if a monolayer of organic impurities was adsorbed onto the oxide surface, peaks appeared in the resulting spectra superimposed upon the background slope of a clean junction. These peaks by and large corresponded to the IR, and Raman vibrational mode energies of the adsorbed species. Figure 1.2 shows a spectrum obtained when approximately one monolayer of polyvinylacetate was adsorbed on the Aℓ-oxide surface of an Aℓ/Aℓ-oxide/Pb tunnel junction (obtained in the author's laboratory). IET spectra differ slightly from their IR and Raman counterparts partly due to the adsorbed nature of the compounds in question.

The following sections will describe briefly the fundamental tunnelling processes at work in MIM tunnel junctions which give rise to the technique of IETS. More comprehensive treatments may be found in several review articles (23-28) and two books on the subject (29,30).

Fig.1.1 - IET Spectrum of an undoped Aℓ/Aℓ-oxide/Pb tunnel junction.

As shown in the figure, the applied bias across the junction is often expressed in wavenumbers to comply with IR nomenclature. (1 MeV ≃ 8.065 cm^{-1} (26). The most prominent feature is the Aℓ-O bulk phonon stretching peak. Traces of adsorbed hydrocarbon contaminants manifest themselves in the weak CH stretching feature c.a. 2895 cm^{-1}. A broad OH stretch is also observed due to the adsorbed surface hydroxyl layer on the oxide.

Fig.1.2 - IET spectrum of an Aℓ/Aℓ-oxide/polyvinyl acetate/Pb tunnel junction.

The junction was liquid-phase doped with a solution of polyvinylacetate (PVA) in acetone (∿ 0.01% w/v). Several polymeric features are now apparent superimposed upon the background curve of an undoped device. Comparison between this IET spectrum of PVA and its IR counterpart has shown that the polymer is hydrolysed at the oxide surface, and probably adsorbed as polyvinylalcohol. Acetic acid is produced as a hydrolysis by-product and is also adsorbed. This spectrum is discussed further in Chapter 5.

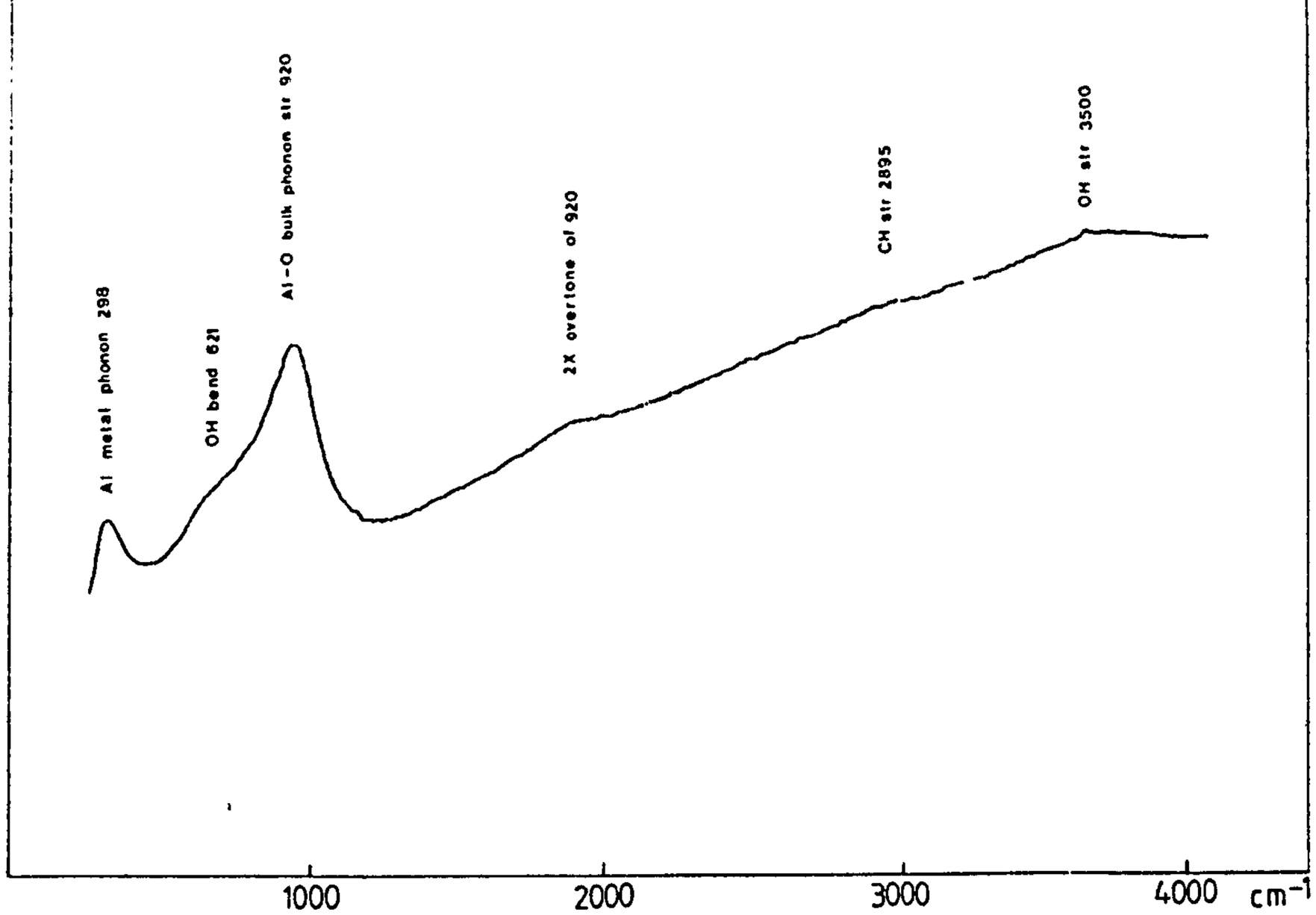
Al metal phonon 298
OH bend 621
Al-O bulk phonon str 920
2X overtone of 920
CH str 2895
OH str 3500
1000
2000
3000
4000
cm⁻¹

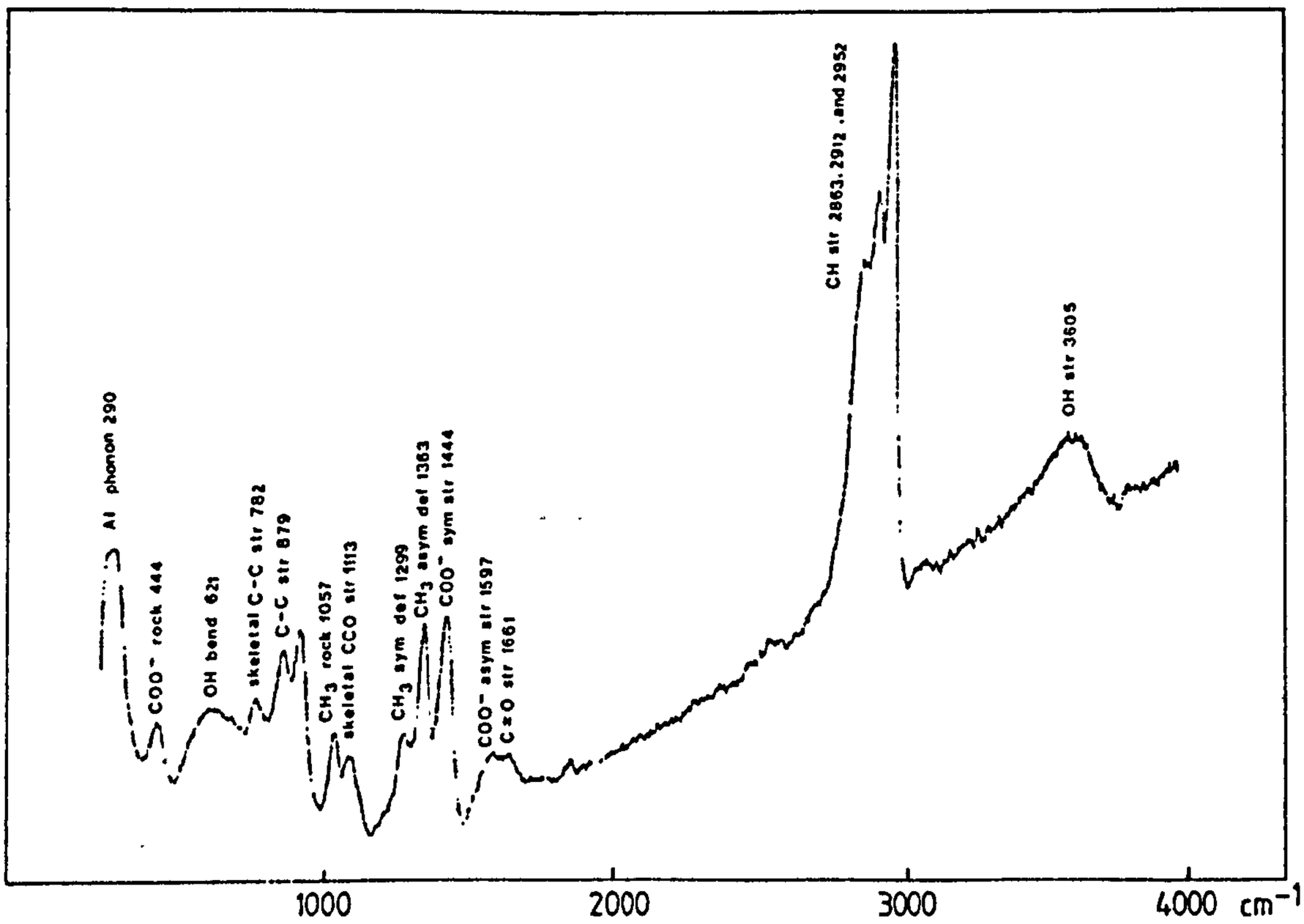
Al phonon 290
COO⁻ rock 444
OH bend 621
skeletal C-C str 782
C-C str 879
CH3 rock 1057
skeletal CCO str 1113
CH3 sym def 1299
CH3 asym def 1363
COO⁻ sym str 1444
COO⁻ asym str 1597
C=O str 1661
CH str 2863.2912 .and 2952
OH str 3605
1000
2000
3000
4000
cm⁻¹

1.2.1 Tunnelling in Metal-Insulator-Metal (MIM) Junctions

Consider two metal electrodes, M_1, and M_2 separated by a thin insulating layer, I, of thickness, s. Structures of this type are usually formed on an insulating substrate by vacuum evaporation techniques utilizing shadow masks. The electrodes are evaporated typically to a thickness of a few hundred nm. Figure 1.3 shows a schematic diagram of such a M_1-I-M_2 junction with a variable dc bias supply, V_b, connected across the electrodes. In IETS one of the electrodes employed is a superconductor, and for this reason tunnelling in a M_1-I-M_2 (superconductor) junction will be discussed . It will be seen later (and also in Chapter 3) that the superconducting properties of the electrode may also be utilized to verify that tunnelling does in fact occur. To reach the superconducting states of most metals very low temperatures (< 10K) are required. The most commonly used superconducting electrode is Pb whose transition temperature of $\sim$ 7K may be achieved conveniently by immersing the MIM device in liquid helium. At these temperatures, superconductors exhibit a small band of forbidden energies (a few meV) of width 2Δ centred at the Fermi level, E_F in the conduction band. Taking this into account, the energy level diagram of the net M_1-I-M_2 (S/C) system with no applied bias and assuming a symmetric, rectangular barrier may be represented as shown in Fig.1.4(i). Nomenclature for the symbols used are given in the legend. (A more general energy level diagram for a practical barrier has been discussed by Simmons (22)). When the junction is in this un-biased state the Fermi levels of the two metals, E_{F_1} and E_{F_2} coincide. If a small negative bias, V, is applied to M_1 (say) then E_{F_1} is raised relative to E_{F_2} by an amount eV distorting the band structure as shown in Fig.1.4(ii) where e is the electronic charge. Provided that the insulating layer is sufficiently thin, i.e. $s \lesssim 3$ nm, and that $V > \Delta/e$, then electrons may

Fig.1.3 - Schematic representation of a thin film M_1-I-M_2 tunnel junction.

The insulating layer is comprised of the oxide of the base electrode metal (M_1) into which organic impurities may be incorporated, and is usually $\lesssim$ 30 Å thick. A small, variable negative bias, V_b, may be applied to M_1 as shown.

Fig.1.4(i) - The corresponding energy level diagram of the M_1 -I-M_2 tunnel junction above with no applied bias, M_2 is a superconductor, T $\gtrsim$ OK.

g_1 (E) and g_2 (E) are the electron density of states functions for M_1 and M_2. Filled states in the conductor bands E_{F_1} and E_{F_2} are represented by the hatched areas. M_2 exhibits a small band of forbidden energies (a few meV) 2Δ centred at its Fermi level by virtue of its superconductivity. Thermal smearing of the electron energy distributions in the vicinity of E_{F_1}, and $E_{F_2} - \Delta$ have been omitted for simplicity.

The insulating barrier has been assumed to have a symmetrical rectangular form, Φ_1, and Φ_2 represent the M_1-I, and I-M_2 interfacial barrier heights respectively. E_g is the forbidden energy gap height, between the top of the (filled) valance band, and bottom of the conduction band of the insulator.

Fig.1.4(ii) - The corresponding energy diagram when a small negative bias, V is applied to M_2.

The band structure becomes distorted as shown, and the Fermi levels are separated by an amount eV. φ_1, φ_2, and E_g remain unaltered. Electrons may now tunnel elastically from filled states in M to empty states in M_2 through the classically forbidden region provided s is of the order $\lesssim$ 30A. If V>(hν+Δ)/e electrons may also tunnel inelastically by losing a quantum of energy, hν in exciting a molecular oscillator within the barrier. No net tunnel current will flow for V<Δ/e.

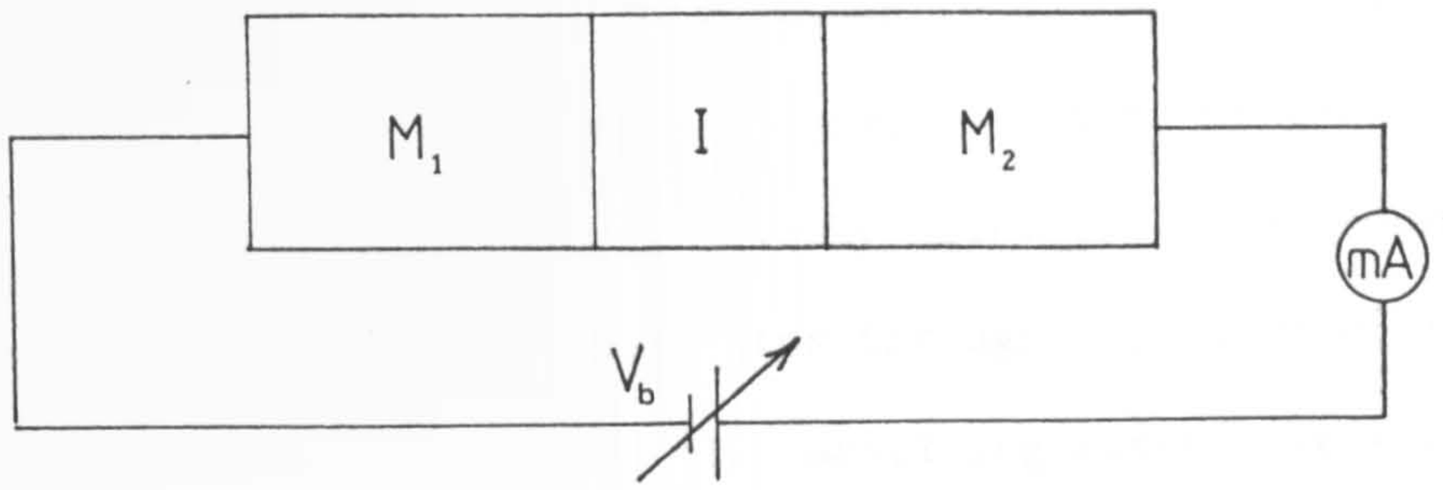

(i) $V_b = 0$.

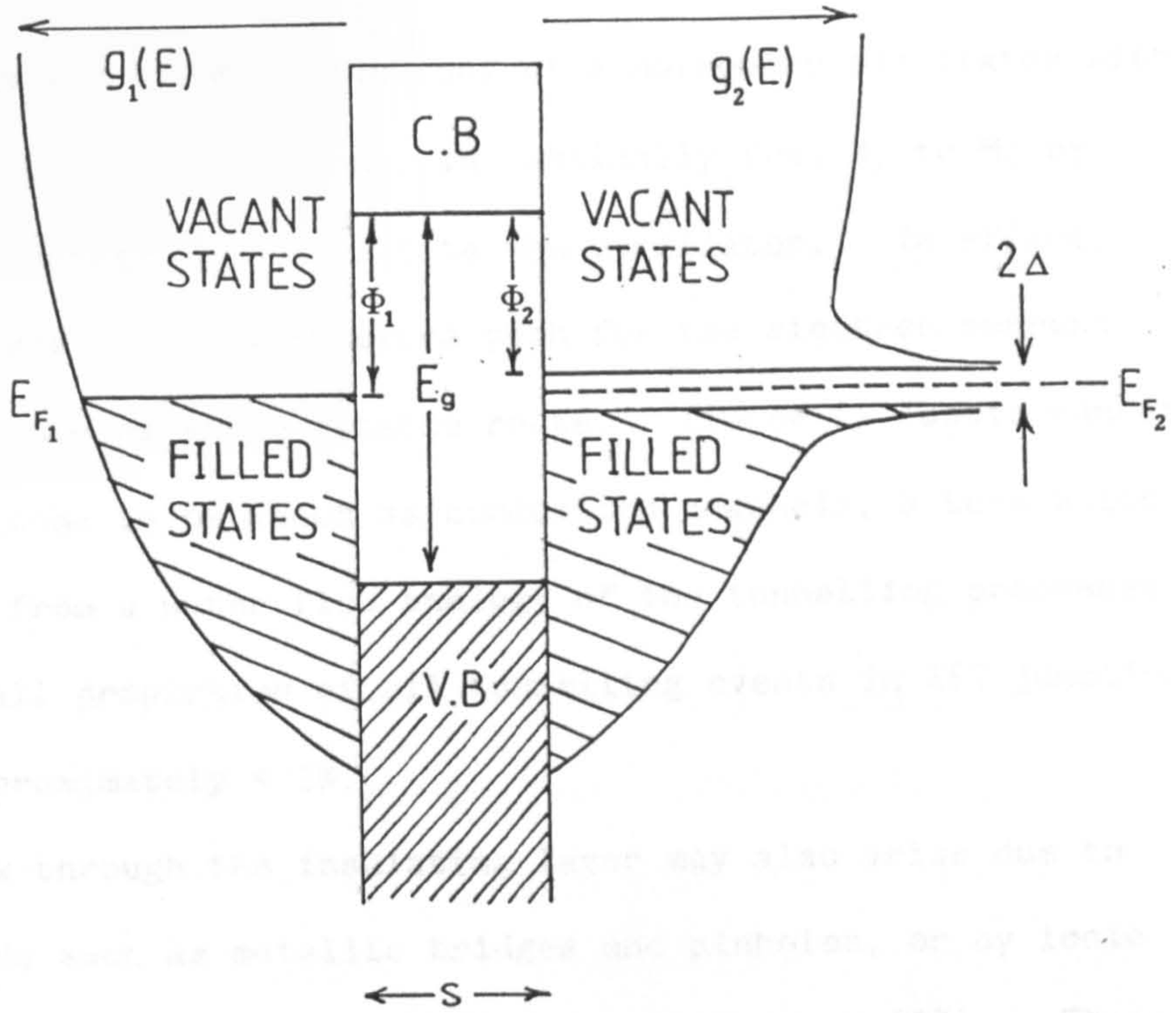

(ii) $V_b = V$,

$eV = E_{F_1} - E_{F_2}$

$= h\nu + \Delta$

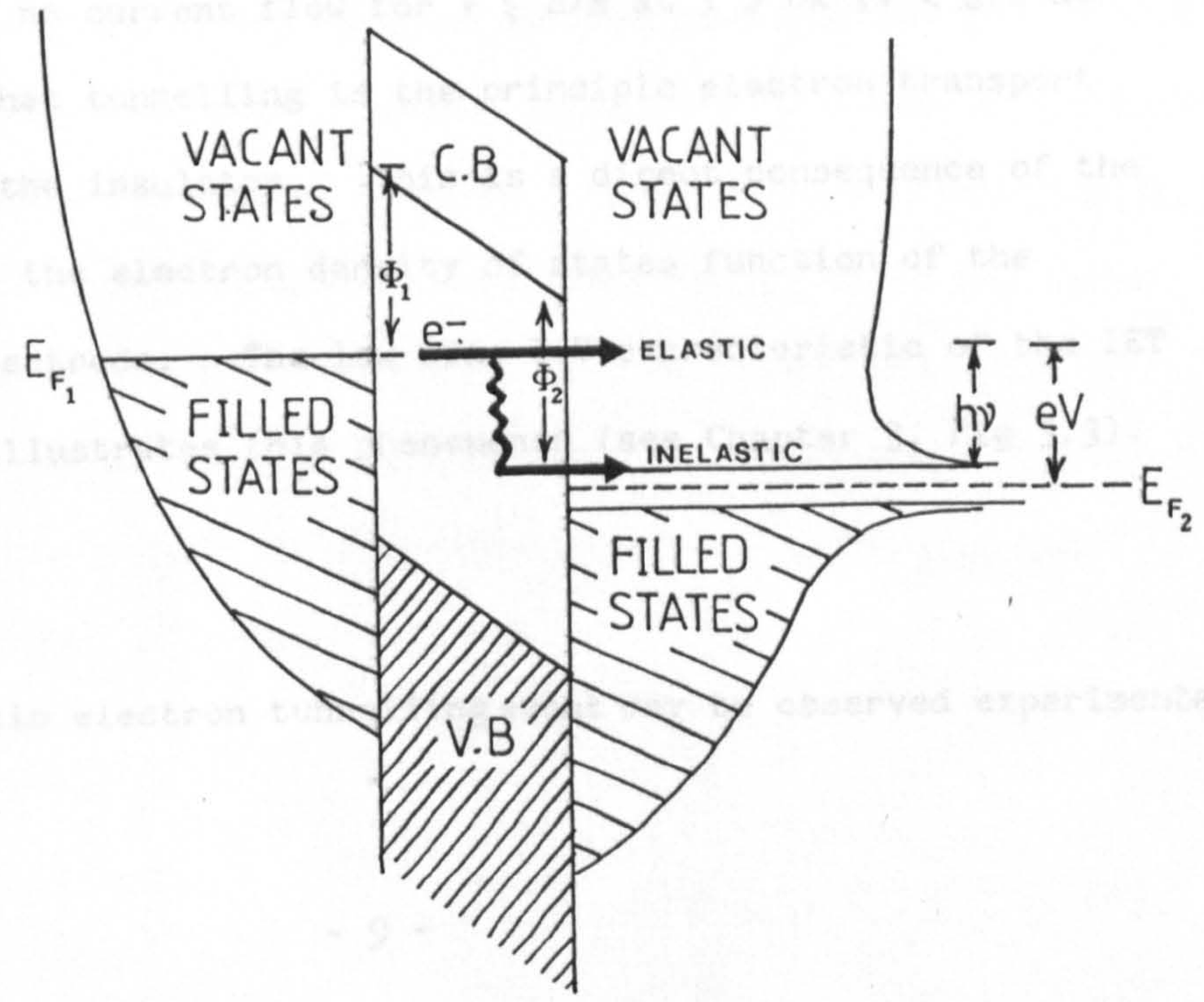

tunnel from filled states in M_1 to empty states in M_2 through the classically forbidden region between the valence and conduction bands of the insulator. If tunnelling is accomplished isoenergetically, i.e. if in the energy diagrams electrons traverse horizontal paths through the barrier, it is termed elastic; approximately 99% of all tunnelling events are elastic. If the magnitude of V is such that $V \geq (h\nu + \Delta)/e$ where h is Planck's constant and ν is the vibrational frequency of a molecular oscillator within the barrier. electrons may also tunnel inelastically from M_1 to M_2 by losing a quantum of energy $h\nu$ to excite the oscillator. In effect, this inelastic process provides an extra path for the electron current flow in addition to the existing elastic route. (These inelastic tunnel current paths have come to be known as conduction channels, a term which perhaps originates from a water flow analogy of the tunnelling processes (31).) Only a small proportion of all tunnelling events in IET junctions are inelastic - approximately < 1%.

Charge flow through the insulating layer may also arise due to defects in the oxide such as metallic bridges and pinholes, or by ionic conduction because the layer is not uniform and continuous (24). These mechanisms are not discussed here. However, it should be mentioned that the observation of no current flow for $V \leq \Delta/e$ at $T \geq$ OK ($V < \Delta/e$ at $T =$ OK) verifies that tunnelling is the principle electron transport mechanism through the insulator. This is a direct consequence of the energy gap, 2Δ, in the electron density of states function of the superconducting electrode. The low bias I-V characteristic of the IET junction clearly illustrates this phenomenon (see Chapter 3, Fig.3.3).

1.2.2 IETS

An inelastic electron tunnelling event may be observed experimentally

as an increase in slope of the (elastic) I-V characteristic of the IET junction in the vicinity of the event as shown in Fig.1.5(a). For illustration purposes the magnitude of the increase has been greatly exaggerated, in fact such increases are only of the order $\lesssim$ 1%. Derivatives of the I-V characteristic are usually taken (electronically) to reveal the increases more easily. IET spectra are plots of the second derivative d^2V/dI^2, of the I-V characteristic as a function of applied bias. The quantity d^2V/dI^2 is plotted rather than d^2I/dV^2 because it is easier to measure (see Chapter 3); in fact the two second derivatives are related though the identity $d^2I/dV^2 = - (dI/dV)^{-3}\ d^2V/dI^2$, and over the voltage range used for IETS dI/dV is slowly varying, therefore the two are almost directly proportional. Spectra display the increases in conductance as peaks at energies corresponding to the vibrational modes of the molecular oscillators within the barrier. Experiments are usually performed at 4.2K by immersing the IET junction in liquid He; this considerably reduces thermal broadening of the IET peaks and also utilizes the superconducting properties of the Pb electrode mentioned above. Third derivative data (obtained numerically by computer techniques) are sometimes utilized to estimate peak positions with a greater degree of accuracy.

As mentioned earlier, IET spectra exhibit features due to the oxide layer itself such as phonon excitations (23-28), and also vibrational modes due to electronic transitions (32-35). However, most attention in the literature has to date been given to the observation of IR and Raman like molecular vibrations due to adsorbed layers of dopant molecules on the oxide surface (several hundred articles have been published). Subsequent work has shown that an adsorbed monolayer will provide optimal spectral sensitivity for IETS (36).

Fig.1.5(a)

The I-V characteristic for an IET junction in the vicinity of an inelastic event. Non-linear low bias behaviour due to superconductivity of the electrodes is not shown. A slight increase in conductance is observed at $V=(h\nu+\Delta)/e$ due to the onset of inelastic tunnelling. At T=OK the onset is well defined as shown by the solid line. In practice, i.e. for T>OK thermal smearing of the electron energy distributions causes the gradual increase as indicated by the broken line.

Fig.1.5(b)

The first derivative of the I-V characteristic. The increase in conductance appears as a step.

Fig.1.5(c)

The second derivative. At OK the increase in conductance will appear as an infinitely sharp spike. In practice a 'thermally smeared' curve is observed.

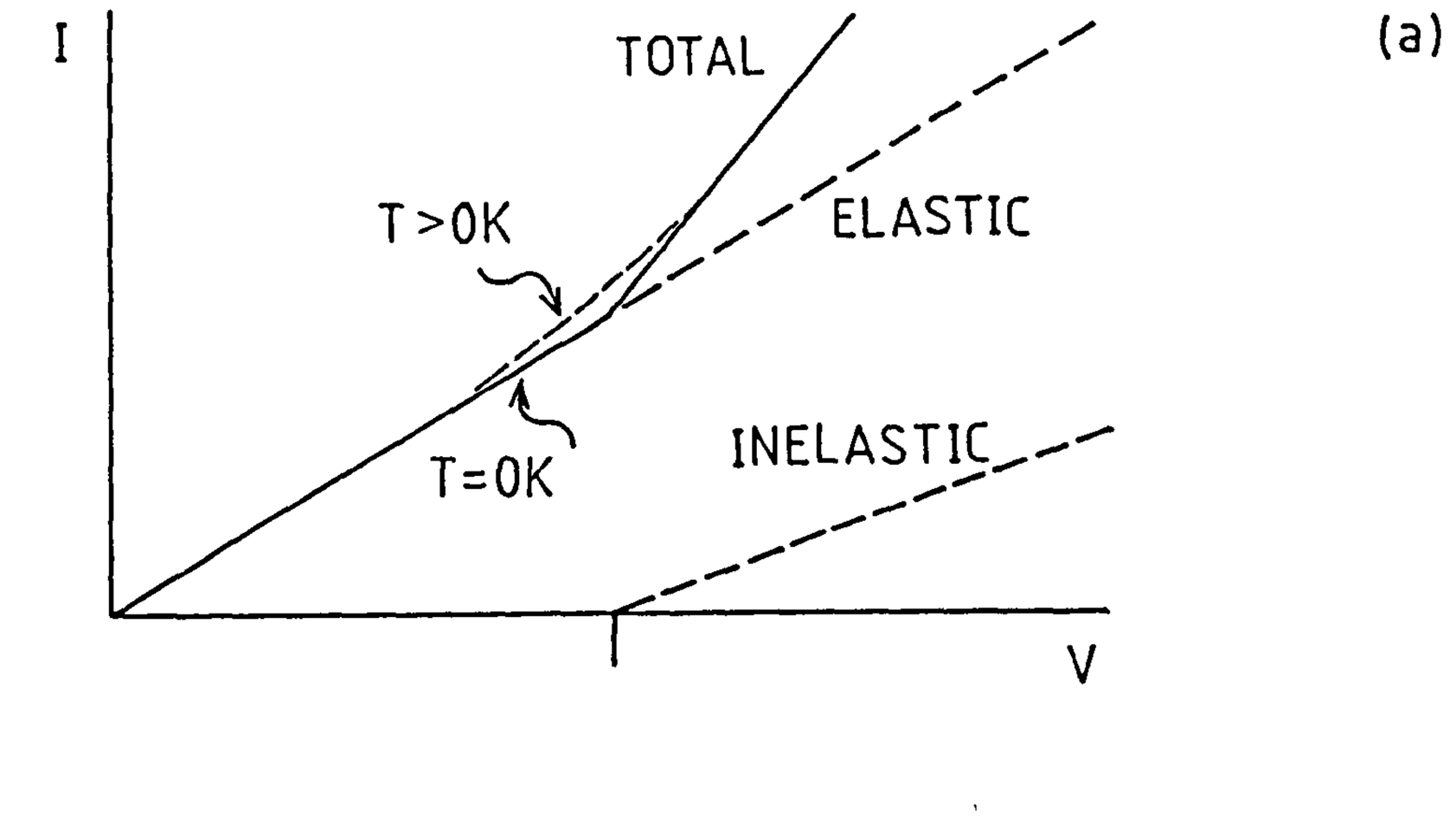
I
TOTAL
ELASTIC
T>0K
T=0K
INELASTIC
V

(a)

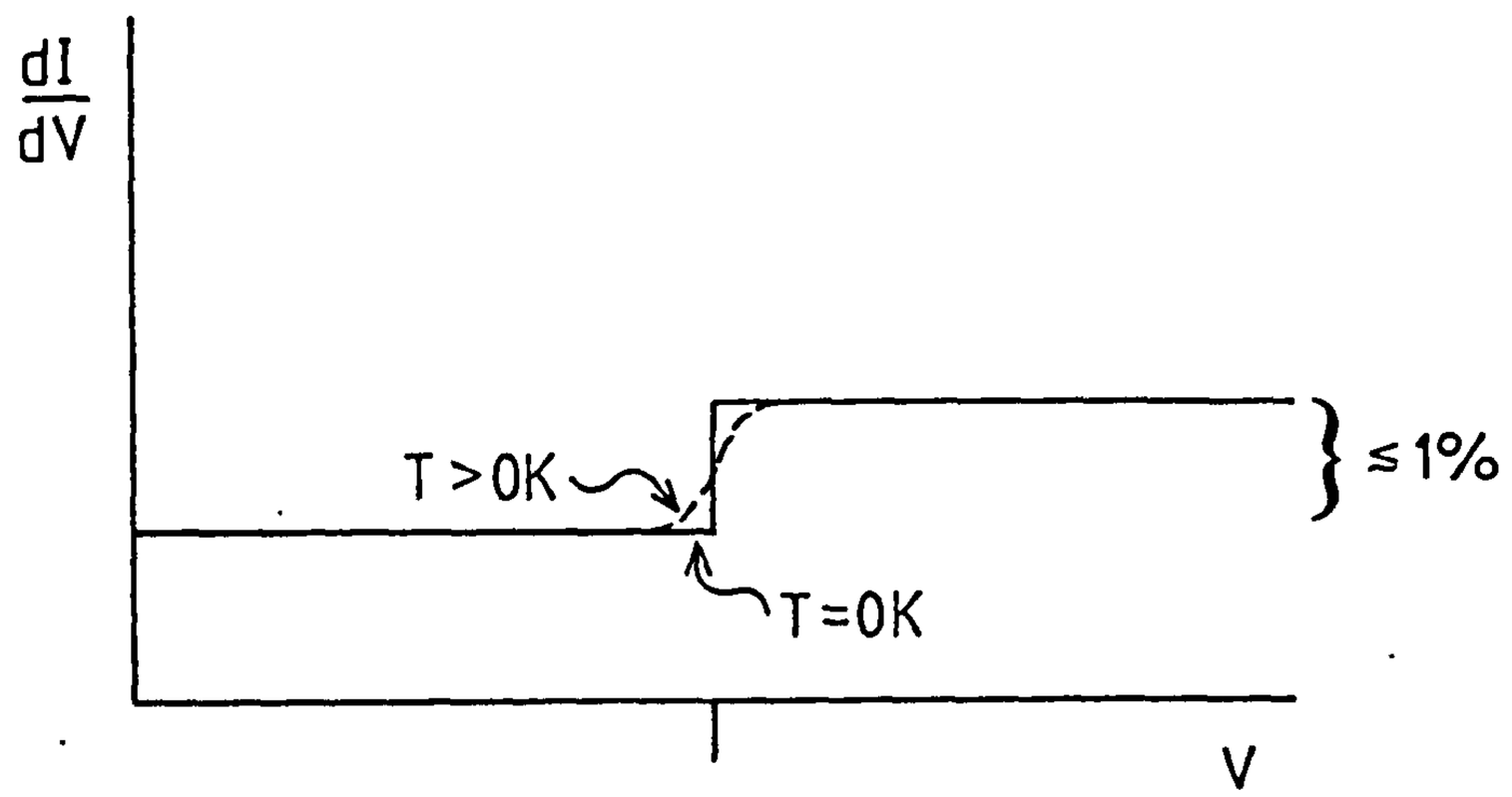
dI/dV
T>0K
≤1%
T=0K
V

(b)

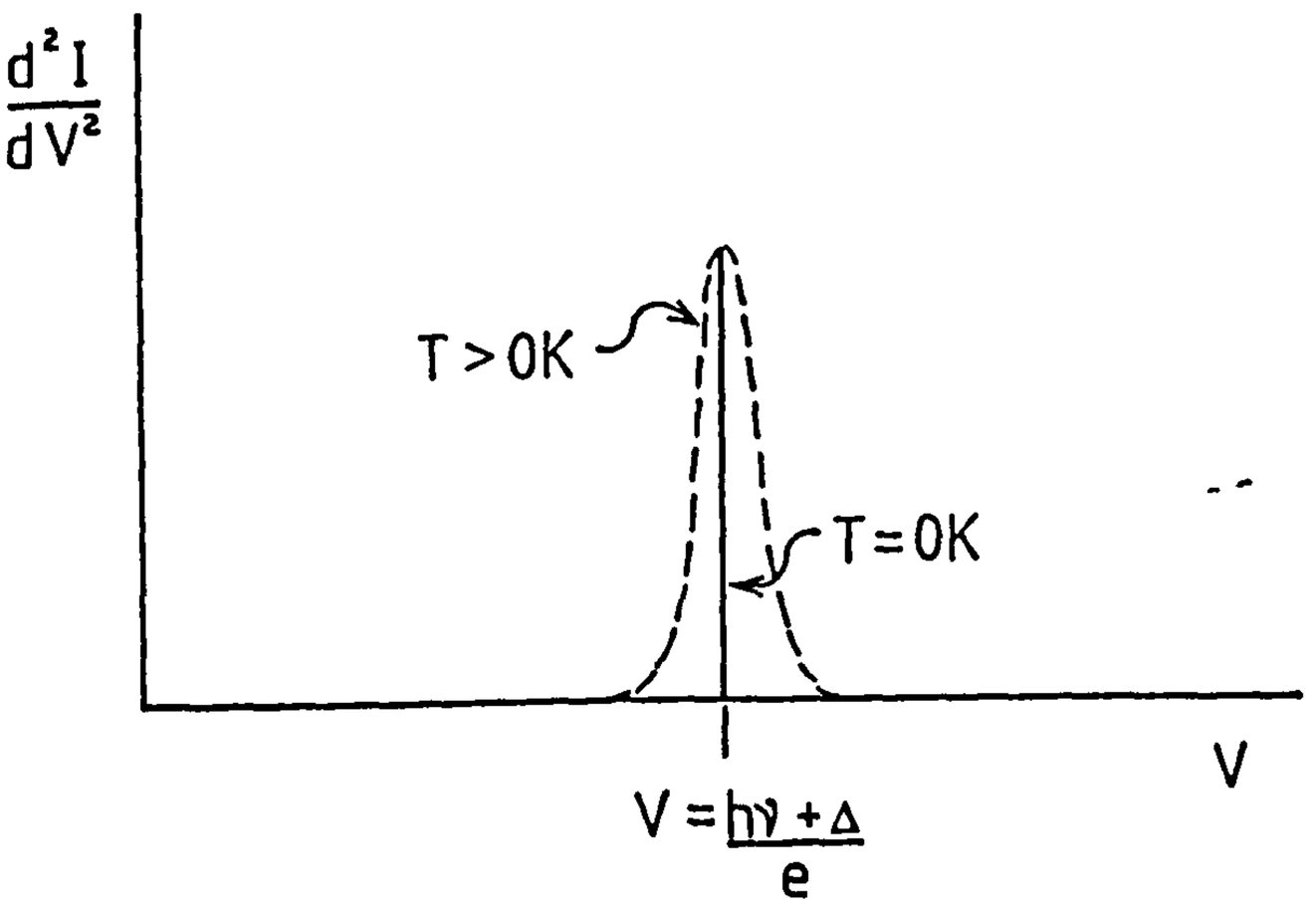
d²I/dV²
T>0K
T=0K
V
V = hν + Δ / e

(c)

1.3 METHODOLOGY OF THE PRESENT WORK

The present work will demonstrate that certain polymeric adhesives may yield IET spectra. Polymers have been successfully incorporated into IET junctions by the techniques of liquid-phase doping from solution (15), and glow-discharge polymerization (3,4,38,39). Results from the latter in particular have been promising, and suggest that the Aℓ-oxide layers are not damaged during polymer deposition.

With the intension of gaining further insight into polymeric adsorption on a monomolecular level, related monomers and solvents have also been investigated by vapour-phase, and infusion doping (23). For the most part these (volatile) compounds are only weakly adsorbed on Aℓ-oxide, and therefore would not readily yield IET spectra when either liquid-, or vapour-phase doped. Infusion doping with solvents by their introduction to the Aℓ-oxide surface through grain boundaries in the top Pb electrode has proved fruitful; a simple model of the dynamics of the infusion process has been proposed and published arising from this work (37). Unfortunately infusion doping with monomers has not been successful; possible explanations for this are discussed.

Supplementary work to fabricate IET junctions having Aℓ-oxide layers of reproducible composition and structure has also been undertaken; these oxides were formed by glow-discharge oxidation under controlled conditions, and serve as a useful starting point for further adsorption studies. Preliminary work to vapour-phase dope these oxides with ethylacetate and D_2O has been completed. Extension of the techniques to facilitate doping with a wider range of compounds would be the next logical step.

A brief account of the approach that was adopted for the above work is now given. It is this work which forms the basis of the experimental chapters of this thesis (Chapters 3 to 7).

1.3.1 Incorporation of Polymers into IET Junctions by Liquid-phase Doping

IETS is particularly appropriate for the study of organic compounds used as adhesives or adhesion promoters adsorbed on aluminium oxide since, as was mentioned earlier, aluminium is a widely studied and commercially important material for adhesive bonding. Other workers have used the technique to investigate both epoxides and their mixtures with aliphatic amines (14), cyanoacrylates (40), and silane coupling agents (41) adsorbed on aluminium oxide. However, none of these incorporated polymers in IET junctions, although in some cases small molecules were used which then polymerized on the oxide surface. IET spectra of some synthetic polymers incorporated directly into IET junctions by the technique of liquid-phase doping are presented and assigned, the first time to the best of the author's knowledge that this has been achieved. Several polymers including polyvinylacetate (PVA) which is widely used as an adhesive for wood and paper, polymethylmethacrylate (PMMA) which forms the matrix phase in certain rubber-modified reactive adhesives used for bonding metals and other substrates, and polyvinylalcohol (PVOH) also used as an adhesive for paper have been investigated.

By comparing IET, and IR spectra of the above polymers, it has been possible to investigate the nature of their adsorption of aluminium oxide.

Other related polymers have been investigated leading to an improved understanding of their surface chemistries. Full details of the polymers studied appear in Chapter 5.

1.3.2 Incorporation of Glow-discharge Polymerized (GDP) Films into IET Junctions

In recent years several applications for plasma-, or glow-discharge

polymerization have emerged. These include the deposition of thin protective polymer films on the walls of reaction vessels (38), and Si O_2 films for semiconductor device applications (48,49). Metal surfaces have also been treated for the improvement of adhesive joints (3,39,50) which is of particular interest in the present work.

The general principle of the technique is that a controlled flow of monomer vapour is introduced into a sealed, evacuated chamber within which a radio frequency glow-discharge may be established. Energy from the dischrage is imported to the monomer molecules which are then ionised, thus generating active centres for polymerization. A GDP film may then be deposited on any electrically isolated substrate held within the discharge. The structure of such films depends mainly on the operating conditions of the discharge, and to a lesser extent the nature and flow-rate of the monomers. GDP films formed in this way are generally highly crosslinked, relatively pinhole free, and to date have been of the order of a few μm thick. Thinner but continuous films a few tenths of nm's thick are required for IETS analyses. Details of the apparatus developed to deposit such films on the oxidized Aℓ base electrodes of IET junctions is described in Chapter 6.

An immediate advantage of the glow-discharge polymerization technique in the context of IETS is that it precludes the need for solvents which are obviously essential for liquid-phase doping. Any polymer-solvent interactions are thus avoided; it is possible that such inter-actions may lead to slight variations in peak position and intensity as will be discussed in Chapter 5. Spectra obtained by liquid-phase doping and glow-discharge polymerization therefore provide valuable complementary information concerning the nature of polymeric adsorption. Generally speaking, the glow-discharge technique offers considerable promise for

for further work, since films can be deposited relatively quickly and easily in a controlled atmosphere if necessary.

The first IETS study of GDP films was due to Magno and Adler in 1976 (51). They deposited films of benzene and ethylene on Aℓ- and Mg-oxides; however, evidence for the polymerization of these compounds was not particularly clear.

In the present work several monomers including vinylacetate, methylmethacrylate, ethylacrylate and acrylonitrile have been successfully glow-discharge polymerized and incorporated in IET junctions. The spectra of GDP vinylacetate, and methylmethacrylate are in good agreement with their liquid-phase doped counterparts.

By suitably modifying the operating conditions of the glow-discharge, thicker films of polyvinylacetate, and polymethylmethacrylate have been deposited for subsequent IR spectroscopic analyses. The IR spectra obtained were in good agreement with those previously recorded by other workers (52). The above IET and IR spectra and those of other compounds studied are presented and discussed in Chapter 6.

1.3.3 Infusion Doping of IET Junctions with Solvents and Monomers

Infusion doping was considered to be one possible method for investigating the adsorption of monomers and associated solvents. A common practice amongst IET spectroscopists is to investigate the adsorption of members of a homologous series of compounds on the metal oxide surface. Monobasic, C_n-aliphatic acids for example have been studied in this way upto n=18 (42)). Such studies give an insight as to which functional groups of the compounds are actively involved in adsorption, and also general trends regarding peak positions and intensities as the chain length is increased. By the same token, an

investigation of monomers and solvents may assist in interpreting the results obtained from the respective polymers.

The technique of infusion doping relies on the migration of dopant molecules to the oxide surface of the base electrode of a completed, undoped IET junction by penetration through the grain bounderies of the counter electrode metal. To date infusion doping has only been studied for Aℓ/Aℓ-oxide/Pb junctions (43,44,45). Previous workers have eliminated edge effects by suitable masking and have established that a decreased infusion rate is associated with an increase in thickness of the Pb electrode (44,45).

It has been suggested that the combined presence of CO_2 and water vapour at the Pb electrode generates formic acid - a frequent contaminant in infusion doping (45). Accordingly, in the present work a CO_2 free environment was employed; formic acid contamination was not apparent in the resulting IET spectra. Rapid and accurate low-bias junction conductance measurements were taken during infusion by employing a digital multimeter interfaced to a microcomputer. Broadly speaking, decreases in junction conductance indicate corresponding increases in thickness of the insulating barrier (46,47). Intermittent conductance measurements are therefore valuable in estimating the optimum infusion time (it is recalled that a monolayer thickness of adsorbed material gives optimum spectral sensitivity).

However, it has been suggested that other polar solvents may also assist in the infusion process (44). Consequently it was not clear at the outset whether or not compounds with a limited solubility in water would yield good quality IET spectra. Phenol, for example, is only slightly soluble in water but gives good quality spectra when doped in this way. It was decided to perform a series of experiments to determine

whether or not vinylacetate, and methylmethacrylate could be infused in the presence of water vapour or acetone. These experiments proved unsuccessful; blank spectra were obtained corresponding to oxide/hydroxyl layer thickening only. However, some physical insight was gained regarding the dynamics of the infusion process. Conductance changes during the infusion of pure water, and water/acetone mixtures were monitored; plots of junction conductance of a function of time revealed clear evidence of regions of different slope. A simple model has been proposed and published which to a first approximation predicts the form of these plots (37). Full details of the infusion doping apparatus and the above model are given in Chapter 4.

1.3.4 Preparation of IET Junctions having Aℓ-oxide Layers formed by Glow-discharge Oxidation under Controlled Conditions

The majority of compounds studied in the present work have been adsorbed on to Aℓ-oxides which were formed simply by exposing the freshly evaporated Aℓ base electrodes to an atmosphere of laboratory air at room temperature for 1 or 2 minutes; these are commonly referred to as room, or thermal oxides (18,19,23). They are believed to have an amorphous structure (53-58), and their surface is populated by adsorbed hydroxyl groups and traces of low molecular weight hydrocarbon contaminants (23,24). Clearly, the atomospheric conditions during oxide growth will affect their surface compositions. On the whole, thermal oxides formed routinely in the author's laboratory are acceptably clean for IETS work. Levels of contamination are frequently checked by fabricating blank junctions (i.e. Aℓ/Aℓ-oxide/Pb) and recording their IET spectra. However, on occasion, peaks due to the adsorbed carboxylate anion are also present. A probable cause of these peaks is small quanitities of

adsorbed formic acid which is known to strongly chemisorb as the formate anion (59,60,61). The formic acid may be air-borne, or, in the context of infusion doping may be produced as a result of reactions between atmospheric CO_2 and water vapour at the Pb electrode (45). Elimination of these carboxylate peaks from blank IET spectra is essential; interpretation of the adsorption of several other compounds on Aℓ-oxide also hinges on their presence. For example, carboxylic acids dissociate on Aℓ-oxide and are subsequently chemisorbed as their carboxylate anion giving rise to the aforementioned peaks (60). Moreover, in the context of the present work, certain ester polymers also give rise to these peaks (15).

Clearly, one must be able to differentiate between carboxylate peaks due to the dopant in question, and those which arise partly as an artifact of the device fabrication procedure. It was therefore considered appropriate and desirable to produce routinely contamination-free slightly hydrated oxides and investigate the feasibility of doping them in situ. An apparatus has been developed to this end, and is fully described in Chapter 7. The apparatus also permitted the oxides to be vapour-phase doped with certain compounds without breaking vacuum.

Blank junctions and those vapour-phase doped with D_2O have shown no evidence of carboxylate features. Ethylacrylate, a monomer used for the manufacture of synthetic resins, has also been successfully doped, and its adsorption is briefly discussed in Chapter 7.

1.4 SUMMARY OF THE WORK PRESENTED IN THIS THESIS

Firstly, the essential theory of elastic and inelastic tunnelling will be described in Chapter 2. This will be developed to illustrate the fundamental principles of the technique of IETS.

The implementation of IETS in the author's laboratory including junction fabrication and assessment together with the principles of the spectrometers operation are given in Chapter 3.

Chapters 4 to 7 account for the majority of the experimental work already outlined above; results, discussions and conclusions are included in each of these chapters.

Finally, general conclusions drawn from the above results are presented in Chapter 8 together with a discussion of their inter-relationship, and some suggestions for further study.

REFERENCES - Chapter 1

1. See for example "Adhesion Aspects of Polymer Coatings", K.L.Mittal (Ed.), Plenum Press, New York (1983).

2. See for example "Durability of Structural Adhesives", A.J.Kinloch (Ed.), Applied Science, London (1983).

3. N.Inagaki and H.Yasuda. J. Appl. Polym. Sci., 26, 3333 (1981).

4. S.M.Ojha, in Physics of Thin Films, G.Hass, M.H.Francombe and J.L.Vossen (Eds.). Academic Press, New York and London (1982), pp.237-296.

5. A.G.Guy. "Essentials of Material Science", McGraw-Hill Inc., Tokyo (1976).

6. A.Doroszkowski, (Research Department ICI Paints Division, Slough Berkshire). Paper presented at "The Metal-Polymer Interface" Royal Soceity of Chemistry, Faraday Division, Industrial PhysicaL Chemistry Group,Girton College, Cambridge, July 1984.

7. K.Kendal and J.C.Padget, (ICI New Science Group, Runcorn, Cheshire). Ibid.

8. D.L.Allara. Polym. Sci. Technol., 12(B), 751 (1980).

9. O.D.Hennemann and W.Brockman. J. Adhesion., 12, 297 (1981).

10. F.J.Boerio et al, Ibid, 13, 159 (1981).

11. R.C.Furneaux, G.E.Thomson and G.C.Wood. Corros. Sci., 18(10), 853 (1978).

12. D.Briggs in "Practical Surface Analysis by Auger and X-ray Photoelectron Spectroscopy", D.Briggs and M.P.Seah (Eds.), Wiley and Sons, London (1983), pp.366-

13. E.C.Millard, Lecture 34, "The International Adhesion Conference", Nottingham (1984). The Plastics and Rubber Institute (organisers).

14. J.Comyn, C.C.Horley, D.P.Oxley, R.G.Pritchard and J.L.Tegg. J. Adhesion., 12, 171 (1981).

15. R.R.Mallik, R.G.Pritchard, C.C.Horley and J.Comyn. To appear in Polymer.

16. R.R.Mallik and D.P.Oxley. Paper presented at "The Metal-Polymer Interface", Royal Society of Chemistry, Faraday Division, Industrial Physical Chemistry Group, Girton College, Cambridge, July 1984.

17. R.R.Mallik et al, Poster Paper 1, "The International Adhesion Conference", Nottingham (1984). The Plastics and Rubber Institute (organisers).

18. R.C.Jaklevic and J.Lambe. Phys. Rev. Lett., 17, 1139 (1966).

19. J.Lambe and R.C.Jaklevic. Phys. Rev., 165, 821 (1968).

20. I.Giaever. Phys. Rev. Lett., 5(4), 147 (1960).

21. J.C.Fisher and I.Giaever. J. Appl. Phys., 32(2), 172 (1961).

22. J.G.Simmons. J. Appl. Phys., 34(6), 1793 (1963).

23. P.K.Hansma. Phys. Rep. C., 30(2), 146-206 (1977).

24. R.G.Keil, T.P.Graham and K.P.Roenker. Appl. Spectrosc., 30(1), 1 (1976).

25. Kirtley. J. Am. Chem. Soc., 80, 217 (1980).

26. H.W.White and T.Wolfram. Methods Exp. Phys., 16(A), 149 (1980).

27. P.N.Shott and B.O.Field. Surf. Int. Anal., 1(2), 63 (1979).

28. W.H.Weinberg. Ann. Rev. Phys. Chem., 29, 115 (1978).

29. "Inelastic Electron Tunnelling Spectroscopy", T.Wolfram (Ed.) Springer-Verlag, Heidelberg (1978).

30. "Tunnelling Spectroscopy - Capabilities, Applications and New Techniques", P.K.Hansma (Ed.), Plenum Press, New York (1982).

31. Reference 30, Chapter 1.

32. A.Leger, J.Klein, M.Belin and D.Defourneau. Solid State Comm., 11, 1331 (1972).

33. S. de Cheveigne, J.Klein, A.Leger, M.Belin, and D.Defourneau. Phys. Rev. B., 15, 750 (1977).

34. H.Luth, V.Roll and S.Ewart. Phys. Rev. B., 18, 4241 (1978).

35. A.Adane, A.Fauconnet, J.Klein, A.Leger, M.Belin and D.Defourneau. Solid State Comm., 16, 1071 (1975).

36. J.D.Langan and P.K.Hansma. Surf. Sci., 52, 211 (1975).

37. R.R.Mallik, R.G.Pritchard, D.P.Oxley, C.C.Horley and J.Comyn. Thin Solid Films, 112, 193 (1984).

38. N.Inagaki, K.Nakazawa and K.Katsuura. J. Polym. Sci., Polym. Chem. Lett., 19, 335 (1981).

39 N.Inagaki, M.Itami and K.Katsuura. Int. J. Adhesion and Adhesives, 2(3), 169 (1982).

40. S.Reynolds, D.P.Oxley and R.G.Pritchard. Spectrochim. Acta., 38(A), 103 (1982).

41. D.M.Brewis, J.Comyn, D.P.Oxley, R.G.Pritchard, S.Reynolds and C.R.Werret., Surf. Int. Anal., 6(1), 40 (1984).

42. Ref. 30, Chapter 1.

43. R.C.Jaklevic and M.R.Gaerttner. Appl. Phys. Lett., 30(12), 646 (1977).

44. R.C.Jaklevic and M.R.Gaerttner. Appl. Surf. Sci., 1, 479 (1978).

45. W.J.Nelson, D.G.Walmsley and J.M.Bell. Thin Solid Films, 79, 229 (1981).

46. W.F.Brinkman, R.C.Dynes and J.M.Rowell. J. Appl. Phys., 41(5), 1915 (1970).

47. "Tunnelling Phenomena in Solids", E.Burstein and S.Lundqvist (Eds.) Plenum Press, New York (1969).

48. L.L.Alt, S.W.Ing Jnr., and K.W.Leandle. J. Electrochem. Soc., 110, 465 (1963).

49. D.R.Secrist and J.D.Mackenzie. J. Electrochem. Soc., 113, 914 (1966).

50. A.Moshonov and Y.Avny. J. App. Polym. Sci., 25, 771 (1980).

51. P.Magno and J.G.Adler. Thin Solid Films, 42, 237 (1977).

52. The Mercke Index of Chemicals and Drugs (9th Edn.) M.Windholz (Ed.), Rahway, N.J. (1976).

53. S.M.Bedair, F.Hofmann and H.P.Smith. J. App. Phys., 39, 4026C-4028C.

54. C.Beundort, C.Keller, H.Seidel and F.Theime. Surf. Sci., 67(2), 589 (1977).

55. D.Norman, S.Brennan, R.Jaeger and J.Stohr. Ibid., 105, L.297-L306 (1981).

56. F.Jona. J. Phys. Chem. Solids., 25, 2155 (1967).

58. C.B.Bargeron, B.H.Hall and A.N.Jette. Surf. Sci., 120, L483-L486, (1982).

59. B.F.Lewis, M.Moseman and W.H.Weinberg. Surf. Sci., 41, 142 (1974).

60. J.T.Hall and P.K.Hansma. Ibid., 76, 61 (1978).

61. S. de Cheveigne et al. Ibid., 105, 377 (1981).

CHAPTER 2

THEORETICAL ASPECTS OF ELASTIC, AND INELASTIC ELECTRON TUNNELLING IN THIN INSULATING LAYERS

This chapter will cover the basic theoretical framework of the quantum mechanical phenomenon of electron tunnelling. In the first instance, (elastic) electron tunnelling across a hypothetical rectangular potential barrier is considered; this particular case is then extended to describe elastic tunnelling in a thin film metal-insulator-metal (MIM) junction. Expressions will be derived for the probability of an electron being transmitted through the hypothetical barrier, and for the electron tunnelling currents flowing from one metal to another for the MIM junction under an applied bias.

Inelastic electron tunnelling in MIM junctions will then be considered; the associated theories of IETS which stem from the phenomenon will also be outlined. Finally, factors affecting IETS peak width and resolution are discussed.

2.1 FUNDAMENTAL CONCEPTS OF ELECTRON TUNNELLING

2.1.1 The Rectangular Potential Barrier.

Consider the rectangular potential barrier depicted in Fig.2.1. The barrier potential function, V(x), may be defined

$$V(x) = \begin{cases} 0, & x < 0 \quad \text{(region I)} \\ V_o, & 0 < x < a \quad \text{(region II)} \\ 0, & x > a \quad \text{(region III)} \end{cases}$$

Now, let an electron of total energy, E, in region I be incident upon the barrier in the increasing x direction. For the present work the case where $E < V_o$ is of particular interest. Classically for $E < V_o$ the electron will have unit probability of being reflected from the barrier. However, quantum mechanical considerations predict that it has a finite probability of being transmitted through the barrier, which is critically dependent on the barrier thickness.

The wave motion of the incident electron may be described by the one-dimensional time-independent Schrodinger equation (SE)

$$-\frac{\hbar^2}{2m}\frac{d^2\psi(x)}{dx^2} + V(x)\phi(x) = E\phi(x) \qquad \ldots \quad 2.1$$

where $\phi(x)$ is the electron wave function, m is the electron mass, and $h = h$ (Plancks constant)$/2\pi$. Mathematically the above equation is much simpler than the time-dependent, or many dimensional SE's because it is an ordinary rather than partial differential equation and may be solved analytically. For $E < V_o$ the general solutions of 2.1 in regions I, II and III are:

$$\text{I} \quad \phi_1(x) = Ae^{ikx} + Be^{-ikx}, \quad x < 0 \qquad \ldots \quad 2.2$$

$$\text{II} \quad \phi_2(x) = Ce^{k_1 x} + De^{-k_1 x}, \quad 0 < x < a \qquad \ldots \quad 2.3$$

$$\text{III} \quad \phi_3(x) = Fe^{ikx} + Ge^{-ikx}, \quad x > a \qquad \ldots \quad 2.4$$

Fig.2.1

An electron of total energy, E, approaching a hypothetical rectangular potential barrier of height, V_o, and width a.

Fig.2.2.

An electron is now incident upon a slowly varing potential barrier whose shape is given by V(x)-E. This corresponds to a more realistic barrier potential. All symbols are defined in the text. (Figure transcribed from reference 6.)

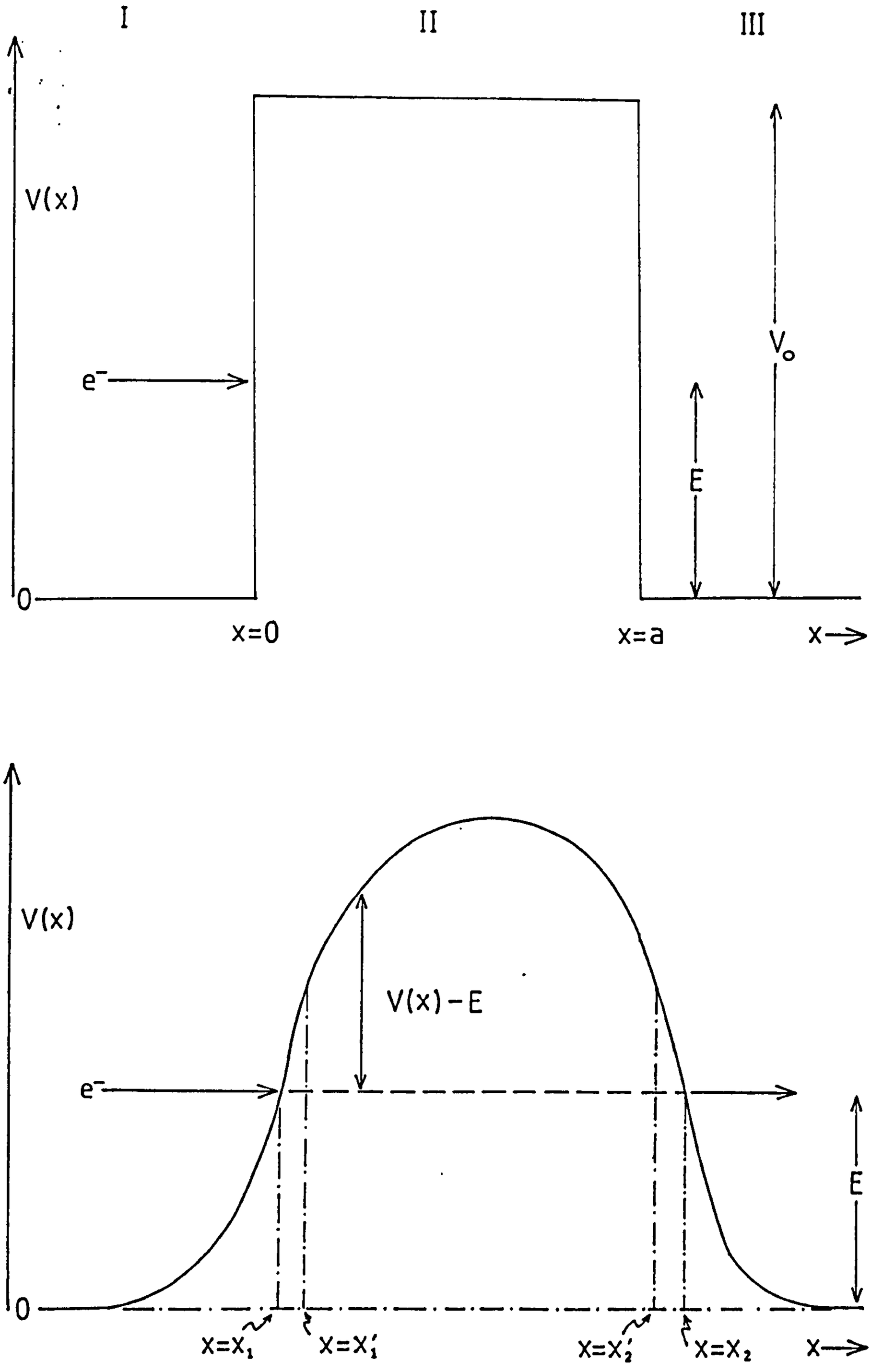
I
II
III
V(x)
e⁻
0
x=0
V₀
E
x=a
x→
V(x)
V(x)-E
e⁻
V(x)=V₀
E
0
x=x₁
x=x₁'
x=x₂'
x=x₂
x→

where $k = \left(\frac{2mE}{\hbar^2}\right)^{\frac{1}{2}}$, and $k_1 = \left(\frac{2m(V_o-E)}{\hbar^2}\right)^{\frac{1}{2}}$

are the propagation numbers and A to F are constants. It is noted that in region I the solution $\psi_1(x)$ is composed of a linear combination of plane wave functions due to the incident (Ae^{ikx}) and reflected (Be^{-ikx}) waves. Similarly, in region II, $\psi_2(x)$ is composed of a linear combination of incident and reflected waves. $\psi_3(x)$ can be simplified since there can be no reflected wave, therefore G = 0. Equations 2.2 to 2.4 must satisfy the conditions that the eigen function $\psi(x)$, and its derivative $\psi'(x)$ are everywhere finite (i.e. there are no singularities) and continuous. By applying the continuity conditions at the boundaries x = o, and x = a, the constants A, B, C, and D may be found in terms of F (say); the following equations are obtained.

Continuity conditions at x = o

$$\psi(o): \quad A + B = C + D \qquad \ldots \quad 2.5$$

$$\psi'(o): \quad ik(A-B) = k_1(C-D) \qquad \ldots \quad 2.6$$

continuity conditions at x = a

$$\psi(a): \quad Ce^{k_1 a} + De^{-k_1 a} = Fe^{ika} \qquad \ldots \quad 2.7$$

$$\psi'(a): \quad k_1(Ce^{k_1 a} - De^{-k_1 a}) = ikFe^{ika} \qquad \ldots \quad 2.8$$

The quantity of particular interest in the present work is the probability of an electron being transmitted through the barrier. Accordingly, the transmission coefficient, T, is defined in terms of the ratio of intensities of the probability fluxes incident upon, and transmitted through the barrier. The probability flux is essentially the rate of flow of probability per unit area normal to the direction of flow; it is proportional to the average velocity of the particle, and its position probability density (i.e. the intensity of the particle wave function at a given reference point).

The transmission coefficient as defined by Eisberg and Resnick (1) is therefore given by:

$$T = \frac{\upsilon\, F^*F}{\upsilon\, A^*A} \qquad \ldots \quad 2.9$$

where υ is the group velocity, and F* and A* are the complex conjugates of F and A respectively.

Equation 2.9 may be expressed as:

$$T = \frac{\upsilon\, F^*F}{\upsilon\, A^*A} = \left|\frac{F}{A}\right|^2 = \left|\frac{F}{A}\right|^2 \qquad \ldots \quad 2.9a$$

It is therefore necessary to evaluate the ratio F/A. The <u>modus operandi</u> for obtaining this quantity from the simultaneous equations 2.5 to 2.8 is outlined below:

(i) C can be elminated by combining equations 2.7 and 2.8 to give an expression for D in terms of F

$$D = \frac{F}{2}\left(1 - \frac{ik}{k_1}\right) e^{ika + k_1 a} \qquad \ldots \quad 2.10$$

(ii) Similarly, D can be eliminated from equations 2.7 and 2.8 to give

$$C = \frac{F}{2}\left(1 + \frac{ik}{k_1}\right) e^{ika - k_1 a} \qquad \ldots \quad 2.11$$

(iii) Now, equations 2.5 and 2.6 may be combined to eliminate B, giving an equation in A, C, and D, i.e.

$$A = \frac{k_1}{2ik}\,(C-D) + \frac{(C+D)}{2} \qquad \ldots \quad 2.12$$

(iii) Finally, substituting the expressions for C, and D (equations 2.10 and 2.11) into equation 2.12 gives an equation in A and F only, from which $|F/A|^2$ can be determined; one obtains

$$\left|\frac{F}{A}\right|^2 = \frac{4k^2k_i^2}{(k^2+k_1^2)\,\sinh^2(k_1a) + 4k^2k_1^2}$$

Substituting for k, and k_1 this expression may be manipulated to give

$$\left|\frac{F}{A}\right|^2 = T = \left[1 + \frac{(e^{k_1 a} - e^{-k_1 a})^2}{16\frac{E}{V_o}\left(1 - \frac{E}{V_o}\right)}\right]^{-1}, \quad E < V_o \quad \ldots \quad 2.13$$

which simplifies to

$$T = \left[1 + \frac{V_o^2 \ \mathrm{Sinh}^2(k_1 a)}{4E \quad (V_o - E)}\right]^{-1}, \quad E < V_o \quad \ldots \quad 2.14$$

It is noted that if $E << V_o$, then $k_1 >> k$, and $k_1 a >> 1$. Equation 2.13 then simplifies further to give:

$$T \simeq 16\frac{E}{V_o}\left(1 - \frac{E}{V_o}\right)e^{-2k_1 a} \quad \ldots \quad 2.15$$

This corresponds to the situation where transmission through the barrier is vanishingly small as is the case for electron tunnelling. Equation 2.15 illustrates clearly that the transmission coefficient is extremely sensitive to small changes in thickness of the insulating barrier. For example, if a (reasonable) value of 4 eV is assumed for the mean barrier height, V_o, and E is set to say $V_o/10$, then equation 2.15 becomes:

$$T \simeq 1.44\ e^{-1.95 \times 10^{10} a} \quad \ldots \ 2.15a$$

In a typical experimental situation, a is usually of the order of a few nm. However, even with such a thin insulating layer the probability that an electron will penetrate the barrier is very small; moreover, if its thickness is increased only slightly the probability decreases sharply as indicated below.

a/nm	T
0.1	0.2
1	4.9×10^{-9}
2	1.7×10^{-17}
10	3×10^{-85}

Thus an electron has a small but finite probability of tunnelling through the barrier provided that the latter is sufficiently thin.

An interesting situation arises when one considers the classical limit for T, i.e. as $a \to \infty$ for $E < V_o$. Under such circumstances T becomes infinitessimally small; the electron would be reflected from the barrier at the interface between regions I, and II. Indeed the probability of reflection may be estimated by a quantity known as the reflection coefficient (2), R, which is calculated in a similar manner to T, but is defined as the ratio of reflected to incident probability fluxes in region I, i.e.

$$R = \left|\frac{B}{A}\right|^2 \qquad \ldots \quad 2.16$$

and clearly, the general expression

$$R + T = 1 \qquad \ldots \quad 2.17$$

holds for all a.

2.1.2 Approximate Solutions of the Schrodinger Equation (SE) for Slowly Varying Potential Barrier Functions

The discussion above has shown that solutions of the one-dimensional, time-dependent SE for an electron incident upon a simple rectangular barrier gives some physical insight regarding the nature of tunnelling. Broadly speaking, the associated mathematics were relatively straightforward, allowing the transmission coefficient to be derived without making any approximations. In general however, practical barriers are non-rectangular (3), and consequently solving the SE exactly becomes much more complicated; therefore approximate methods are necessarily employed. As will now be seen, an approximate equation for the transmission coefficient may be derived using the Wentzel-Kramers-Brillouin-Jefferies (WKBJ) approximation, usually called the WKB approximation (4,5,6). This approximation is most applicable to "nearly Classical" situations, i.e. when transmission through

the barrier is small.

Consider tne hypothetical, non-rectangular potential barrier shown in Fig.2.2, with classical turning points x_1, and x_2. V(x) is now a slowly varying potential as opposed to the previously constant potential of the rectangular barrier. The SE may now be written in the form of a second order homogeneous ordinary differential equation, i.e.

$$\frac{d^2\psi(x)}{dx^2} - p^2(x)\psi(x) = 0 \qquad \ldots \quad 2.18$$

where $p^2(x) = 2m\,(V(x) - E)/\hbar^2$ ... 2.19

A solution of the form

$$\psi(x) = Kq(x)e^{-S(x)} \qquad \ldots \quad 2.20$$

is assumed for equation 2.18, where K is a constant, and q(x) is slowly varying. Equation 2.20 may be written

$$\phi(x) = K_1 e^{-S(x)} \qquad \ldots 2.21$$

where $K_1 = Kq(x)$. For convenience the functional notation will be dropped, i.e. call $\psi(x) = \phi$. Now, the identity

$$\frac{1}{\phi}\frac{d\phi}{dx} = \frac{d}{dx}(\ln \phi) \qquad \ldots \quad 2.22$$

gives

$$\frac{d}{dx}\left(\frac{1}{\phi}\frac{d\phi}{dx}\right) = \frac{d^2}{dx^2}(\ln \phi)$$

$$= \frac{d^2}{dx^2}\{\ln K_1 e^{-S(x)}\}$$

$$= \frac{d^2}{dx^2}\{\ln K_1 - S(x)\}$$

$$\frac{d}{dx}\left(\frac{1}{\phi}\frac{d\phi}{dx}\right) = -\frac{d^2S(x)}{dx^2} + \frac{d^2K_2}{dx^2} \qquad \ldots 2.23$$

where $K_2 = \ln K_1$, and $\frac{d^2K_2}{dx^2} = 0$ since q(x) is slowly varying. The LHS of equation 2.23 may be evaluated to give:

$$\frac{d}{dx}\left(\frac{1}{\psi}\frac{d\psi}{dx}\right) = \frac{1}{\psi}\frac{d^2\psi}{dx^2} - \left(\frac{1}{\psi}\frac{d\psi}{dx}\right)^2 = \frac{-d^2S(x)}{dx^2} \quad \ldots \quad 2.24$$

Equations 2.21 and 2.22 give

$$\frac{-d^2S(x)}{dx^2} = \frac{1}{\psi}\frac{d^2\psi}{dx^2} - \left(\frac{1}{\psi}\frac{d\psi}{dx}\right)^2$$

$$= \frac{1}{\psi}\frac{d^2\psi}{dx^2} - \left(\frac{d}{dx}\{\ln\psi\}\right)^2$$

$$= \frac{1}{\psi}\frac{d^2\psi}{dx^2} - \left(\frac{d}{dx}\{K_2 - S(x)\}\right)^2$$

$$\frac{-d^2S(x)}{dx^2} = \frac{1}{\psi}\frac{d^2\psi}{dx^2} - \left(\frac{dS(x)}{dx}\right)^2 \quad \ldots \quad 2.25$$

since terms involving $\frac{dK_2}{dx}$ are zero.

Rewriting equation 2.18 gives

$$\frac{1}{\psi}\frac{d^2\psi}{dx^2} = p^2(x) \quad \ldots \quad 2.26$$

Hence equations 2.25 and 2.26 may be combined to give

$$\left(\frac{dS(x)}{dx}\right)^2 - \frac{d^2S(x)}{dx^2} = p^2(x) \quad \ldots \quad 2.27$$

Therefore

$$\frac{dS(x)}{dx} = \left(p^2(x) + \frac{d^2S(x)}{dx^2}\right)^{1/2}$$

$$S(x) = \pm \int_{x_1}^{x} \left(p^2(x) + \frac{d^2S(x)}{dx^2}\right)^{\frac{1}{2}} dx \quad \ldots \quad 2.28$$

and for $p^2(x) >> \frac{d^2S(x)}{dx^2}$ this gives the first approximation to the exponent

of equations 2.19 and 2.20, i.e.

$$S_1(x) = \pm \int_{x_1}^{x} p(x)dx \quad \ldots \quad 2.29$$

or

$$\frac{d^2S_1(x)}{dx^2} = \pm \frac{dp(x)}{dx} \quad \ldots \quad 2.30$$

A simple predictor-corrector approach (7) may now be adopted to obtain an improved approximation $S_2(x)$. This is achieved by back-substituting

equation 2.30 (the corrector) into equation 2.28 (the predictor) to give

$$S_2(x) = \pm \int_{x_1}^{x} \left(p^2(x) + \frac{dp(x)}{dx} \right)^{\frac{1}{2}} dx \qquad \ldots 2.31$$

It is noted that if $\frac{dp(x)}{dx} << p^2(x)$, then the first, and second approximation

$S_1(x)$ and $S_2(x)$ (equations 2.29 and 2.31) are equivalent. Under these conditions the WKB approximation $\psi_W(x)$ for the eigenfunction in the barrier region is given by inserting equation 2.29 into equation 2.21, to give

$$\psi_W(x) = K_1 \, e^{\int_{x_1}^{x} p(x)dx}, \qquad \ldots 2.32$$

where $p(x) = \left[2m(V(x) - E)\right]^{\frac{1}{2}} / \hbar$

Since the case where the transmission coefficients is small is of concern here only the negative exponential solution is of importance inside the barrier. (The other solution corresponds to a small reflection from the distant interface, i.e. Region II/Region III (6)).

The WKB approximation to the transmission coefficient, T_W, may now be evaluated (6) as follows.

Consider the WKB solution, $\psi_W(x)$ of the form given in equation 2.32 at co-ordinates x_1', and x_2' near to x_1, and x_2 respectively inside the barrier region as shown in Fig.2.2. These co-ordinates are chosen such that the condition

$$p(x_1') = p(x_2') \qquad \ldots \quad 2.33$$

holds. Then, the ratio of the WKB solutions at these co-ordinates may be written

$$\frac{\psi_{W_{x_2'}}(x)}{\psi_{W_{x_1'}}(x)} = \frac{K_1 \, e^{-\int_{x_1}^{x_2'} p(x)dx}}{K_1 \, e^{-\int_{x_1}^{x_1'} p(x)dx}} = e^{\int_{x_1'}^{x_2'} p(x)dx} \qquad \ldots \quad 2.34$$

Where $\psi_{W_{x_1'}}(x)$, and $\psi_{W_{x_2'}}$ are the WKB solutions at points $x=x_1'$, and $x=x_2'$ respectively. $\psi_W(x)$ is slowly varying near these points since $d^2\psi/dx^2 = 0$ in these regions, therefore the approximate expression

$$\frac{\psi_{W_{x_1'}}(x)}{\psi_{W_{x_2'}}(x)} = e^{-\int_{x_1}^{x_2} p(x)dx} \qquad \ldots 2.35$$

gives the attenuation of the wave function inside the barrier. Thus T_W is given by

$$T_W = \left| \frac{\psi_{W_{x_1}}(x)}{\psi_{W_{x_2}}(x)} \right|^2 = e^{-2\int_{x_1}^{x_2} p(x)dx}$$

It is noted that if V(x) is assumed to be a constant, V_o, between $x_1 = 0$, and $x_2 = a$, i.e. the barrier is rectangular and of width, a, then equation 2.36 reduces to

$$T_W = e^{-2K_1 a} \qquad \ldots 2.36$$

Apart from the pre-exponential factor of $16\frac{E}{V_o}\left(1-\frac{E}{V_o}\right) \sim 1.44$, this is the same result as that obtained for the exact transmission coefficient for $E \ll V_o$ (equation 2.15).

2.2 ELASTIC ELECTRON TUNNELLING ACROSS THIN FILM METAL-INSULATOR-METAL (MIM) JUNCTIONS

A comprehensive review of the extensive literature on tunnelling in MIM junctions has been given by Duke (8); Burstein and Lundqvist (9) have compiled a readable exposition of the work of several authors covering various aspects of tunnelling phenomena in solids. Much of the work covered in the above articles stems from the pioneering work of Giaever (10), Fisher and Giaever (11), Simmons (3) and Josephson (12) to name a few. The present section considers the theoretical aspects of elastic tunnelling in MIM junctions in terms of a free-electron model of the electron density of states (due to Sommerfield (13)), and the Fermi functions for the junction. A fuller treatment has been given by Solymar (14).

2.2.1 The Elastic Tunnel Current

Fig.2.3a shows a simplified energy diagram of a M_1-I-M_2 plane parallel junction at T=0K with no applied bias across the electrodes. For simplicity the case where neither metal is superconducting is considered here. The thickness of the metals is not critical, but as was seen earlier, for an appreciable tunnelling current to flow the thickness, S, of the insulating layer is of the order $\lesssim$ 3 nm. For the present discussion it is reasonable to consider the trapezoidal barrier shown, although it should be remembered that practical barriers are somewhat more complex (3). When a small negative bias is applied to M_1 (say), the Fermi energies become separated by an amount eV as shown in Fig.2.3b. Elastic tunnelling of electrons from filled states in M_1 to empty states in M_2 through the barrier is now possible. Under the conditions of applied bias indicated in the figure, the number of electrons per unit time $n_e(E)$ which have sufficient energy to tunnel from M_1 to M_2 in the incremental energy range

Fig.2.3a

Simplified energy diagram for a MIM junction at T=OK with no applied bias; the Fermi energies E_{F_1} and E_{F_2} of the two metals are coincident. $g_1(E)$ and $g_2(E)$ are the density of electron states of the metals, ψ_1 and ψ_2 their work functions, and φ_1 and φ_2 interfacial barrier heights. The shaded regions represent filled states. For convenence neither metal is considered to be superconducting. (See also Fig.1.)

Fig.23b

When a dc bias, V is applied the Fermi energies become separated by an amount eV. The arrow represents an elastic electron tunnelling path. (Inelastic events not shown.)

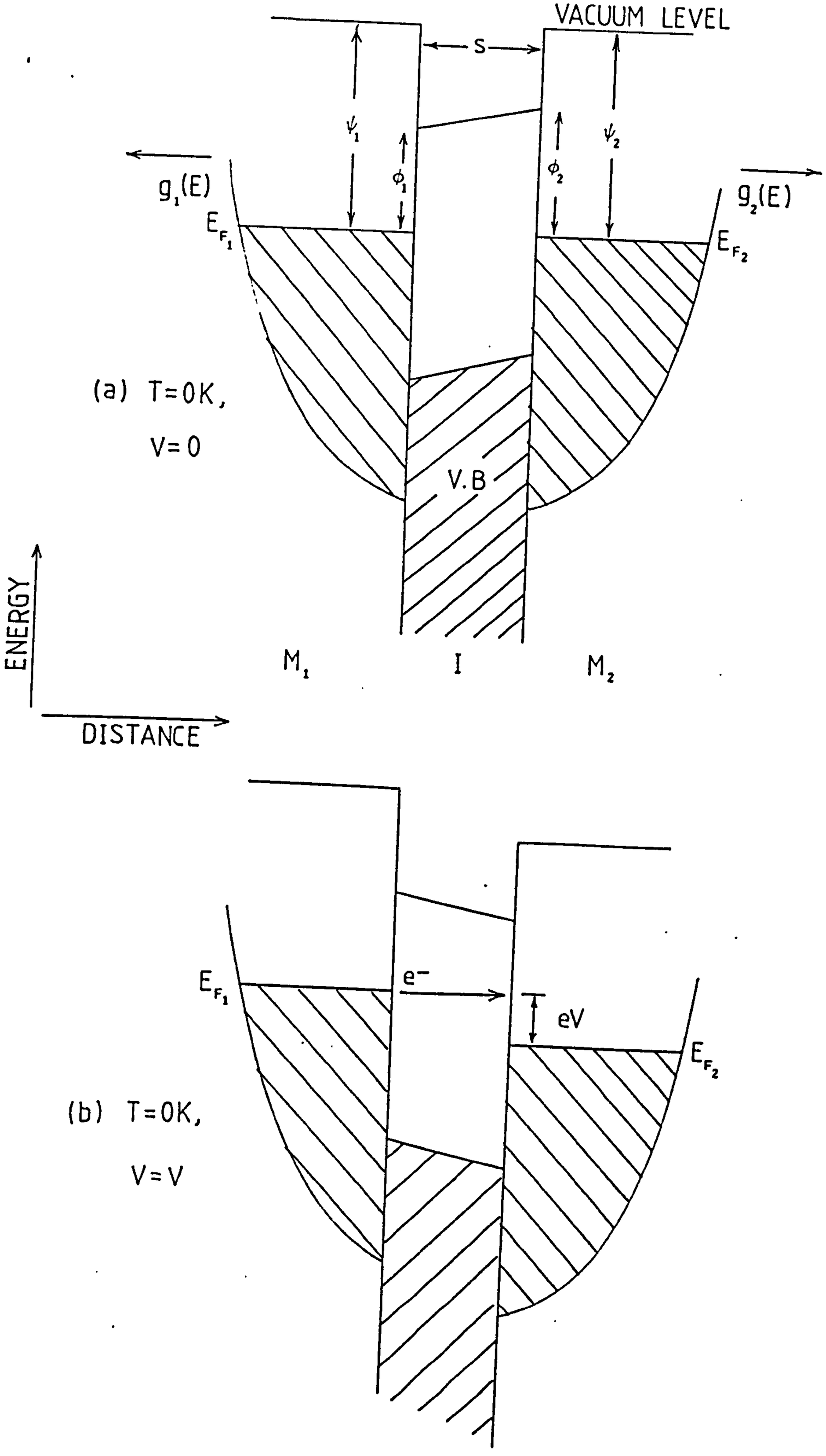

(a) T=0K,

V=0

(b) T=0K,

V=V

dE is proportional to the number of filled states in M_1, i.e.

$$n_e(E)dE \quad \alpha \quad g_1(E)f(E)dE \qquad \ldots \quad 2.37$$

where f(E) is the Fermi distribution function, and all energies are measured relative to E_{F_i}. The number of tunnelling electrons is also proportional to the number of empty states in M_2,

$$n_e(E)dE \quad \alpha \quad g(E+eV)[1-f(E+eV)]dE \qquad \ldots \quad 2.38$$

If the probability of tunnelling from M_1 to M_2 across the barrier $P_{1\rightarrow 2}(E)$ is now introduced, then the corresponding incremental tunnel current $dI_{1\rightarrow 2}$ may be written as

$$dI_{1\rightarrow 2} \propto P_{1\rightarrow 2}(E)g_1(E)g_2(E+eV)f(E)[1-f(E+eV)]dE \qquad \ldots \quad 2.39$$

By a similar analysis the incremental tunnel current in the opposite direction is given by

$$dI_{2\rightarrow 1} \propto P_{2\rightarrow 1}(E)g_2(E+eV)g_1(E)f(E+eV)[1-f(E)]dE \qquad \ldots \quad 2.40$$

It is assumed that the probability of electron tunnelling in either direction is equal, i.e.

$$P_{1\rightarrow 2}(E) = P_{2\rightarrow 1}(E) = P(E) \qquad \ldots \quad 2.41$$

Now, the net incremental elastic tunnel current, dI, is just

$$dI = dI_{1\rightarrow 2} - dI_{2\rightarrow 1} \qquad \ldots \quad 2.42$$

and therefore the total elastic tunnel current may be written

$$I \alpha \int dI \quad \alpha \int (dI_{1\rightarrow 2} - dI_{2\rightarrow 1}) \ ,$$

i.e.

$$I \alpha \int P(E)g_1(E)g_2(E+eV)[f(E)-f(E+eV)]dE \qquad \ldots \quad 2.43$$

Since the applied bias is small the Fermi energies of the two metals are not separated by a large energy and may be considered approximately equal; it will be assumed that

$$E_{F_1} \simeq E_{F_2} = E_{F_o} \qquad \ldots \quad 2.44$$

it follows that the total energy of the tunnelling electrons will also be

approximately E_{F_o}. Over the small range of energies the density of states functions may be considered to be slowly varying (in the vicinity of E_{F_o}) and written

$$\left.\begin{aligned} g_1(E) &\simeq g_1 \\ g_2(E+eV) &\simeq g_2(E) \simeq g_2 \end{aligned}\right\} \quad \ldots \quad 2.45$$

where g_1 and g_2 are taken as "nearly constant". Similarly, over the small energy range, dE, P(E) may be considered energy-independent, and written

$$P(E) \simeq P \quad \ldots \quad 2.46$$

Hence equation 2.43 reduces to

$$I \simeq A\, P g_1 g_2 \int [f(E)-f(E+eV)]dE \quad \ldots \quad 2.47$$

where A is a constant. Now by definition, the derivative of f(E) is given by

$$\frac{df(E)}{dE} = \lim_{\delta E \to 0} \left(\frac{f(E+\delta E) - f(E)}{\delta E} \right) \quad \ldots \quad 2.48$$

hence for small δE

$$\delta E \frac{df(E)}{dE} \simeq f(E+\delta E) - f(E) \quad \ldots \quad 2.49$$

Therefore for small applied bias, the Fermi function can be expressed

$$f(E) - f(E+eV) \simeq -eV\frac{df(E)}{dE}. \quad \ldots \quad 2.50$$

If $\frac{df}{dE}$ is approximated by a delta function (a step function) then the above equation may be substituted into equation 2.47 to give the final expression for the elastic tunnel current,

$$I \simeq A\, P g_1 g_2 eV \quad \ldots \quad 2.51$$

Hence, for small applied bias and at temperature T=OK the elastic tunnel should increase in an Ohmic manner, i.e. the low bias I-V characteristic of the tunnel junction should be linear.

The simple argument above serves to illustrate some of the fundamental concepts of elastic tunnelling based upon the density of

electron states, and the Fermi functions of the two metals, and as such provides some physical insight of the phenomenon. Elastic tunnelling is however usually expressed in terms of the tunnel current density as will now be discussed (8,9,15).

2.2.2 The Elastic Tunnel Current Density

The tunnel current density is defined as the number of electrons incident upon the barrier per unit area per second, multiplied by the probability that tunnelling will occur (15). As before, a plane-parallel tunnel junction configuration is assumed.

Consider electrons tunnelling from M_1 to M_2 in the x direction only, as indicated in Fig.2.3b. The number of quantum states, N(V), in the elemental volume dV of momentum space $dp_x dp_y dp_z$ is given by (15)

$$N(V)dV = \frac{2m^3}{h^3} \, du_x du_y du_z \qquad \ldots \quad 2.52$$

where u_x, u_y, and u_z are the components of electron velocity in cartesian space. A fraction f(E) of these quantum states can be occupied, therefore the total number of electrons per unit volume in the electrode is

$$N = N(u)dV = \int_{-\infty}^{\infty}\int_{-\infty}^{\infty}\int_{-\infty}^{\infty} \frac{2m^3}{h^3} f(E) du_x du_y du_z \qquad \ldots \quad 2.53$$

Introducting the transition probability across the barrier in the positive x direction donated by $P(E_x)$, the rate at which electrons tunnel through unit area normal to the x direction is

$$N_{1\rightarrow 2} = \frac{2m^3}{h^3} \int_{-\infty}^{\infty}\int_{-\infty}^{\infty}\int_{-\infty}^{\infty} f(E)P(E_x)u_x du_x du_y du_z \qquad \ldots \quad 2.54$$

where $N_{1\rightarrow 2}$ is the number of electrons per unit time, per unit area. Now

$$mu_x \, du_x = dE_x$$

therefore equation 2.54 simplifies to

$$N_{1\rightarrow 2} = \frac{2m^2}{h^3} \int_0^{\Phi} P(E_x)dE_x \int_{-\infty}^{\infty}\int_{-\infty}^{\infty} f(E)dv_y dv_z \quad \ldots \quad 2.53$$

where Φ is the metal-insulator interfacial barrier height. Equation 2.55 may be simplified further by converting to spherical polar co-ordinates (7,15) by setting

$$\left.\begin{aligned} v_y &= v_r \operatorname{Cos}\theta \\ v_z &= v_r \operatorname{Sin}\theta \end{aligned}\right\} \; dv_y dv_z = v_r dv_r d\theta$$

where v_r is now the radial component of electron velocity in a plane normal to the direction of tunnelling. Hence, equation 2.55 becomes

$$N_{1\rightarrow 2} = \frac{2m^2}{h^3} \int_0^{\Phi} P(E_x)dE_x \int_0^{\infty}\int_0^{2\pi} f(E)v_r dv_r d\theta \quad \ldots \quad 2.56$$

assuming conservation of momentum in the plane of the junction. Proceeding as before

$$mv_r dv_r = dE_r$$

where E_r is the radial component of electron energy in a plane normal to the direction of tunnelling, therefore

$$N_{1\rightarrow 2} = \frac{2m}{h^3} \int_0^{\Phi} P(E_x)dE_x \int_0^{\infty}\int_0^{2\pi} f(E)d\theta dE_r \quad \ldots \quad 2.57$$

Evaulating the angular dependent integral simplifies the above to give

$$N_{1\rightarrow 2} = \frac{4\pi m}{h^3} \int_0^{\Phi} P(E_x)dE_x \int_0^{\infty} f(E)dE_r \quad \ldots \quad 2.58$$

The current density due to electrons tunnelling from M_1 to M_2 is given by

$$J_{1\rightarrow 2} = N_{1\rightarrow 2} \quad e$$

i.e.

$$J_{1\rightarrow 2} = \frac{4\pi me}{h^3} \int_0^{\Phi} P(E_x)dE_x \int_0^{\infty} f(E)dE_r \qquad \ldots \quad 2.59$$

Following a similar mathematical approach to the one above, the current density in the opposite direction can be determined:

$$J_{2\rightarrow 1} = \frac{4\pi me}{h^3} \int_0^{\Phi} P(E_x)dE_x \int_0^{\infty} f(E+eV)dE_r \qquad \ldots \quad 2.60$$

So finally, the net current density

$$J = J_{1\rightarrow 2} - J_{2\rightarrow 1}$$

is given by

$$J = \frac{4\pi me}{h^3} \int_0^{\Phi} P(E_x)dE_x \int_0^{\infty} [f(E)-f(E+eV)]dE_r \qquad \ldots \quad 2.61$$

which assumes that the probability of tunnelling, $P(E_x)$, is equal in both directions.

The above 'direct approach' for calculating the elastic tunnel current density is exact within the limits of the approximations that are made to the barrier potential; it has been widely used where relatively simple potentials exist (16). However, when applied to problems possessing complicated potentials the mathematics become extremely cumbersome (17-20). A more flexible, and elegant method where the elastic current density is calculated to a good approximation was first introduced by Bardeen (21). He used it to explain Giaevers observation of an energy gap in the I-V characteristics of MIM tunnel junctions where one or both of the metals are superconducting (10). Bardeen's approach, usually referred to as the effective or transfer Hamiltonian

theory of tunnelling (8,9,21) has also been successfully applied to the theories of inelastic electron tunnelling as will be seen in Section 2.3. Before completing the present section on elastic tunnelling with an outline of this approach, it is appropriate and useful at this point to consider briefly a fundamental aspect of the approach; that is the treatment of tunnelling as a perturbation effect, and some interesting results which transpire.

2.2.3 Time Dependent Perturbation Theory Applied to Electron Tunnelling

Because the phenomenon of tunnelling is observed with an extremely small probability (see 2.1.1) it may be viewed as a small perturbing interaction between electron states on either side of the potential barrier. Small perturbation terms may then be added to the corresponding Hamiltonians which describe the electron wave functions (21,22). Hence, perturbation theory (2,23) may be used to calculate the rate at which electrons tunnel across the barrier, and therefore the tunnel current. In order to illustrate this, the time-dependent Schrodinger equation

$$H\Psi(r,t) = -\frac{\hbar}{i}\frac{\partial}{\partial t}\psi(r,t) \qquad \ldots \quad 2.62$$

is considered.

, and a solution of the form

$$\Psi(r,t) = \psi_m(r)e^{-iE_m t/\hbar} \qquad \ldots \quad 2.63$$

is assumed for the unperturbed system in question. The Hamiltonian may be broken up into two parts

$$H = H^o + H'(t) \qquad \ldots \quad 2.64$$

where H^o is time independent, and $H'(t)$ is the small perturbation (due to tunnelling in this case) which causes transitions between stationary states determined by H^o. Using the method of variation of constants (2),

the perturbed wave function, $\Psi(t)$, may be expressed as a linear combination of unperturbed functions, $\Psi^{o}(t)$, to give

$$\Psi(t) = \sum_{n} a_n(t)\Psi_n^{o}(r,t) \quad \ldots \quad 2.65$$

where $a_n(t)$ are the expansion coefficients. The wave function is assumed to be normalized for all times, i.e.

$$1 = \int \Psi^{*}\Psi \, d\tau \quad \ldots \quad 2.66$$

where Ψ^{*} is the complex conjugate of Ψ. Using equation 2.65 this gives:

$$1 = \int \sum_{n} a_n^{*}(t)\, \Psi_n^{o*}(r,t) \sum_{n'} a_{n'}(t)\Psi_{n'}^{o}(r,t)\, d\tau$$

$$= \sum_{n} \sum_{n'} a_n^{*}(t)a_{n'}(t) \int \Psi_n^{o*}(r,t)\Psi_{n'}^{o}(r,t)\, d\tau$$

$$1 = \sum_{n} \sum_{n'} a_n^{*}(t)a_{n'}(t) \int \psi_n^{o*}(r)\psi_{n'}^{o}(r) e^{-\frac{i}{\hbar}(E_n - E_{n'})t} \, d\tau \quad \ldots \quad 2.67$$

and since zeroth order functions are assumed to be orthonormal, i.e.

$$\int \Psi_n^{o}(r)\, \Psi_{n'}^{o*}(r)dr = \delta_{nn'} \quad \ldots \quad 2.68$$

where $\delta_{nn'}$ is the Kronecker delta, equation 2.67 becomes

$$\sum_{n} |a_n(t)|^2 = 1 \quad \ldots \quad 2.69$$

Now, the zeroth order wave functions must satisfy the zeroth order Schrodinger equation

$$H^{o}\, \Psi^{o}(r,t) = \frac{-\hbar}{i} \frac{\partial \Psi^{o}}{\partial t}(r,t) \quad \ldots \quad 2.70$$

and the perturbed equation which is

$$(H^{o} + H'(t))\, \Psi(r,t) = -\frac{\hbar}{i} \frac{\partial \Psi}{\partial t}(r,t) \quad \ldots \quad 2.71$$

Substituting the expansion given by equation 2.65 into equation 2.71 gives

$$H^{o}\sum_{n} a_n(t)\Psi_n^{o}(r,t) + H'(t)\sum_{n} a_n(t)\Psi_n^{o}(r,t) =$$

$$-\frac{\hbar}{i}\sum_{n} \dot{a}_n(t)\Psi_n^{o}(r,t) - \frac{\hbar}{i}\sum_{n} a_n(t)\frac{\partial}{\partial t}\Psi_n^{o}(r,t) \quad \ldots \quad 2.72$$

where $\dot{a}_n(t) = \frac{da_n}{dt}(t)$. But, by inspection of equation 2.71, it is seen that the first term on the LHS and last term on the RHS of equation 2.72 cancel, leaving

$$\sum_n a_n(t)\, H'(t)\, \Psi_n^o(r,t) = -\frac{\hbar}{i}\sum_n \dot{a}_n(t)\, \Psi_n^o(r,t) \qquad \ldots \quad 2.73$$

Premultiplying through by $\Psi_m^{o*}(r,t)$, integrating over $d\tau$, and utilizing the orthonormal property of the $\Psi^o(r,t)$' gives an expression for $\dot{a}_m(t)$

$$\dot{a}_m(t) = -\frac{i}{\hbar}\sum_n a_n(t) \int \Psi_m^{o*}\, t)H'(t)\Psi_n^o\,(r,t)dt \qquad \ldots \quad 2.74$$

Substituting for the $\Psi_n^o(r,t)$'s (see equation 2.63) into this expression gives the important result

$$\dot{a}_m(t) = -\frac{i}{\hbar}\sum_n a_n(t)H'_{mn}(t)\, e^{-\frac{i}{\hbar}(E_n-E_m)t} \qquad \ldots \quad 2.75$$

where

$$H'_{mn}(t) = \int \phi_m^{o*}(r)H'(t)\, \phi_n^o(x)d\tau \qquad \ldots \quad 2.76$$

is the integral over the time-independent wave functions, $\phi^o(r)$, and is referred to as the matrix element. Thus equation 2.75 describes a set of n first-order differential equations, each having a factor $a_n(t)$. It is now possible to consider the effect on the system of "switching on" a small perturbation.

Assume first that the system is initially in the state $\Psi_\ell^o(r,t)$ at time t=0. A perturbation is then switched on at t=0, and off at t=t'. Here t' is chosen such that the total effect of the perturbation is small. For the present example t' is chosen to be sufficiently short to ensure that the total probability of a transition out of the state $\Psi_o^o(r,t)$ is very small; i.e. such that the build-up of probability density in states other than $\Psi_o^o(r,t)$ is negligible (19). This being the case the expansion coefficients $a_n(t)$ may be set to a(o) plus small first

order corrections (effectively zero).

Then at time t=0

$$\left.\begin{aligned} a_n(0) &= 0 \quad , \quad n \neq \ell \\ a_\ell(0) &= 1 \end{aligned}\right\} \qquad \ldots \quad 2.77$$

Substituting these values into the RHS of equation 2.75 gives

$$\dot{a}_m(t) = -\frac{i}{\hbar} H'_{m\ell}(t)\, e^{-\frac{i}{\hbar}(E_\ell - E_m)t} \qquad \ldots \quad 2.78$$

which may be integrated to yield $a_m(t)$, i.e.

$$a_m(t) = -\frac{i}{\hbar} \int_0^t H'_{m\ell}(t) e^{-\frac{i\omega_{\ell m}}{\hbar}t} \, dt \quad , \qquad \ldots \quad 2.79$$

$$m \neq \ell$$

where for convenience the substitution

$$\omega_{\ell m} = \frac{E_\ell - E_m}{\hbar} = 2\pi\nu_{\ell m} \qquad \ldots \quad 2.80$$

has been made; $\nu_{\ell m}$ is the frequency corresponding to the energy difference between states $\Psi^o(r,t)$, and $\Psi^o_m(r,t)$. To a first-order approximation, the probability of finding the systems in state $\Psi^o_m(r,t)$ is given by $|a_m(t)|^2$.

Now if at time t=t′ the perturbation is switched off, the total transiton probability out of state $\Psi^o(r,t)$ to all other states $\Psi^o_m(r,t)$ may be found by summing over all the $|a_m(t)|^2$ terms at t=t′; the total transition rate, $N_{\ell\to m}$, out of state $\Psi^o(r,t)$ is then found by dividing by the transition probability by t′:

$$N_{\ell\to m} = \frac{1}{t_1} \sum_m |a_m(t)|^2$$

$$= \frac{1}{t_1} \int_{E_m} |a_m(t)|^2 \frac{dn}{dE_m} \, dE_m \qquad \ldots \quad 2.81$$

where $\frac{dn}{dE_m}$ is the number of accessible (empty) final states per unit energy.

By a change of variable (using equation 2.80; $dE_m = \hbar d\omega_{\ell m}$) and substituting for $|a_m(t)|^2$ using equation 2.79 the integral in 2.31 may be evaluated, and plotted as a function of $\omega_{\ell m}$. It can be shown that for reasonable observation times, the most significant contribution to the resulting integral occurs over a narrow energy range, $\Delta E_m = \hbar \Delta\omega_{\ell m}$. In this range, a main peak occurs in the integral whose width varies as $1/t'$, and the corresponding range of $\omega_{\ell m}$ values under this peak is about

$$\Delta\omega_{\ell m} \simeq \frac{1}{t'} \qquad \ldots \quad 2.82$$

Hence the uncertainty in energy of the system may be written as

$$\Delta E = \hbar \Delta\omega_{\ell m} \simeq \frac{\hbar}{t'} \qquad \ldots \quad 2.83$$

which is approximately what one would expect by consideration of the uncertainty principle. Since this energy range is very small, for all practical purposes it may be assumed that $H'_{\ell m}(t)$ and $\frac{dn}{dE_m}$ are constant. Equations 2.79 and 2.81 then give the final result

$$N_{\ell \to m} = \frac{2\pi}{h} |H'_{\ell m}(t)|^2 \frac{dn}{dE_m} \qquad \ldots \quad 2.84$$

Known as the "Golden Rule" of first order, time-dependent perturbation theory (24). It has been used to calculate transition rates in several quantum mechanical phenomena, and predicts that the transfer rate is proportional to the appropriate metrix element squared.

2.2.4 Bardeen's Method for Obtaining the Elastic Tunnel Current Density

A rigorous description of Bardeen's method (21) is beyond the requirements of this thesis. Briefly, he calculated inter-electrode tunnelling rates using first order time dependent perturbation theory (2,5,6).

As outlined in the previous sub-section, tunnelling was considered as a small perturbing interaction between electron states on either side of the potential barrier. A central factor of the approach was the assumption that the Hamiltonian for the $M_1I.M_2$ junction can be written as the sum of three terms (21,25)

$$H = H_1 + H_2 + H_T \qquad \ldots \quad 2.85$$

where H_1 , and H_2 are the Hamiltonians which describe the electron wave functions on M_1, and M_2, and H_T is the transfer Hamiltonian describing the tunnelling of electrons from M_1 to M_2 through the insulating layer; i.e. the wave functions for the electrons in M_1 and M_2 are solutions to H_1 and H_2 respectively, and the wave function for the tunnelling electrons solutions to H_T. Bardeen used WKB approximations to the wave functions, and showed that the electron wave function in the barrier region due to tunnelling was exponentially decaying with distance. He then calculated the elastic transition rate (per unit time) between the electrodes by isolating the matrix element for tunnelling, and applying the Golden Rule (see Section 2.2.3). From this the total elastic tunnel current density was obtained. (This "transfer Hamiltonian" approach has been used effectively by Kirtley, Scalapino, and Hansma (26) to calculate <u>inelastic</u> tunnel current densities and will be discussed further in Section 2.3.) An outline of Bardeens method is now presented. The reader is referred to Duke (8), Kirtley (16), and Kane (22) for a more detailed description.

Tunnelling through the rectangular potential barrier shown in Fig.2.4a will be considered. The first step is to conceptually divide the barrier into two parts as shown in Figs.2.4b and 2.4c (16). Here the initial state wave function $\psi_i(x)$ is localized on the left side of the barrier by extending the barrier such that $x_2 = \infty$ (Fig.2.4b). Similarly

Fig.2.4a

A rectangular potential barrier of height V_o, and width, a. Also shown in the "exact" calculated exponentially decaying wave function in the barrier region from $x=x_1$ to $x=x_2$. The incident and reflected waves on the left are matched using continuity conditions (see Section 2.1.1) to a transmitted wave on the right. The transmission probability is the square of the ratio of incident to transmitted amplitudes. The amplitudes shown are for the illustration purposes only.

Fig.2.4b

In the transfer Hamiltonian formalism, x_2 is extended to infinity for calculation of the initial state wave function, $\phi_i(x)$.

Fig.2.4c

Similarly, x_1 is extended to $-\infty$to calculate the final state wave function, $\psi_f(x)$. An interaction potential is used to transfer an electron from the initial to final state. (Diagrams modified after Kirtley (16).)

(a)

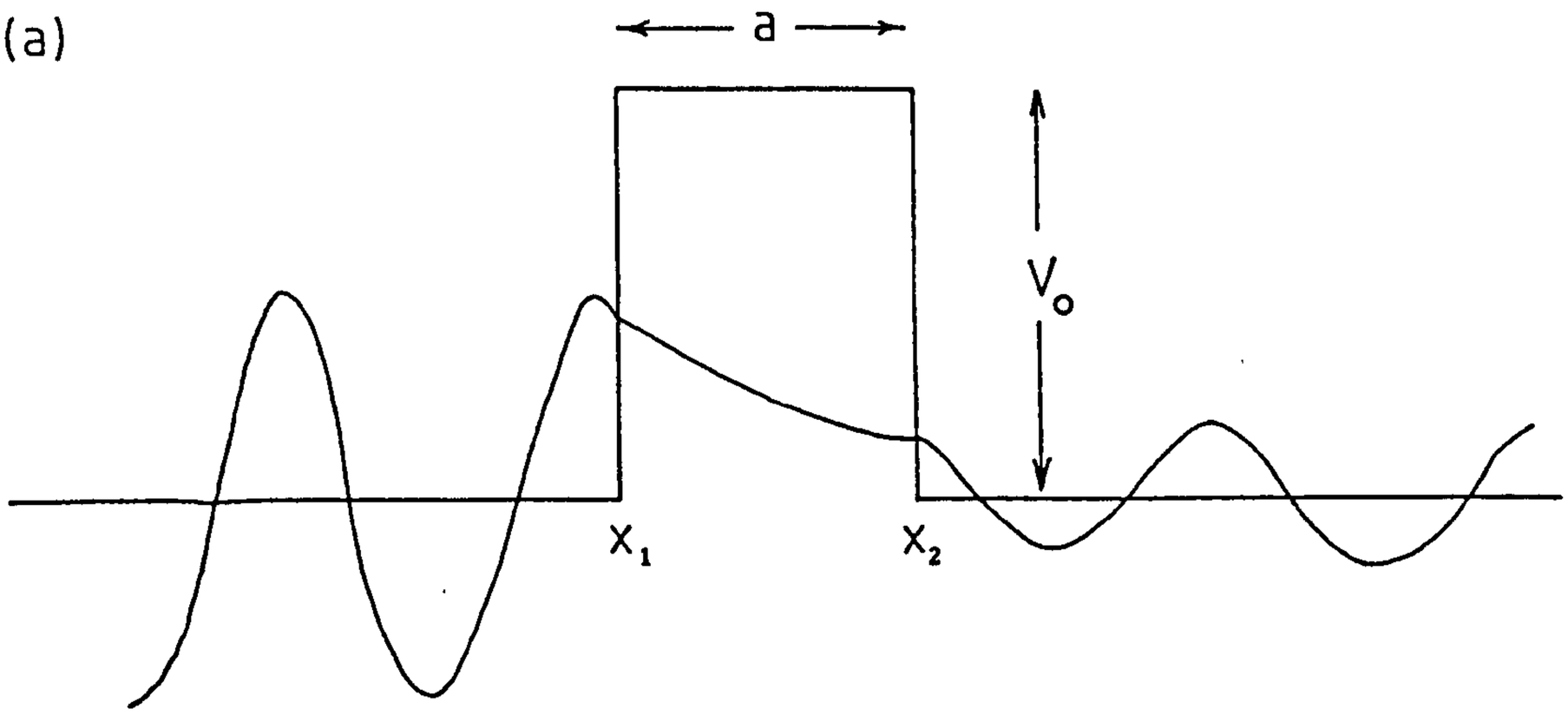

(b)

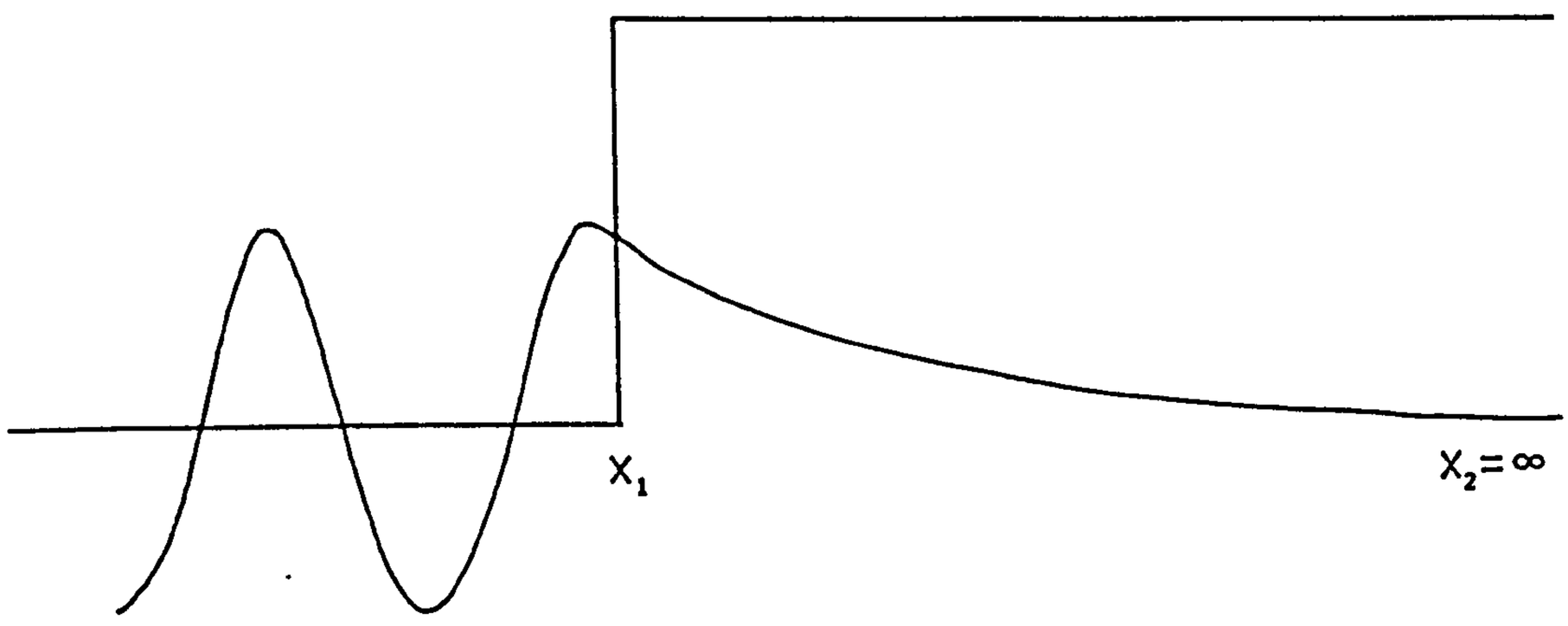

(c)

the final state $\psi_f(x)$ is localized by setting $x_1 = -\infty$. Both $\psi_i(x)$, and $\psi_f(x)$ are exponentially attenuated in the barrier region as shown in the figures, i.e.

$$\begin{aligned} \psi_i(x) &= Ae^{-k_1 x} \quad , x \geq x_1 \\ \psi_f(x) &= Be^{k_1 x} \quad , x \leq x_2 \end{aligned} \qquad \ldots \quad 2.86$$

where $k_1 = \left(\frac{2M(V_o - E)}{\hbar^2}\right)^{\frac{1}{2}}$. Now, these barrier solutions must match to the 'correct' solutions (which are simusoidally varying outside the barrier region as shown) at the interfaces x_1 and x_2. More specifically, $\psi_i(x)$ must match to the correct solution for $x \leq x_1$, and $\psi_f(x)$ must match to the correct solution for $x \geq x_2$. Multiple scattering effects are ignored in this approach, and the exponentially decaying wave from the left ($\psi_i(x)$) is not included when matching wave functions at the right hand interface ($x=x_2$).

Now, in the barrier region, i.e. for $x_1 \leq x \leq x_2$, both $\psi_i(x)$ and $\psi_f(x)$ are correct solutions of the Hamiltonian, H. To start the derivation, the electron is assumed to be initially in state $\psi_i(x)$ and then its transition rate into state $\psi_f(x)$ is calculated. The wave function in the barrier region may be expressed as a linear combination of initial and final states,

$$\Psi(x\ t) = C(t)\psi_i(x)e^{\frac{-iE_i t}{\hbar}} + D(t)\psi_f(x)e^{\frac{-iE_f t}{\hbar}} \qquad \ldots \quad 2.87$$

This is substituted into the time dependent Schrodinger equation (equation 2.62) which may be written

$$\frac{\partial}{\partial t}\Psi(x,t) = \frac{H}{i\hbar}\Psi(x,t)$$

to give

$$\psi_i\left[\dot{C}e^{\frac{-iE_it}{\hbar}} - C\frac{iE_i}{h}e^{\frac{-iE_it}{\hbar}}\right] + \psi_f\left[\dot{D}e^{\frac{-iE_ft}{\hbar}} - D\frac{iE_f}{h}e^{\frac{-iE_ft}{\hbar}}\right] = \frac{H}{ih}\left[C\psi_i e^{\frac{-iE_it}{\hbar}} + D\psi_f e^{\frac{-iE_ft}{\hbar}}\right] \quad \ldots \quad 2.88$$

Where the functional notation has been dropped for convenience, and the dot represents differentiation with respect to time. Since tunnelling is being considered as a weak perturbation, $C \simeq 1$, $D \simeq 0$, and the normalization (22),

$$\frac{d}{dt}(CC^* + DD^*) = 0$$

imples that $\dot{C} \simeq 0$ also. Substituting these values into equation 2.88 gives

$$\dot{D} = \frac{1}{i\hbar}\frac{}{\dot{\psi}_f}(H - E_i)\psi_i e^{\frac{i}{\hbar}(E_f - E_t)t} \quad \ldots \quad 2.89$$

and assuming that ψ_i, and ψ_f are normalized

$$\dot{D} = \int \psi_f^* \dot{D}\psi_f dx = \frac{1}{i\hbar}\int \psi_f^*(H-E_i)\psi_i dx \; e^{\frac{i}{\hbar}(E_f-E_i)t} \quad \ldots \quad 2.90$$

Now as discussed in Section 2.2.3, the perturbed Hamiltonian may be written as

$$H = H^o + H'$$

and ψ_i, and ψ_f are eigenfunctions of H^o, i.e. they satisfy the equations

$$H^o\psi_i = E_i\psi_i \quad ,$$

$$H^o\psi_f = E_f\psi_f \quad ,$$

therefore

$$H\psi_f = H^o\psi_f + H'\psi_f \quad ,$$

$$= E_f\psi_f + H'\psi_f$$

This implies that

$$\frac{1}{i\hbar}\int \psi_i^*(H-E_f)\psi_f dx = -\frac{1}{ih}\int \psi_i^* H'\psi_f dx \qquad \ldots \quad 2.91$$

By inspection it is observed that this expression is analogous to the matrix element given by equation 2.76. Accordingly, the effective matrix element for tunnelling in the direction of increasing x, $T_{i\to f}$ as the LHS of equation 2.91, i.e.

$$T_{i\to f} = \int \psi_i^*(H-E_f)\psi_f dx \qquad \ldots \quad 2.92$$

From the conditions defined in equation 2.86 and the paragraph below it, ψ_f, is a correct solution of the exact Hamiltonian H for $x > x_1$, therefore the above integral is zero for $x > x_1$. By adding the symmetric term

$$T' = -\int \psi_f(H-E_i)\psi_i^* dx$$

(which is zero for $x < x_2$) to equation 2.92 gives

$$T^e_{i\to f} = \int_{x_b}^{-\infty} (\psi_i^*(H-E_f)\psi_f - \psi_f(H-E_i)\psi_i^*)dx \qquad \ldots \quad 2.93$$

$$x_1 < x < x_2$$

Where $T^e_{i\to f}$ is the matrix element for elastic tunnelling. The extra term does not alter the result over the range of integration shown since the lower limit, x_b, is taken to lie in the barrier region where the integral is zero. Now, the present discussion is concerned with elastic tunnelling, therefore

$$E_i \simeq E_f \simeq E_o$$

so equation 2.93 becomes

$$T^e_{i\to f} = \int_{x_b}^{-\infty} (\psi_i^* H\psi_f - \psi_f H\psi_i^*)dx \qquad \ldots \quad 2.94$$

Since the terms $\psi_i^* E_o \psi_f$, and $\psi_f E_o \psi_i^*$ cancel. Writing the Hamiltonian explicitly as

$$H = -\frac{\hbar^2}{2m}\frac{d^2}{dx^2} + V(x)$$

equation 2.94 becomes

$$T^e_{i\to f} = -\frac{\hbar^2}{2m}\int_{x_b}^{-\infty}\left(\psi_i^* \frac{d^2\psi_f}{dx^2} - \psi_f \frac{d^2\psi_i^*}{dx^2}\right)dx \quad \ldots \quad 2.95$$

as the matrix elements involving V(x), also cancel. Integrating this expression by parts gives the result

$$T^e_{i\to f} = -\frac{\hbar^2}{2m}\left[\psi_i^* \frac{d\psi_f}{dx} - \psi_i \frac{d\psi_f^*}{dx}\right]_{x_b} \quad \ldots \quad 2.96$$

since $\psi_f \to 0$ as $x \to -\infty$. The electron tunnel current operator, $j(x)$, may be defined as (22)

$$j(x) = -\frac{i\hbar}{2m}\left(\psi^*(x)\frac{d\psi}{dx} - \psi(x)\frac{d\psi^*}{dx}\right) \quad \ldots \quad 2.97$$

therefore equation 2.96 simplifies to

$$T^e_{i\to f} = -i\hbar\, j(x) \quad \ldots \quad 2.98$$

This may then be used to first calculate $N^e_{i\to f}$ the transition rate per unit time for electrons tunnelling elastically from initial to final states using the Golden Rule as defined in equation 2.84, i.e.

$$N^e_{i\to f} = \frac{2\pi}{h}\left|T^e_{i\to f}\right|^2 \frac{dn}{dE_f} \quad \ldots \quad 2.99$$

where $\frac{dn}{dE_f}$ is the number of empty (accessible) final states per unit energy. Finally, the total elastic tunnel current, $I^e_{i\to f}$, is obtained in a similar manner as before (see Section 2.2.1) by summing over all

possible initial and final momentum states (16) to give

$$I^{e}_{i\to f} = \frac{4\pi e}{h} \sum_{k_i} \sum_{k_f} |T^{e}_{i\to f}|^2 \, [f(E_i) - f(E_f+eV)]\delta(E_i-E_f) \qquad \ldots \quad 2.100$$

where V is the applied bias. (E_f should not be confused with E_F the Fermi Energy). The δ (step) function is defined

$$\delta(E_i-E_f) = \begin{cases} 0, & E_i \neq E_f \\ 1, & E_i = E_f \end{cases}$$

which ensures that $I^{e}_{i\to f} = 0$ unless $E_i = E_f$.

2.3 INELASTIC ELECTRON TUNNELLING IN MIM JUNCTIONS : ELECTRON ELECTRON-MOLECULE INTERACTIONS

Consider the simplified energy diagram for a M_1-I-M_2 junction at T=OK with a small negative bias, V, applied to M_1; the Fermi-levels of the metals are separated by an amount eV as shown in Fig.2.3b. Suppose now that a molecular oscillator of vibrational frequency is implanted in the barrier, and the applied bias is such that $V > h\nu/e$. In addition to the elastic (isoenergetic) electron tunnelling paths shown in the diagram, an additional path is now possible, *viz* electrons may tunnel inelastically from filled states in M_1 to empty lower energy states in M_2 by losing a quantum of energy, $h\nu$ in exciting the oscillator. Electron-molecule interactions (27) are not the only ones which give rise to inelastic tunnelling events; phonon excitations in the metal electrodes (28.29,30) and electronic transitions have also been reported (31).

Inelastic electron tunnelling interactions were first identified by Jaklevic and Lambe (27). Scalapino and Marcus (32) offered the initial theoretical explanation of the phenomenon in terms of a one-electron model. They assumed that the tunnelling electron interacted with the dipole moment (plus its image) of a molecular oscillator in the insulating barrier, situated near to a metal-insulator interface. Such interactions were shown to give rise to infra-red (IR) like vibrational modes in the corresponding IET spectra. The Scalapino-Marcus theory was extended by Lambe and Jaklevic (33) to include interactions between the tunnelling electrons and polarizabilities of the molecules to predict Raman like modes. Ten years later, Kirtley, Scalapino, and Hansma (26) proposed a somewhat more complex theory utilizing Bardeen's effective Hamiltonian approach (described earlier). Relative, and absolute IETS peak intensities were calculated which were in good agreement with

experimental data.

The present section begins with a description of these theories and some important predictions to which they give rise regarding peak intensities, and selection rules. Finally, the two main factors effecting resolution in IETS are discussed namely thermal and instrumental peak broadening.

2.3.1 The Scalepino-Marcus, and Lambe-Jaklevic Theories

Scalapino and Marcus (SM) assumed that the electric field of a tunnelling electron interacted with a Coulomb potential of a molecular dipole of energy $h\nu_n$ (and its image) situated near to one of the metal electrodes (32) as shown in Fig.2.5. Electron-molecule coupling was then viewed as a perturbation of the barrier height, and an expression was duly derived for the ratio of inelastic to elastic junction conductances. The theory will now be outlined in terms of the concepts developed in the previous sections.

From Fig.2.5 it is seen that the components of dipole moment and its image parallel to the interface cancel, while those perpendicular to the interface, P_x, are additive. Hence a net dipole sum of $2P_x$ perpendicular to the interface results. Thus the interaction potential $U_{int}(x)$ between the electron at position $(x, r_\perp)$ (co-ordinates as defined in the figure) and the molecule at the origin, O, is given by

$$U_{int}(x) = \frac{2eP_x x}{(x^2+r_\perp^2)^{3/2}} \quad \ldots \quad 2.101$$

If $U_{int}(x)$ is treated as the perturbing Hamiltonian leading to inelastic tunnelling, then the inelastic tunnelling current may be calculated in a similar manner to the elastic tunnelling current above. Using equation 2.76, the matrix element for inelastic tunnelling is

Fig.2.5

In the Scalapino-Marcus theory a molecular dipole is situated near to one of the metal electrodes. An image dipole is induced in the metal as shown. The component of dipole moment parallel to the plane of the junction and its image are equal and opposite and therefore cancel. The component perpendicular to the plane of the junction P_x, and its image P_x add to give a net perpendicular dipole sum of $2P_x$. Since point dipoles are assumed in the theory the dipole sum will act through point O, and may then interact with the electron and position $(x, r_\perp)$.

Fig.2.6

In the Kirtley-Scalapino-Hansma theory a series of point charges and their images in <u>both</u> metals are considered. The charges are located by position vectors $\underline{R}_1$, $\underline{R}_2$, $\underline{R}_3$ ... etc., relative to an arbitrary origin, O, on the surface of one metal. The electron is located by position vector $\underline{r}$.

SM

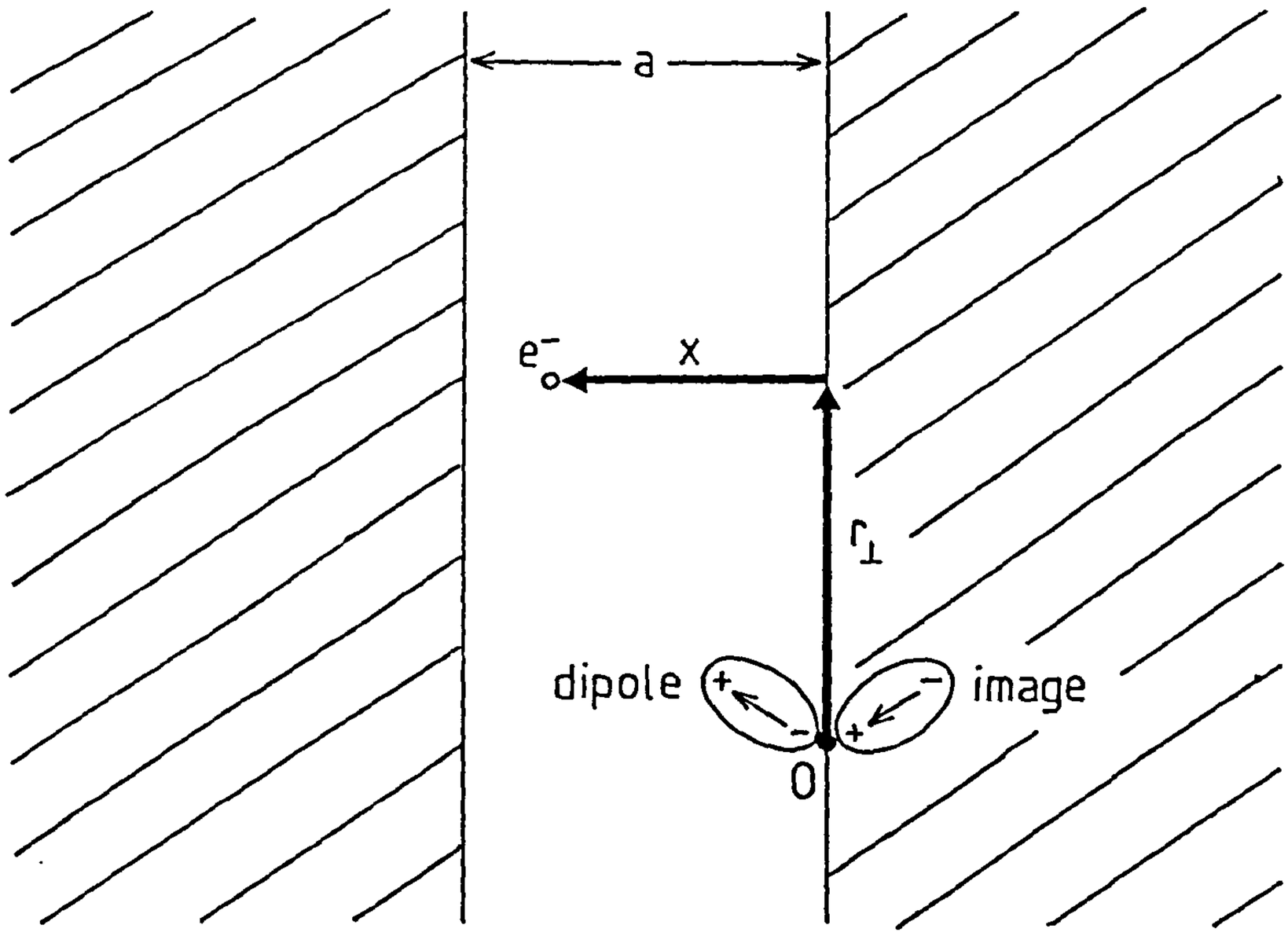
a
e^-_o
x
$r_\perp$
dipole
+
−
image
0
METAL
INSULATOR
METAL

KSH

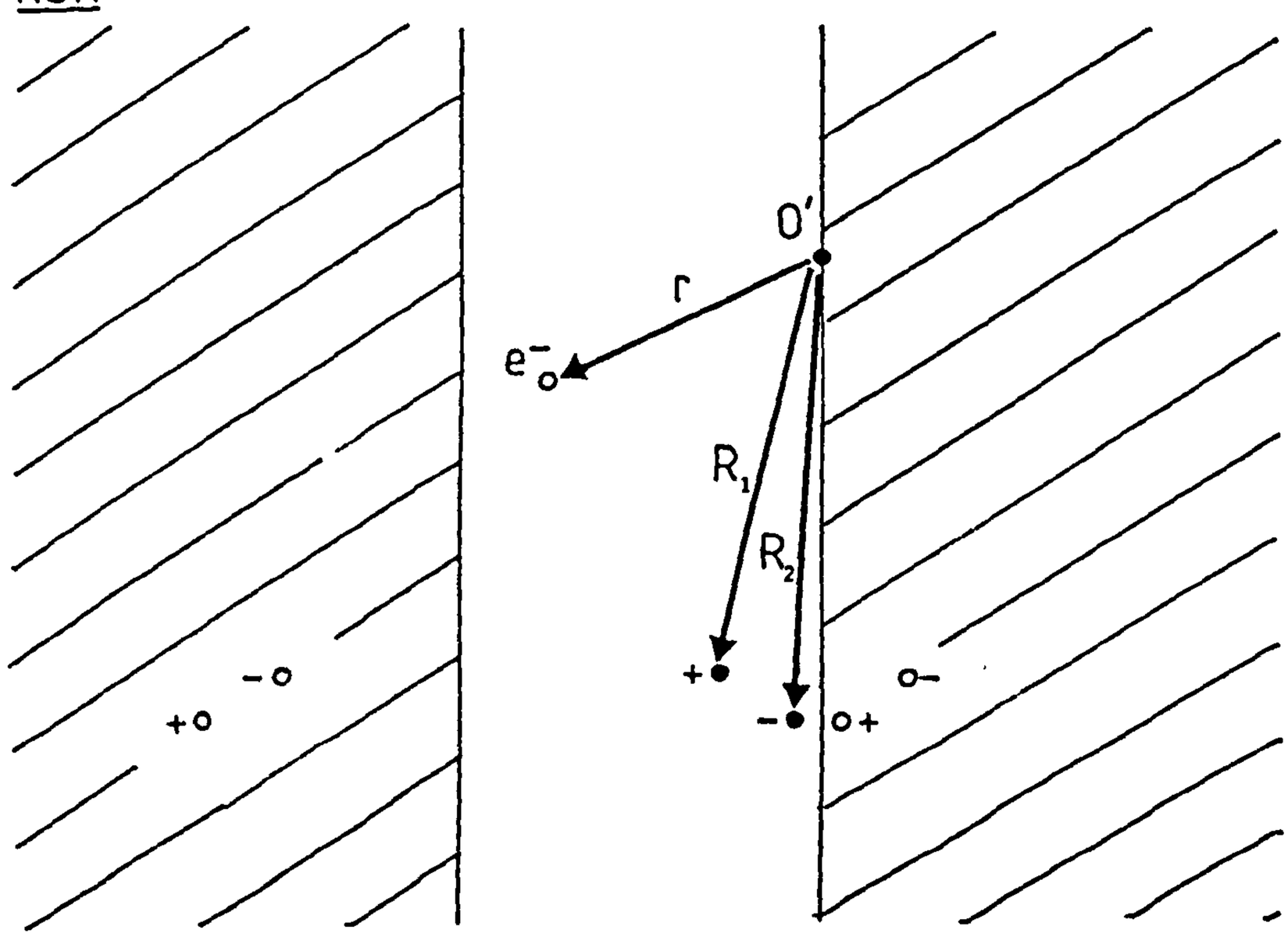
O'
r
e^-_o
R_1
R_2
+
−
+O
−O
O+
O−

$$T_{i\to f}^{in} = \int \varphi_i^* U_{int}(x) \varphi_f' dx \qquad \ldots \quad 2.102$$

where φ_i, and φ_f' the initial, and final state wave functions respectively are eigen functions of the unperturbed Hamiltonian for the system. It is noted from the Golden Rule (equation 2.84) that the transition rate (and therefore the current and conductance also) for inelastic tunnelling is proportional to the matrix element squared, i.e.

$$N_{i\to f}^{in} = \frac{2\pi}{\hbar} \left| T_{i\to f}^{in} \right|^2 \frac{dn}{dE_f} \qquad \ldots \quad 2.103$$

which is analogous to equation 2.99 as one might expect. Now, since the inelastic perturbation is assumed to be small (i.e. $h\nu_n/e \ll V_o$ for a simple rectangular barrier - see Fig.2.1), and electron energy is conserved in the plane parallel to the interface, then in the vicinity of $h\nu_n/e$ the electron wave functions φ_i and φ_f may be given by the WKB approximations ϕ_i and ϕ_f of the type shown in equation 2.86. Consequently, the matrix element for inelastic tunnelling may be considered approximately constant. Thus, the matrix element (equation 2.102) may be evaluated over the barrier region x=0 to x=a, by taking the pre-exponential constants A and B of the wave functions ψ_i and ψ_f outside the integral to give

$$T_{i\to f}^{in} = 2AB^* \frac{eP_x}{a} g(Z) \qquad \ldots \quad 2.104$$

where $Z = r_1/a$, and $g(Z) = \frac{1}{Z} - \frac{1}{(1+Z^2)^{\frac{1}{2}}}$. Summing over all initial and final momentum states as before gives the inelastic tunnel current

$$I_n^{in} = \frac{4\pi e}{\hbar} \sum_{k_i} \sum_{k_f} \left| T_{i\to f}^{in} \right|^2 f(E_i)[1-f(E_f+eV)]\delta(E_i-E_f-h\nu_n) \qquad \ldots \quad 2.105$$

Here I_n^{in} is the current due to the excitation of the n^{th} vibrational mode of frequency ν_n (16), and again, the delta function is defined $\delta(x)=0$ for $x\neq 0$, implying that $I_n^{in}=0$ unless $E_i=E_f+h\nu_n$.

An important difference between this expression and the elastic analog (equation 2.100) is the form of the Fermi-factors. The physical reason for the difference is that in the case of elastic tunnelling it was assumed that tunnelling in either direction was equally probable. For inelastic tunnelling the excitation energies (and low temperatures which give rise to thermal smearing of the electron energy distributor) are such that all of the molecules will be in their ground state; therefore no 'backflow' from final to initial states will occur, i.e. inelastic tunnelling is a 'one-way' process (34). As was mentioned earlier, it is assumed that momentum is conserved parallel to the plane of the interface, and that the density of states of the metal electrodes are independent of energy in the vicinity of E_{F_o} (see equation 2.44) (35). Hence the desired quantity i.e. the ratio of the inelastic junction conductance (due to the excitation of the n^{th} vibrational mode) divided by the elastic conductance, is obtained by invoking the Golden Rule; the conductance ratio is given by the ratio of the squares of the corresponding matrix elements, i.e.

$$\frac{G_n^{in}}{G^e} = \frac{|T_{i\to f}^{in}|^2}{|T_{i\to f}^{e}|^2} \theta(eV - h\nu_n) \qquad \ldots \quad 2.106$$

where the θ function defined as

$$\theta(x) = \begin{cases} 1, x>0 \\ 0, \text{ otherwise} \end{cases}$$

has been introduced and represents a switching on of the Fermi function for $eV > h\nu_n$.

The inelastic matrix element has already been given by equation 2.104, it therefore remains to evaluate the elastic matrix element from

equation 2.96 to give

$$T^{e}_{i\to f} = \hbar^2 \frac{AB^*}{m} \qquad \ldots \quad 2.107$$

substituting for $T^{in}_{i\to f}$, and $T^{e}_{i\to f}$ into equation 2.106 the expression below is obtained

$$\frac{G^{in}_n}{G^e}(r_1) = \frac{2me}{V_o}\left|\frac{e}{\hbar a}\right| P_x^2\, g^2(Z)\, \theta(eV-h\nu_n) \qquad \ldots \quad 2.108$$

Here the factor V_o is the distance between the molecular dipole, and the location where the electron penetrated the barrier (see Fig.215), consequently, a local view of the tunnelling electron is considered. To obtain the total inelastic conductance due to one vibrational mode of one oscillator, equation 2.108 is integrated over r_1 using the integral

$$2\pi \int_{r_o}^{a} r_1 g^2 \frac{r_1}{a}\, dr_1 \simeq 2\pi x^2 \ln\left|\frac{a}{r_o}\right| , \qquad \ldots \quad 2.109$$

multiplied by N oscillators per unit area, and then summed over all the n possible vibrations of each oscillator to give the final result

$$\frac{G^{in}}{G^e} = N\frac{4\pi me^2}{V_o h^2} \ln\left|\frac{a}{r_o}\right|_n |\langle n|P_x||0\rangle|^2 \cdot \theta(eV-h\nu_n) \qquad \ldots \quad 2.110$$

Here $\langle n|$ denotes the first excited state of the n^{th} vibrational mode, and $h\nu_n$ denotes its energy $|\langle n|P_x|0\rangle|^2$ is the square of the dipole matrix element for the transition of an oscillator from its ground state, $|0\rangle$ to the n^{th} vibrational state; it is proportional to the predicted increases in junction conductance.

A few important remarks are made regarding the derivation of the above result, and some predictions arising from it.

(i) In the integral, equation 2.109, it was necessary to take lower and upper cutoffs for (r_1/x). Since these cutoffs appear in a logarithm,

their values were not critical, but, they preclude quantitative predictions of peak intensities; the theory of Kirtley, Scalepino, and Hansma avoids cutoffs and is discussed very briefly in the next section.

(ii) For reasonable values of a, r_o, V_o, N, n, and P_x, the calculated magnitude of the increase in conductance due to a monolayer of OH^- ions was $\sim$ 1% (32, 33), which was in fair agreement with experimental observations.

(iii) Since dipole orientated parallel to the interface cancel with their images while those perpendicular reinforce, one would expect vibrational modes with a net oscillating dipole moment perpendicular to the surface to give rise to stronger IETS peaks. This phenomenon is sometimes referred to as the orientational selection rule.

(iv) The magnitude of the conductance increase is proportional to $|\langle n|P_x|o\rangle|^2$, the square of the corresponding dipole matrix element. According to the SM theory, only modes involving a change in dipole moment should be observed, i.e. IR active modes. In practice peak intensities in IET and IR spectra compare quite favourably, notwithstanding the obvious constraints imposed due to the adsorbed nature of monomolecular films in the former. However, further peaks appear in IET spectra that are absent in IR spectra. Lambe and Jaklevic (LJ) subsequently offered a possible explanation for this incomplete correlation. They pointed out that other mechanisms for electron-molecule interactions exist, and in particular, interaction through the polarizability, α, of the molecule (33). A tunnelling electron may induce a dipole moment in the molecule and then interact with the induced dipole. The associated interaction energy between the tunnelling electron and the induced dipole (plus its image in the nearest metal) was given by

$$U_{int}^{R}(\alpha) = -\frac{4e^2\alpha x^2}{(x^2+r_\perp^2)^3} \qquad \ldots \quad 2.111$$

Vibrational modes to which this interaction term gives rise are those observed in Raman spectroscopy and are therefore referred to as Raman active. Following the procedure of SM, LJ derived an expression similar to equation 2.110 for the ratio of elastic to inelastic conductance due to the excitation of Raman active modes. In their expression the matrix element $|\langle n|P_x|o\rangle|$ was replaced by $|\langle n|\alpha|o\rangle|$. LJ calculated conductance increases of the order 0.1 to 0.5% for Raman interactions as opposed to the 1% for IR modes (34). Indeed, observations of Raman active modes for benzene (36), anthracene (37) and ferrocyanide (38) have been reported in the literature.

2.3.2 The Kirtley-Scalapino-Hansma Theory

The SM and LJ theories were successful in predicting peak intensities to within an order of magnitude. However, inevitable difficulties arose (16), for example:

(1) They assumed that momentum parallel to the interface was conserved in the tunnelling process, this is not strictly true since off-axis scattering of the electrons may be appreciable.

(2) When the tunnel currents (and hence conductance) were calculated as a function of the electron-molecule interaction distance r_1 (see equation 2.108) it was assumed that the electron wave function was localized on a small scale with respect to r_1. The integral given by equation 2.109 is divergent under these conditions; it was therefore necessary to introduce cut-offs r_o and a.

(3) Their assumed molecular potential functions $U_{int}(x)$, and $U^R_{int}(x)$ ignored molecular structure, and considered the behaviour of the molecule in question as a whole.

Kirtley, Scalapino, and Hansma (KSH) took care to avoid these difficulties when formulating their theory which is highlighted below in point form.

(i) In the first instance KSH used a different and somewhat more complicated molecular potential to that of SM and LJ. Rather than making the dipole approximation KSH took the molecular potential to be the sum of Coulomb potentials due to a set of partial charges localized on each atom of the moelcule. Their positions were specified by a series of n position vectors $\underline{R_n}$ with respect to an arbitrary origin where n refers to the n^{th} atom; the electron was similarly located by position vector $\underline{r}$, as shown in Fig.2.6. The partial charges arise from an uneven distribution of the electrons involved in bonding. Symmetry considerations will in fact simplify the molecular potential.

(ii) Images of the partial charges were considered in both metal electrodes (also shown in Fig.2.6); cf. SM and LJ theories in which the nearest image only is considered.

(iii) Bond polarizabilities were not included.

(iv) Off axis scattering was considered.

(v) As was the case for SM and LJ, KSH defined initial and final state wave functions using WKB approximations. However, contrary to SM and LJ who weighted WKB functions to describe the electron tunnelling matrix elements within the barrier, KSH used a transfer Hamiltonian formation to transfer electrons across the barrier. This allowed their more complicated interaction potential to be incorporated.

For elastic tunnelling KSH used the time-independent, $zero^{th}$ order Hamiltonian to transfer electrons across the barrier, with no energy loss, while for inelastic tunnelling they used the electron-molecule interaction potential. The ratio of inelastic to elastic

conductance was then calculated as before. Their final expression for the conductance ratio included integrals over all possible initial and final angular directions for tunnelling electrons, which accounted for the possible off axis scattering angles. Several important predictions arise from the KSH theory, namely:

(i) The change in the ratio of inelastic to elastic junction conductances due to a monolayer of OH^- ions was calculated to be 0.5%. Experimental values are of the order 0.4%.

(ii) When the molecules in the insulating barrier are situated relatively close to one of the metal electrodes the orientational selection rules are the same as in the SM and LJ theories, i.e. dipoles oscillating perpendicular to the plane of the interface should couple more strongly with tunnelling electrons than those parallel to it and hence give rise to stronger IET lines. However, the reverse is true for molecules positioned towards the centre of the barrier; here dipoles oscillating parallel to the interface give stronger IET lines. The reasons for this are essentially two-fold. Firstly, off-axis scattering leads to constructive and destructive interference between the corresponding matrix elements of the scattering dipoles. This is because the matrix elements have relative phases. Secondly, the KSH dipole potential function is odd in the co-ordinate parallel to the dipole. If the IET junction is considered as a parallel plate capacitor then the dipole function integrates to zero for dipoles perpendicular to the interface but does not integrate to zero for those parallel to it. The net effect of these two factors is illustrated in Fig.2.7, where the angle averaged matrix element squared, A_{nm}, is plotted as a function of position in the barrier for dipoles orientated perpendicular, and parallel to the interface (39).

Fig.2.7

Plot of, A_{nm}, the angle averaged matrix element squared for inelastic tunnelling as a function of the position of a point dipole in a square barrier of height 2 eV, and width 15 Å according to the theory of KSH. A_{nm} is proportional to the inelastic tunnelling cross section.

Dipoles oscillating perpendicular to the interface are more likely to excite an inelastic transition if close to one of the metal electrodes, but dipoles oscillating parallel to the interface are favoured towards the centre of the barrier. In the regions where the solid and dashed curves intersect for each particular mode there is no favoured orientation.

Diagram re-drawn from Kirtley and Hall (39).

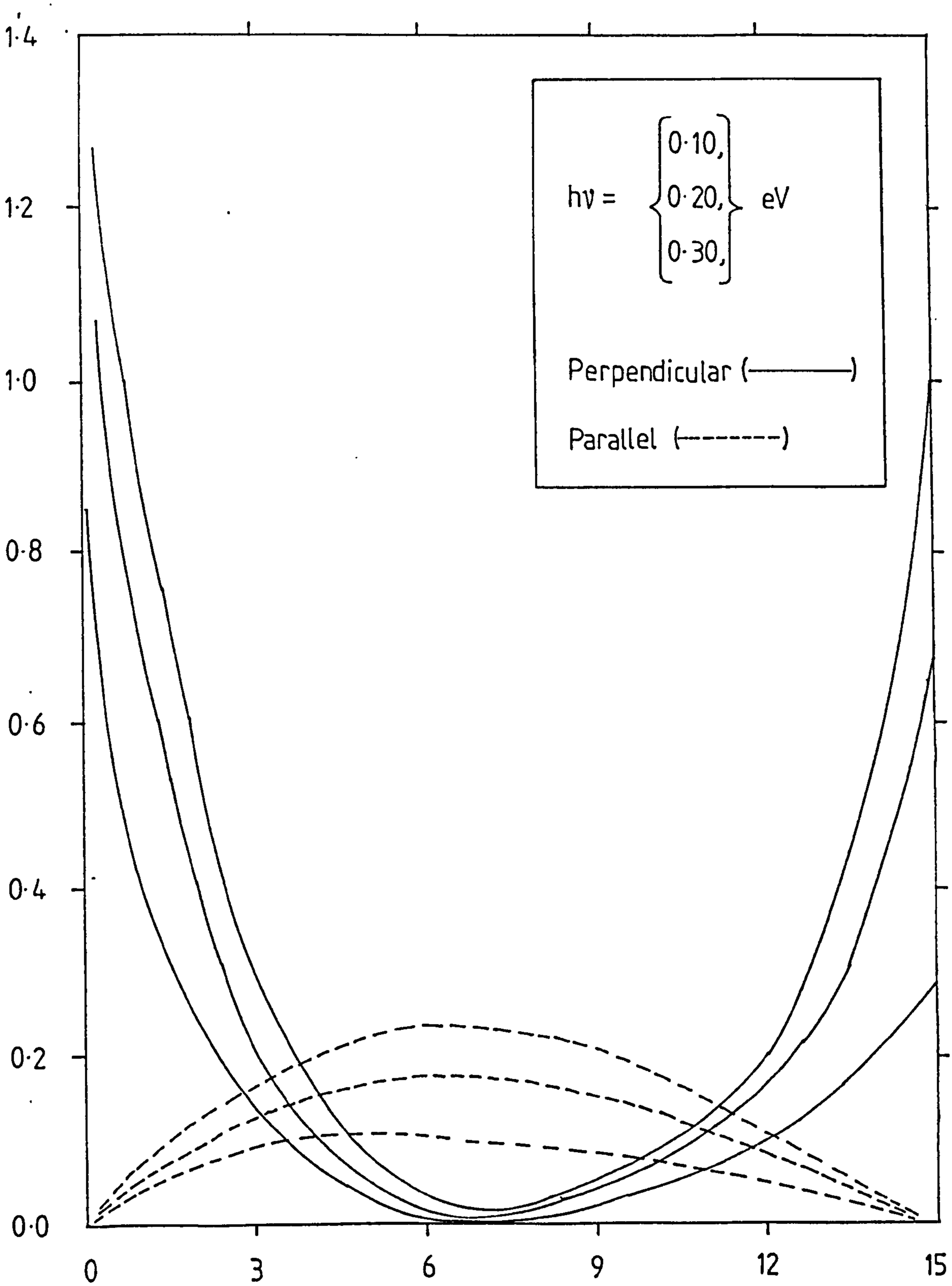
1·4
1·2
1·0
0·8
0·6
0·4
0·2
0·0
A_{nm} (10^{-9} A^2)
0
3
6
9
12
15
POSITION (Å)
hν = {0·10, 0·20, 0·30,} eV
Perpendicular (———)
Parallel (- - - - - -)

(iii) Raman active modes should be observed, even if molecular polarizability is not included in the electron-molecule interaction potential. This is a consequence of (2) above. Consider an IR inactive mode with two oscillating dipoles separated such that their dipole moments cancel. Depending on the molecules position in the barrier the two dipoles will have different weights in the matrix element sum (see Fig.2.7) and may not necessarily cancel each other out.

(iv) By similar reasoning to (iii) above modes which are neither IR or Raman active (i.e. optically forbidden modes) should also be observed.

(v) The changes in the ratios of inelastic to elastic conductances for certain vibrational modes are dependent on bias polarity. Crudely, this may be interpreted in terms of a simple two-step tunnelling model (40). Consider a molecule situated near to the left hand side (say) of the insulating barrier of a typical IET junction. In the left to right bias direction an electron will first interact with the molecule (i.e. lose energy to it), and then tunnel through the remainder of the insulating layer with a reduced energy. In the other bias direction the electron will first tunnel elastically at its initial energy, and then interact with the molecule. Now, since tunnelling probability increases with electron energy the second process is favoured.

To some extent, the predictions of the KSH theory have been bourne out experimentally. Peak intensities and orientational behaviour of several adsorbates including the methylsulphonate anion (39,41), the formate anion (42), and carboxylate anions (43) have shown qualitative agreement with the KSH predictions. Recent work on inorganic ions (44) has shown evidence for optically forbidden modes in IET spectra. The first attempt to investigate intensities of IR and Raman active modes in IET spectra was made by Bogatina et al (45). In studying organic

solvents they concluded that no evidence existed to suggest that the intensities of Raman active modes compared with IR active modes varied in any systematic manner.

It is fairly clear from the preceeding discussion that the KSH theory has enjoyed some degree of success. Considerable scope exists for further work to compare theory with experiment, and at present it is still too early to speculate whether the theory will be effective for complicated molecular species.

2.4 RESOLUTION IN IETS

In addition to the natural line width of a vibrational mode, there are essentially two contributions to peak broadening and hence resolution, these are:

(1) Thermal broadening due to smearing of the electron energy distributions near the Fermi energy.

(2) Instrumental broadening due to the modulation technique used to detect vibrational modes.

Natural linewidths are considered to be negligible, and this section will discuss the resulting peak shape and resolution on IETS due to (1) and (2) above. Finally, a brief outline of the effect of superconducting electrodes on resolution is given.

2.4.1 Thermal Broadening

Lambe and Jaklevic were the first to discuss this phenomenon (33). Following their approach, consider an IET vibrational mode of energy $h\nu$. For T > OK electrons may be excited into states above the Fermi energy because of the Fermi-tail. Therefore, the applied bias voltage, V, required to excite a mode may be greater than $h\nu/e$. Fig.2.8 illustrates this situation where the thermally smeared Fermi function, f(E), represents filled states in M_1 of an M_1-I-M_2 junction, and 1-f(E) represents unfilled states in M_2. The expression for the inelastic tunnelling current may be written in the form

$$I^{in} = C \int_{-\infty}^{\infty} f(E)[1-f(E+eV-h\nu)]dE \qquad \ldots \quad 2.112$$

For simplicity, the constant C contains the density of states functions and the inelastic tunnelling matrix element, both assumed to

Fig.2.8

Schemetic energy diagram for a M_1-I-M_2 junction at T>OK under applied bias V. This indicates the origin of thermal broadening of IETS peaks. The region bounded by the Fermi function f(E) and the M_1-I interface represents filled states in M_1. The region bounded by [1-f(E)] and the I-M_2 interface represents empty states in M_2. δ_1 and δ_2 are two possible initial and final energy states which arise due to thermal smearing of the Fermi functions near the Fermi levels E_{F_1}, and E_{F_2} of the metals. As can be seen, the bias voltage necessary to cause a transition from δ_1 to δ_2 is given by $V = (h\upsilon+\delta_1-\delta_2)/e$.

Diagram re-drawn from Keil et al (30).

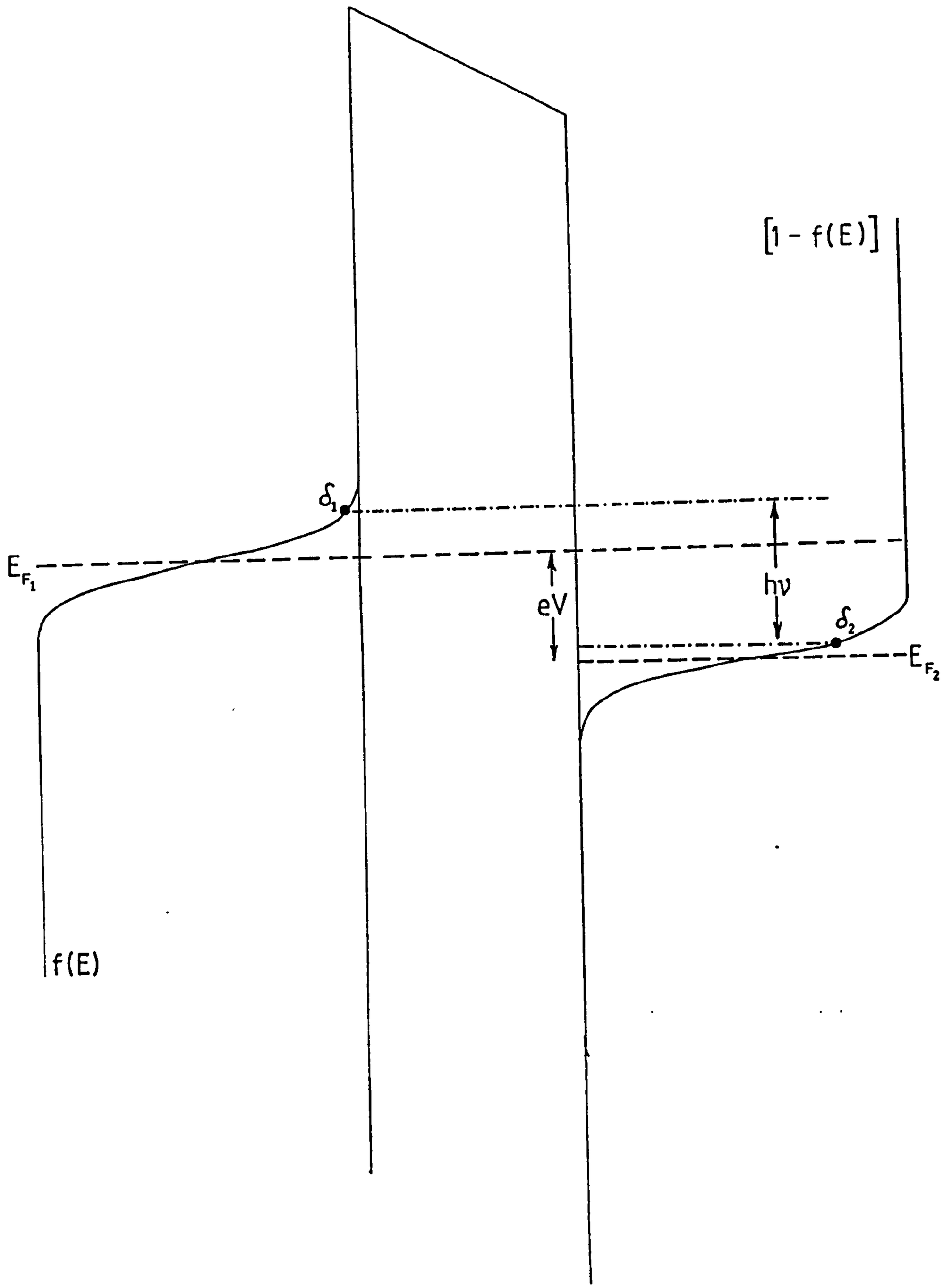
[1 - f(E)]
δ_1
E_{F_1}
eV
hν
δ_2
E_{F_2}
f(E)
METAL 1
INSULATOR
METAL 2

be slowly varying over a small range of energies in the vicinity of E_F. The integral can be evaluated to give

$$I^{in} = C(eV-h\nu)\frac{e^x}{e^x-1} \quad \ldots \quad 2.113$$

where $x = (eV-h\nu)/kT$, k is Boltzmann's constant. The second derivative of equation 2.113 is

$$\frac{d^2I^{in}}{dV^2} = C\frac{e^2}{kT}e^x\left[\frac{(x-2)e^x + (x+2)}{(e^x-1)^3}\right] \quad \ldots \quad 2.114$$

The function F(x) in the square bracket is plotted in Fig.2.9a and has a full width at half maximum (FWHM) of 5.4 kT/e. Jennings and Merrill (46) have confirmed this temperature dependence experimentally. Clearly very low temperatures are essential in IETS, since at room temperature ($\sim$ 300K) the thermal FWHM is $\sim$ 140 meV (1120 cm^{-1}), while at 4.2K it is $\sim$ 2 meV ($\sim$ 16 cm^{-1}).

2.4.2 Modulation Voltage Broadening

When taking IET spectra an ac modulation voltage $V_\omega \cos\omega t$ is applied to the IET junction superimposed upon a slowly increasing dc bias, V. (See Chapter 3). The quantity $\frac{d^2I}{dV^2}$ is proportional to the second harmonic current response, $i_{2\omega}$, of the junction. Klein et al first discussed analytically the effect of modulation voltage on peak width (47). They wrote the tunnel current as

$$I = f(eV + eV_\omega \cos\omega t) \quad \ldots \quad 2.115$$

and the second harmonic response as

$$i_{2\omega} = \frac{2}{\tau}\int_\tau f(eV + eN_\omega \cos\omega t)\cos 2\omega t\, d\tau \quad \ldots \quad 2.116$$

Fig.2.9

The thermal broadening function F(x) where
$x = (eV-h\nu)/kT$.

(a) Both electrodes normal.

(b) One electrode superconducting assuming an energy gap $\Delta = 3$ kT (corresponding to Pb at 4.2K).

Curve b is taller and narrower than curve a, and is offset in energy by an amount $\simeq 0.8\Delta$. The constant C is described in the text.

Diagram re-drawn from Kirtley (48).

Fig.2.10

The modulation voltage broadening function.

$$\Phi\left(\frac{E}{eV_\omega}\right) = \frac{2eV_\omega}{3\pi}\left[1 - \frac{E}{eV_\omega}^2\right]^{3/2}, \quad |E|<eV_\omega$$

re-drawn after Kirtley (48).

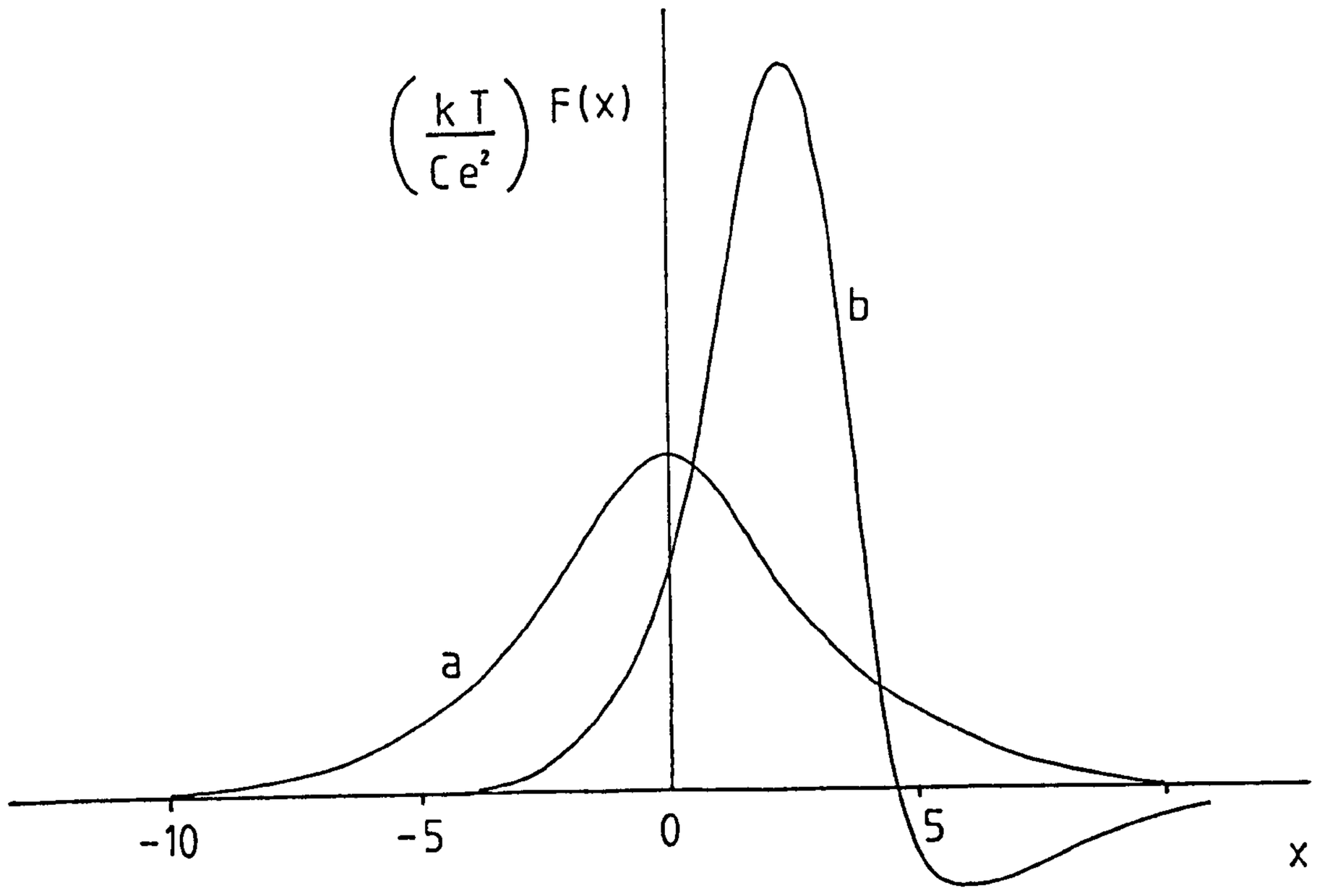
$\left(\frac{kT}{Ce^2}\right) F(x)$
b
a
-10
-5
0
5
x

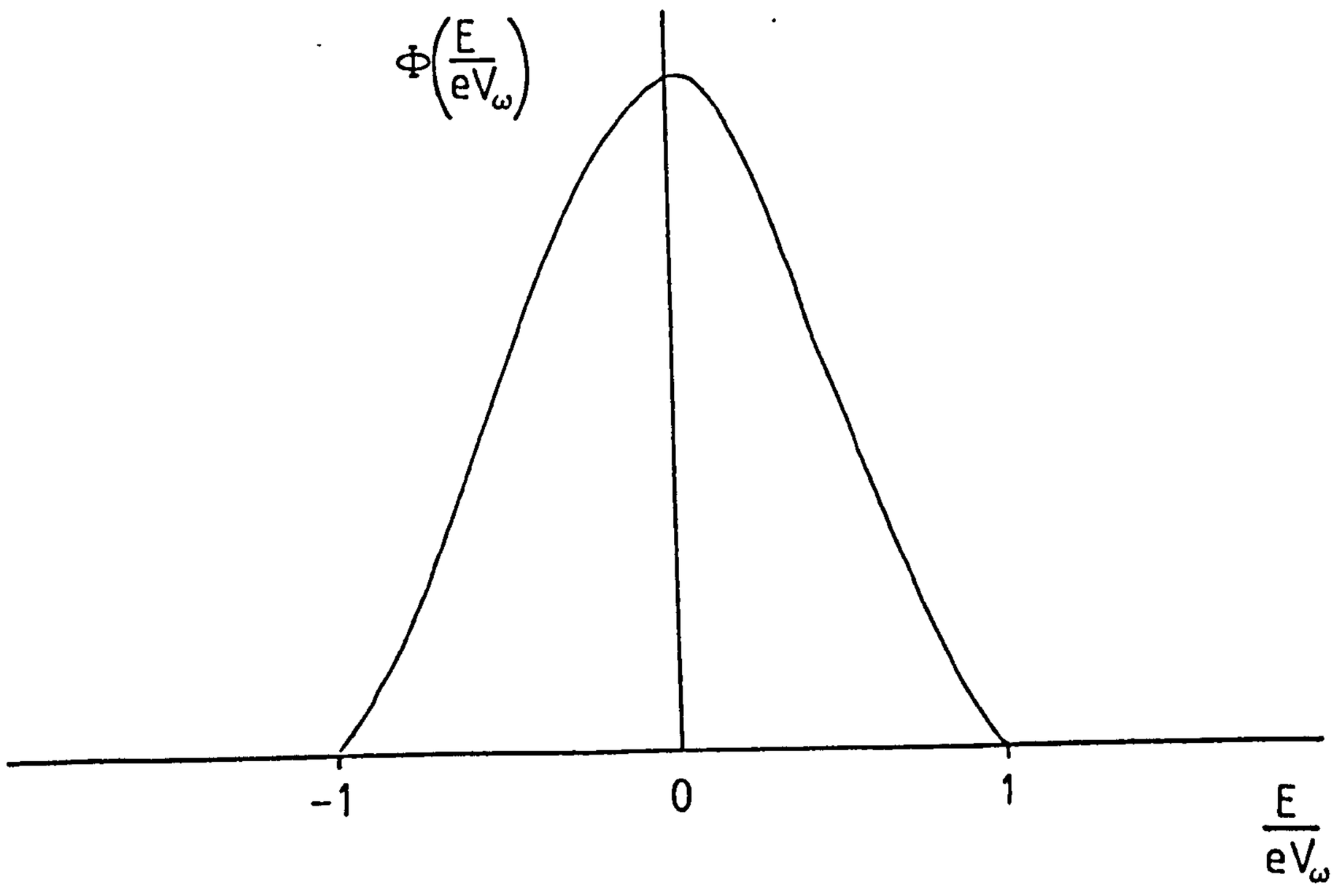
$\Phi\left(\frac{E}{eV_\omega}\right)$
-1
0
1
$\frac{E}{eV_\omega}$

changing the variable by putting $E = eN_\omega \cos\omega t$ and integrating by parts twice gives

$$i_{2\omega} \propto \int_{-eV_\omega}^{eV_\omega} f''(eV+E)[(eV_\omega)^2 - E^2]^{3/2} dE \qquad \ldots \quad 2.117$$

Hence, $i_{2\omega}$ is a convolution (7) of the exact second derivative f"(eV+E) with an instrumental function $\Phi(E)$ defined (47,48)

$$\Phi\left(\frac{E}{eV_\omega}\right) = \begin{cases} \frac{2eV_\omega}{3}\left|1 - \frac{E}{eV_\omega}^2\right|^{3/2}, & |E|<eV_\omega \\ 0, & |E|>eV_\omega \end{cases} \qquad \ldots \quad 2.118$$

which is plotted in Fig.2.10. The FWHM for this function is 1.22 eV_ω (or 1.7 eV_{rms} where $V_{rms} = V_\omega/\sqrt{2}$). This implies that for the FWHM of the modulation broadening function, , to be comparable with that of the termal broadening function F at 4.2K, a V_ω of 1.7 mV (or a V_{rms} of 1.2 mV) is required. Most IET spectra are in fact run under these conditions (i.e. at 4.2K with a V_ω of 1.7 mV). The total broadening due to thermal and instrumental effects combined at 4.2K is given approximately by (46,48)

$$\text{Total FWHM} = [(1.73V_{rms})^2 + (0.47T)^2]^{\frac{1}{2}} \text{ meV} \qquad \ldots \quad 2.120$$

2.4.3 The Effect of Superconducting Electrodes

It is now well known that below a critical temperature, T_C, some metals become superconductors, i.e. they show no resistance to direct currents and low frequency alternating currents (49,50). (Normal resistance may be restored below T_C if a magnetic field greater than a critical value B_C is applied to the specimen; its superconductivity

is then said to be 'quenched'.) The highest value of T_C for an element is 9.3K, for Nb, and the lowest yet reported is 0.01K for W. IETS experiments are commonly performed at 4.2K by immersing the tunnel junction (usually Aℓ-I-Pb) in liquid He. Although the main reason for doing this is to reduce thermal broadening to an acceptable level (see above), the Pb electrode becomes superconducting as a consequence. (T_C^{Pb} = 7.2K).

The effects of superconductivity on IETS peak position and shape are therefore noteworthy, and may be understood by considering the original theory of superconductivity proposed by Bardeen, Cooper and Schrieffer (BCS) (51). They proposed that below T_C, electrons (which are Fermions) may interact via latticephonons to form electron pairs called 'Cooper pairs' which then behave as Bosons. Cooper pairs have a strong tendency to 'condense' into a single state, known as the BCS ground state; since they are not constrained by the Pauli exclusion principle. The net result is a new electron energy distribution, such that the total energy of the system is less than that of a normal metal at the same temperature. Because all the Cooper pairs in the BCS ground state have the same energy, it follows that the superconductor can have no dc, and low frequency ac resistance. The new electron energy distribution is characterized by the following:

(i) An energy gap of 2Δ centred at the Fermi level appears (see Fig.1.4), whose width corresponds to the energy required to break up a Cooper pair at a given temperature. For Pb at 4.2K Δ = 1.2 meV.

(ii) The BCS density of electron states function N(E) is given by

$$N_{sc}(E) = \begin{cases} N_n(E) \cdot \dfrac{|E|}{(E^2-\Delta^2)^{\frac{1}{2}}} , & |E| > \\ 0 , & |E| < \Delta \end{cases} \qquad \ldots \quad 2.120$$

where the subscripts sc, and n refer to superconducting, and normal respectively.

From (ii) it is seen that $N_{sc}(E)$ tends asymptotically towards infinity as the gap is approached from above and below (see Fig.1.4). The energy gap has a marked effect on the low-bias I-V characteristic of a M_1-I-M_2 (superconductor) tunnel junction (the case where both metals are superconducting is not considered here) as shown in Fig.3.3. Consequently the energy range over which IET events may occur is slightly reduced. This is illustrated in Fig.2.9b where the FWHM of the thermal broadening function is less than that for the normal electrode at the same temperature (the FWHM at 4.2K for Pb superconducting, assuming that Δ = 1.1 meV, is 2.9 kT, while for Pb normal it is 5.4 kT (48)). Additionally, some asymmetry is introduced and the function is offset to a higher energy by an amount approximately equal to Δ, hence the peak position, E, is given by $E = h\nu + \Delta$. Peak energies quoted in cm^{-1} for the IET spectra presented in this thesis have been corrected for the superconducting energy gap.

REFERENCES - Chapter 2

1. R.Eisberg and R.Resnick. Quantum Physics of Atoms, Molecules, Solids, Nudei and Particles, J.Wiley and Sons, New York (1974).

2. H.L.Strauss. Quantum Mechanics, An Introduction, Prentice-Hall Inc., New Jersey (1968).

3. J.G.Simmons. J. Appl. Phys., 34(6), 1793 (1963).

4. H.Jeffreys. Proc. Lond. Math. Soc., 23, 42B (1924).

5. L.I.Schiff. Quantum Mechanics (2nd Edn.), Mcgraw-Hill Book Co. Inc., New York (1955).

6. R.A.Smith. Wave Mechanics of Crystalline Solids, Chapman and Hall Ltd., London (1963).

7. E.Kreyszig. Advanced Engineering Mathematics (4th Edn.), J.Wiley and Sons, New York (1979).

8. C.B.Duke. Tunnelling in Solids, Solid State Physics (Supplement 10), Academic Press, New York (1969).

9. E.Burstein and S.Lundqvist. Tunnelling Phenomena in Solids, Plenum Press, New York (1969).

10. I.Giaever. Phys. Rev. Lett., 5(4), 147 (1960).

11. J.C.Fisher and I.Giaever. J. Appl. Phys., 32(2), 172 (1961).

12. B.D.Josephson. Phys. Rev. Lett., 1, 251 (1962).

13. A simplified account of Sommerfields theory may be found in F.K.Richtmyer, E.H.Kennard and T.Lauritsen, Introduction to Modern Physics (5th Edn.), McGraw-Hill Book Co. Inc., Tokyo (1956) pp.100-105.

14. L.Solymer. Superconductive Tunnelling and Applications, Chapman and Hall, London (1972).

15. T.J.Coutts. Electrical Conduction in Thin Metal Films, Elsevier, Amsterdam (1974).

16. J.Kirtley. Chapter 2 in Tunnelling Spectroscopy, Capabilities, Applications and New Techniques, P.K.Hansma (Ed.), Plenum Press, New York (1982).

17. A.D.Brailsford and L.C.Davis. Phys. Rev., B 2, 1708 (1970).

18. L.C.Davis. Phys. Rev. B 2, 1714 (1970).

19. C.Caroli, R.Combescot, P.Nozieres and D.Saint-James. Solid State Phys., 5, 21 (1972).

20. T.E.Feuchtwang. Phys. Rev. B20, 430 (1979).

21. J.Bardeen. Phys. Rev. Lett., 6, 57 (1982).

22. E.O.Kane. Chapter 1 in Reference 9.

23. H.A.Enge, M.R.Wehr and J.A.Richards. Introduction to Atomic Physics, Addison-Wesley, Reading Massachusetts (1978).

24. E.Fermi. Nuclear Physics, University of Chicago Press, Chicago (1949).

25. P.K.Hansma. Phys. Rep., 30(C), 145 (1977).

26. J.Kirtley, D.J.Scalapino and P.K.Hansma. Phys. Rev. B14, 17, 1113 (1966).

27. Chapter 1. ref. 18.

28. R.T.Payne. Phys. Rev., 139, A570 (1965).

29. R.G.Keil, T.P.Graham and P.Roenker. Appl. Spectroscopy, 30 1 (1976).

31. A.Leger, J.Klein, M.Belin and D.Defourneau. Solid State Comm., 11, 1381 (1972).

32. D.J.Scalapino and S.M.Marcus. Phys. Rev. Lett., 18, 459 (1967).

33. J.Lambe and R.C.Jaklevic. Phys. Rev., 165, 821 (1968).

34. R.C.Jaklevic and J.Lambe. Chapter 18 in Reference 9.

35. W.A.Harrison. Phys. Rev., 123, 85 (1961).

36. N.I.Bogatina, I.K.Yanson, B.I.Verkin and A.G.Batrak. Sov. Phys. JETP 38, 1162 (1974).

37. M.G.Simonsen, R.V.Coleman and P.K.Hansma. J. Chem. Phys., 61, 3789 (1974).

38. K.W.Hipps, U.Mazur and M.S.Pearce. Chem. Phys. Lett., 68, 433 (1979).

39 J.Kirtley and J.T.Hall. Phys. Rev., b22, 848 (1980).

40. I.K.Yanson, N.I.Bogatina, B.I.Verkin and O.I.Shklyarevskii. Sov. Phys. JETP, 35, 540 (1973).

41. J.T.Hall and P.K.Hansma. Surf. Sci., 71, 1 (1978).

42. W.J.Wang, and H.W.White. Surf. Sci., 118 321 (1982).

43. J.T.Hall and P.K.Hansma. Surf. Sci., 76, 61 (1978).

44. K.W.Hipps and U.Mazur. Chapter 8 in Tunnelling Spectroscopy, Capabilities, Applications and New Techniques, P.K.Hansma (Ed.), Plenum Press, New York (1982).

45. N.I.Bogatina. Opt. Spectrosc., 38, 43 (1974).

46. R.J.Jennings and J.R.Merril. J. Phys. Chem. Solids, 33, 1261 (1972).

47. J.Klein, A.Leger, M.Belin, D.Defourneau, M.J.L.Sangster. Phys. Rev. B7, 2336 (1973).

48. J.Kirtley. J. Am. Chem. Soc., 80, 217 (1980).

49. H.M.Rosenberg. The Solid State (2nd Edn.), Clarendon Press, Oxford (1978).

50. A.C.Rose-Innes and E.H.Rhoderick. Introduction to Superconductivity, Pergaman Press, Oxford (1969).

51. J.Bardeen, L.N.Cooper and J.R.Schrieffer. Phys. Rev., 108, 1175 (1957).

CHAPTER 3

BASIC EXPERIMENTAL TECHNIQUES FOR IETS; JUNCTION FABRICATION, DOPING, AND SPECTROMETER OPERATION

The general systems for IET junction fabrication, doping and subsequent spectroscopic analysis are essentially unchanged from those implemented and described by other workers (1, 2, 3). However, during the course of the present experimental work various modifications to the vacuum evaporation systems were deemed necessary; these are fully described in Chapters 6 and 7. Only a summary of the now 'standard' vacuum deposition and IET junction doping techniques adopted in our laboratory is therefore given here.

The IET spectrometer design, construction, and implementation have been described in considerable detail by Tunnicliffe (1) and Reynolds (2). For the purpose of this thesis, it is appropriate to present a general description of its operation and capabilities.

3.1 VACUUM EVAPORATION SYSTEMS AND IET JUNCTION FABRICATION

3.1.1 The Vacuum System and Maintenance of Cleanliness

A schematic diagram of the vacuum system employed for the evaporation of the thin film IET junction electrodes is shown in Fig.3.1, it is fairly typical of a conventional rotary and diffusion pumped arrangement. However, stringent controls were imposed to ensure an acceptably low level of contamination which is vital if good quality IET junctions are to be routinely produced. In order to illustrate conveniently the functions of the various components of the system, a typical sequence of events culminating in the fabrication of a set of IET junctions will be described in 3.1.2. However, the present section addresses itself to the evaporation chamber cleaning procedure.

Firstly, the chamber pressure was reduced from atmospheric to $\sim$ 100 m Torr by means of the rotary pump, this having served its purpose, (i.e. to back the diffusion pump) was then isolated, and the diffusion pump was utilized to reduce further the pressure, attaining a final value of $\leq 10^{-5}$ Torr. The liquid N_2 traps, low vapour pressure rotary pump oil (Santovac-5, a polyphenyl ether) and a series of baffles serve to restrict the possibility of 'backstreaming' of (contaminant) hydrocarbon vapour into the chamber during the latter operation.

It is mentioned at this juncture, that when dealing with vacuums of this order, small leaks in the system are an infrequent nuisance, and may arise due to a variety of causes, (for example, damaged 'O' ring seals, poor valve mechanisms, dust, etc.). Leaks are usually detected by carefully squirting the suspect component(s) with small volumes of acetone and checking the Pirani and/or Penning gauge for a 'kick' caused by a surge in pressure due to the penetration of the acetone into the system.

The next step was to introduce a controlled flow of gas (usually air or O_2) into the chamber via a needle valve inlet and perform a dc

Fig.3.1 - Schematic Diagram of the standard vacuum system employed for routine IET junction fabrication.

Key to diagram:

a. Aℓ jig

b. Glass slide

c. Brass shadow mask and slide holder

d. Molybdenum boat (Pb evaporation source)

e. Steel shutter (prevents cross-evaporation of Aℓ and Pb)

f. Tungsten filament (Aℓ evaporation source)

g. Glow-discharge electrode pole

The liquid N_2 traps (in conjunction with Santovac-5 rotary pump oil) reduces the possibility of 'backstreaming' of hydrocarbon vapour into the chamber.

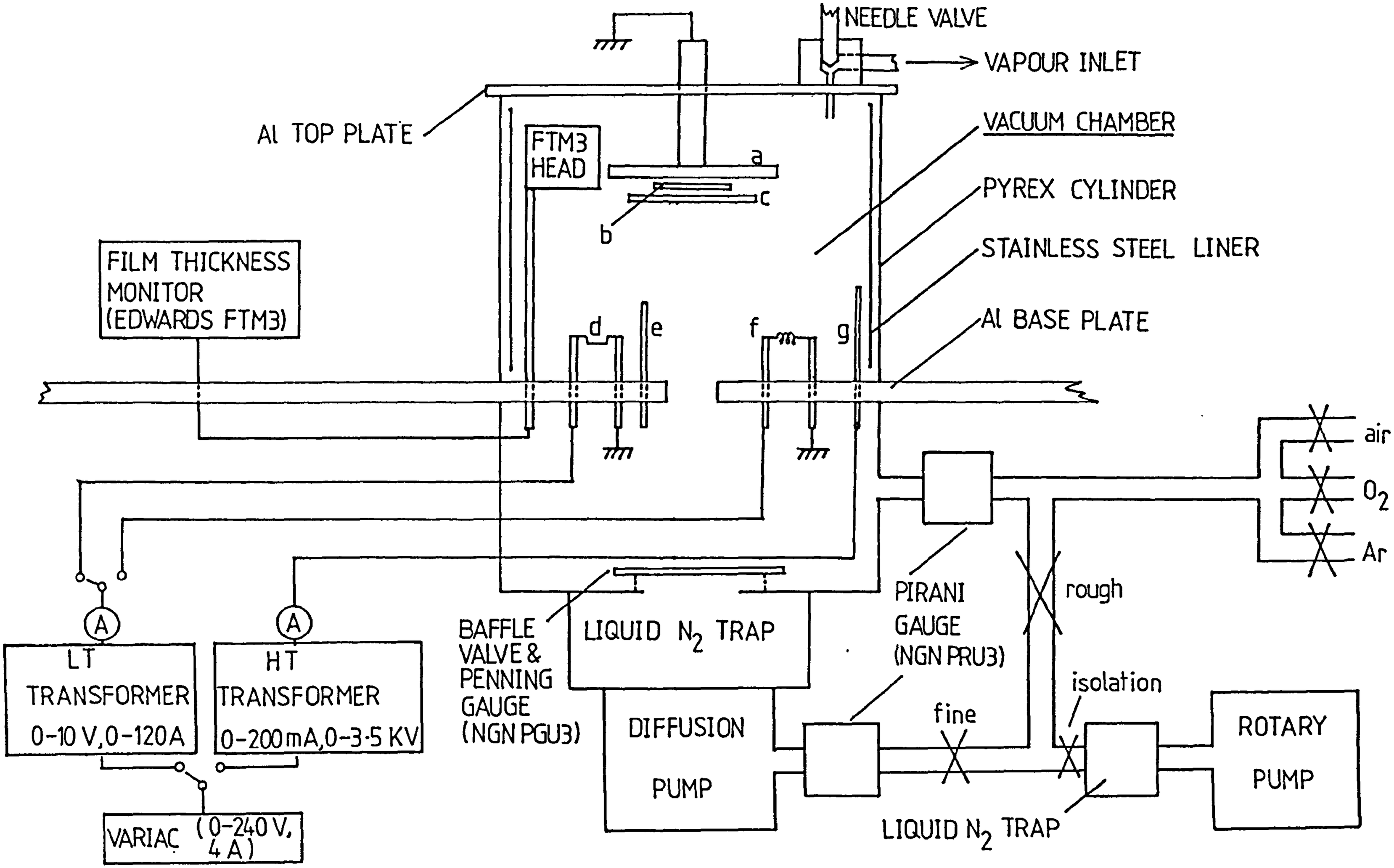
NEEDLE VALVE
VAPOUR INLET
Al TOP PLATE
FTM3 HEAD
a
b
c
VACUUM CHAMBER
PYREX CYLINDER
STAINLESS STEEL LINER
Al BASE PLATE
FILM THICKNESS MONITOR (EDWARDS FTM3)
d
e
f
g
air
O_2
Ar
A
A
LT TRANSFORMER 0-10 V, 0-120A
HT TRANSFORMER 0-200 mA, 0-3·5 KV
VARIAC (0-240 V, 4 A)
BAFFLE VALVE & PENNING GAUGE (NGN PGU3)
LIQUID N_2 TRAP
DIFFUSION PUMP
PIRANI GAUGE (NGN PRU3)
rough
fine
isolation
ROTARY PUMP
LIQUID N_2 TRAP

glow-discharge oxidation clean, typically at a pressure of ∿ 50 m Torr with a current of ∿ 100 mA for a few minutes. Energetic ions comprising the discharge may then bombard all surfaces coming into contact with the discharge within the chamber, and any resulting chemical debris is then pumped away by the diffusion pump. The glow-discharge was followed by a flash evaporation of Aℓ usually to a thickness of a few thousand Å's (this process is known as 'gettering') as indicated by the quartz crystal monitor thus completing the cleaning procedure. Reducing contamination to an acceptable level is crucial in IETS, and for this reason the importance of the Aℓ getter cannot be over-emphasized. Its function is essentially to afford a passivating layer over any residual contamination which had not been removed from the internal surfaces of the vacuum chamber during the glow-discharge clean.

Since indigenous contamination invariably builds up during the period when the vacuum system is 'shut down', the above procedures were performed at the start of each day of experimental work; the glow-discharge clean was performed prior to all tunnel junction base-electrode evaporations to ensure that the insulating substrate onto which they were to be evaporated and shadow masks were sufficiently contaminant-free for IETS purposes (see also 3.1.2, and 3.1.4)

3.1.2 Device Fabrication

Upon completion of the chamber cleaning procedure described in 3.1.1, the (four stage) device fabrication was performed. This involves: base-electrode evaporation, oxidation and doping, and finally counter-electrode evaporation, as summarized below.

(i) Base-electrode Evaporation

The chamber was evacuated to $\lesssim 10^{-5}$ Torr (see 3.1.1), and the

base-electrodes were evaporated from the resistively heated tungsten filament source onto a clean insulating substrate (a 76 x 11 mm glass microscope slide). Electrode thicknesses of ∿ 2000 Å were typical. The electrode geometry was suitably defined by positioning a brass shadow mask directly above the slide. The base-electrode material for the present work was Aℓ (Balzers research grade - 99.999% pure) although less commonly Mg, Pb and certain other metals are of interest.

(ii) Base-electrode Oxidation

In essence, two methods were commonly employed to oxidize the electrode. The first and most widely used in our laboratory (for its simplicity and success rate) was to vent the vacuum chamber to an atmosphere of room air allowing a (hydrated) thermal oxide to form on the metal electrodes in a few seconds. One unfortunate drawback of this method is that should any potential contaminants be present in the air, they may also be incorporated into the oxide layer. In practice this occurs very infrequently, perhaps due to the fairly short exposure time required to grow the oxide layer.

The second oxidation method was to introduce a controlled flow of pure O_2 into the chamber and perform a dc glow-discharge oxidation; typical conditions were ∿ 100 mA current at ∿ 50 m Torr partial pressure of O_2 for a few minutes.

In both cases an oxide of approximate thickness 10-20 Å was formed. A great deal of controversy exists in the literature as to the characterization of the structure of these oxides, whose growth depends critically on several parameters, for example, substrate temperature, residual gases, ambient pressure, and so on. A variety of surface analytical techniques have been employed to assist in determining their structure, including ESCA (4), LEED (5), and surface IR (6, 7). However,

it is believed by Hansma et al, that the structure of the thermal oxide resembles that of γ-alumina (8). The interested reader is referred to the above literature and the references therein.

(iii) Doping the Oxide

There are three general techniques by which dopant molecules may be incorporated onto the oxide surface, namely: liquid-phase, vapour-phase, and infusion doping which are described in 3.1.3. It is worth mentioning at this point that in the former two techniques, dopant molecules (either in solution, or neat) are introduced directly onto the oxide surface while in the latter they are incorporated indirectly after the evaporation of the counter-electrode. Doping by the former two techniques in our laboratory is normally performed after having removed the Aℓ base electrodes from the vacuum chamber. Should the growth of a thermal oxide be desired this is of no cause for concern, since such an oxide may be conveniently formed during the transit of the slide to the doping area. However, if a plasma oxide has been produced, subsequent removal from the chamber will serve to thicken the oxide layer by further thermal growth, negating the possibility of doping onto a (say) virgin plasma oxide. To this end, a system has been developed by the author to facilitate vapour phase doping (or undoped device fabrication) in situ by the incorporation of a mask change-over arrangement within the vacuum chamber. This system is described in Chapter 7. Unfortunately it is extremely difficult, though desirable, to implement a similar system for liquid-phase doping. This can be readily appreciated when one considers the inherent difficulties associated with operating a diffusion pump at constant elevated pressures (≥ 100 m Torr); such pressures would invariably arise if large drops of dopant liquid introduced into the vacuum chamber were to accumulate.

One way of performing liquid-phase doping of uncontaminated plasma

oxides would be to implement a sophisticated arrangement where the doping chamber may be isolated from the main evaporation chamber, similar, for example, to that of Walmsley and his co-workers (9). In such arrangements the elimination of contamination is not a straightforward consideration; partly for these reasons, liquid-phase doping in situ is not a matter of course in our laboratory.

(iv) Counter-electrode Evaporation

Upon completion of the oxide doping, the glass slide was replaced within the vacuum chamber, and the counter-electrodes were evaporated in a similar manner to that of the base-electrodes. In the present work the metal used was Pb, although Au, Ag, Sn, Th, and In have been used by other workers (10, 11).

Slight shifts in peak positions of certain vibrational modes in the resulting IET spectra due to different metals are observed ($\lesssim$ 1% for hydrocarbon modes, a few % for the OH group). These shifts have been accounted for by Kirtly and Hansma (12), and appear to show some dependence on the atomic radius of the counter-electrode metal. It is fair to say that for ease of fabrication, success rate, plus the fact that it is a superconductor at liquid He temperatures (those at which IETS is usually performed), Pb is the most widely used counter-electrode metal at the present time. The thickness of the Pb electrode is not critical, but generally speaking a policy of 'the thicker the better' is used. This inhibits the possible infusion of contamination (see 3.1.3 (iii), but at the same time does not introduce any resistive effects since Pb has zero resistance at 4.2K by virtue of its superconductivity. The Pb electrode thicknesses were usually of the order $\gtrsim$ 3000 Å.

In summary of the above device fabrication, schematic diagrams illustrating the geometry, and a cross-section through a completed, doped

junction are shown in Figs.3.2a, and 3.2b respectively.

3.1.3 Doping of IET Junctions

In general, the chemical and physical nature of the dopant, together with the particular dopant-oxide system of interest will determine which one (or more) of the doping techniques are applicable. For example, a factor may be simply whether the dopant is a solid, liquid, or (infrequently) a gas at STP - the conditions under which IET junctions are normally doped. Solids are usually liquid-phase doped from solution, but can also be vapour-phase doped by melting them in a resistively heated molybdenum boat within the vacuum chamber - an example of this being phenol crystals. On the other hand, some dopants are only weakly physisorbed on the oxide, this being the case infusion doping (where applicable) sometimes proves successful, although vapour-phase, and liquid-phase doping have also been employed; however, this requires subsequent cooling of the masks, substrate and doped oxide by means of a liquid N_2 fed 'cold finger' during the counter-electrode evaporation (13).

Other factors influencing adsorption and hence the choice of doping techniques may be the dopants vapour pressure, potential reactions at and/or with the oxide surface, and possibly solvent effects. The latter of these factors is discussed briefly in Chapter 5.

(i) Liquid-phase Doping

The dopant in question was dissolved in an appropriate 'spectrograde' organic solvent (ethanol, acetone, and benzene are commonly used) or de-ionised, millipored ($\leq 10^{-7}$ mU) water. It is essential that the solvents are pure since it is known that small amounts of hydrocarbon contamination may lead to spurious IETS data. The optimum solvents, and solution concentrations were ascertained by a 'trial-and-error' method on

Fig.3.2a - Geometry of a complete IET junction.

The junction is the cross-over region of the Aℓ, and Pb electrodes. Five junctions are evaporated onto a glass microscope slide which is then mounted in a PCB edge connector for subsequent 4-point electrical measurements - facilitated by the 4-terminal geometry.

Fig.3.2b - Cross-section through a completed IET junction.

Typical thicknesses of the 'sandwich' layers are shown.

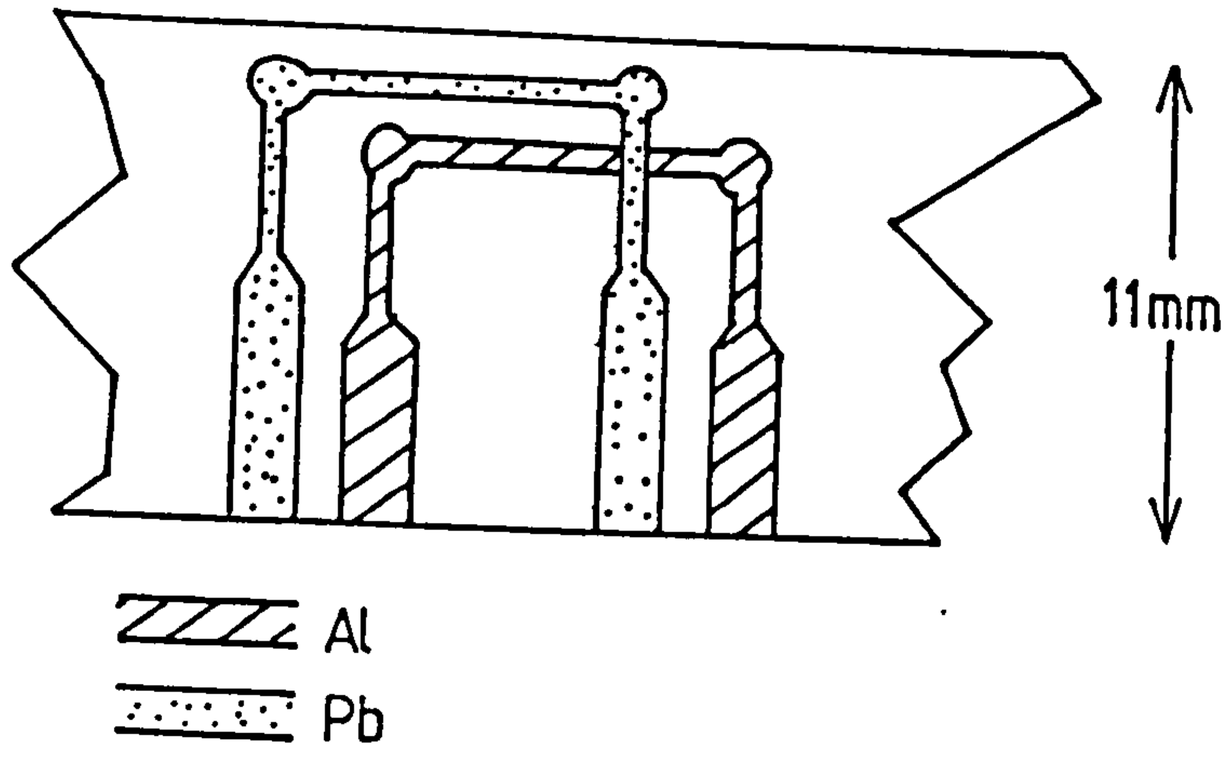
11mm
Al
Pb

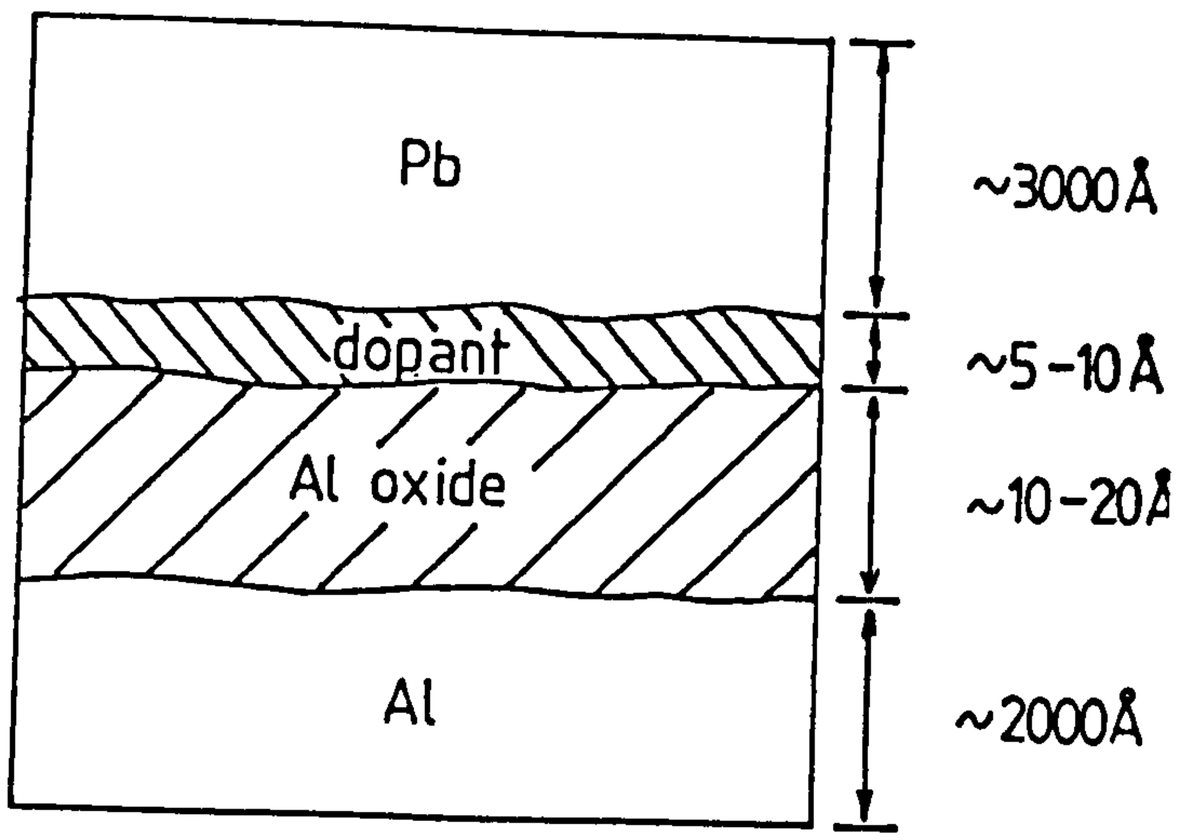
Pb
dopant
Al oxide
Al
~3000Å
~5-10Å
~10-20Å
~2000Å

several sets of IET junctions. This involves doping with a solution of fixed concentration, measuring the resulting IET junction resistances (and in some cases capacitances) which are indicative of surface coverage (see 3.1.5), and then modifying the solution concentration as necessary (14). Usual concentrations lie in the approximate range 0.1 to 0.01% w/v (1 to 0.1 $mg.ml^{-1}$).

Doping is achieved by mounting the glass slide on the turntable of a rotary spinner (oxidized base electrodes facing upwards) by means of a vacuum chuck, pouring a few drops of dopant onto the electrodes, and then spinning the slide and $\sim$ 2500 r.p.m to remove any excess solution. The slide is then removed from the spinner, and speedily replaced in the vacuum chamber awaiting the evaporation of the counter-electrode.

(ii) Vapour-phase Doping

A simple but effective vapour-phase doping technique has been devised by Reynolds (2, 15). This technique involves placing a few ml of pure dopant (usually liquid) in a petri-dish, positioning the glass slide with oxidized base electrodes face down on the edge of the dish, and finally covering the arrangement with an upturned beaker. A saturated vapour of the dopant is hopefully established in the beaker, and thus dopant molecules impinge directly onto the oxide surface, hence doping is achieved. The oxide may be exposed to the vapour somewhere in the region of a few seconds to a few minutes, again adopting a trial-and-error approach to determine the most suitable. The slide is then removed, and the counter-electrode evaporated as usual.

The vapour doping technique was not used extensively by the author, since the compounds relevant to this thesis do not satisfactorily adsorb (if at all) on the oxide by this method. However, during the course of the work concerning the preparation of oxides under controlled conditions

(Chapter 7), certain vapour-phase doping experiments were judiciously attempted.

(iii) Infusion Doping

The development of a technique by the author allowing contamination-free infusion doped IET junctions to be prepared routinely is described in some detail in Chapter 4. For this reason only a brief description of the technique, and precautions that should be taken in order to avoid contamination are described here.

The essential dynamics of the infusion process are that dopant molecules migrate to free adsorption sites on the oxide surface of an undoped Aℓ- Aℓ oxide-Pb IET junction by penetration through the grain-boundaries of the Pb electrode (16). The experimental details were as follows:

A set of completed, undoped Aℓ- Aℓ oxide-Pb IET junctions on a glass slide was placed in a sealable chamber into which an atmosphere of pure dopant and water vapour could be introduced. The chamber had previously been purged with an inert gas (e.g. N_2) in order to exclude atmospheric CO_2 since it is now widely believed that the combined presence of CO_2, and water vapour at the lead electrode produces formic acid contamination (17, 18). A mixture of dopant and pure water was conveniently introduced into the chamber via a syringe, and self-sealing membrane. A flow of N_2 was maintained during this procedure which inhibited infusion, and also prevented any possible ingress of room air. The N_2 flow was then terminated and the infusion process thus commenced as described above.

An increase in insulating barrier thickness of the tunnel junction due to the formation of monolayers of dopant, and to a lesser degree oxide thickening can be observed by monitoring the junction resistance and/or capacitance as a function of time (18). The former was achieved in

practice by mounting the glass slide in a PCB edge-connector within the chamber, and feeding connecting leads to a DVM via the self-sealing membrane. This allowed accurate 4 terminal resistance measurements to be made in situ. A diagram of the circuitry is shown in Fig.4.5 (Chapter 4). The latter was measured intermittently during the infusion process with a Wayne-Kerr a.c. bridge (Model No. B224) by removal of the glass slide from the chamber. Accurate junction capacitance measurements are in general quite difficult to obtain, mainly due to the fact that large voltage drops across an IET junction ($\gtrsim$ 1V), may ruin the insulating layer causing shorts and other defects (although some devices will withstand up to $\sim$ 2V). In general, low bias ($\sim$ 100 mV) capacitance measurements are accurate to about 20%. Approximate capacitance measurements were occasionally made before, and after doping as a supplement to the resistance measurements.

The infusion process could be terminated, and to some degree reversed by the re-establishment of a controlled flow of N_2 ; falls in junction resistance of as much as $\sim$50% have been observed. The rate at which infusion (and reverse-infusion) occurs is critically dependent on the thickness, and deposition rate of the Pb electrode (17). Generally speaking, thin, slowly deposited electrodes will result in an increased infusion rate. A thickness of $\sim$ 3000 Å deposited at $\sim$ 10 Å s^{-1} as measured by the quartz crystal monitor (Edwards FTM3) was found to be optimal. This afforded a managable degree of control of the infusion (and reverse-infusion) process with the N_2 'flushing', and also near monolayer coverage of dopant to be achieved over an acceptably short period ($\sim$ 1 hour).

3.1.4 The Reduction of Contamination in IETS

In order to prepare routinely IET junctions of good integrity

(i.e. ones having uncontaminated and continuous oxides, and electrodes free from pin-holes and other defects), a rigorous cleaning procedure was employed prior to junction fabrication and doping. This has been described in some detail by Langley (13), Tunnicliffe (1), and others (3). Following these workers, some of the precautions taken are listed in order below. These are in addition to those measures already described pertaining to the vacuum system, and junction doping (see 3.1.1 and 3.1.3 respectively).

1. The glass-slides were degreased by thoroughly wiping with Balzers substrate cleaners 1 and 2, applied with clean tissues.
2. The slides, and all materials coming into direct contact with them (slide holder, masks, also sample bottles, glassware used for sample preparations etc.) were then cleaned by immersing them in Decon 90, a strongly alkaline detergent solution, and then agitating them in an ultrasonic bath. The (brass) masks were additionally scrubbed with steel wool or abrasive nylon scourers to remove any previously evaporated deposits.
3. All materials were then profusely rinsed, firstly in filtered tap water for a few minutes, and then finally in de-ionised millipored water.
4. Where possible they were then hung in an oven to dry at $\sim 70^{o}C$. Certain materials and apparatus were not oven dried for obvious reasons (PTFE seals and PCB edge connectors for infusion doping work, neoprene 'O' ring seals, rubber bungs etc.). Any residual water on all surfaces was removed with a hot-air gun.
5. Disposable vinyl gloves were worn throughout the junction fabrication process, and tweezers were used where applicable. This avoided the introduction of fingertip grease.

3.1.5 Junction Viability for Subsequent Electrical Measurements

Before attempting to perform any meaningful electrical measurements such as recording I-V characteristics or IET spectra, the overall quality of the completed junctions was routinely checked as follows:

(i) Electrode Continuity

This was easily tested by measuring the 'spade to spade' electrode resistances using a low-power ohm-meter (see (ii)). Any visible defects such as scratches were rectified by careful application of good electrical conductivity silver paint. 'Fuzzy' or overlapping electrode geometry (which rarely occurs) could be improved by delicate scraping with any handy fine pointed instrument (e.g. scalpels, tweezers).

In general, electrode resistances of up to a few 10's of ohms were acceptable, and indicative of electrode thicknesses of the order a few thousand Å's.

(ii) Insulating Barrier Thickness

Broadly speaking, good quality tunnel spectra may be obtained if the insulating barrier (comprising oxide plus adsorbed dopant layer) is fairly uniform in cross section, and of the order $\lesssim 30$Å thick. The barrier thickness may be estimated by making approximate junction resistance and capacitance measurements at low bias ($\lesssim$ 100 mV). Of the two, junction resistances are both easier to measure, and more reproducible, and so perhaps offer a more reliable guide to the effective thickness.

(a) Resistance measurements: Following Brinkman, Dynes, and Rowell (19), Giaever (20) has shown that the approximate resistance of a MIM tunnel junction is exponentially dependent on mean barrier height and thickness (in eV and Å respectively) of the insulating layer, and inversely proportional to junction area. For our junctions, of nominal area

$\sim$ 0.25 mm^2, and assuming a reasonable value for the barrier height* junction resistances in the approximate range a few 10's to a few 100's of ohms indicate near monolayer coverage of dopant molecules on the oxide surface - the optimum for IETS.

Junction resistances were measured with a low-power ohm-meter so as to apply only a small voltage ($\sim$ 10 mV) across the junction, thus avoiding possible damage to the barrier. Junctions having resistances in the above range generally yield IET spectra of an acceptable quality on our spectrometer and are indicative of near monolayer coverage for typical IET junction areas of $\sim$ 0.25 mm^2

(b) Capacitance measurements: Measurements were made using a Wayne-Kerr a.c. bridge (Model B224) at 1 kHz with peak to peak amplitude of 100 mV. Absolute capacitance measurements of doped IET junctions are not necessarily meaningful unless compared with those of undoped junctions preferably fabricated at the same time, this ensures similar oxide layers are formed. Even then the interpretation is not complete unless a large number of measurements have been taken to guarantee that the results are statistically significant. If the total capacitance of an IET junction, C_T, is considered to be the series sum of capacitances due to the oxide, hydrated layer (due to adsorbed hydroxyls on the oxide surface), and subsequent monolayers of dopant, then C_T is given by:

$$C_T = \epsilon_o A \frac{1}{\frac{d_{ox}}{\epsilon_{ox}} + \frac{d_{oH}}{\epsilon_{oH}} + \frac{d_{m1}}{\epsilon_{m1}} + \frac{d_{m2}}{\epsilon_{m2}} + \ldots}$$

* See, for example, ref.2, Chapter 5 and references therein.

where A is the junction area d and ε have their usual meanings, and the subscripts ox, oH, m_1, m_2, ... refer to oxide, hydroxyl layer, monolayer 1, monolayer 2, and so on.

When one considers that the relative permittivity of water (assumed to be similar to ε_{oH})is ∿ 80 while those of Aℓ oxide and some organics are ∿ 8, and ≈ a few respectively, then considerable thickness dependent variations in C_T can be envisaged. Inserting some reasonable values for the d's ($d_{ox} \simeq 20$ Å, $d_{oH} \sim 1$ Å, $d_m \sim 5$ Å) shows that the contribution due to the d_{oH}/ε_{oH} term in the denominator is minimal, and the other terms effectively dominate.

It is unfortunate that for junctions of low resistance the a.c. conductance, and capacitance terms cannot be satisfactorily balanced on the bridge, unless > 0.5 V is placed across the junction with the measurement probes; this is dangerously close to the region in which most tunnel junctions fail (∿ 0.5 - 1.5 V), consequently, only those junctions having resistances of greater than ∿ several tens of ohms could be adequately investigated. Although in Chapter 4 it will be seen that it was possible to partially infusion dope a tunnel junction, then further dope and measure the ensuing change in capacitance, presumably due to the deposition of dopant monolayers (and perhaps slight oxide thickening effects) - capacitance date of this kind are more convincing than those obtained from junctions of low resistance.

(iii) Electrical Measurements on IET Junctions at 4.2K

At 4.2K Pb is a superconductor. The I-V characteristic of an Aℓ-I-Pb tunnel junction at low bias (≲ 5 mV), and at 4.2K shows a marked deviation from linear behaviour due to the existence of the superconducting energy gap, 2Δ, in the Pb density of states centred about the Fermi level $E_{F_{Pb}}$. It follows that at T = OK this gap precludes the possibility of

tunnelling (elastic or inelastic) from one metal to the other, through the insulating barrier, until the energy supplied to electrons due to the applied bias, V, exceeds the half-gap energy Δ; i.e. no tunnelling will occur until $V > \Delta/e$. (See Chapter 2.)

Existence of this non-linear behaviour, and hence evidence for superconducting tunnelling was verified experimentally by employing an a.c. modulation technique. Essentially, a small modulation current superimposed upon the standing current was applied to the junction in the expected vicinity of the non-linearity ($\sim$ 1 - 1.5 mV bias). This produced a distorted voltage response, V_{ac}, across the junction, and the level of distortion - a measure of the non-linearity, was visually inspected by feeding the voltage response signal to an oscilloscope. Fig.3.3 illustrates graphically how the low-bias I-V characteristic of a Metal 1-Insulator-Metal 2 (superconductor) tunnel junction gives rise to this distorted response. Junctions showing little or no distortion were usually rejected.

The principles of the modulation technique, as utilized in the operation of the IET spectrometer, are described in 3.2.1.

Fig.3.3 - Low bias I-V characteristics for a Metal 1-insulator-Metal 2 (M_1-I-M_2) tunnel junction:

(a) One metal superconducting at OK, the threshold at $V = \Delta/e$ is due to the gap in electron density of states 2Δ centred around the Fermi-level.

(b) One metal superconducting at T>OK. The threshold is not so clearly defined as in (a) due to thermal excitation of electrons in the vicinity of either side of the energy gap.

(c) Both metals normal.

The figure shows that if a sinusoidal modulation signal δ coswt is applied to the junction in the region of a non-linearity (in this case due to gap-related structure) a distorted voltage response will result. (See also Fig.3.4b for a better graphical illustration.) The response may be inspected on an oscilloscope.

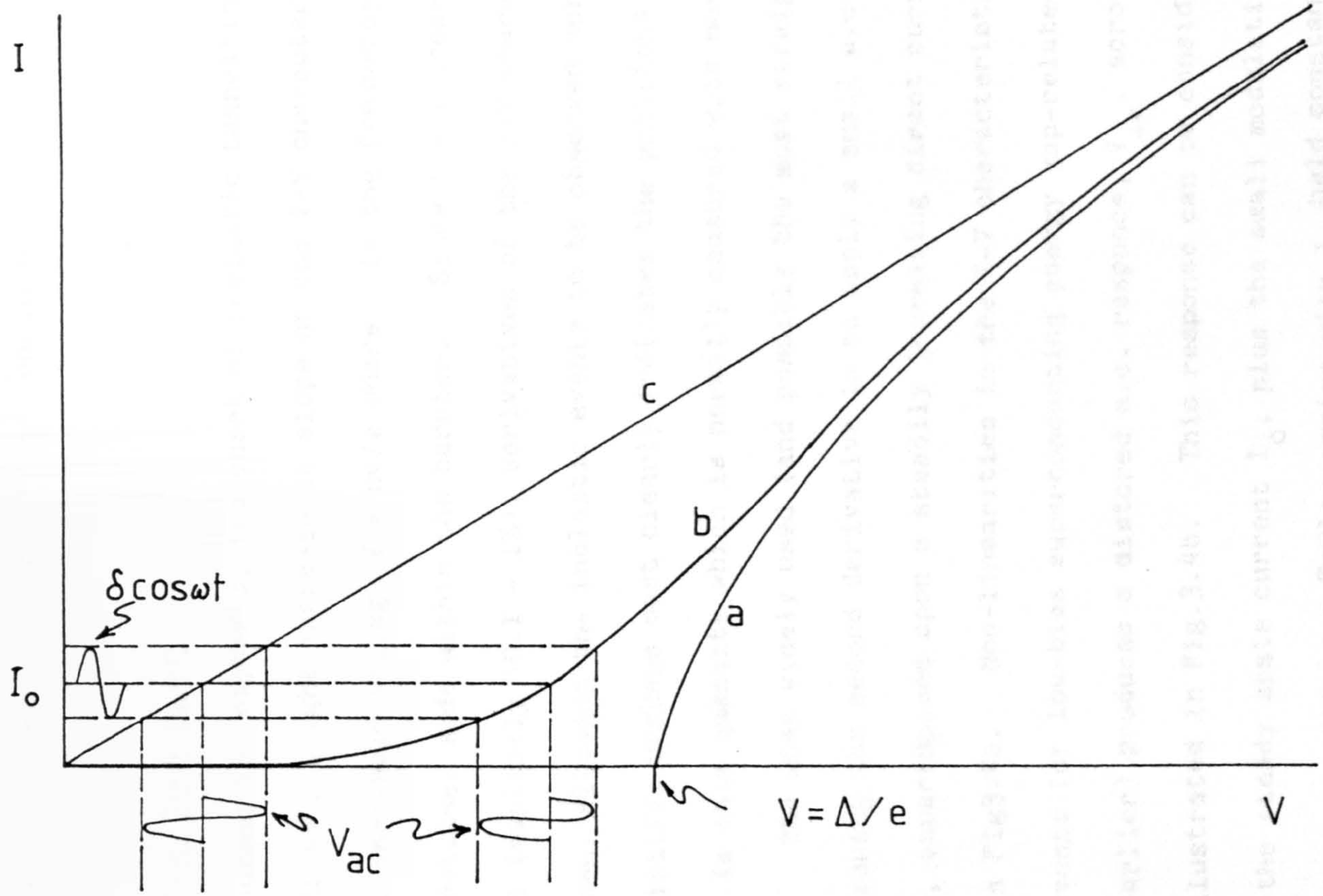
I
c
b
a
δcosωt
I_o
V_{ac}
V = Δ/e
V

3.2 THE IET SPECTROMETER

In this section a relatively simple and straightforward overview of the spectrometer design and operation is presented. The general approach will be to consider suitably accurate measurements of quantities proportional to the inelastic electron tunnel currents; these are essentially derived from the I-V characteristics of the junctions.

3.2.1 Modulation Techniques

As discussed in Chapter 2, the onset of inelastic tunnelling manifests itself as a slight increase in slope of the I-V characteristic at a particular threshold voltage $V = h\nu/e$ where is the frequency of a particular vibrational mode within the barrier. Since the increases are extremely small (typically $\sim$0.1 - 1%), derivatives of the I-V characteristic are usually taken, allowing the inelastic events to be observed more easily. The second derivative perhaps most clearly indicates the positions of such events, and it is this quantity which is normally measured with most IET spectrometers. The most widely used (and possibly the most straightforward) method for measuring the second derivative is to apply a small a.c. modulation signal, $\delta\cos\omega t$, superimposed upon a steadily increasing direct current, I_o, as indicated in Fig3.4a. Non-linearities in the I-V characteristic due to inelastic events (or low-bias superconducting energy gap-related structure as described earlier) produces a distored a.c. responce, V_{ac}, across the junction as illustrated in Fig.3.4b. This response can be considered as a function of the steady state current I_o, plus the small modulation current $\delta\cos\omega t$, and thus expanded as a Taylor series with I_o held constant (i.e. approximating to constant current conditions) as follows:

Fig.3.4a

Basic circuit showing how the modulation, and constant current supply are applied to the tunnel junction. A second harmonic voltage response $V_2\omega$ is developed across the junction which is proportional to $\frac{d^2V}{dI^2}(I_o)$.

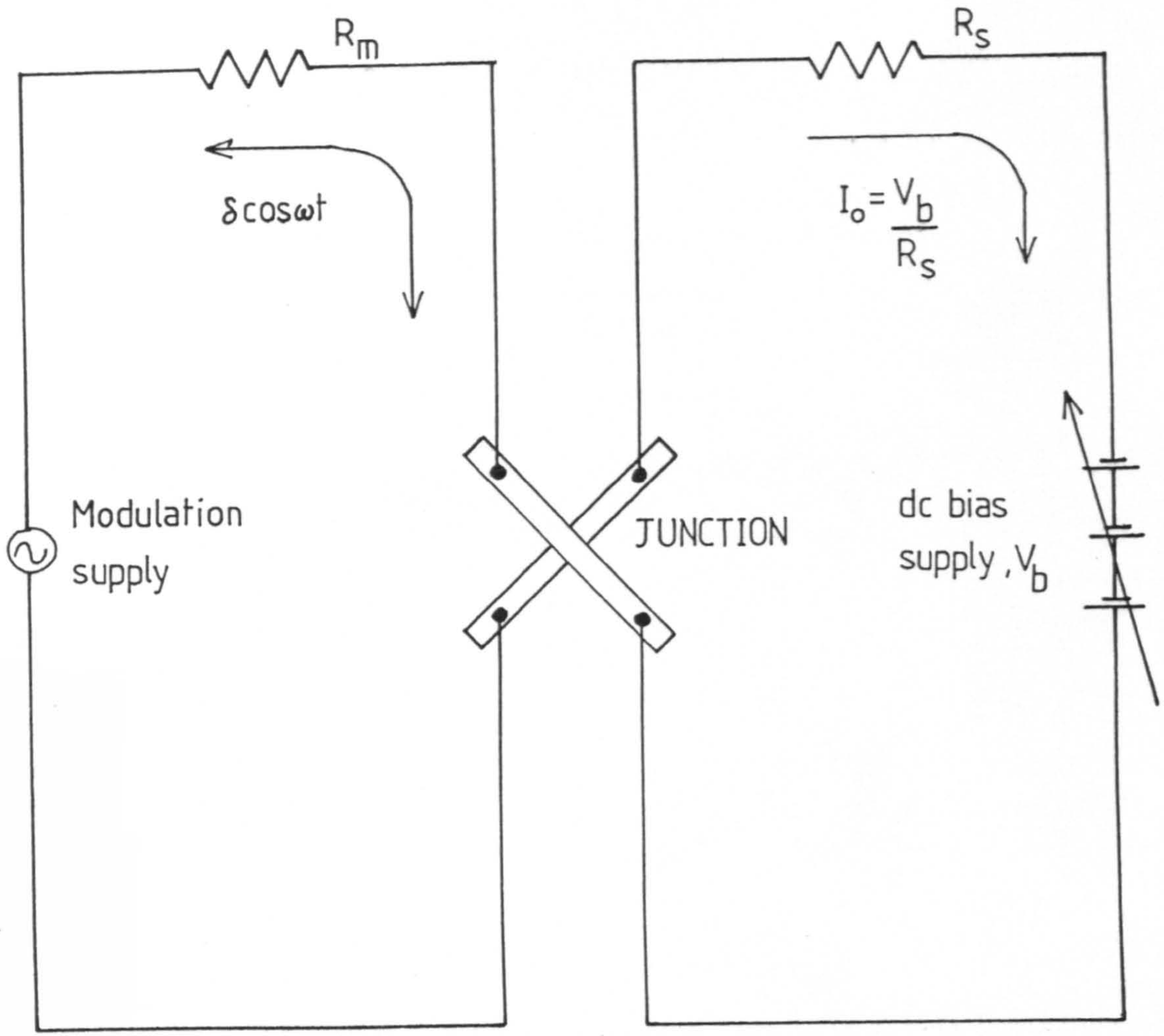
R_m
R_s
$\delta \cos\omega t$
$I_o = \frac{V_b}{R_s}$
Modulation supply
JUNCTION
dc bias supply, V_b

Fig.3.4b

A hypothetical I-V characteristic is shown with a sinusoidal modulation current of amplitude δ, applied superimposed upon the standing current I_o. The resulting voltage response V_{ac} is severely distorted due to the non-linearity of the curve.

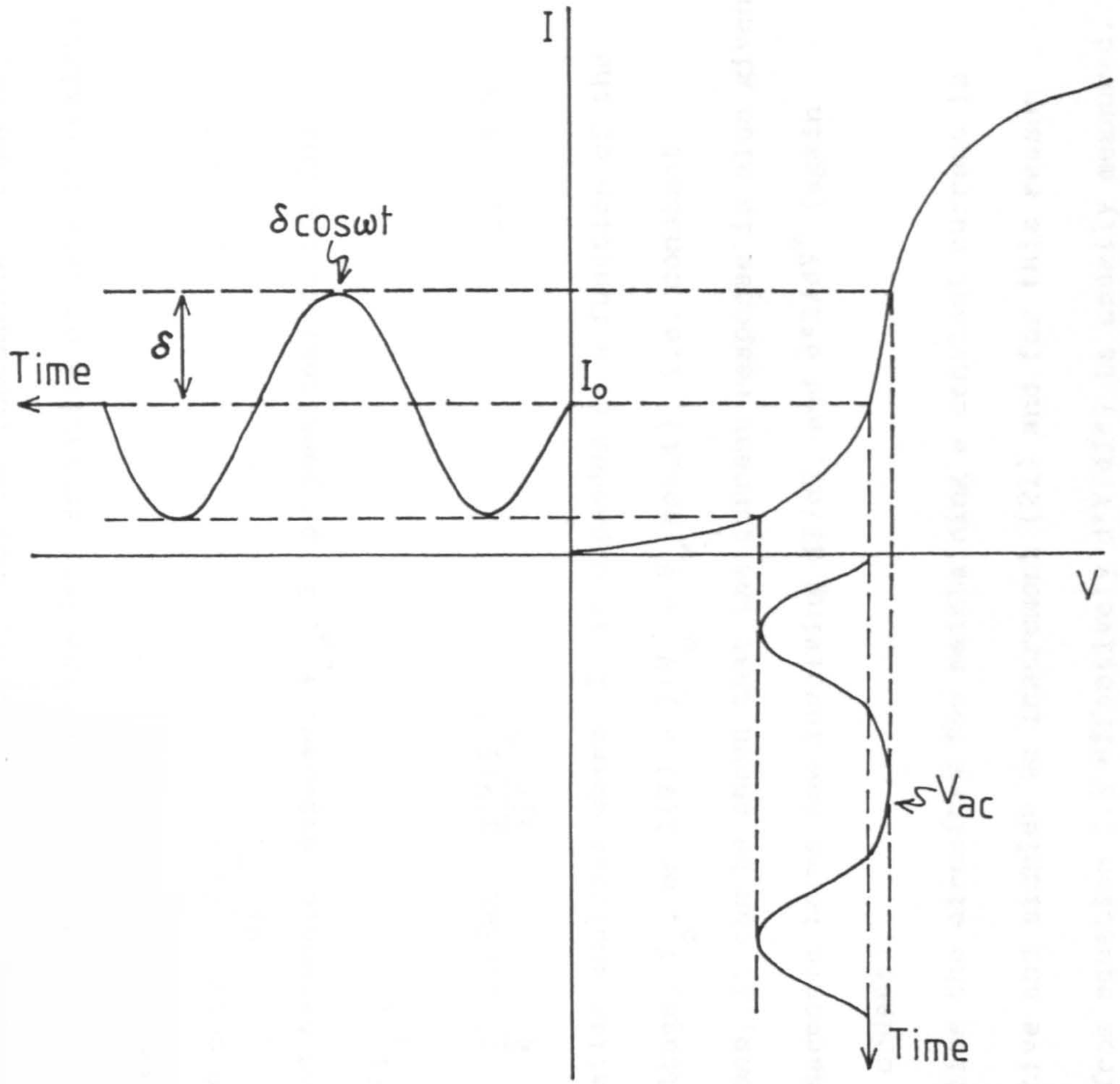
I
δcosωt
δ
Time
I_o
V
V_{ac}
Time

$$V(I) = V(I_o + \delta \cos\omega t)$$

$$= V(I_o) + \delta \cos\omega t \frac{dV(I_o)}{dI} + \frac{(\delta \cos\omega t)^2}{2!} \frac{d^2V(I_o)}{dI^2} + \ldots$$

$$= V(I_o) + \delta \cos\omega t \frac{dV(I_o)}{dI} + \frac{\delta^2}{4}(1+\cos 2\omega t)\frac{d^2V(I_o)}{dI^2} + \ldots$$

Ignoring 3rd and higher order terms, this gives:

$$V(I) = V(I_o) + \delta \cos\omega t \frac{dV(I_o)}{dI} + \left(\frac{\delta^2}{4}\frac{d^2V(I_o)}{dI^2} + \frac{\delta^2}{4}\cos 2\omega t \frac{d^2V(I_o)}{dI^2}\right) \quad \ldots 3.1$$

From equation 3.1, it is observed that the fundamental response, $V\omega$, of the device is proportional to the 1st derivative or dynamic resistance, $\frac{dV(I_o)}{dI}$, of the junction, i.e.

$$V_\omega = \delta \cos\omega t \frac{dV(I_o)}{dI} \quad \ldots 3.2$$

moreover, the 2nd harmonic response, $V_{2\omega}$, is proportional to the 2nd derivative, $\frac{d^2V(I_o)}{dI^2}$,

$$V_{2\omega} = \frac{\delta^2}{4} \cos 2\omega t \frac{d^2V(I_o)}{dI^2} \quad \ldots 3.3$$

By a similar analysis where I is expanded as a function of the steady state voltage, V_o, or $I(V) = I(V_o + V_\omega \cos\omega t)$, i.e. constant voltage conditions, it can be shown that the current response is also given by a series of harmonic terms now involving dI/dV, and d^2I/dV^2 (again ignoring higher orders).

In practice the circuitry for maintaining a constant current is both more sensitive and simpler to instrument (21) and for this reason $V_{2\omega}$ (and hence from equation 3.3 effectively d^2V/dI^2) is usually measured. Unfortunately, the price paid for these advantages is that information regarding absolute peak intensities cannot be directly retrieved. However, should absolute intensites be desired, d^2I/dV^2 can be calculated by

computer methods using the identity*

$$\frac{d^2V}{dI^2} = -\frac{1}{G^3}\frac{d^2I}{dV^2} \qquad \ldots \quad 3.4$$

if $G = \frac{dI}{dV}$ is approximately constant over the range of interest (which it usually is for ∿ 0 - 500 mV bias).

It should be mentioned that absolute peak intensity data are not frequently used in IET spectral analyses, since at the present time the selection rules governing this aspect of IETS are not well understood. However, qualitative data regarding relative peak intensities (normalized to say the Aℓ oxide phonon peak c.a. ∿ 115 mV) are sometimes useful as a consequence of the 'orientational selection rules' discussed in Chapter 2. Analyses of this nature can be performed almost as effectively using the quantity d^2V/dI^2. (Since no shifts in peak position - i.e. mode energy are introduced, and $-G^3$ is smoothly varying over the region of interest

* $\frac{d^2I}{dV^2} = \frac{d}{dV}\left(\frac{dI}{dV}\right)$

$= \frac{dI}{dV} \cdot \frac{d}{dI}\left(\frac{dI}{dV}\right)$

$= \frac{dI}{dV}\frac{d}{dI}\left(\frac{1}{\frac{dV}{dI}}\right)$

$= \frac{dI}{dV}\left(\frac{0 - \frac{d^2V}{dI^2}}{\left(\frac{dV}{dI}\right)^2}\right)$

$\frac{d^2I}{dV^2} = -\frac{dI^3}{dV} \cdot \frac{d^2V}{dI^2}$

or $\frac{d^2V}{dI^2} = -\frac{1}{G^3}\frac{d^2I}{dV^2}$ where $G = \frac{dI}{dV}$

as just mentioned).

A quantity sometimes utilized by experimentalists if $G^{-1}(dG/dV)$, which more closely resembles the density of vibrational oscillator strengths (22) and it is the above quantity that is usually plotted in the computer software routines that will be discussed in 3.2.5.

3.2.2 Principles of Spectrometer Operation - the Use of a Lock-in Amplifier (LIA) for a.c. Signal Recovery

The essential functions of the IET spectrometer are to:

(i) apply an a.c. modulation current superimposed upon a slowly increasing current to the junction,

(ii) detect the second harmonic voltage, $V_{2\omega}$, developed across the junction (which is proportional to d^2V/dI^2 as discussed),

(iii) plot $V_{2\omega}$ as a function of increasing bias voltage to thus obtain the IET spectrum.

A block diagram of a basic system which achieves the above objectives by employing a constant-current a.c. modulation technique is shown in Fig.3.5. At the root of the system is the lock-in amplifier (LIA). The general operation of the spectrometer is as follows. Firstly, the modulation signal, $\delta \cos\omega t$ superimposed upon a constant current is applied to produce an a.c. response, V_{ac}, across the junction as described earlier. V_{ac} is then input to the signal channel of the LIA, while the modulation current source - whose frequency has now been doubled to 2ω, is simultaneously fed into the reference channel. $V_{2\omega}$, the second harmonic component of V_{ac} may then be extracted by a powerful phase-sensitive, or lock-in detection technique (as will be discussed below) and then plotted as a function of increasing bias voltage on a chart recorder to obtain the IET spectrum.

Fig.3.5

Block diagram of a basic a.c. modulated constant-current IET spectrometer. The modulation current and slowly increasing current are applied to produce a second harmonic response $V_{2\omega}$ which is detected by the LIA, and plotted as a function of bias, V_b, as shown.

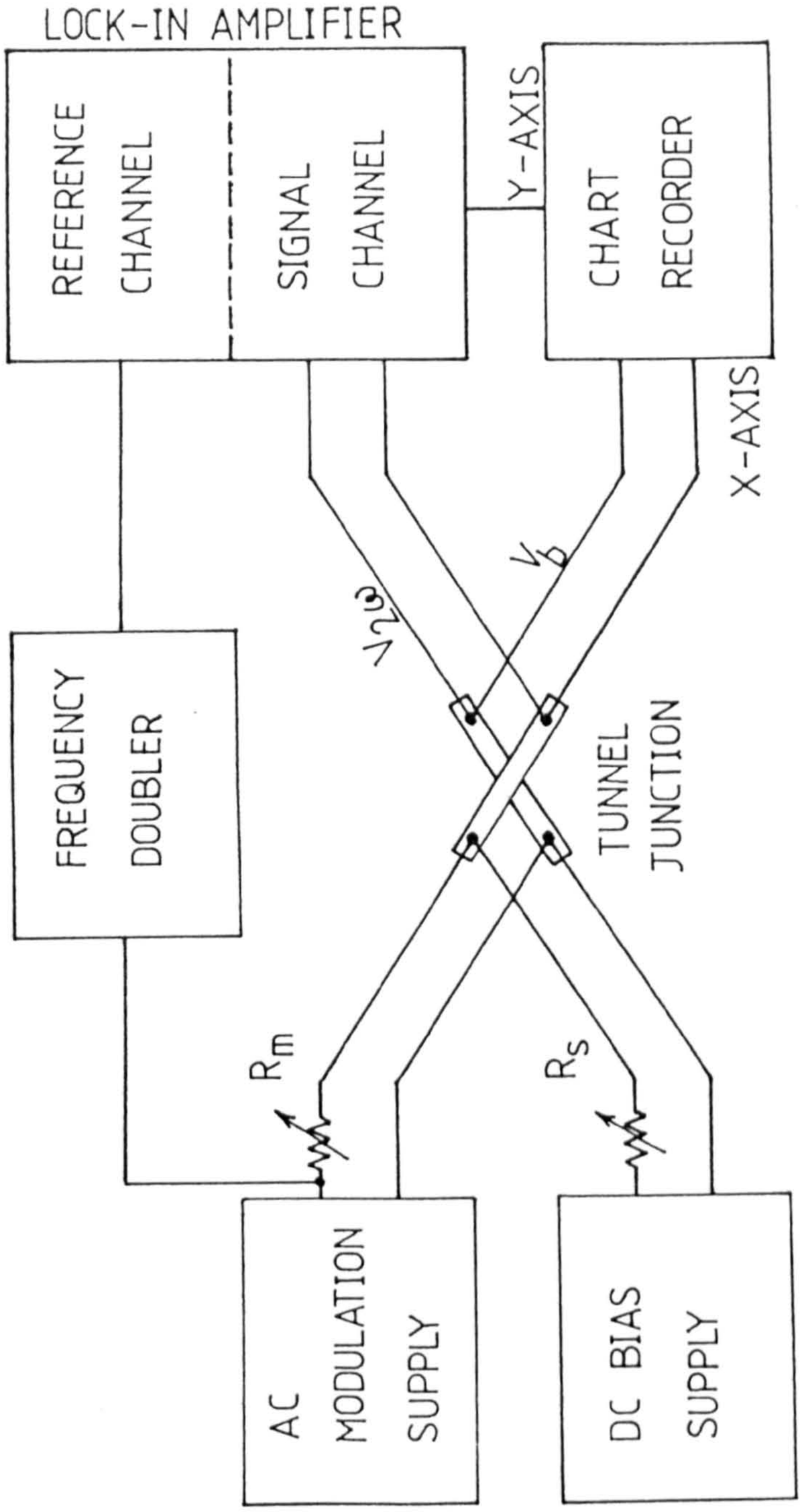
LOCK-IN AMPLIFIER
REFERENCE CHANNEL
SIGNAL CHANNEL
Y-AXIS
CHART RECORDER
X-AXIS
FREQUENCY DOUBLER
$\sqrt{2}\omega$
$\sqrt{2}$
TUNNEL JUNCTION
R_m
R_s
AC MODULATION SUPPLY
DC BIAS SUPPLY

The advantages of employing a LIA are essentially two-fold, firstly - and as will be discussed in 3.2.4, by the choice of a suitable operating frequency the effect of '1/f' noise can be considerably reduced. Secondly, small drifts in frequency of the oscillator are irrelevant; since the two inputs to the LIA (signal and reference) emanate from the same source, i.e. the modulation supply, their frequencies are always identical.

If the LIA is considered to be an ideal analogue signal multiplier (i.e. with no intrinsic noise (31)) having two voltage inputs - one a signal, V_s, and the other a reference, V_r, then its output, V_{out}, will simply be given by:

$$V_{out} = V_s V_r$$

Now, if both inputs are sinusoidal, of the same frequency, ω_s, and having a phase difference, φ, such that

$$V_s = V_s \cos\omega_s t \quad , \quad V_r = V_r \cos(\omega_s t + \varphi)$$

then by using a well known trigonometrical identity the LIA output will be given by:

$$V_{out} = \tfrac{1}{2} K V_s V_r \{\cos(2\omega_s t + \varphi) + \cos\varphi\} \qquad \ldots \quad 3.5$$

where K is a constant. If this output is then smoothed by a low-pass filter whose cut-off frequency is much lower than ω_s, the 2ω component will be removed, leaving only the frequency independent (constant) component, φ, i.e.

$$V_{out} = \tfrac{1}{2} K V_s V_r \cos\varphi$$

By adjusting φ to zero using a phase shift circuit in the reference channel, V_{out} will be a maximum,

$$V_{out} = \tfrac{1}{2} K^1 V_s V_r$$

and assuming V_r is approximately constant

$$V_{out} = K^1 V_s$$

where $K^1 = \tfrac{1}{2} K V_r$

In the above analysis the LIA was assumed to be 'noise-free'; however, in practice a noise signal will inevitably exist. Consider one component of noise, V_n, at frequency, ω_n, given by:

$$V_n = V_n \cos\omega_n t$$

The LIA output due to the product of this signal and the reference signal is

$$\begin{aligned} V_{n,out} &= V_n V_s \\ &= (V_n \cos\omega_n t)(V_s \cos\omega_s t) \\ &= \tfrac{1}{2} K V_n V_s \{\cos(\omega_n+\omega_s)t + \cos(\omega_n-\omega_s)t\} \quad \ldots \quad 3.6 \end{aligned}$$

The low-pass smoothing filter will remove the sum frequency component, $\omega_n + \omega_s$, leaving

$$V_{n,out} = \tfrac{1}{2} K V_n V_s \cos(\omega_n-\omega_s)t$$

Attenuation of the difference frequency component, $\omega_n-\omega_s$, will be determined by the pass-band of the filter. The noise (power) bandwith of the low-pass filter in the present spectrometer is given by (2) $\Delta\omega = \pi/2T$ where T is the time constant. If a signal is being extracted from a white noise background of bandwidth, $\delta\omega$, then the ratio of input to output noise powers, i.e. the signal to noise power ratio, is $\delta\omega/\Delta\omega$, and hence the signal to noise voltage ratio is $(\delta\omega/\Delta\omega)^{\frac{1}{2}}$. It follows that the signal to noise voltage ratio is proportional to $T^{\frac{1}{2}}$. In principle, this ratio may be improved by increasing the time constant, which will be highlighted in 3.2.4. Of course, over long spectral scan times other considerations such as drifts in the system must also be considered.

It is noted here that some workers have opted to incorporate the IET junction in a constant current bridge circuit arrangement (23-26), rather than the modulation technique described above. These circuits are not described here, further than to say that in such circuits unwanted

signals at the fundamental frequency, ω, are removed prior to amplification by the LIA. A drawback of such systems is that the bridge will go marginally out of balance during a spectral scan due to small changes in dynamic resistance of the junction.

3.2.3 Spectrometer Instrumentation

A circuit diagram of the spectrometer constructed primarily by Tunnicliffe (1, 3) and Reynolds (2) is given in Fig.3.6. The operation, essentially the same as the basic system just described in 3.2.2 is as follows.

The glass slide was mounted in a printed-circuit board (PCB) edge connector to which fine enamelled copper leads had been soldered. The leads were fed through a low thermal conductivity (German silver) tube for rigidity. The device was then immersed in a standard 50L Dewar of liquid He. Contacts between the cooled junctions and spectrometer were made using a length of 25 way screened cable, and 'D' type connector pieces. Subsequequent I-V measurements were made using a four-terminal technique which is vital if accurate voltage measurements are to be made, as parasitic resistive effects due to voltages that may have been developed across leads and junction electrodes are effectively eliminated. (The principle of this technique is illustrated in Fig.3.7.)

The d.c. supply was applied to the junction via a motor driven potentiometer (Rayleigh Instruments MP120) and series resistor R_s, chosen from R_1 to R_{11} whose values varied from <1Ω to several kΩ, depending on the corresponding IET junction resistance (this ensured large voltages were not developed across the junction which could lead to failure). A potential divider at the spectrometer input stage served to ensure that any noise pick-up at the junction was minimized. A 50 kHz modulation supply* from

* The reasons for the choice of this frequency are discussed in 3.2.4.

Fig.3.6

Circuit diagram of the IET spectrometer. Its operation is essentially the same as the block diagram of Fig.3.5 The tuned pre-amplifier rejects unwanted signal at the fundamental frequency ω. Capacitor, C_1, prevents any direct current from flowing along the measurement leads to earth, ensuring no voltage drops across the leads, and hence maintaining the 4-terminal measurement configuration. (See fig.3.7)

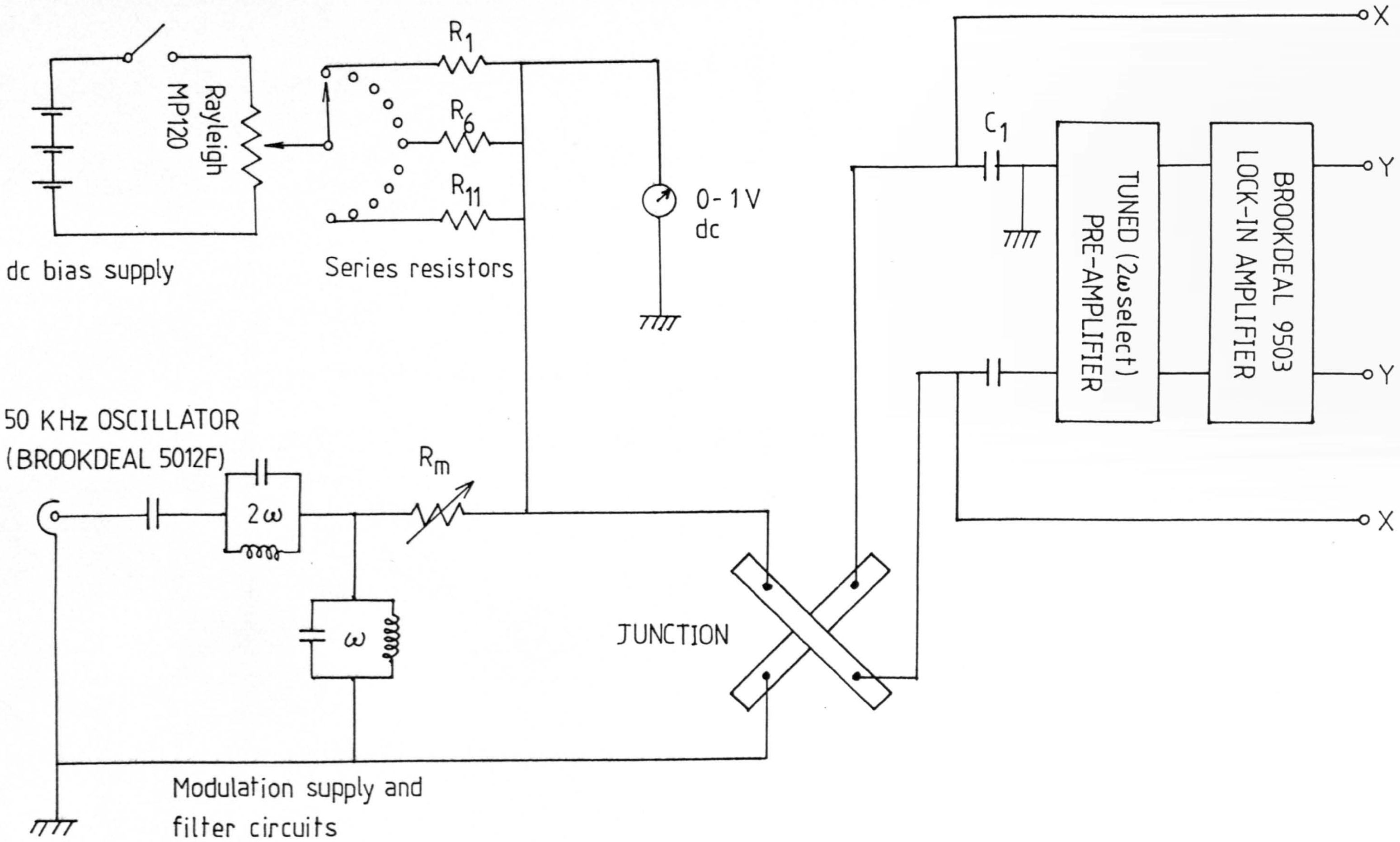
X
Y
Y
X
BROOKDEAL 9503
LOCK-IN AMPLIFIER
TUNED (2ω select)
PRE-AMPLIFIER
C1
R1
R6
R11
Rayleigh
MP120
dc bias supply
Series resistors
0-1V
dc
50 KHz OSCILLATOR
(BROOKDEAL 5012F)
2ω
ω
Rm
JUNCTION
Modulation supply and
filter circuits

Fig.3.7

Equivalent circuit of a four-point probe measurement scheme. Current, I, is supplied to the junction via terminals T_1 and T_2. The voltage drop V_j across the the junction due to its resistance R_j is measured at terminals T_3 and T_4. Parasitic resistances r_1 to r_4 are associated with the measurement leads. Provided that the input impedance of the voltmeter is sufficiently high, then ohmic potential drops across r_3 and r_4 will be negligible compared with that across R_j, while those across r_1 and r_2 are irrelevant.

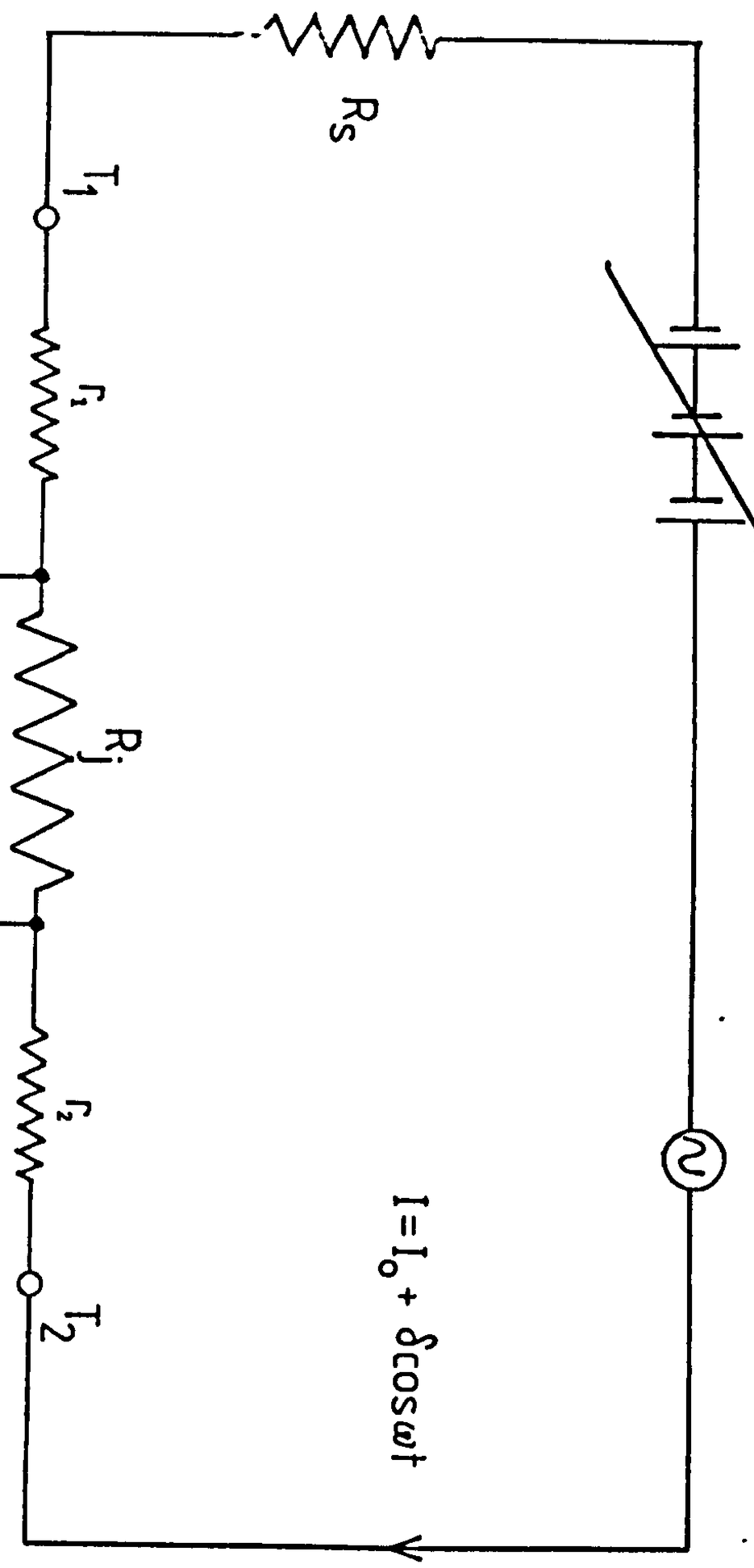
Rs
T1
r1
T3
r3
Vj, V2ω
Rj
r4
T4
r2
T2
Vb
Vω
I=Io+δcosωt

a Brookdeal 5012F module within the LIA typically of amplitude a few mV peak to peak (either measured on an oscilloscope, or using the LIA as a voltmeter) was applied simultaneously to the junction as shown. The second harmonic response, $V_2\omega$, was then detected by the LIA (Ortec-Brookdeal 9503). A tuned pre-amplifier (built in the School of Physics (1, 2)) incorporated in the line between junction and LIA served to further attenuate unwanted signals and the fundamental frequency, ω, and also boost the second harmonic input to the LIA. An overall gain of the LIA/pre-amplifier system of the order 10^7 at the second harmonic frequency was achieved (2). The preamplifier has a Q of $\sim$60, and offers considerable rejection of any signals at the fundamental frequency, ω. (The ratio of the gains at 2ω, and ω is approximately 50:1 (30).) Capacitor C_1 prevented any direct current from flowing along the measurement leads to earth, which would allow a dc voltage to develop across these leads, ruining the four-terminal measurement configuration. The outputs X, and Y, corresponding to the applied bias voltage and $V_2\omega$ respectively were either recorded on a chart recorder (Bryans 25000 A4) or stored in digital form on a magnetic disc (by means of an analogue-to-digital converter) for subsequent manipulation with a mini-computer (DEC LSI-11). The IET spectrometer may also be operated via the computer which offers certain advantages over the analogue system, as will be discussed in 3.2.5.

3.2.4 The Reduction of Noise, and Achievable Resolution

As discussed earlier, the increases in conductance of the IET junctions due to inelastic events are extremely small. Corresponding second harmonic voltage responses, $V_2\omega$, developed across the junction may be as small as 10 nV. Consequently, the reduction of electrical noise was, and is a major consideration. In addition to employing a LIA for a.c.

signal recovery the following precautions were also taken.

The entire spectrometer was housed in an earthed screened room with 1.6 mm thick Aℓ sheets. Electromagnetic interference from air-bourne sources, for example, radio-waves, was thus minimized. At 100 kHz (the second harmonic frequency) the skin depth of Aℓ is ≃ 0.26 mm, hence the chosen thickness of Aℓ offers substantial screening (3). Screened cables were also used where possible, ground loops were avoided, and the mains supply was fed through a filter circuit (Belling-Lee, Type L1822).

Finally, the operating frequency, 50 kHz, of the modulation supply ensured that the '1/f' noise appearing at the junction was maintained at an acceptabely low level, and comparable to that of other workers (27, 28). This is due to the fact that the high modulation frequency enables the amplification, and detection of signals by the LIA arrangement to be 'shifted' to a more convenient frequency where '1/f' noise is drastically reduced. At 50 kHz '1/f' noise is negligible compared with the second harmonic signal, $V_2\omega$, and noise from other sources (31). Noise appearing at the junction is then predominantly frequency-independent (i.e. it is said to have a "white" spectral distribution).

As described in Chapter 2, the ultimate resolution attainable in IETS is dictated by the sum of the contributions due to (i) instrumental broadening, and (ii) thermal broadening. The former is mainly dependent upon the amplitude of the modulation voltage supply, and the time constant setting on the LIA (assuming high quality electrical components with low noise figures are used in the circuitry). The latter is effectively reduced due to the immersion of the junction in liquid He, which consequentially renders the Pb electrode in its superconducting state. Initially one might consider this to be highly advantageous, not only on the merit of the zero resistance properties of the Pb, but additionally that

the characteristic line shape of a peak in d^2V/dI^2 with one electrode superconducting is intrinsically narrower than for both electrodes normal (see 2.4.3.). This should lead to better resolution, but unfortunately in practice there is little to be gained in terms of resolution with the Pb superconducting, since the dominant broadening effects are those due to the modulation voltage (for voltages $\gtrsim$ 0.5 mV (22)). Consider the simple argument below (10).

The magnitude of the second harmonic voltage response, $V_2\omega$, varies with the square of the applied modulation voltage, V_{mod}. Thus to increase resolution by reducing V_{mod} will have the effect of reducing the signal, $V_2\omega$ obtained across the junction (i.e. $V_2\omega$ falls off as V_{mod}^2). Now, the improvement in signal to noise (S/N) ratio that can be obtained by increasing the time constant, T_{CR}, on the LIA increases with the square root of the time constant. So, to maintain the same S/N ratio for a reduced V_{mod} will necessarily increase the required time constant and hence overall spectral scan-time.

If one assumes for the sake of argument that a hypothetical $V_2\omega$ signal has a magnitude of one unit, and if V_{mod} is then halved, $V_2\omega$ will be quartered ($V_2\omega \propto V_{mod}^2$); with this weaker resulting $V_2\omega$ signal in order to maintain the same S/N ratio would require a time constant 16 times greater ($S/N \propto T_{CR}^{\frac{1}{2}}$), and hence a proportionally longer spectral scan-time.

At 4.2K, the full width at half maximum (FWHM) of the thermal broadening function is given by 5.4 K_bT or 2.9 K_bT for Pb normal, or superconducting respectively where K_b = 0.08617 meV (22), (the super-conducting energy gap, Δ, for Pb at 4.2K is 1.2 meV). This corresponds to peak widths of $\sim$ 1.95, and 1.05 meV respectively. Similarly, the FWHM peak width due to modulation voltage broadening is given by 1.7 ΔV_{mod}^{rms}. Thus for modulation broadening to be commensurate with thermal

broadening at 4.2K would require V_{mod}^{rms} 1.13 or $\sim$ 0.6 meV for Pb normal, or superconducting respectively. With a V_{mod}^{rms} of $\sim$ 0.6 meV, a spectral scan time of $\lesssim$ 7 hours would be required (29) to obtain the same S/N ratio obtained with a V_{mod}^{rms} of 1.13 meV with our spectrometer, which is prohibitively long. The usual approach taken by IET spectrocopists is to reach a compromise by trading off good resolution (essentially requiring a low V_{mod} and hence weaker signal as discussed) against greater spectral scan-time. Most spectra in our laboratory were run with $V_{mod}^{rms} \simeq \sqrt{2}$ meV which with the appropriate time constant (usually 1 - 10 seconds) gave both acceptable resolution ($\lesssim$ 1 meV) and scan times ($\sim$ 1-2 hours). Summarizing in the words of Hansma (10) "there is a big price to pay for improvements in resolution".

3.2.5 Computer Methods

The main drawback with the analogue system thus far described is that the IET spectral data are recorded on a sheet of paper. The associated and sometimes tedious difficulties of manipulating data in such form will suggest themselves to the reader. It was for reasons of ease of data storage, and subsequent handling and analysis that the spectrometer has been interfaced to a computer. The system used where applicable was designed and built chiefly by Reynolds (30) who has also given a comprehensive account of its operation, and capabilities (2). No attempt is made here to describe the system explicitly, rather, it is intended merely to illustrate its potential.

A simplified block diagram of the system is shown in Fig.3.8. Filter circuits have been omitted. The mini-computer (DEC LSI-11) ramps up the bias voltage, V_b, across the junction in steady increments by means of a digital-to-analogue converter (DAC). The resulting second harmonic

voltage signal, $V_2\omega$, developed across the device and subsequently detected by the LIA, or the junction current may then be accurately measured with a Solatron-Schlumberger 7055 programmable DVM. The bias is simultaneously measured by another similar DVM. Their outputs are in a form compatible with the LSI-11, which allow the data to be stored in blocks on a magnetic floppy disc.

The DVM's and the peripherals indicated in Fig.3.8 are interfaced to the LSI-11 via serial RS232 lines operating between 600 and 9.6K baud rates. All other connecting leads are fully screened for reasons described earlier. The computer is operated by a real time operating system (RT-11) which enables the disc-drive unit, printer and plotter to be used by entering commands on the VDU screen. User written software may then be entered directly via the VDU or from another floppy disc. The existing software due to Reynolds enables the following generalized data-logging routines to be performed.

(1) Log I-V data

I-V measurements may be taken over a chosen bias range, and the I-V characteristics and/or their derivatives may be plotted (see below).

(2) Log IET spectra

Fully calibrated IET spectra may be recorded in a given bias range (usually 40 - 500 mV). $V_2\omega$ ($\propto d^2V/dI^2$) and V_b are measured, and (1/G) dG/dV is calculated. A complete record of the data is stored on a header file.

(3) Plot specific portions of the data

The above second derivative data may be plotted in an expanded form for closer scrutiny. Peak energies may be digitized via a stylus adaptor on the plotter. Various data may be superimposed allowing useful visual comparisons between them to be made. Linear, or

Fig.3.8

Simplified block diagram of the computer data acquisition system interfaced to the IET spectrometer (due to Reynolds (2)). The LSI-11 controls the bias supply with the aid of a DAC. Resulting data from the spectrometer are measured with two DVM's and are then stored on floppy disc for subsequent analysis.

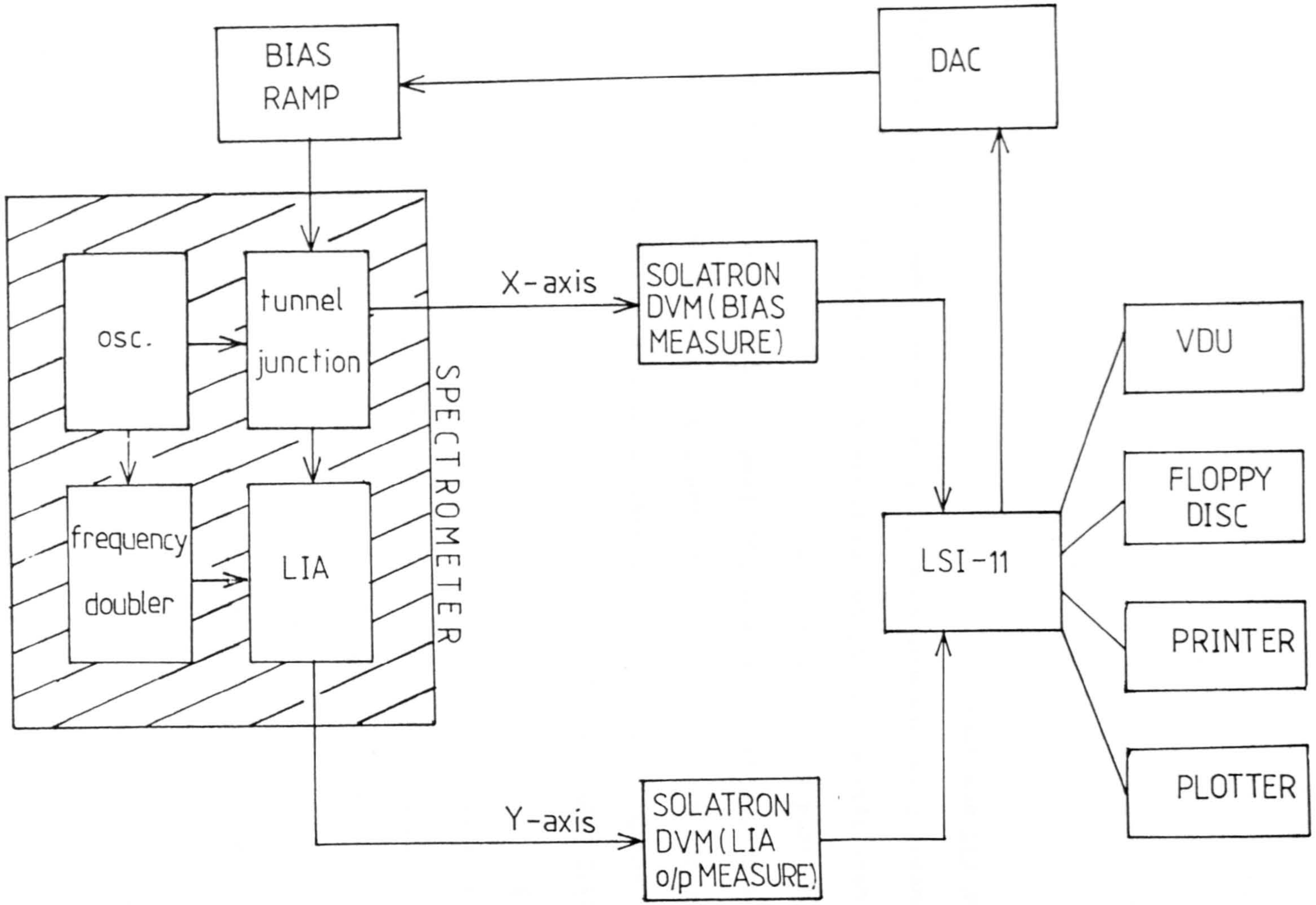
BIAS
RAMP
DAC
osc.
tunnel
junction
X-axis
SOLATRON
DVM(BIAS
MEASURE)
VDU
SPECTROMETER
frequency
doubler
LIA
LSI-11
FLOPPY
DISC
PRINTER
PLOTTER
Y-axis
SOLATRON
DVM(LIA
o/p MEASURE)

quadratic backgrounds may be numerically substracted from the logged spectra which in some cases offers an enhancement of weak spectral features.

(4) Plot the data in 'journal ready' form

Axes of the second or (numerically differentiated) third derivative versus bias plots are fully labelled as defined by the user. Backgrounds may also be subtracted, and spectra superimposed.

(5) Calculate barrier parameters

The I-V data logged as in (1) above may be operated upon to yield junction barrier parameters for a trapezoidal barrier as predicted by the theory of Brinkman, Dynes and Rowell (i.e. φ_1, φ_2 the work functions meV on either side of the barrier, and its thickness, d in $\mathring{A}$).

(6) Digitize graphical data

Other graphical data (e.g. IR spectra) may be stored digitally.

The stylus adaptor is placed at various points on the region of interest, the data are then digitized and their co-ordinates may be displayed on the VDU screen.

Full descriptions of (1) to (6) above may be found in Reference 2. During the course of the present work, 2, 3, and 4 were used for the logging and display of IET spectra.

CHAPTER THREE - REFERENCES

1. D.L.Tunnicliffe. Ph.D.Thesis, 1983. School of Applied Physics, Leicester Polytechnic.

2. S.Reynolds. Ph.D. Thesis, 1983. School of Applied Physics, Leicester Polytechnic.

3. D.P.Oxley, et al. Surf. Int. Anal., 2(1), 31 (1980).

4. H.E.Evans, W.M.Bowser and W.H.Wernberg. Applications of Surf. Sci., 5, 258 (1980).

5. F.Jona. J. Phys. Chem. Solids, 25, 2155 (1967).

6. J.B.Peri and R.B.Hannan. J. Phys. Chem., 64, 1526 (1960).

7. M.L.Hair. Infra-red spectroscopy in surface chemistry. Edward Arnold publ. New York 1967.

8. P.K.Hansma, D.A.Hickson and J.A.Schwartz. J. Catal., 48, 237 (1977).

9. D.G.Walmsley. Private Communication.

10. Tunnelling spectroscopy, capabilities, applications and new techniques. P.K.Hansma Ed., Plenum Press, New York, 1982.

11. P.K.Hansma. Phys. rep(C), 30(2), 145 (1977).

12. Kirtley and Hansma. Phys. Rev. B 13, 2910 (1976)

13. A.J.Langley. Ph.D. Thesis, 1982. School of Physics, Leicester Polytechnic.

14. M.G.Simonson, R.V.Coleman and P.K.Hansma. J. Chem. Phys., 61, 3789 (1974).

15. S.Reynolds, D.P.Oxley and R.G.Pritchard. Spectrochim. Act., 38A(1), 103 (1982).

16. R.C.Jacklevic and M.R.Gaertttner. Applications Surf. Sci., 1, 479 (1978).

17. W.J.Nelson and D.G.Walmsley. Thin Solid Films, 79, 229 (1981).

18. R.R.Mallik, R.G.Pritchard, D.P.Oxley, C.C.Horley and J.Comyn. Thin Solid Films, 112, 193 (1984).

19. W.F.Brinkman, R.C.Dynes and J.M.Rowell. J. Appl. Phys., 41(5), 1915 (1970).

20. I.Giaver in Tunnelling Phenomena in Solids (Chapter 3). E.Bur stein, and S.Lundqvist (Eds.) Planum Press, New York (1969).

21. R.G.Keil, T.P.Graham and K.P.Roenker. Appl. Spectrosc., 30, 1 (1976).

22. J.Kirtley. J. Am. Chem. Soc., 80, 217 (1980).

23. J.G.Adler and J.E.Jackson. Rev. Sic. Inst., 37, 1049 (1965).

24. J.G.Adler, T.T.Chen and J.Straus. Rev. Sci. Inst., 42, 362 (1971).

25. N.EIB, AND P.N.HENRIKSEN, UNPUBLISHED WORK, UNIV. OF AKRON, AKRON OH 44325, U.S.A.

26. P.N.Shott and B.O.Field. Spectrochim. Acta., 35(A), 301 (1978).

27. J.Lambe and R.C.Jaklevic. Phys. Rev., 165, 821 (1968).

28. D.G.Walmsley, I.W.McMorris, W.E.Timms, W.J.Nelson, J.L.Tomlin and T.J.Griffin. J. Phys. E. Sci. Instrum., 16, 1052 (1983).

29. T.M.Ginnai, Ph. D. Thesis, School of Applied Physics, Leicester Polytechnic, 1982.

30. S.Reynolds, L.D.Gregson, C.C.Horley, D.P.Oxley and R.G.Pritchard. Surf. Int. Anal., 2, 6 (1980).

31. T.D.S.Hamilton. Handbook of Linear Integrated Electronics for Research. McGraw Hill (UK) Book Co. Ltd., (1977).

CHAPTER 4

CONDUCTANCE CHANGES DURING THE INFUSION DOPING OF IET JUNCTIONS

4.1 INTRODUCTION

There are three methods by which monolayers have been incorporated into IET junctions, namely liquid phase-, vapour phase-, and infusion doping. Chapter 5 describes how the first of these has been successfully employed to obtain IET spectra of adsorbed polymers. However, this technique fails when one attempts to investigate certain volatile monomers and solvents, as does the second method of vapour phase doping. An improved understanding of the adsorption of such compounds is desirable since it could provide valuable insight into the behaviour of the respective polymers liquid phase doped from solution; the third technique of infusion doping was thought to offer some promise for the study of monomers and solvents.

Infusion doping is a relatively new technique in IETS, first reported in 1977 by Jaklevic and Gaerttner (1,2). Dopant molecules may be introduced onto the Aℓ-oxide surface of a completed, undoped Aℓ/Aℓ-oxide/Pb IET junction by penetration of the Pb counter electrode. This effect has been verified by simple masking experiments whereby vacuum grease was carefully applied over the Pb electrode prior to doping. Subsequent IET spectroscopic analysis revealed that no infusion had occurred, as indicated by 'clean' spectra (2,3). Similar masking of the edges of the junctions showed that for the electrode geometry and substrates used, the dominant route for infusion was indeed directly through the Pb electrode. As will be discussed in Section 4.3.1., the rate at which infusion occurs is critically dependent upon the thickness, and deposition rate of the Pb electrode (1-4). The possible use of other top electrode materials has been investigated, since thin Pb films are generally unstable under

infusion doping conditions, i.e. water-rich vapours which adsorb upon the films in the form of a dew, and quickly attack them. However, most other metals have proved ineffective; Aℓ, Ag, Cr, and Cu have all been tried unsuccessfully while Sn, and Au only show limited potential (3). In the present work Pb films were used throughout.

Although the molecular dynamics of the infusion process are not yet fully understood, it is believed that the presence of water vapour is essential (1,2), and increases dopant mobility (4). Since the majority of compounds studied to date by infusion doping have been miscible in water, it was not clear at the outset whether or not compounds with only limited solubilities would give spectra when infusion doped in the presence of water. Phenol for example is only slightly soluble in water but gives good quality IET spectra when doped in this manner (2).

Consequently, a programme of experiments was undertaken to investigate the possibility of infusing the water-soluble monomers vinylacetate, and methylmethacrylate in the presence of water.

A problem often encountered in infusion doping experiments is that of formic acid contamination. As just mentioned water vapour appears to be essential for successful infusion; the boiling point of formic acid ($\sim 100.5^{o}C$) is very close to that of water and it is therefore not surprising that formic acid is a common impurity in water at the p.p.m. level. Formic acid may also arise due to possible reactions between atmospheric CO_2, and water vapour at, and catalysed by the Pb electrode during infusion (4). Accordingly, a simple apparatus has been devised by the author which allows experiments to be performed in a sealed doping chamber purged with N_2 prior to infusion in order to exclude CO_2. No evidence of formic acid contamination has since been apparent in the resulting IET spectra. Additionally, the apparatus allows rapid changes

in IET junction conductance which occur during infusion to be monitored accurately at low-bias by means of a digital multimeter interfaced to a microcomputer. (Full details of the apparatus are given in 4.3.1). These conductance measurements taken in conjunction with the corresponding changes in junction capacitance clearly indicate an increase in thickness of the insulating barrier during infusion doping, and therefore allow the optimum infusion time to be estimated. (It is recalled from Chapter 3 that a monolayer of adsorbed molecules corresponds to optimum spectral sensitivity in IETS.)

Un fortunately, the experiments with vinyl acetate and methylmethacrylate have proved unsuccessful. The infusion doped IET spectra which were obtained corresponded merely to thickening of the oxide/hydroxyl layer. However, infusion with solvents, in particular water, and water/acetone mixtures has proved fruitful. Using above apparatus it has been possible to record plots of IET junction conductance as a function of infusion time. These plots show clear evidence of regions of different slope. A crude model of sequential monolayer growth has been proposed and published (5) which to a first approximation predicts the form of these plots. In this model the growth of an initial monolayer corresponding to hydroxyl ion coverage is assumed, followed by the formation of subsequent monolayers of acetone.

The above experiments involving the infusion of water, and water/acetone mixtures, together with the model for sequential monolayer growth largely form the basis of this chapter.

4.2 THEORETICAL ASPECTS

4.2.1 Elastic Tunnelling at Low-bias during Infusion Doping

As discussed in Chapter 2, if the insulating barrier of a metal-insulator-metal (MIM) device is sufficiently thin, i.e. of the order $\lesssim$ 30 Å, then electrons may tunnel through the classically forbidden region, and emerge at the other side of the barrier with a finite probability. The tunnelling probability falls off rapidly in a negative exponential manner as the barrier thickness is increased, which is reflected in the corresponding increase in junction resistance, or conversely the decrease in conductance. Approximately 99% of electrons constituting the tunnel current tunnel elastically.

Brinkman, Dynes and Rowell (6) using a trapezoidal barrier model, and the Wantzel-Kramers-Brillouin (WKB) approximation have shown that the conductance, G, of a junction of area A_j at low applied bias due to the elastic tunnel current is given by:

$$G = \gamma' \frac{\bar{\Phi}^{\frac{1}{2}}}{S} A_j \exp(-K S \bar{\Phi}^{\frac{1}{2}}) \quad \ldots \quad 4.1$$

where γ' is a constant, Φ is the mean barrier height in eV, s is the barrier thickness in Å, and K is a parameter whose numerical value is approximately equal to unity for the units quoted. For the region of interest in the present work, the pre-exponential factor $\bar{\Phi}^{\frac{1}{2}}/S$ is smoothly varying and may be considered to be constant in comparison with the corresponding variations in the exponential term. Taking the above considerations into account, the junction conductance may be expressed to a good approximation (7) by:

$$G \simeq \gamma A_j \exp(-S \bar{\Phi}^{\frac{1}{2}}) \quad \ldots \quad 4.2$$

where the parameter has a roughly constant value during infusion doping. It follows that for low bias (i.e. $V_b \ll \bar{\Phi}$), the I-V characteristic will

be linear with slope G, as one would expect. Equation 4.2 is the starting point for the simple model for the variation of junction conductance with infusion time proposed in 4.2.2.

In practice, the low-bias I-V characteristic is linear up to $\sim$ 100 mV (slight deviations of a few % due to inelastic events need not concern us here). If a small and constant current, i, is applied to the junction at low bias, then increases in barrier thickness will be manifested in corresponding near-ohmic increases in the junction potential. It is essential that the junction potential should be monitored using a four-point probe measurement technique for reasons already discussed in Chapter 3 (see Section 3.2.3).

4.2.2 Model Conductance Changes during Infusion Doping

As will be seen in 4.4.1, experimental conductance versus time (G-t) plots obtained from IET junctions during infusion doping are fairly reproducible. They would also appear to have characteristic forms depending mainly upon the nature of the dopant compound in question, and the thickness and microstructure of the Pb electrode. The forms of these plots can be partly understood in terms of the following preliminary analysis.

The infusion of dopant molecules into IET junctions will in general modify the nature of the potential barrier, resulting in local variations in its height and width. Overall, these changes will produce a net decrease in junction conductance as a direct consequence of equations 4.1, and 4.2. As a first step towards analysing these decreases, a relatively straightforward model was proposed. Firstly, the following assumptions were made.

(i) The infusion of dopant molecules results in uniform, and sequential

formation of monolayers on the Aℓ-oxide surface; i.e. it is stipulated that one monolayer must be completed before the consecutive layer(s) may be grown.

(ii) The mean barrier height, Φ, remains constant during infusion. Any resultant conductance changes estimated using equation 4.2 are therefore primarily due to increases in insulating barrier thickness, S.

(iii) Monolayers are adosrbed in a uniform manner in equal times, t_m, independent of the nature of the previous monlayer, or underlying surface.

(iv) The junction is of planar composition, i.e. essentially possessing a 'smooth' or 'undulating' oxide surface containing no defects in its topography.

The model has a number of necessary approximations. For example, in assumption (iii) above, no account is taken of 'sticking probability' between like, or unlike monolayers. Clearly this will effect the time taken to form a monolayer. The first monolayer will adsorb onto an Aℓ-oxide surface, which possesses a number of free adsorption sites in the form of surface hydroxyls, and local acidic and basic sites. Subsequent layers are offered the surface of the previously deposited monolayers, which may not be conductive to strong adsorption. One would intuitively expect the initial monolayer to be more tightly bound, and formed more quickly than subsequent monolayers. Another consideration - the phenomenon of an initial delay associated with the time required to penetrate the Pb electrode could also play an important role in the rate of infusion.

For a crude initial model nominal values of the mean barrier height, Φ, were tacitly assumed to be constant throughout infusion. In

fact, Φ, may vary in quite a complex manner (6,8).

Using the above assumptions it will be demonstrated that the following simple analysis predicts discontinuities in the slope of the G-t plots, corresponding to the formation of successive monolayers on the oxide surface.

(a) Growth of the first monolayer

It is assumed that the first monolayer is due to hydroxyl ion coverage of the oxide as suggested by Nelson et al (4), (this will be discussed further in 4.4.5). Invoking assumptions (i), and (iii) above, let the first monolayer grow in a uniform manner as indicated in Fig.4.1a.

For a linear time-dependent growth, the area-time relationship may be given simply by:

$$A_c = \beta t$$

$$A_j = \beta t_m \qquad \ldots \quad 4.3a$$

with the constraints

$$A_j = A_u + A_c$$

$$o < t < t_m \qquad \ldots \quad 4.3b$$

where A represents area, and the subscripts c, u, ox, and j refer to covered, uncovered, oxide, and junction respectively; t_m is the time taken to grow one complete monolayer (assumed equal for all monolayers as just discussed) and β is a constant dependent on the mass and density of the dopant.

For the present work it is convenient to normalize the junction conductance, G_j, $(= G_u + G_c)$ to the oxide conductance G_{ox}, and express the results as a function of time, i.e.

$$g_1(t) = \frac{G_u + G_c}{G_{ox}} \qquad \ldots \quad 4.4$$

Fig.4.1a

Schematic representation of the first (hydroxyl) growth. A uniform monolayer growth-rate is assumed. G denotes conductance, and A area. The subscripts c, u, ox, and j refer to covered, uncovered oxide and junction respectively. The thickness of the oxide and hydroxyl layer S, and L in Å are also indicated.

Fig.4.1b

A similar representation of the second (dopant) monolayer growth. It is assumed that the dopant layer thickness M Å is formed on the previously completed hydroxyl layer.

Fig.4.1c

A schematic representation perhaps more closely resembling the dynamics of the infusion process. Dopant molecules arrive at the hydrated Aℓ-oxide surface in a random manner, to gradually form a monolayer of mean thickness, M, Å.

The dopant monolayer may comprise partly of water molecules.

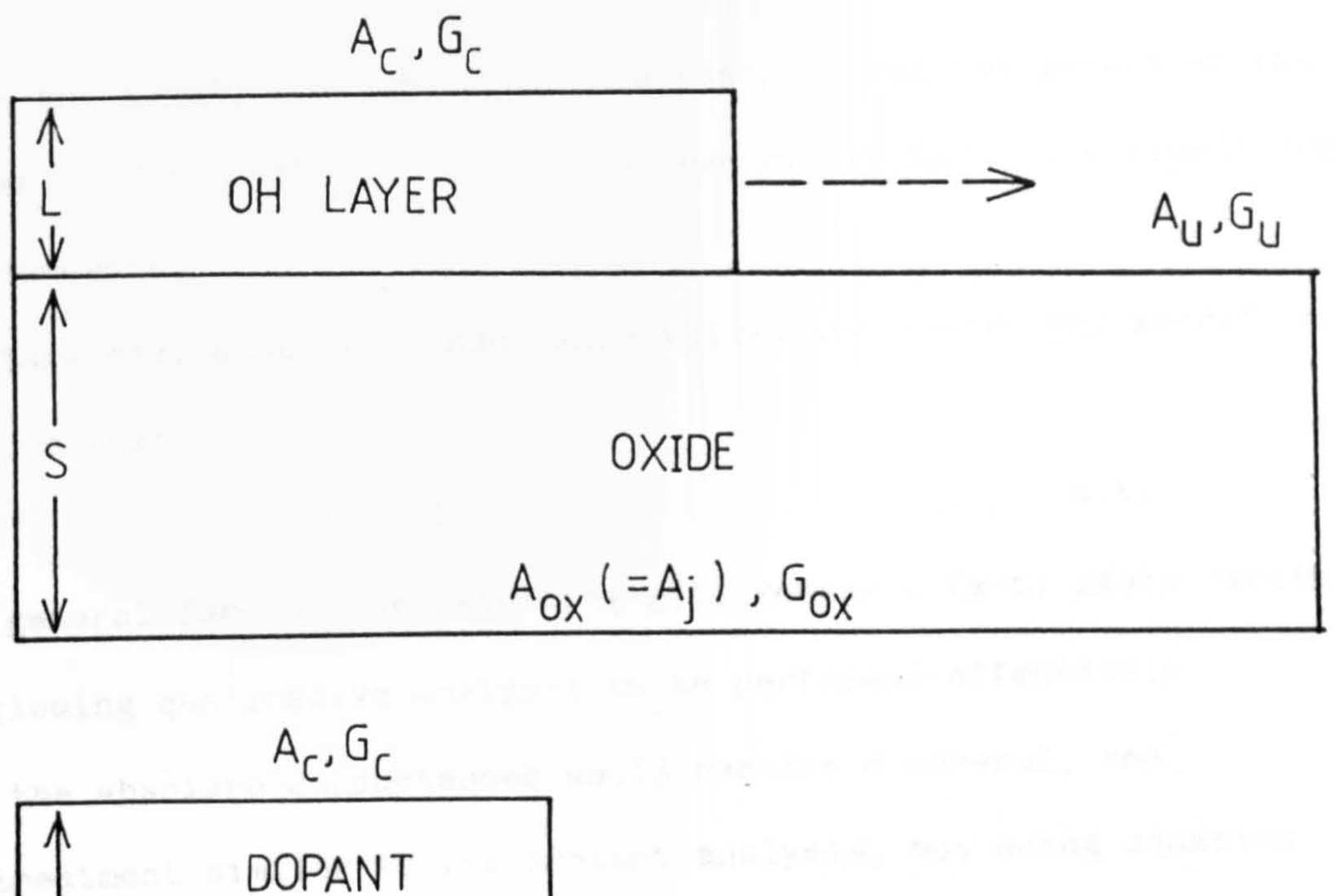
A_C , G_C
L
OH LAYER
A_U , G_U
S
OXIDE
A_{ox} ($=A_j$) , G_{ox}

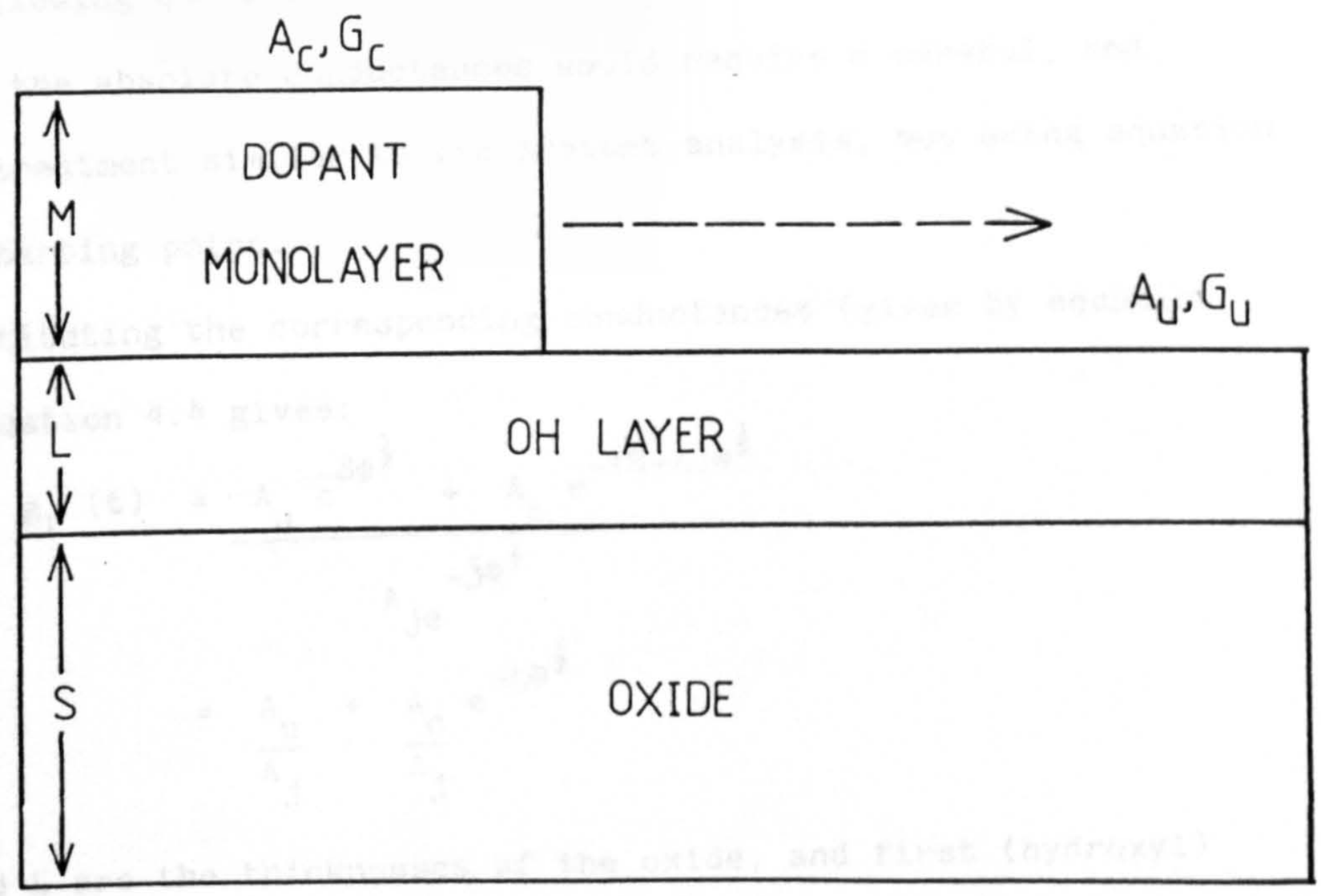
A_C, G_C
M
DOPANT
MONOLAYER
A_U, G_U
L
OH LAYER
S
OXIDE

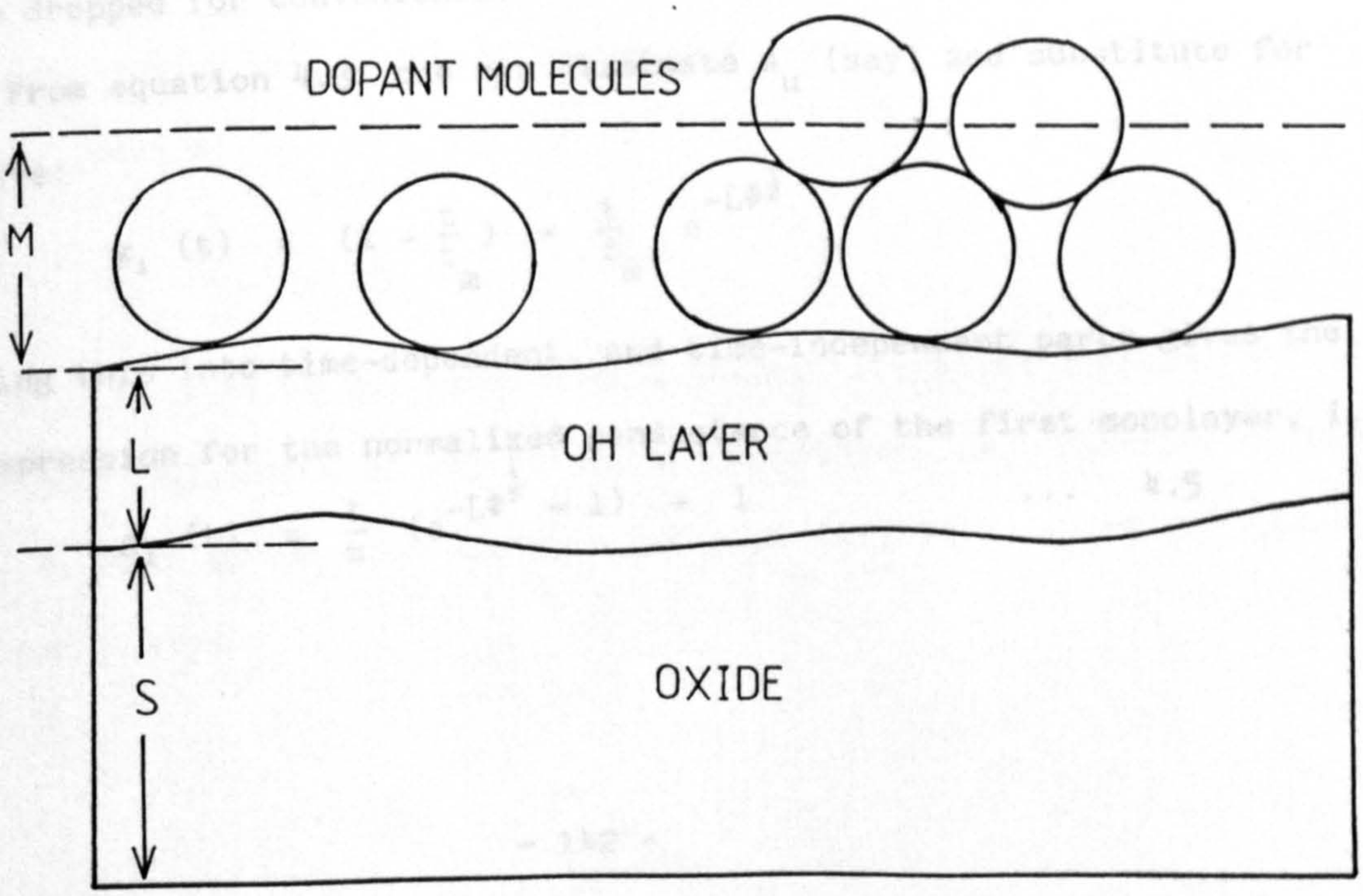
DOPANT MOLECULES
M
L
OH LAYER
S
OXIDE

Hence $g_1(t)$ is the normalized junction conductance during the growth of the first monolayer. The constant, γ , has now been eliminated which simplifies the analysis somewhat.

Unfortunately, absolute conductance values are inevitably sacrificed, since it follows that

$$o < g_1 (t) < 1 \qquad \ldots \quad 4.4a$$

However, the general form of the resulting g(t) versus t (g-t) plots remain unchanged, allowing qualitative analyses to be performed effectively. Retrieval of the absolute conductances would require a careful, and complicated treatment similar to the present analysis, but using equation 4.1 as the starting point.

Substituting the corresponding conductances (given by equation 4.2) into equation 4.4 gives:

$$g_1 (t) = \frac{A_u e^{-S\Phi^{\frac{1}{2}}} + A_c e^{-(S+L)\Phi^{\frac{1}{2}}}}{A_{je}^{-S\Phi^{\frac{1}{2}}}}$$

$$= \frac{A_u}{A_j} + \frac{A_c}{A_j} e^{-L\Phi^{\frac{1}{2}}}$$

where S, and L are the thicknesses of the oxide, and first (hydroxyl) monolayer respectively in $\mathring{A}$. $\overline{\Phi}$ has been written as Φ and the exponential notation dropped for convenience.

From equation 4.3, one can eliminate A_u (say) and substitute for t to give:

$$g_1 (t) = (1 - \frac{t}{t_m}) + \frac{t}{t_m} e^{-L\Phi^{\frac{1}{2}}}$$

Separating this into time-dependent, and time-independent parts gives the final expression for the normalized conductance of the first monolayer, i.e.

$$g_1 (t) = \frac{t}{m} (e^{-L\Phi^{\frac{1}{2}}} - 1) + 1 \qquad \ldots \quad 4.5$$

It is immediately recognised that this is in the form of a linear relationship. As would be expected, equation 4.5 shows

$$g_1(o) = 1 ,$$
$$g_1(t_m) = e^{-L\Phi^{\frac{1}{2}}} \qquad \ldots \quad 4.6$$

Also, the first derivative of equation 4.5, or the slope of the g-t plot is given by:

$$g_1'(t) = \frac{1}{t_m}\left(e^{-L\Phi^{\frac{1}{2}}} - 1\right) \qquad \ldots \quad 4.7$$

i.e., $g_1'(t)$ = constant also as expected.

(b) Growth of the second monolayer*

The second monolayer is now assumed to grow as the previously completed hydroxyl monolayer as shown in Fig.4.1b. Using a similar approach to (a) above, the areas-time relationships are now given by:

$$A_c = \beta(t-t_m) ,$$
$$A_j = \beta(2t_m - t_m) = \beta t_m \qquad \ldots \quad 4.8$$

with constraints

$$A_j = A_u + A_c$$
$$t_m < t < 2t_m \qquad \ldots \quad 4.9$$

It is noted that A_c still runs from 0 to βt_m. The normalized junction conductance during the growth of the second layer as a function of time, $g_2(t)$, is given by:

* It will be seen in (c) below that a general iterative expression holds for the conductance of all subsequent monolayers as a function of time. The present sub-section although not essential is included for clarity of the analysis.

$$g_2(t) = \frac{A_u e^{-(S+L)\Phi^{\frac{1}{2}}} + A_c e^{-(S+L+M)\Phi^{\frac{1}{2}}}}{A_j e^{-S\Phi^{\frac{1}{2}}}}$$

$$= \frac{A_u}{A_j} e^{-L\Phi^{\frac{1}{2}}} + \frac{A_c}{A_j} e^{-(L+M)\Phi^{\frac{1}{2}}}$$

M is thickness of the second (dopant) monolayer in $\mathring{A}$. Proceeding as before, one can eliminate A_u, and substitute for t to give:

$$g_2(t) = \frac{t_m - (t-t_m)}{t_m} e^{-L\Phi^{\frac{1}{2}}} + \frac{(t-t_m)}{t_m} e^{-(L+M)\Phi^{\frac{1}{2}}}$$

i.e.,

$$g_2(t) = e^{-L\Phi^{\frac{1}{2}}} \left\{ \left(\frac{t-t_m}{t_m} \right) \left(e^{-M\Phi^{\frac{1}{2}}} - 1 \right) + 1 \right\} \quad \ldots 4.10$$

which is in the same form as the expression for the first monolayer, although slightly more complicated. From equation 4.10 it is observed that

$$g_2(t_m) = e^{-L\Phi^{\frac{1}{2}}}$$

$$g_2(2t_m) = e^{-(L+M)\Phi^{\frac{1}{2}}} \quad \ldots 4.11$$

and the first derivative of equation 4.10 shows that the slope of the g-t plot during the growth of the second monolayer is:

$$g_2'(t) = \frac{1}{t_m} e^{-L\Phi^{\frac{1}{2}}} (e^{-M\Phi^{\frac{1}{2}}} - 1) \quad \ldots 4.12$$

Now, comparison of equations 4.6, and 4.11 shows that

$$g_1(t_m) = g_2(t_m) = e^{-L\Phi^{\frac{1}{2}}}$$

Again this is as one would expect, since these expressions should match at $t = t_m$ by continuity arguments.

(c) Subsequent monolayers

If the above procedure is extended to the consideration of all further monolayers (of thickness M Å), it can be shown that the general expression for the normalized junction conductance during the growth of the n^{th} monolayer as a function of time is given by:

$$g_n(t) = e^{-\{L+(n-2)M\}\Phi^{\frac{1}{2}}}\left(\frac{t-(n-1)t_m}{t}\right)\left(e^{-M\Phi^{\frac{1}{2}}} - 1\right) + e^{-\{L+(n-2)M\}\Phi^{\frac{1}{2}}} \quad \ldots \quad 4.13$$

for n = 2,3, ...

The corresponding expression for the slope of the g-t plot during the growth of the n^{th} monolayer is therefore

$$g'_n(t) = \frac{1}{t_m}\left(e^{-\{L+(n-2)M\}\Phi^{\frac{1}{2}}}\right)\left(e^{-M\Phi^{\frac{1}{2}}} - 1\right) \quad \ldots \quad 4.14$$

In summary of the above derivations, equations 4.13, and 4.14 show that:

(i) $g_n(t)$ is linear in t with slope dependent on $\Phi^{\frac{1}{2}}$,

(ii) $g'_n(t)$ is a constant.

It is also noted that since the above equations have been normalized to the oxide conductance, G_{ox}, terms involving the oxide thickness, S, are absent.

It will be seen in Section 4.4, that if reasonable values of L, M, and Φ are inserted in equations 4.5 and 4.13, then to a first approximation the form of the resulting g-t plots correspond rather well to the experimental data.

4.2.3 Application of a Microcomputer to the Analysis of Model Conductance - time (g-t) Plots

A microcomputer interfaced to a digital plotter offers certain advantages over manual methods, in terms of ease, and flexibility of data handling. A simple software routine was written in BASIC for a 32K Commodore PET (Model 3032) interfaced to a Watanabe (WX4671) "DIGI-PLOT" plotter. The program requires the user to enter values of first monolayer thickness, L, (assumed to be due to hydroxyl ions) successive monolayer thicknesses, M, (assumed to be equal) the mean barrier height, Φ, (assumed constant throughout infusion) the time taken to grow a monolayer, t_m, (an integer value) and finally the number of monolayers to be grown, n. The computer then evaluates g_1 (t) for the first monolayer using equation 4.5, and g_n (t) for all successive monolayers using equation 4.15. Data may be output on the screen, or as a hard copy in the form of a table or a graph by means of a printer or digital plotter respectively. A listing of the program and sample outputs are given in Appendix 1. Simplified flow charts are shown in Figs. 4.2 and 4.2a.

A graphical output onto the plotter has the advantage over tabular output that it displays the data in a more "user-friendly" form, and allows the discontinuities in slope to be more easily recognized. (This factor becomes more relevant when analysing the experimental G-t plots where the discontinuities are not always particularly well defined. Qualitative estimates of the ratios between slopes were also made for comparison with model data; this will be discussed in 4.4.2, and 4.4.3.) Two model g-t plots obtained using the above method are shown in Figs. 4.3a, and 4.3b. A generalized plot taking into account the time required to penetrate the Pb electrode is shown in Fig.4.4. Further data obtained by choosing reasonable values for successive monolayer thickness, M, and mean barrier height, Φ, will be discussed in 4.4.3

Fig.4.2

Simplified flowchart for the BASIC program to evaluate model normalized junction conductance (see Appendix 1). The conductance of the first monolayer is calculated using equation 4.5, and of all subsequent monolayers using equation 4.13.

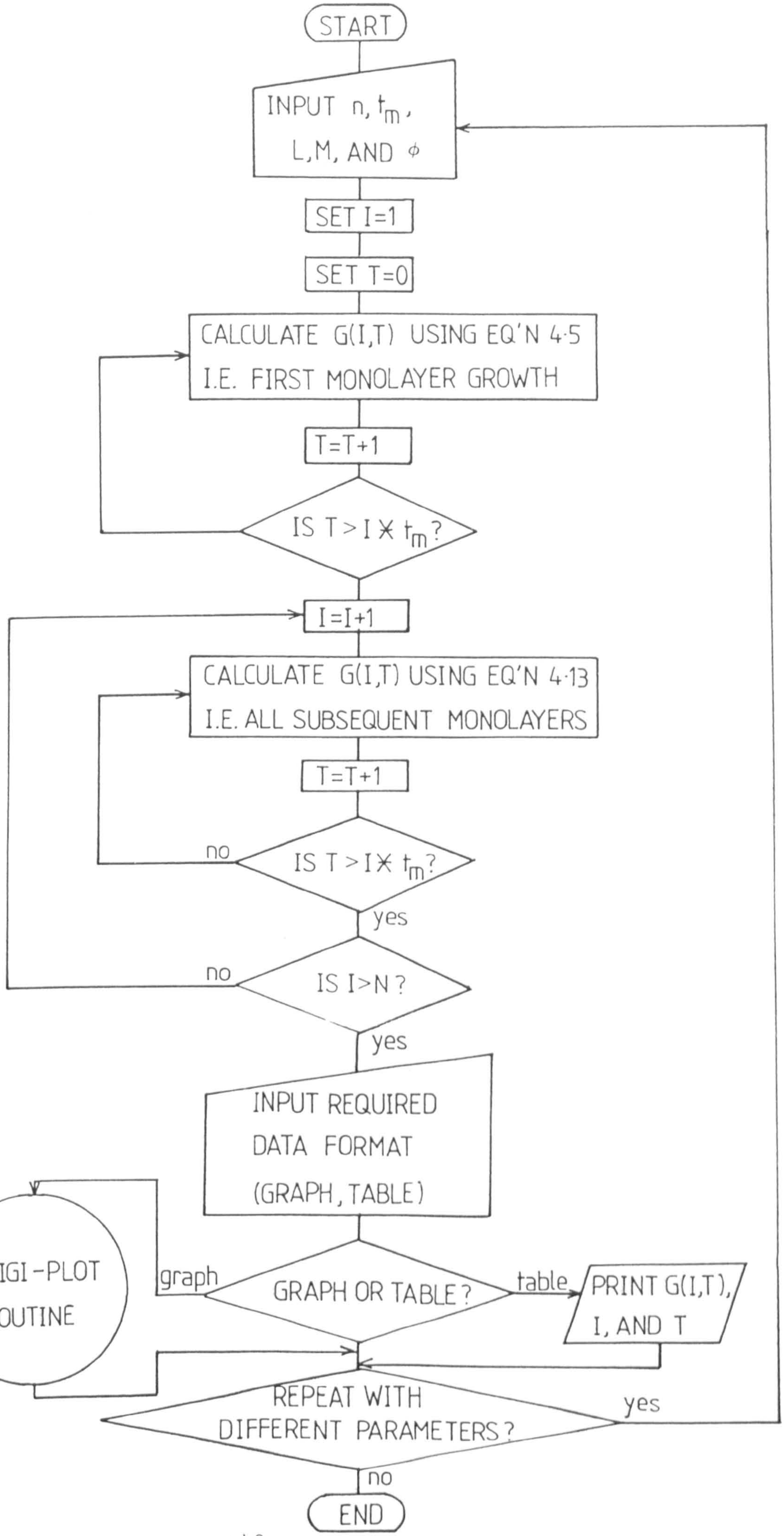
START
INPUT n, t_m, L, M, AND ϕ
SET I=1
SET T=0
CALCULATE G(I,T) USING EQ'N 4·5
I.E. FIRST MONOLAYER GROWTH
T=T+1
IS T > I * t_m?
no
I=I+1
CALCULATE G(I,T) USING EQ'N 4·13
I.E. ALL SUBSEQUENT MONOLAYERS
T=T+1
IS T > I * t_m?
no
yes
IS I>N ?
no
yes
INPUT REQUIRED DATA FORMAT (GRAPH, TABLE)
GRAPH OR TABLE?
graph
table
PRINT G(I,T), I, AND T
DIGI-PLOT ROUTINE
REPEAT WITH DIFFERENT PARAMETERS?
yes
no
END

Fig.4.2

Simplified flowchart for the BASIC program to evaluate model normalized junction conductance (see Appendix 1). The conductance of the first monolayer is calculated using equation 4.5, and of all subsequent monolayers using equation 4.13.

Fig.4.2a

Digital plotter ("Digi-Plot") routine. This may be used to plot model normalized conductances (see Appendix 1) or experimental conductance measurements when suitably modified (see Appendix 3).

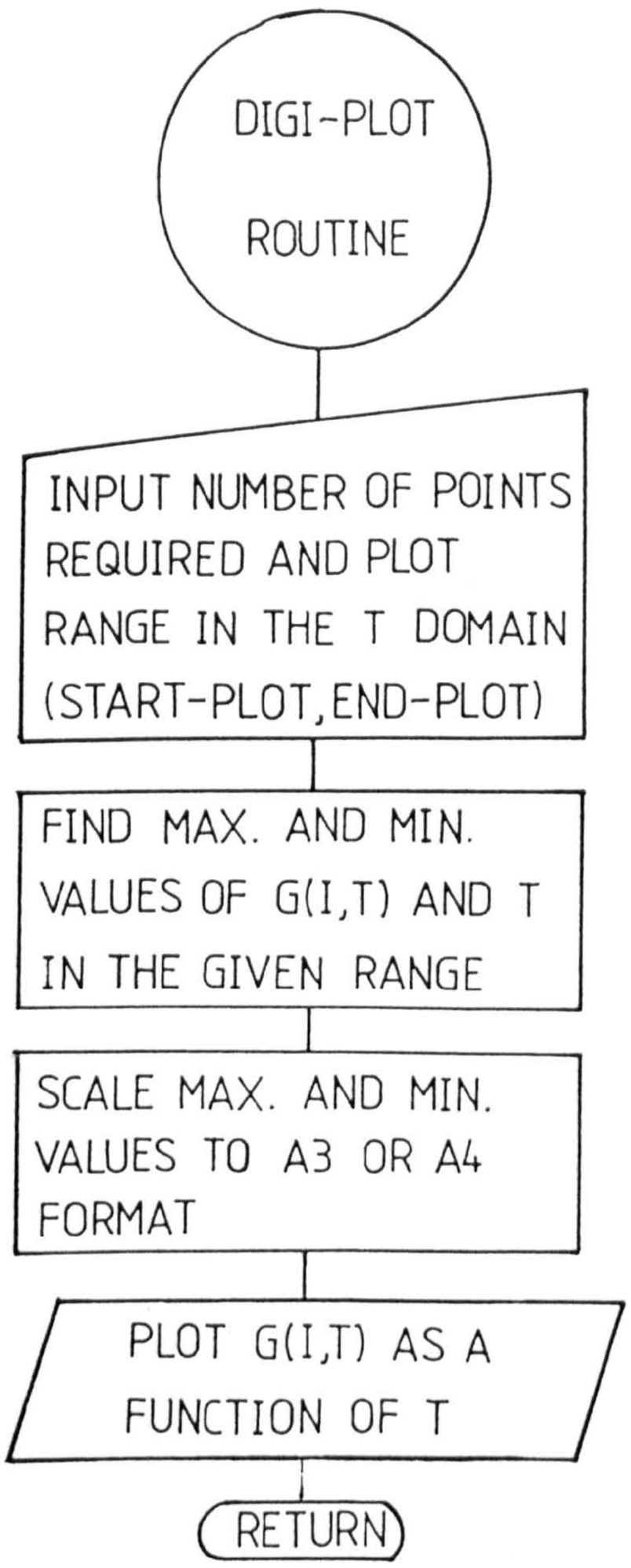
DIGI-PLOT
ROUTINE
INPUT NUMBER OF POINTS REQUIRED AND PLOT RANGE IN THE T DOMAIN (START-PLOT,END-PLOT)
FIND MAX. AND MIN. VALUES OF G(I,T) AND T IN THE GIVEN RANGE
SCALE MAX. AND MIN. VALUES TO A3 OR A4 FORMAT
PLOT G(I,T) AS A FUNCTION OF T
RETURN

Fig.4.3a

A typical model normalized conductance-time (g-t) plot. The junction conductance normalized to the oxide conductance has been evaluated using the program listed in Appendix 1, and then plotted as a function of time using the "Digi-Plot" routine. An arbitrary value of ten units has been chosen for t_m, the time taken to grow each monolayer. A mean barrier height, Φ , of 1 eV, monolayer thicknesses L = 1 Å (hydroxyl layer), and M = 3 Å (dopant layers), have also been chosen.

Regions B, C, and D of slopes $g_1'(t)$, $g_2'(t)$, and $g_3'(t)$ respectively are indicated, and region A corresponding to the time required to penetrate the Pb electrode has been omitted.

Fig.4.3b

As Fig.4.3a, except Φ = 2 eV. The effect of increasing Φ is to steepen the (negative) slope $g_1'(t)$ of region B, and cause the slopes $g_2'(t)$ and $g_3'(t)$ to tend towards zero more rapidly.

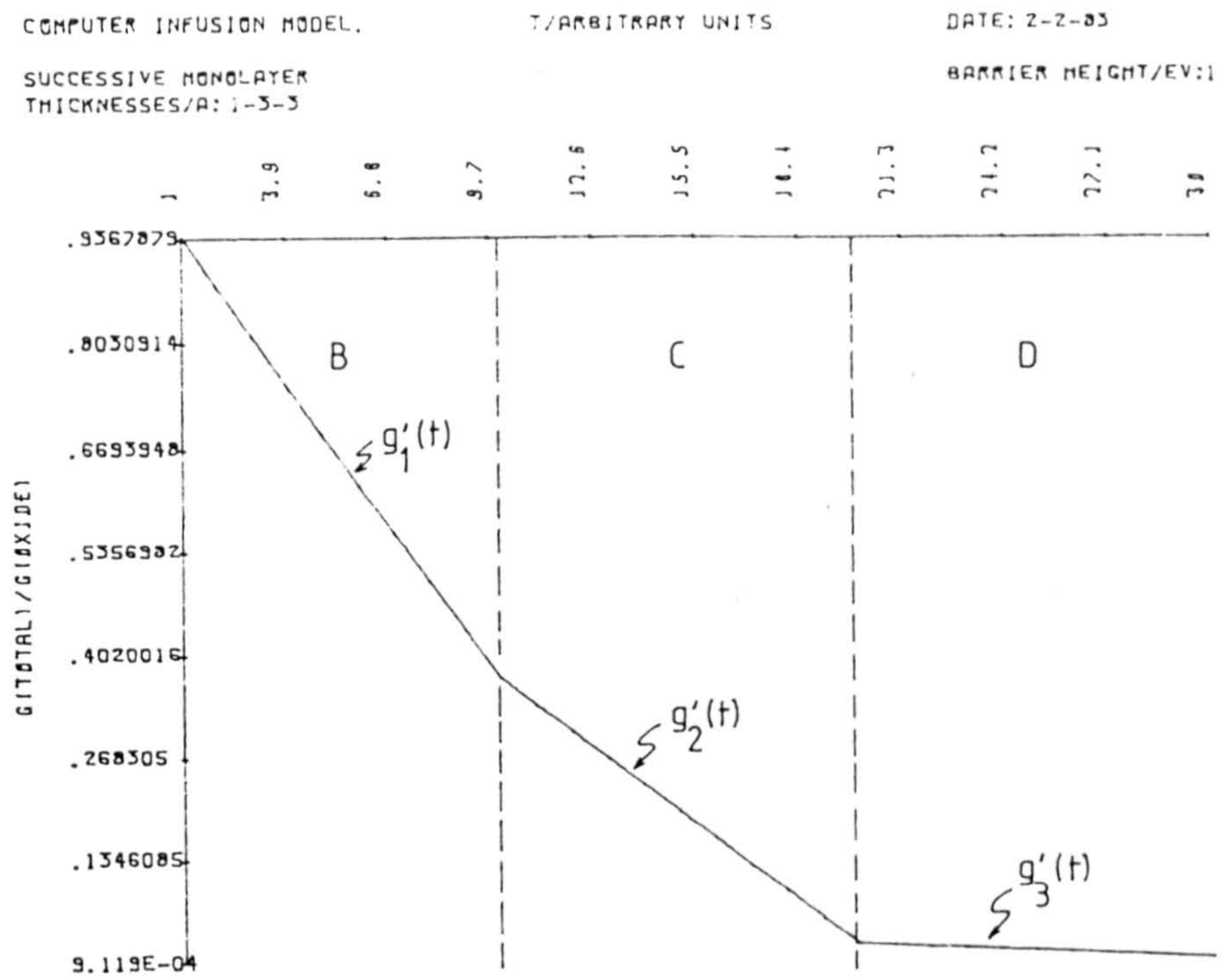
COMPUTER INFUSION MODEL.
T/ARBITRARY UNITS
DATE: 2-2-83
SUCCESSIVE MONOLAYER
THICKNESSES/A: 1-3-3
BARRIER HEIGHT/EV:1
1
3.9
6.8
9.7
12.6
15.5
18.4
21.3
24.2
27.1
30
.9367879
.8030914
.6693948
.5356982
.4020016
.268305
.1346085
9.119E-04
G(TOTAL)/G(OXIDE)
B
C
D
g'1(t)
g'2(t)
g'3(t)

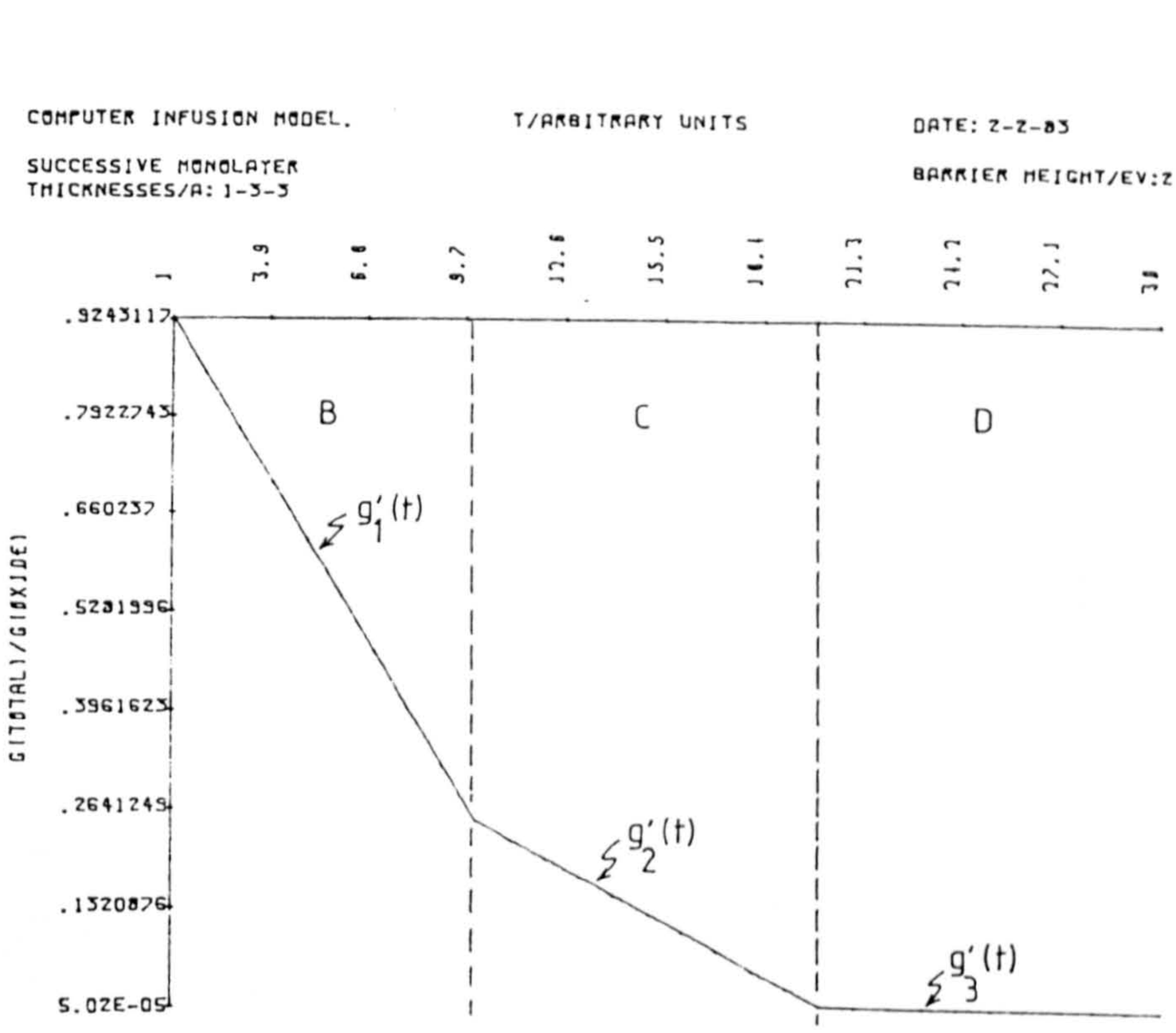
COMPUTER INFUSION MODEL.
T/ARBITRARY UNITS
DATE: 2-2-83
SUCCESSIVE MONOLAYER
THICKNESSES/A: 1-3-3
BARRIER HEIGHT/EV:2
1
3.9
6.8
9.7
12.6
15.5
18.4
21.3
24.2
27.1
30
.9243117
.7922743
.660237
.5281996
.3961623
.2641249
.1320876
5.02E-05
G(TOTAL)/G(OXIDE)
B
C
D
g'1(t)
g'2(t)
g'3(t)

Fig.4.4

A generalized model g-t plot similar to those shown in Figs.4.3a, and 4.3b. Region A, corresponding to the variable time required to penetrate the lead electrode is now indicated. Values of 1 eV, 1 Å, 2 Å, and 10 units were chosen for the parameters Φ, L, M, and t_m respectively (as defined in Fig.4.3a).

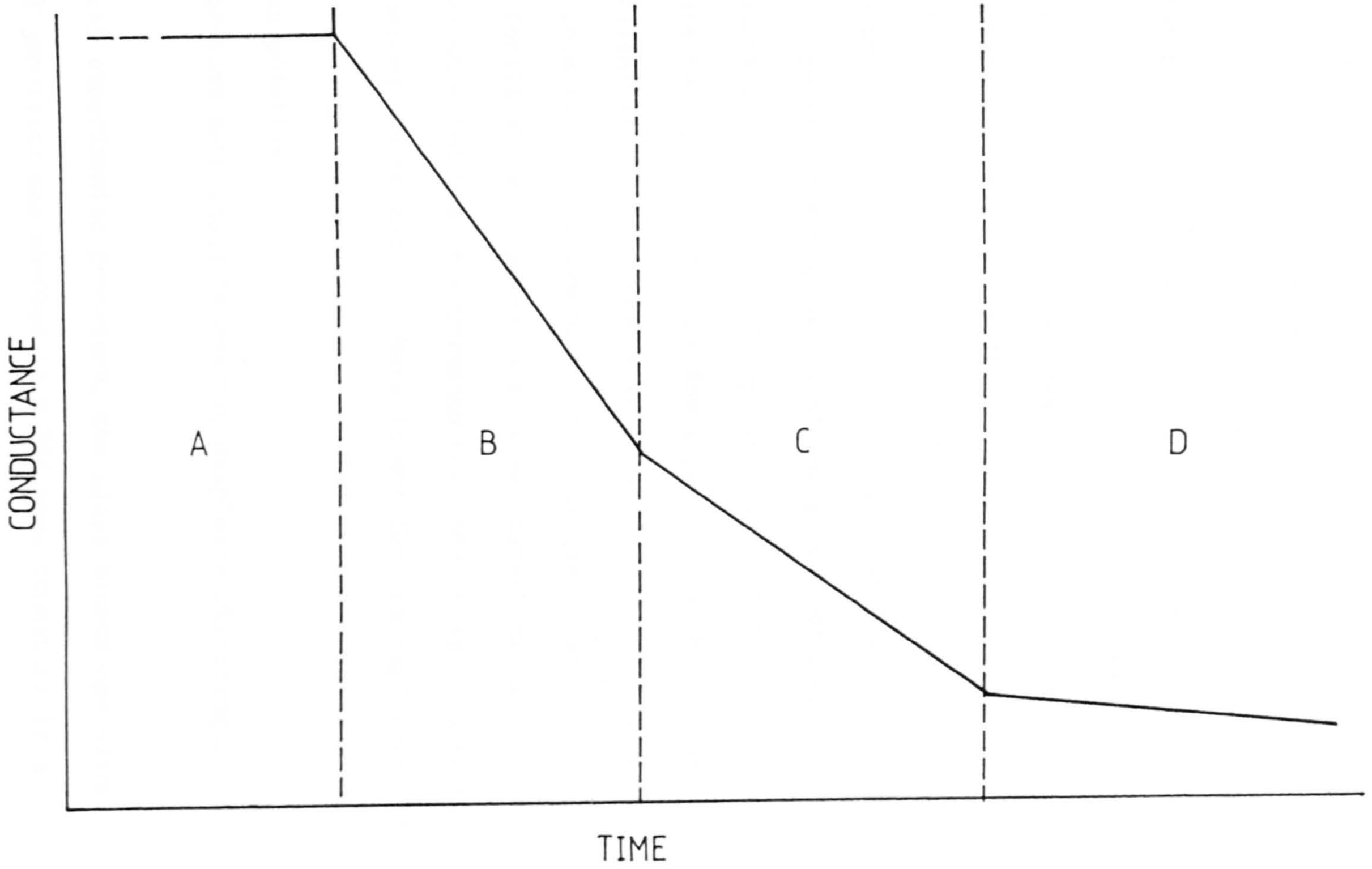
CONDUCTANCE
A
B
C
D
TIME

4.3 EXPERIMENTAL DETAILS

4.3.1 Apparatus for the Measurement of Junction Conductance in situ during Infusion

If equation 4.2 is to be used meaninfully to estimate junction conductance, then measurements must be made at low bias, V_b, i.e. for $V_b \ll \Phi$. This ensures that the junction remains on the approximately linear region of its I-V characteristic. Fresh, undoped IET junction resistances in our laboratory typically lie in the range a few tenths, to a few ohms; consequently, four-point probe resistance measurements are essential. Electrical measurements were made by passing a small and approximately constant current ($\sim$1mA) through the junction, while similtaneously monitoring the junction potential with a digital multimeter (Keithley 192 programmable DMM). Reasons for the choice of the above DMM were:

(i) It has a sufficiently high input impedance ($10^9\Omega$ for measurements up to 20V) to ensure that potential drops developed across the voltage probe leads are negligible in comparison with those across the junction.

(ii) It may be interfaced to a Commodore PET by means of an IEEE 488 serial line, thus facilitating computer control and data-logging. Rapid and accurate conductance and time measurements may then be made routinely. (35 readings per second may be made.) Were it not for the employment of such a system these measurements, which are crucial in the present work, would not have been possible.

(iii) Conductance-time data could be readily displayed utilizing a digital plotter.

In a typical experimental procedure, the glass microscope slide containing the IET junctions was mounted in a PCB edge connector in a sealed chamber. The design of the chamber was such that a controlled atmosphere could be maintained. All glassware, and connecting pieces were

vacuum standard (Quick-fit and J.Youngs) able to maintain a vacuum of $\sim 10^{-5}$Torr) and joints were smeared with vacuum grease to ensure that the system was as gas tight as could be achieved under the present circumstances. Electrical contacts to and from the junctions were made by feeding measurement leads from the edge connector out of the chamber through a self-sealing rubber membrane, to the measurement instruments. Dopant compounds of interest (usually in the liquid-phase) were conveniently introduced by piercing the membrane with a syringe needle, and carefully squirting a few cm^3 of dopant into the bottom of the chamber. The net arrangement during a typical infusion doping experiment is illustrated in Fig.4.5.

4.3.2 Infusion Doping Techniques

Most infusion experiments start with the fabrication of a set of undoped IET junctions. The thickness, and deposition rate of the Aℓ electrodes are not critical. Aℓ electrodes were typically formed to a thickness of $\sim$ 2000-3000 Å deposited at 30 Å s^{-1}, as measured using an Edwards FTM3 quartz crystal monitor. The Aℓ electrodes could either be thermally oxidized by venting the vacuum chamber immediately after evaporation, or glow-discharge oxidized in either air or O_2 as described in Chapters 3 and 7. For the work presented in this chapter, thermal oxides were used unless otherwise stated.

It is believed that the thickness (1-4,9), and deposition rate (4) of the Pb electrode play an important role in determining the rate at which infusion occurs. TEM studies have clearly shown that as a consequence of the resulting lead electrode island structure, infusion is most rapid in IET junctions having thin, slowly deposited Pb films. It is also noted that the infusion rate is greater for junctions having initially higher (undoped) resistances (4).

Fig.4.5

Schematic diagram of the infusion chamber, and experimental arrangement used to measure the junction potential *in situ* during infusion. An approximately constant direct current, i ≃ 1 mA, is passed through the junction, while the junction potential is monitored simultaneously. Increases in potential are generally indicative of a thickening of the insulating layer of the IET junction. The resulting data are stored on a cassette file.

Fig. 1.

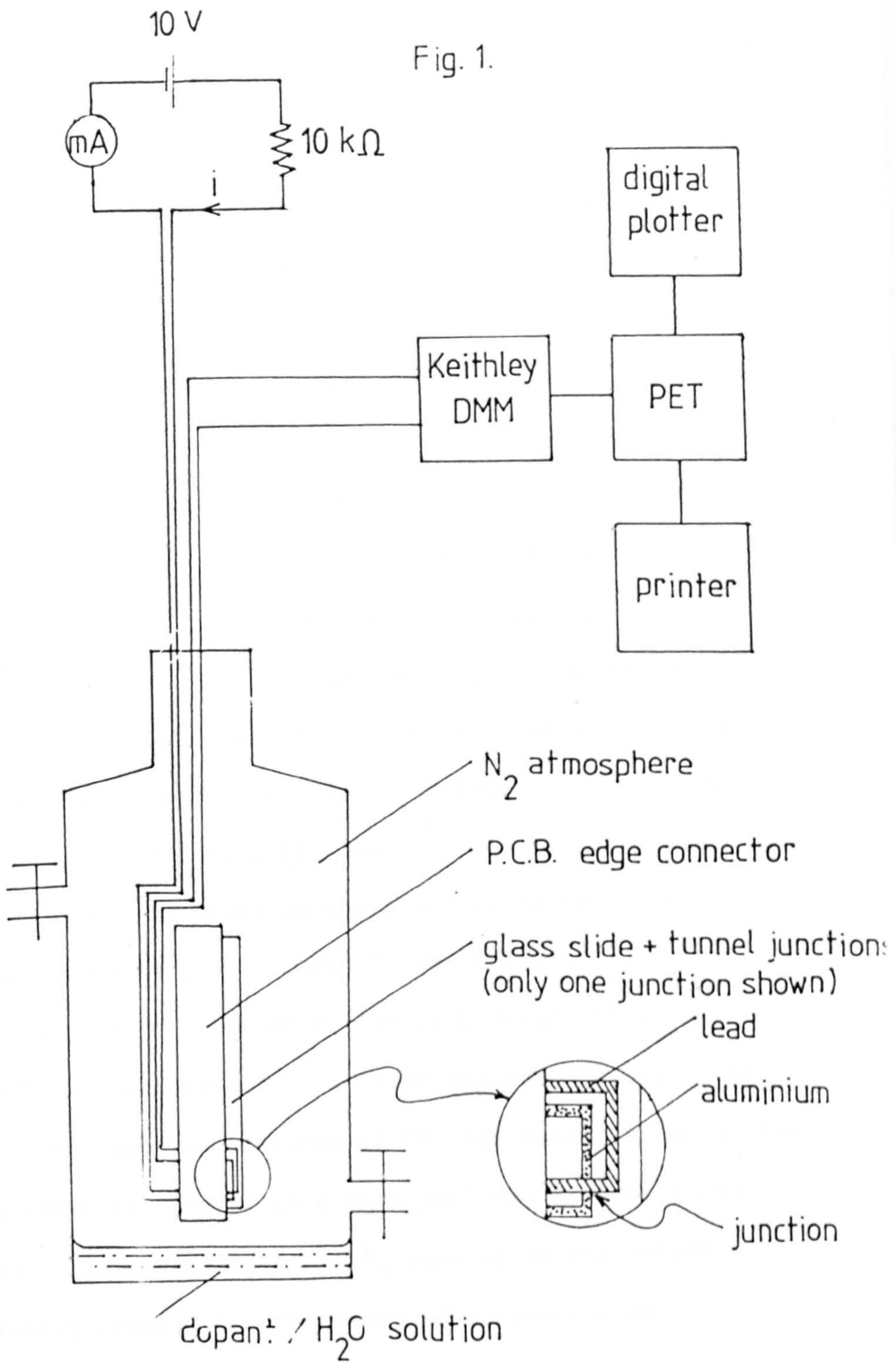
10 V
mA
10 kΩ
i
digital plotter
Keithley DMM
PET
printer
N_2 atmosphere
P.C.B. edge connector
glass slide + tunnel junctions
(only one junction shown)
lead
aluminium
junction
dopant / H_2O solution

Two related considerations must be weighed up when preparing the Pb electrodes for infusion experiments: The first is the desired infusion rate. As just mentioned, thin slowly evaporated films 'speed-up' infusion. Unfortunately this may increase the risk of contamination during the transit of the junctions from the evaporator to the infusion chamber. Hence, the second consideration is controllability; generally speaking the thicker the electrode (which normally implies a slower infusion rate) the less likely it is for contamination to reach the oxide surface. Any ingress of contamination having started to penetrate the Pb electrode may in fact be halted, and, to some degree reversed by flushing the infusion chamber with N_2. However, if the Pb electrode is made too thick, then the doping time required for a successful infusion experiment may be prohibitively long. After a series of preliminary trial Pb evaporations at various evaporation rates and thicknesses, a 'standard' Pb electrode approximately 3000 Å thick, deposited at $\sim$ 10 Å s^{-1} was decided upon, as this was found to give an adequate compromise between the two factors just described. Typical infusion experiments (i.e. ones in which approximately monolayer coverage of the oxide was achieved) took roughly 1 hour, with no apparent signs of contamination in the resulting IET spectra.

The completed-undoped junctions on the glass slide were then mounted in the PCB edge connector, and placed in the infusion chamber. During this procedure, a constant flow of N_2 (British Oxygen Company suppliers, "white spot") was maintained to exclude atmospheric CO_2. As was mentioned earlier, the combined presence of CO_2 and water vapour at the Pb electrode (which presumably behaves as a catalyst) may lead to formic acid contamination (4). The instigation of N_2 purging in the author's laboratory has drastically reduced the frequency of occurrence of contaminated IET junctions.

At this point, a mixture of dopant and pure water was introduced into the chamber as described in 4.3.1. The N_2 has a 'double-role' in the experimental procedure; in addition to reducing the likelihood of contamination, it also provides a convenient means of restricting the infusion of dopant molecules. If the flow is maintained, the infusion process is inhibited as indicated by a constant value of junction conductance. Infusion could thus be commenced at a fairly well defined time by terminating the N_2 flow.

4.3.3 Choice of Dopants

Equations 4.7 and 4.14 suggest that the slope of the g-t plot during monolayer growth is proportional to the (adsorbed) monolayer thickness. If one were to perform a series of experiments where dopants of various mean overall dimensions (when adsorbed on the oxide) were infused, then the model would predict g-t plots having characteristic forms depending mainly on the dopant "size", assuming that the mean barrier height, Φ, remains constant throughout infusion. Moreover, if the model is at least partly valid, a qualitative analysis of the ratios between successive slopes in an experimental G-t plot should give an estimate of the corresponding increment in insulating barrier thickness due to the growth of the successive monolayers. Consider the ratio $g_1'(t)/g_2'(t)$ from equations 4.12, and 4.17, i.e.

$$\frac{g_i'(t)}{g_2'(t)} = \frac{1/t_m \left(e^{-L\Phi^{\frac{1}{2}}} - 1 \right)}{1/t_m \; e^{-L\Phi^{\frac{1}{2}}} \left(e^{-M\Phi^{\frac{1}{2}}} - 1 \right)}$$

which simplifies to

$$\frac{g_1'(t)}{g_2'(t)} = \begin{cases} e^{L\Phi^{\frac{1}{2}}}, & L = M \\ \dfrac{1 - e^{L\Phi^{\frac{1}{2}}}}{e^{-M\Phi^{\frac{1}{2}}} - 1}, & L \neq M \end{cases} \qquad \ldots \quad 4.15$$

Similarly, consider the following ratios for all successive monolayers (n = 2, 3, ...) from equation 4.14

$$\frac{g_n'(t)}{g_{n+1}'(t)} = \frac{1/t_m \left(e^{-\{L+(n-2)M\}\Phi^{\frac{1}{2}}} \right)\left(e^{-M\Phi^{\frac{1}{2}}} - 1 \right)}{1/t_m \left(e^{-\{L+(n-1)M\}\Phi^{\frac{1}{2}}} \right)\left(e^{-M\Phi^{\frac{1}{2}}} - 1 \right)}$$

$$= e^{M\Phi^{\frac{1}{2}}}$$

and hence

$$M = \frac{1}{\Phi^{\frac{1}{2}}} \ln \left(\frac{g_n'(t)}{g_{n+1}'(t)} \right), \qquad \ldots \quad 4.16$$

for n = 2, 3, ...

If an infusion experiment were performed using dopant molecules of fairly well defined overall dimensions, then equations 4.15 and 4.16 should hold. Assuming that a reasonable estimate of the slopes $g_n'(t)$ could be made, then it should be possible to estimate the successive monolayer thicknesses, M, from equation 4.16, where it has been assumed that the first monolayer is due to hydroxyl ion coverage.

It must be emphasized that equations 4.15, and 4.16 should only be used as rough, or 'rule of thumb' guides to monolayer thickness, since many assumptions and approximations have been made on the way.

In some cases it may be difficult to estimate accurately the value of the slopes of the G-t plots, however, it may be possible to locate the points of ~~infusion~~ inflexion between the regions of different slopes. An alternative method for estimating the incremental monolayer thickness is to consider the ratio between the conductances at corresponding points in each region

of the G-t plots. For example, the conductance could be estimated at the points of inflexion between regions. The junction conductance at any point on the G-t plot may be approximately given by equation 4.2. Consider the ratio of conductances at the corresponding discontinuities towards the ends of (say) regions B, and C; call these conductances G_B, and G_C. It is assumed here that the growth of the first (hydroxyl) monolayer, and the second (dopant) monolayer has just been completed. The conductance ratio is given by

$$\frac{G_B}{G_C} = \frac{\gamma A_j e^{-(S+L)\Phi^{\frac{1}{2}}}}{\gamma A_j e^{-(S+L+M)\Phi^{\frac{1}{2}}}}$$

$$= e^{M\Phi^{\frac{1}{2}}} \qquad \ldots \quad 4.17$$

and hence

$$M = \frac{1}{\Phi^{\frac{1}{2}}} \ln \frac{G_B}{G_C} \qquad \ldots \quad 4.18$$

which shows that the incremental monolayer thickness between corresponding points on the G-t plot may be found from the ratio of the conductance at those points. The ratios may equally be taken between any two conductances on the G-t plot to estimate the corresponding change in insulating barrier thickness due to (partial) monolayer formation. If the conductances at two arbitrary points on the curve are given by:

$$G_1 = A_j e^{-(S+t_1)\Phi^{\frac{1}{2}}} \quad , \quad G_2 = A_j e^{-(S+t_2)\Phi^{\frac{1}{2}}}$$

where t_1 and t_2 are the corresponding thicknesses, and $G_1 > G_2$, $t_2 > t_1$, then their ratio is

$$\frac{G_1}{G_2} = e^{(t_2-t_1)\Phi^{\frac{1}{2}}}$$

and hence

$$\Delta t = \frac{\dot{l}}{\phi^{\frac{1}{2}}} \ln \frac{G_1}{G_2} \qquad \ldots \quad 4.19$$

where $\Delta t = t_2 - t_1$, the corresponding increment in thickness between point 1 and point 2.

In order to test the above hypotheses, it is necessary to infuse a range of dopants of having various molecular dimensions and measure the ensuing changes in conductance. One would expect that the limiting factor to the maximum size of molecules which may be infused would be the mean intercrystallite gap width of the Pb electrode. Transmission electron micrographs due to Nelson et al have shown that depending on the thickness and deposition rate, gaps of the order of a few hundred Å's may exist. It should therefore be possible to infuse fairly large molecules. The range of molecules investigated in the present work, and their average maximum dimensions are given in Table 4.1. Of these compounds, only propan-2-ol, acetone, and water gave acceptably reproducible data; a fairly rigorous analysis of the data for acetone and water is presented in Section 4.4. The reason for the poor success rates with 4MP2O, and phenol is believed to lie with their respective low miscibilities in water. It is clear that further work is necessary before the rôle of water vapour in infusion doping can be clarified.

Table 4.1 - The maximum average dimensions of the dopant molecules investigated by infusion doping in this study. These values do not necessarily reflect their dimensions when adsorbed on an Aℓ-oxide surface.

Dopant	Solubility in water	Maximum average dimension/Å
4 methylpenton-2-one (4MP20)	s.s	~ 6
Phenol	s.s (1g dissolves in 15 cm of water at 25°C)	≲ 5
Propan-2-ol	m.	≲ 3
Acetone	m.	≲ 3
water	-	≲ 1

Key: s.s. - slightly soluble
m. - miscible

4.4 RESULTS AND DISCUSSION

4.4.1 Termination of Infusion

As mentioned in Section 4.3.2, once the junction conductance had reached a desired value, infusion could be halted, and partly reversed by the re-introduction of the N_2 flow. This phenomenon may be illustrated by the corresponding resistance-time plots. Figures 4.6a, and 4.6b show typical resistance- and conductance- time plots respectively for an IET junction infusion doped with a 50% v/v solution of acetone/water. (The data were taken at intervals of either 20 or 30s using the internal clock of the PET, stored on cassette file, and plotted using the routine described in Fig.4.2b, suitably modified as shown in Appendix 3.) Falls in resistance of as much as 50% have been observed depending on which compounds were used, and the region in the curve where the process was terminated.

This effect can be appreciated if one considers that the first monolayer may be more tightly bound that subsequent layers as discussed in 4.2.2. Jaklevic and Gaerttner have also observed that phenol, and pyridine for example, could be reversibly infused, while formic acid could not (2). They noted this having infusion doped withthese compounds, recorded IET spectra, and then replaced the junctions in their infusion chamber to achieve the reverse-infusion effect which they achieved by exposing the junctions to pure water vapour for several minutes. Bearing in mind the unknown effects due to immersing and then removing a junction in liquid He one might speculate that the reason for this reversal effect is that formic acid is strongly chemisorbed onto the hydrated Aℓ-oxide surface, while presumably phenol is not. They also noted that formic acid would readily vapour-phase dope onto a "dry" oxide, but would not infuse onto a dry oxide without the external presence of water vapour.

Fig.4.6a

An experimental plot of the junction potential V_j, as a function of infusion time. The data were recorded at 30s intervals using the internal clock of the PET, stored on cassette file "INFDATA26" and plotted using the "Digi-Plot" routine. The constant current supply for the four-point measurement technique, i, was approximately 1 mA, therefore the low value of v_j, corresponds to a junction resistance of $\sim$ 1.8 Ω.^{J} The curve clearly shows the effect of re-introducing a controlled flow of N_2. The final junction resistance falls by $\sim$ 10% of its maximum attained value to eventually stablize at $\sim$ 85 Ω.

Fig.4.6b

A similar plot to Fig.4.6a but for a different set of data. The final junction resistance is now $\sim$ 45 Ω.

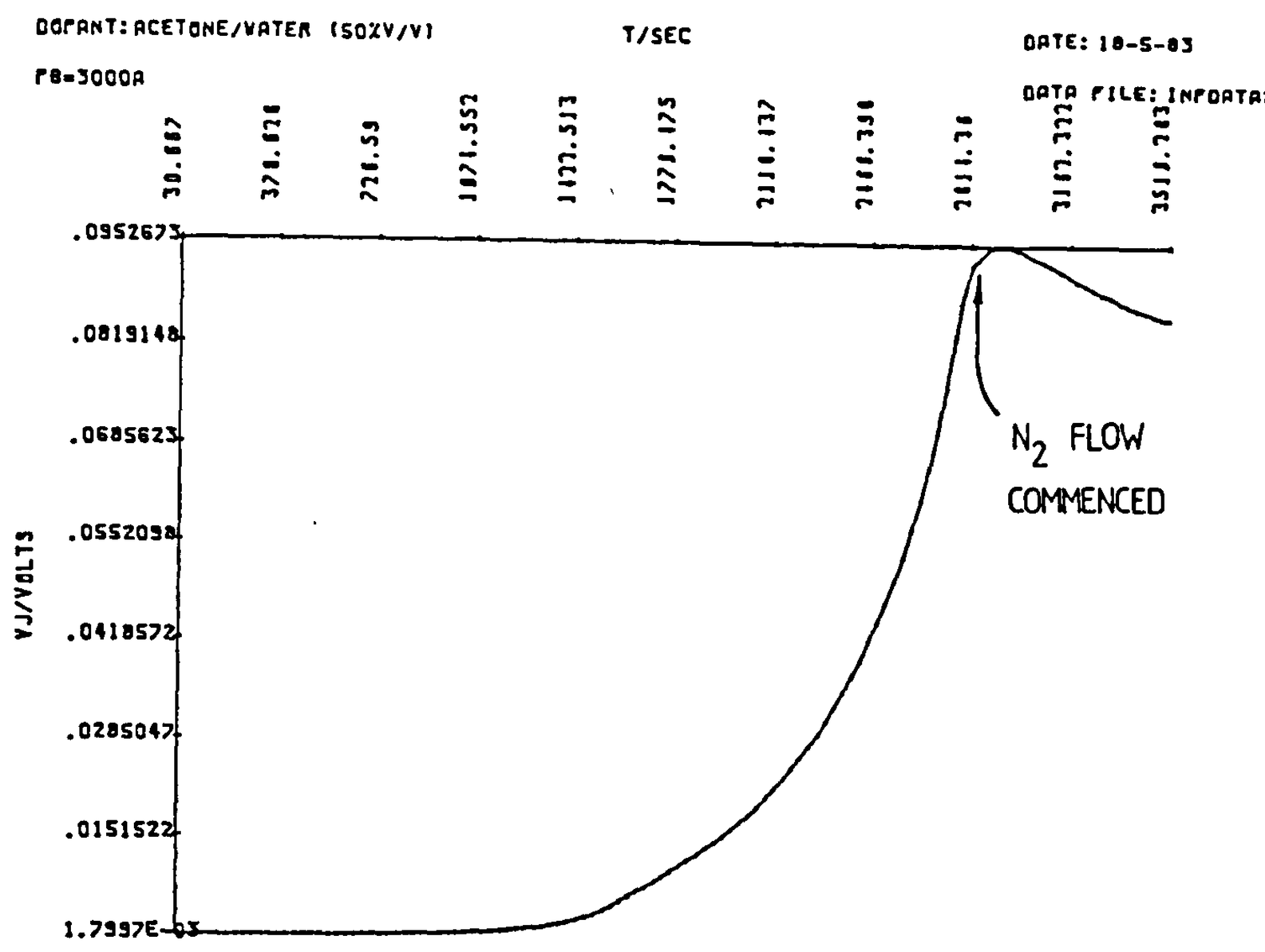
DOPANT: ACETONE/WATER (50%V/V)
T/SEC
DATE: 18-5-83
FB=3000A
DATA FILE: INFDATA26
30.887
378.828
726.59
1071.552
1422.513
1771.175
2118.137
2468.398
2811.36
3167.322
3518.283
.0952673
.0819148
.0685623
.0552098
.0418572
.0285047
.0151522
1.7997E-03
VJ/VOLTS
N2 FLOW
COMMENCED

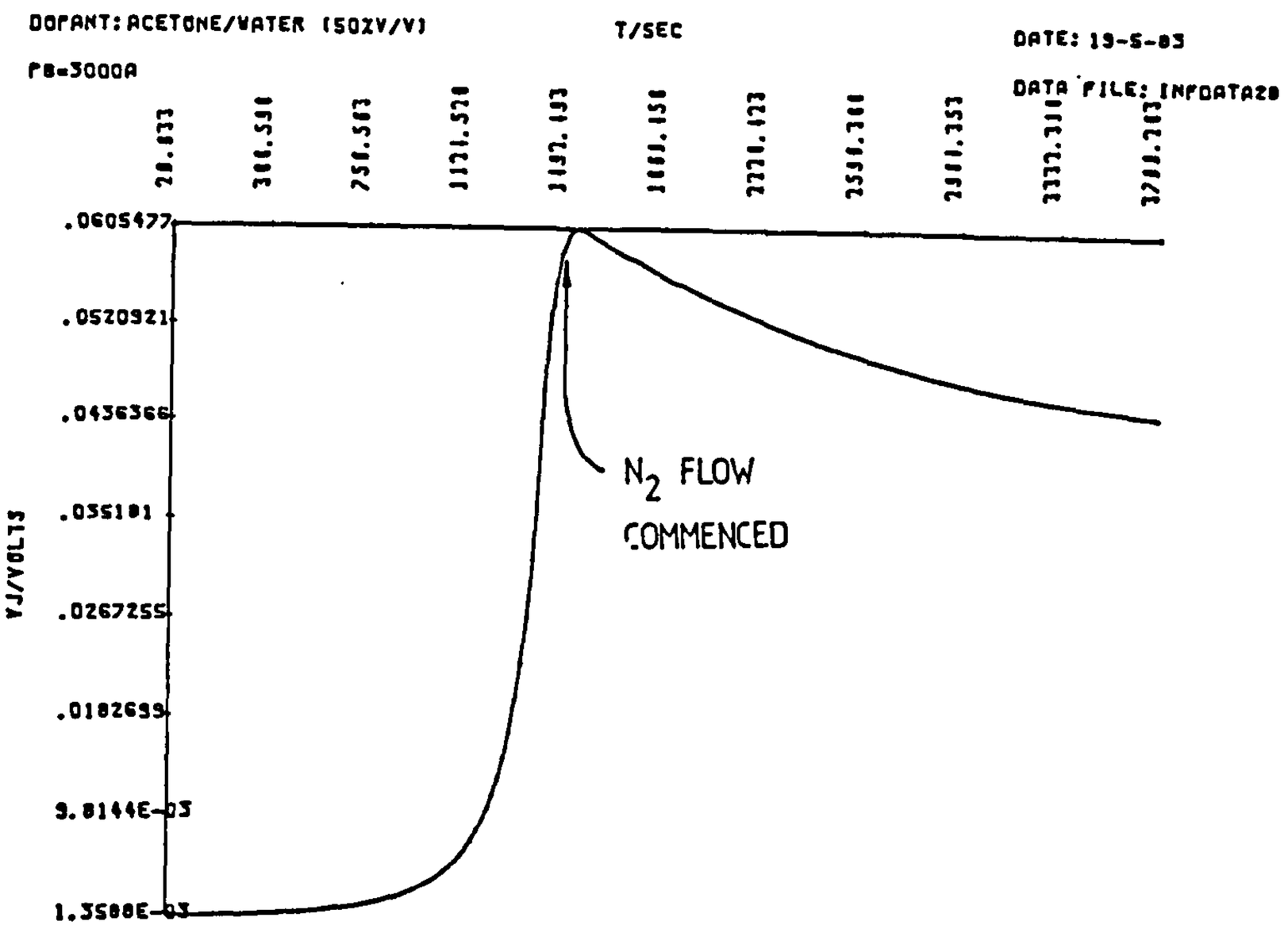
DOPANT: ACETONE/WATER (50%V/V)
T/SEC
DATE: 19-5-83
FB=3000A
DATA FILE: INFDATA28
28.833
388.598
748.363
1121.528
1482.183
1841.158
2228.123
2588.788
2941.353
3332.318
3688.283
.0605477
.0520921
.0436366
.035181
.0267255
.0182699
9.8144E-03
1.3588E-03
VJ/VOLTS
N2 FLOW
COMMENCED

Fig.4.6c

The experimental G-t plot corresponding to Fig.4.6a ("INFDATA26"). The effect of the N_2 flow is less pronounced than for the resistance data. The effect is to halt the decrease in conductance to rapidly attain a fairly constant value of $\sim$ 0.01 S. Some evidence is now discernible for regions of different slope and indicated by the broken line.

Fig.4.6d

Experimental G-t plot corresponding to Fig.4.6b, ("INFDATA28"). The N_2 was commenced sooner in the infusion process than for Fig.4.6c.

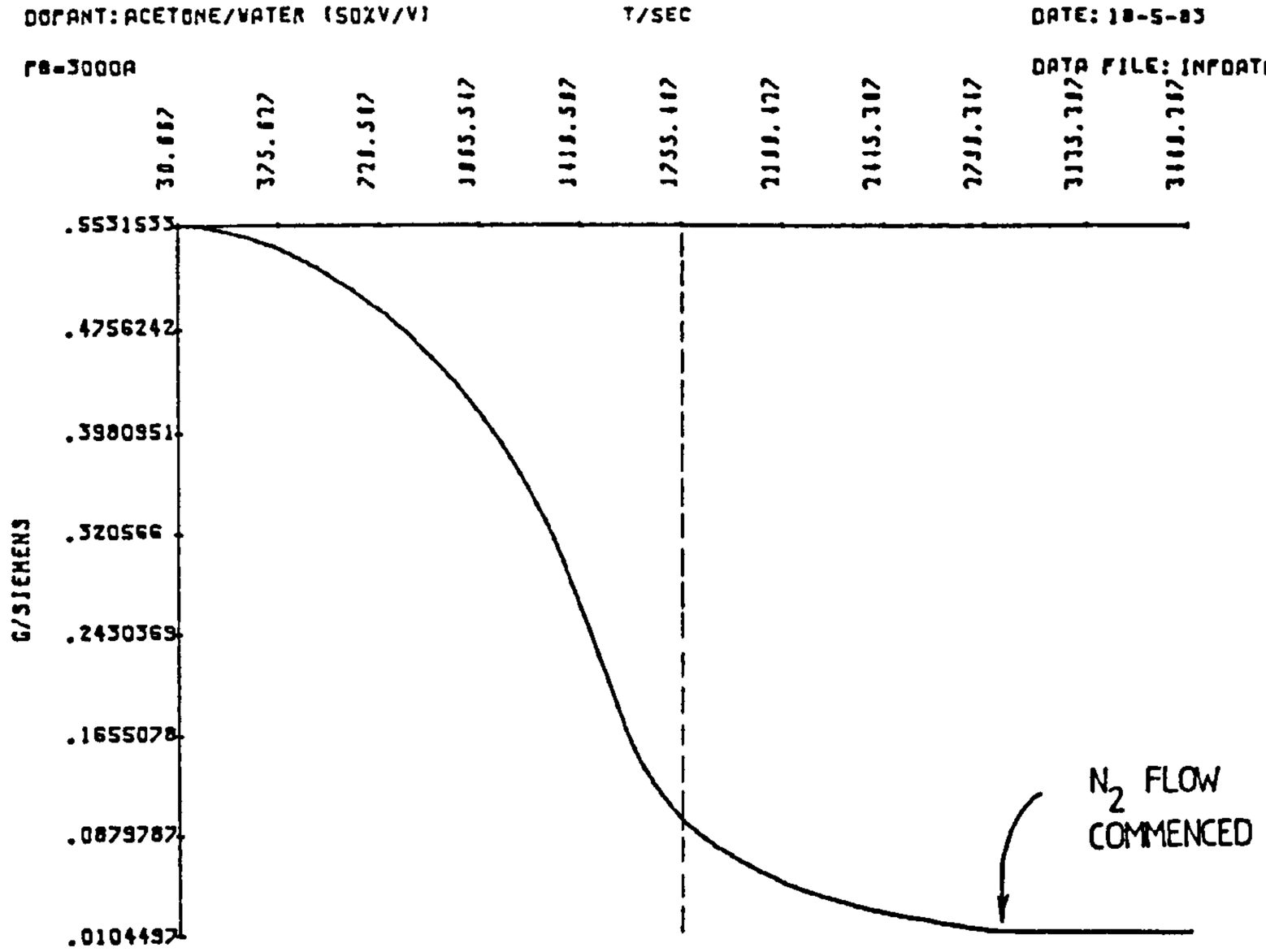
DOPANT: ACETONE/WATER (50%V/V)
T/SEC
DATE: 18-5-83
FB=3000A
DATA FILE: INFDATA26
30.667
375.672
721.507
1065.517
1418.587
1755.117
2108.172
2445.787
2798.717
3133.787
3488.787
.5531533
.4756242
.3980951
.320566
.2430369
.1655078
.0879787
.0104497
G/SIEMENS
N_2 FLOW COMMENCED

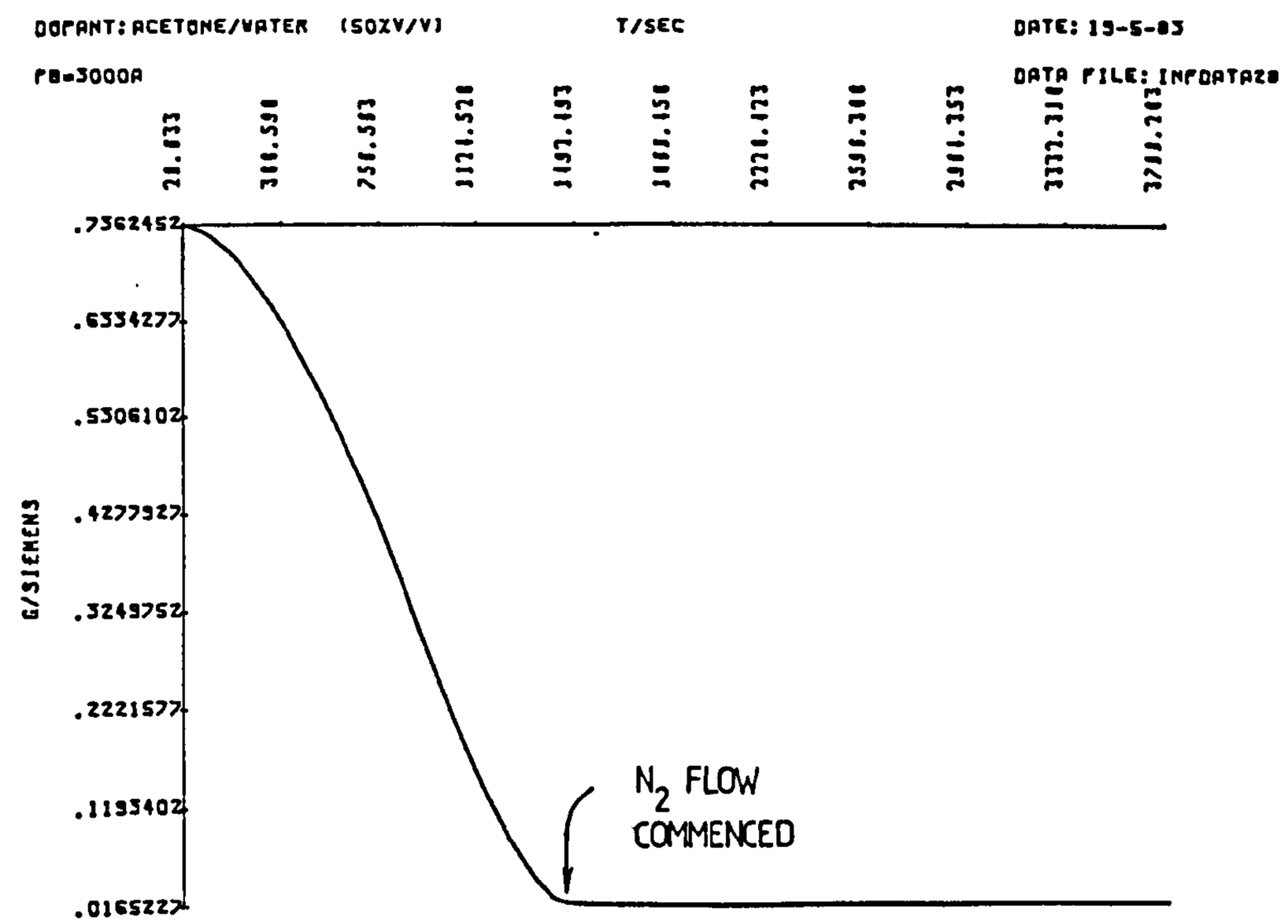
DOPANT: ACETONE/WATER (50%V/V)
T/SEC
DATE: 19-5-83
FB=3000A
DATA FILE: INFDATA28
28.833
388.598
758.583
1121.528
1492.193
1855.158
2226.123
2589.388
2961.353
3332.318
3703.283
.7362452
.6334272
.5306102
.4277922
.3249752
.2221577
.1193402
.0165222
G/SIEMENS
N_2 FLOW COMMENCED

Fig.4.7

Experimental resistance-time plot for an IET junction infusion doped with acetone in the apparent absence of water vapour (infustion was performed in a N_2 atmosphere). The sharp increase in resistance from approximately 1.8 to 3.5 Ω in the period from ∿ 25 to 50 minutes may possibly have been triggered by the ingress of water into the chamber. A small but steady increase in resistance ensued for the next ∿ $2\frac{1}{2}$ hours.

DOPANT: NEAT ACETONE

T/MIN

DATE: 4-3-83

PB=3000A

DATA FILE: INFDATA18

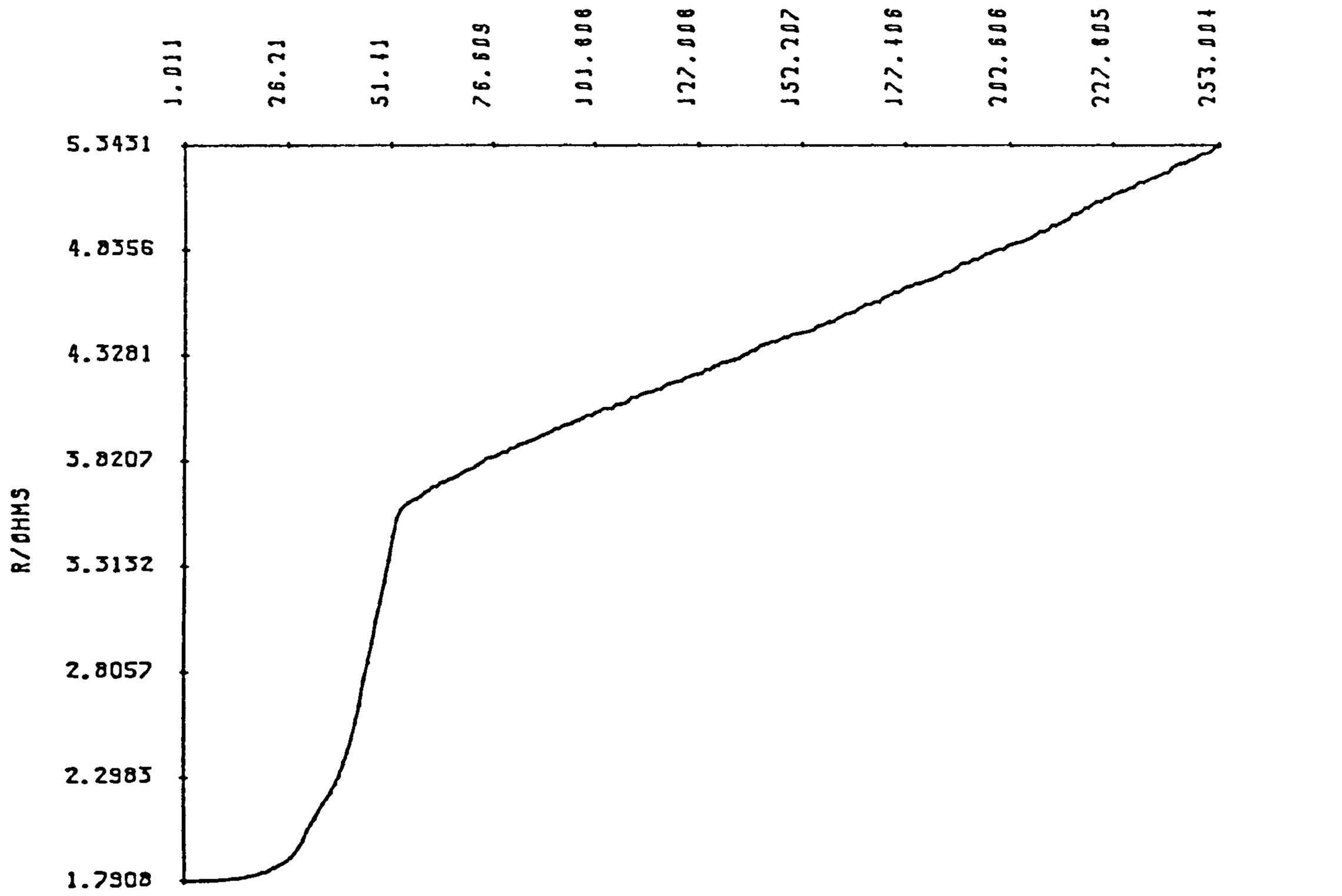

This lends further weight to the argument that water acts as a carrier, hence increasing dopant mobility. In further support of this argument, Fig.4.7 shows the resistance-time plot obtained in the author's laboratory when an IET junction was infusion doped with pure acetone (spectrograde, BDH suppliers) in the absence of water. It is observed that the junction resistance rose only by $\lesssim 4\ \Omega$ over a period of $\gtrsim 4$ hours. The small increase may well have been triggered by the presence of small amounts of indigenous water in the "pure" acetone. In agreement with other workers, the author has verified that undoped IET junctions stored in a clean, dry atmosphere (e.g. in a dessicator) will exhibit no significant increases in resistance over a period of several days. It should be mentioned that small increases in resistance observed over longer periods (several weeks) may be due to the ingress of molecules through microscopic leaks or cracks in the storage vessel, and/or thickening of the Aℓ-oxide layer.

4.4.2 Experimental Conductance-time (G-t) Plots for Water, and Acetone

Several sets of experimental G-t data were obtained for both water, and aqueous solutions of acetone. Two typical sets of data for each are shown in Figs.4.8 and 4.9 (water), 4.10 and 4.11 (acetone). The corresponding resistance-time (R-t) data are also shown, and denoted by an 'a' after the figure numbers. Expansions of the data are denoted by 'b' and 'c'.

4.4.2.1 Water

Comparison between Figs.4.8, and 4.9 shows that the general form of the data is fairly reproducible, the initial differences in junction conductance notwithstanding. The benefit of the accurate four-point junction potential measurements is reflected in the small scatter of the

Fig.4.8a

The experimental junction potential, V_j, versus time plot for water ("INFDATA22"). The current supply, i, in the four point measurement technique employed to measure V_j was approximately 1 mA; therefore the junction resistance R_j is approximately given by $R_j \simeq V_j \times 10^3$. A current of 1 mA was maintained throughout all infusion doping experiments.

Fig.4.8

The corresponding G-t plot.

DOPANT: DE-IONISED MILLIPORED H2O T/SEC DATE: 26-4-83

PB=3000A DATA FILE: INFDATA22

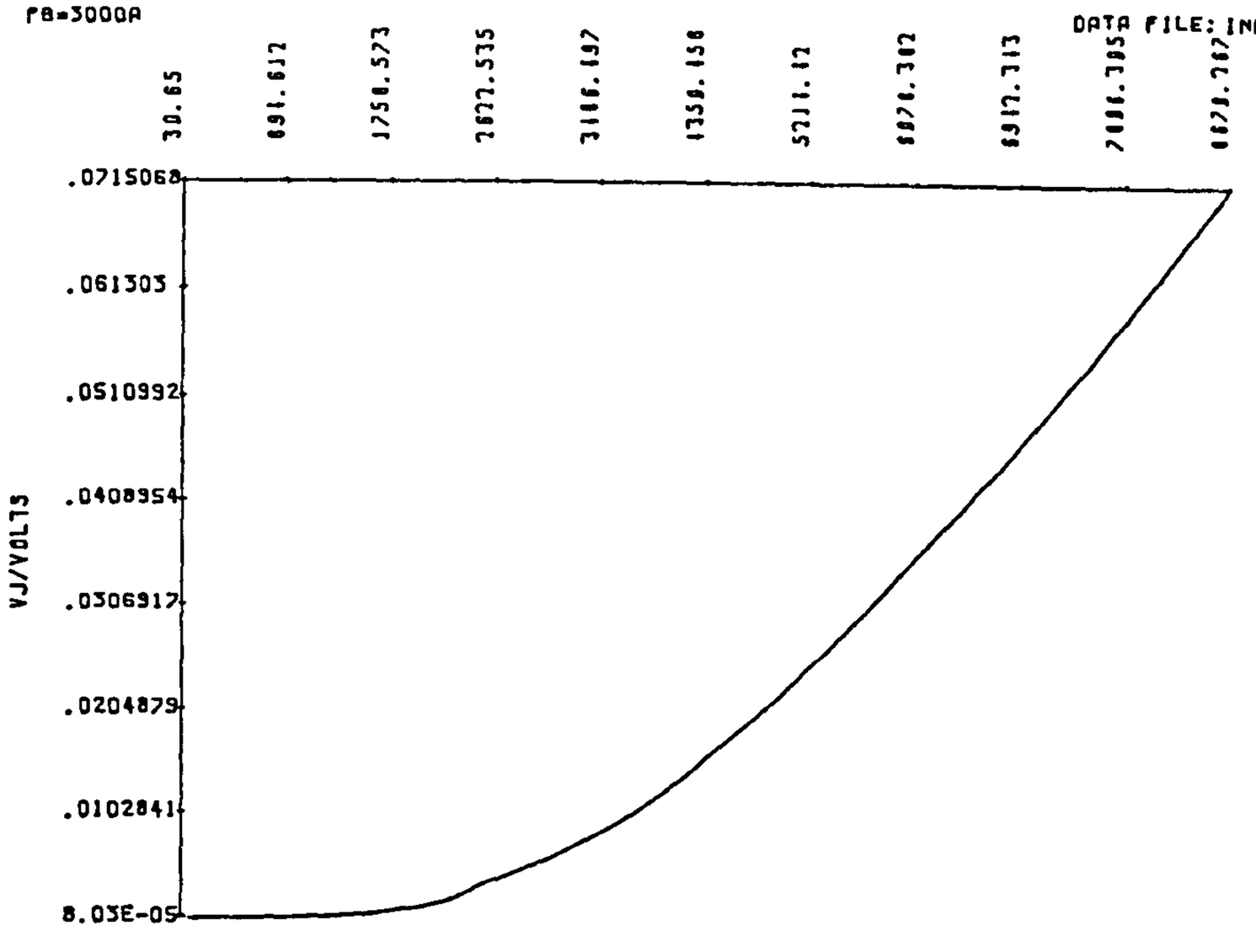

DOPANT: DE-IONISED MILLIPORED H2O T/SEC DATE: 26-4-83

PB=3000A DATA FILE: INFDATA22

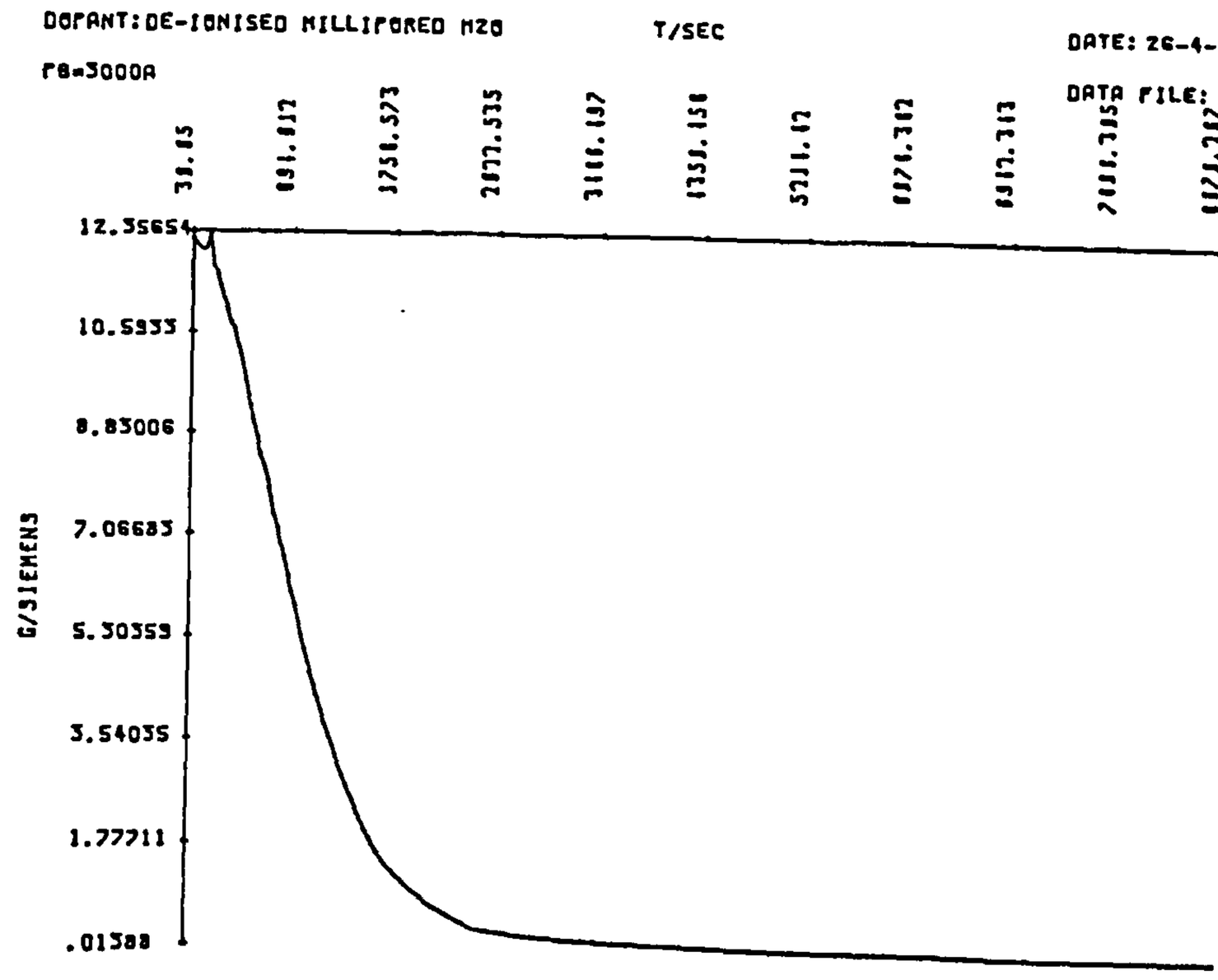

Fig.4.8b

Expansion of Fig.4.8. Regions A, to E, and the corresponding slopes $g_1'(t)$ to $g_4'(t)$ are indicated. ($g_o'(t)$ is not included). The junction conductances G_1^o to G_4 at the estimated discontinuities between regions of different slopes are also shown. The estimated values of G_1 to G_4, and $g_1'(t)$ to $g_4'(t)$ are given in Tables 4.2 and 4.3 respectively.
(nb $g_n'(t) = \frac{dG_n}{dt}$).

Fig.4.8c

Expansion of Fig.4.8 showing how $g_3'(t)$, and G_4 were extracted from the curve. Clearly, estimates of these quantities are susceptible to considerable error.

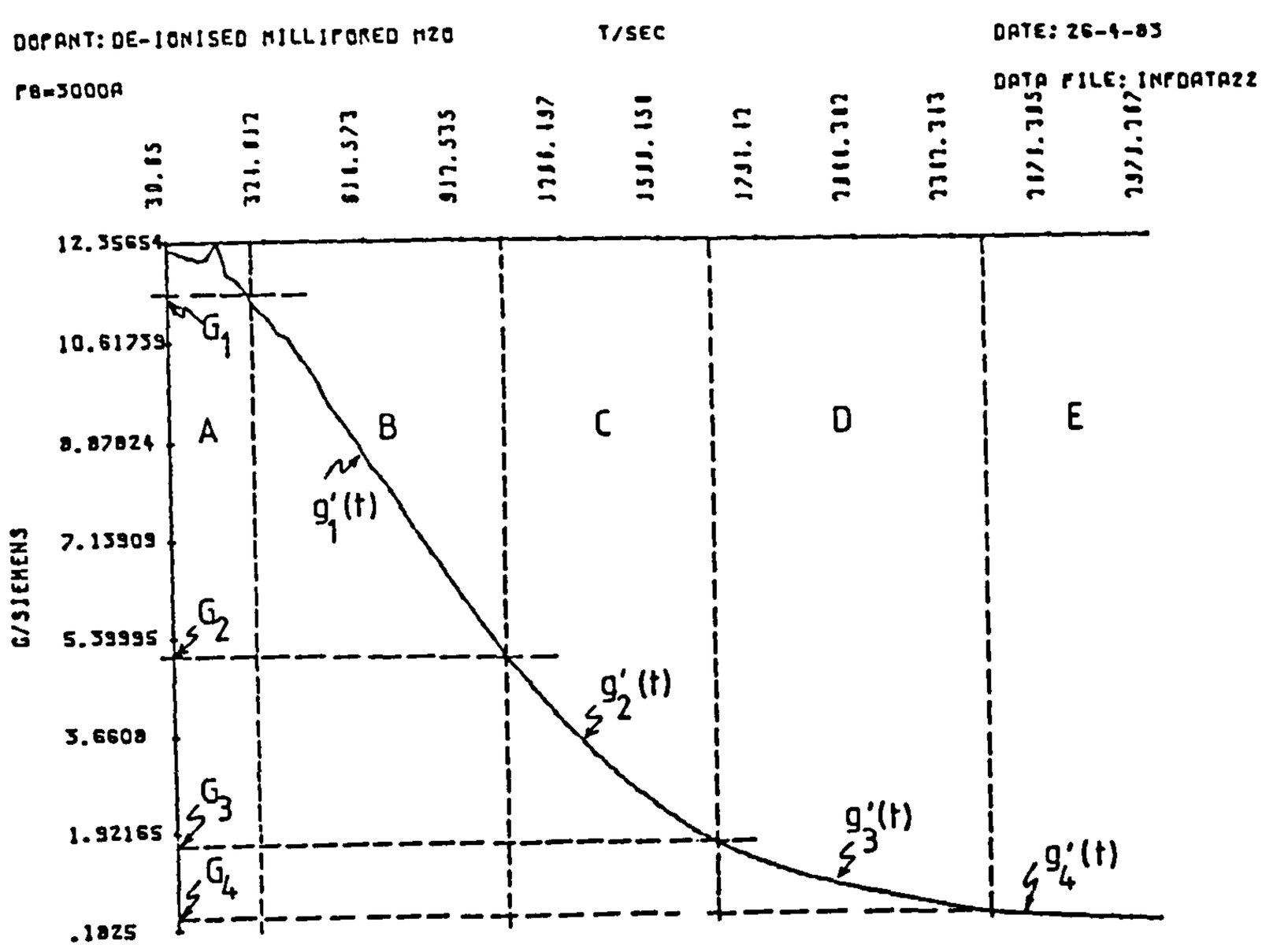
DOPANT: DE-IONISED MILLIPORED H2O
T/SEC
DATE: 26-4-83
DATA FILE: INFDATA22
FB=3000A
30.65
321.812
611.573
917.535
1236.197
1551.158
1231.12
2211.302
2517.313
2171.335
2771.767
12.35654
10.61759
8.87824
7.13909
5.39995
3.6608
1.92165
.1825
G/SIEMENS
A
B
C
D
E
G1
G2
G3
G4
g'1(t)
g'2(t)
g'3(t)
g'4(t)

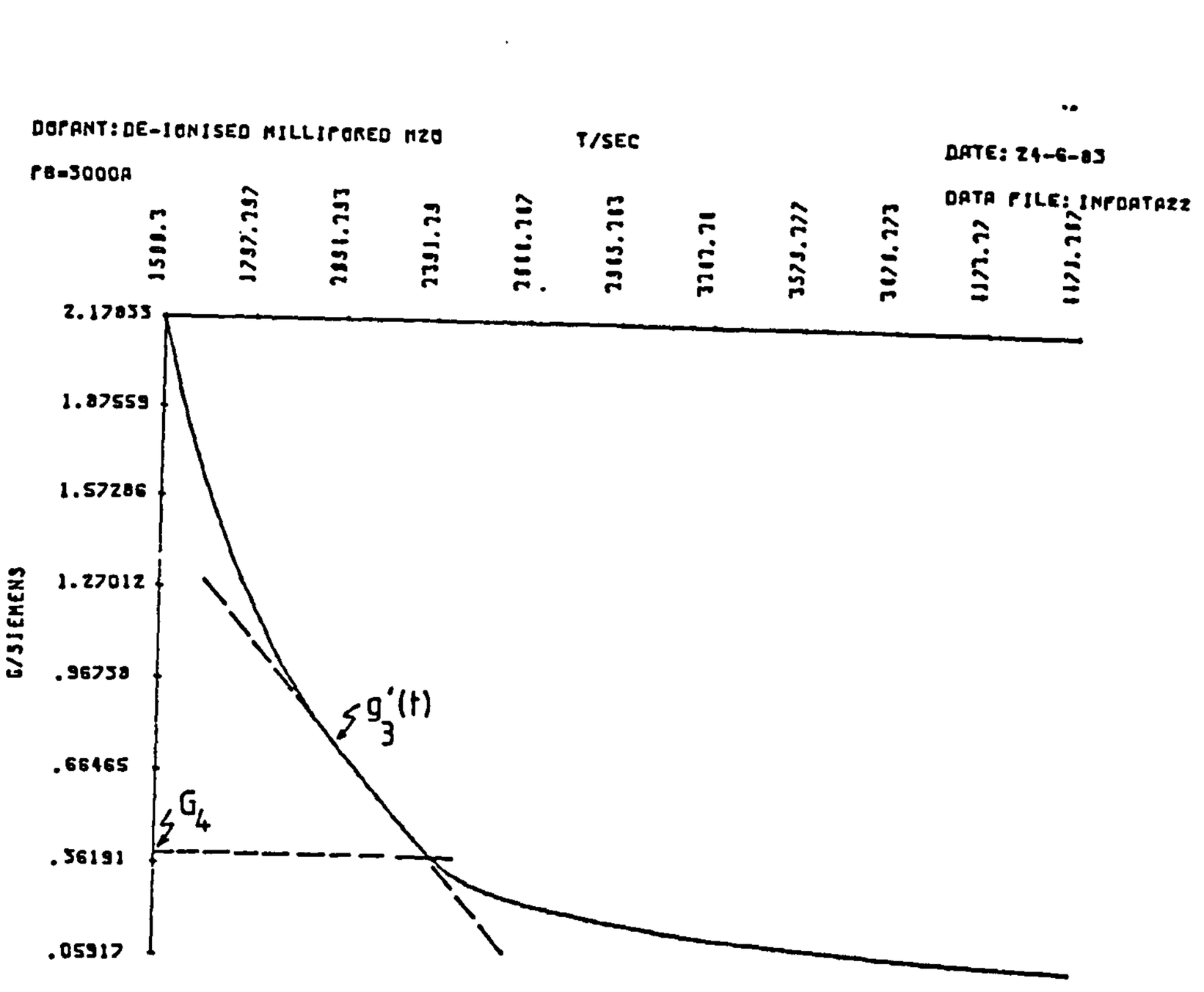
DOPANT: DE-IONISED MILLIPORED H2O
T/SEC
DATE: 24-6-83
DATA FILE: INFDATA22
FB=3000A
1508.3
1797.297
2091.293
2391.29
2611.787
2965.283
3267.78
3573.277
3878.273
4177.27
4471.267
2.17833
1.87559
1.57286
1.27012
.96738
.66465
.36191
.05917
G/SIEMENS
g'3(t)
G4

Fig.4.9

Experimental G-t plot for water ("INFDATA24").

Fig.4.9a

The corresponding junction potential, V_j, versus time plot. The junction resistance R_j is approximately given by $R_j \simeq V_j \times 10^3$. (See caption for Fig.4.8a).

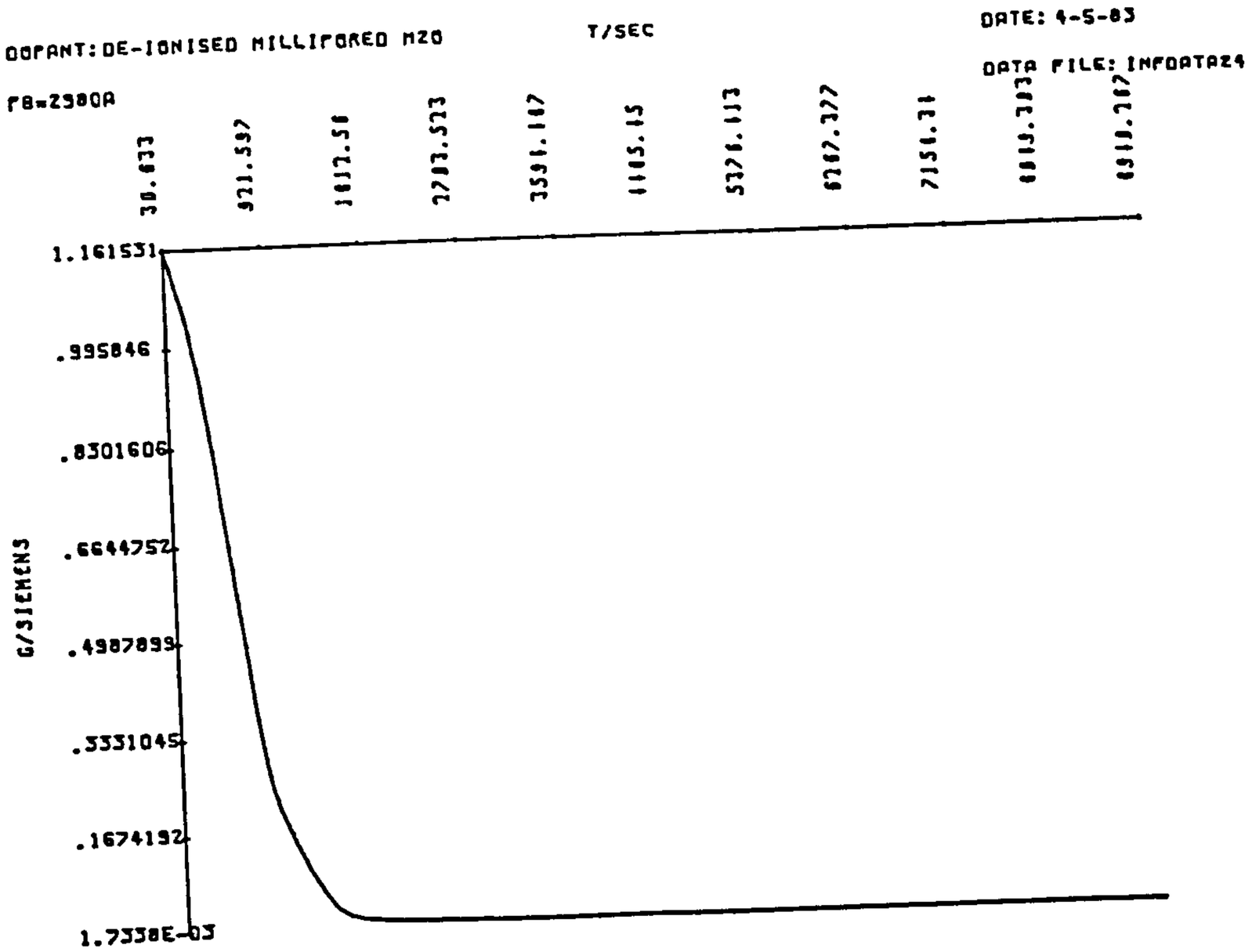
DOPANT: DE-IONISED MILLIPORED H20
T/SEC
DATE: 4-5-83
DATA FILE: INFDATA24
FB=2980A
30.833
921.597
1817.58
2703.523
3591.187
4485.15
5376.113
6267.327
7156.31
8013.383
8918.287
1.161531
.995846
.8301606
.6644752
.4987899
.3331045
.1674192
1.7538E-03
G/SIEMENS

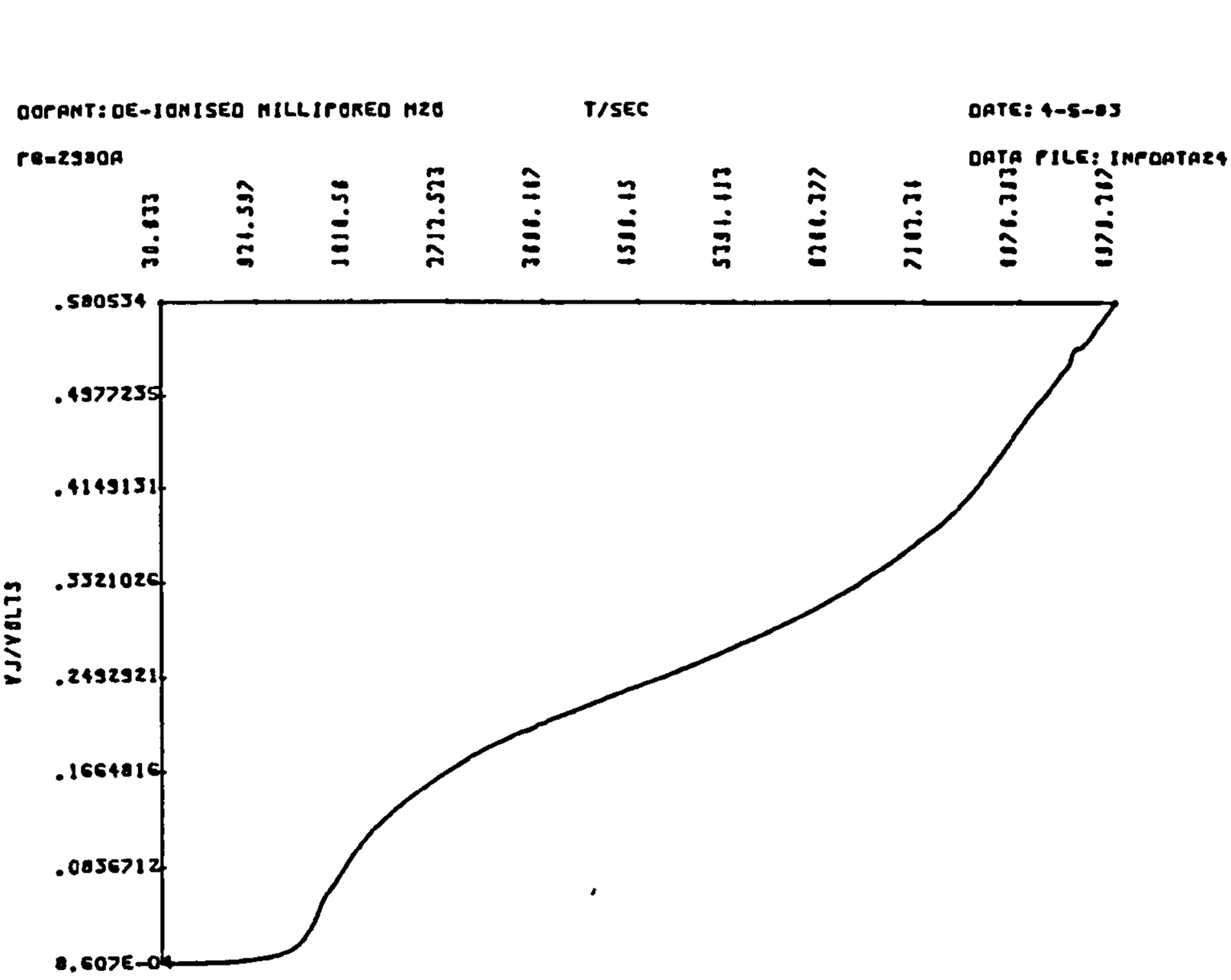
DOPANT: DE-IONISED MILLIPORED H20
T/SEC
DATE: 4-5-83
DATA FILE: INFDATA24
FB=2980A
30.833
921.597
1818.58
2712.523
3606.187
4500.15
5391.113
6280.327
7167.31
8026.383
8931.287
.580534
.497723S
.4149131
.332102G
.2492921
.166481G
.0836712
8.607E-04
VJ/VOLTS

Fig.4.9b

Expansion of Fig.4.9 showing regions A to D, slopes $g_1'(t)$ to $g_3'(t)$, and corresponding conductances G_1 to G_3, and $g_1'(t)$ to $g_3'(t)$ estimated from the curve are given in Table 4.2, and 4.3 respectively.

DOPANT: DE-IONISED MILLIPORED H20 T/SEC

DATE: 4-5-83

FB=2980Å

DATA FILE: INFDATA24

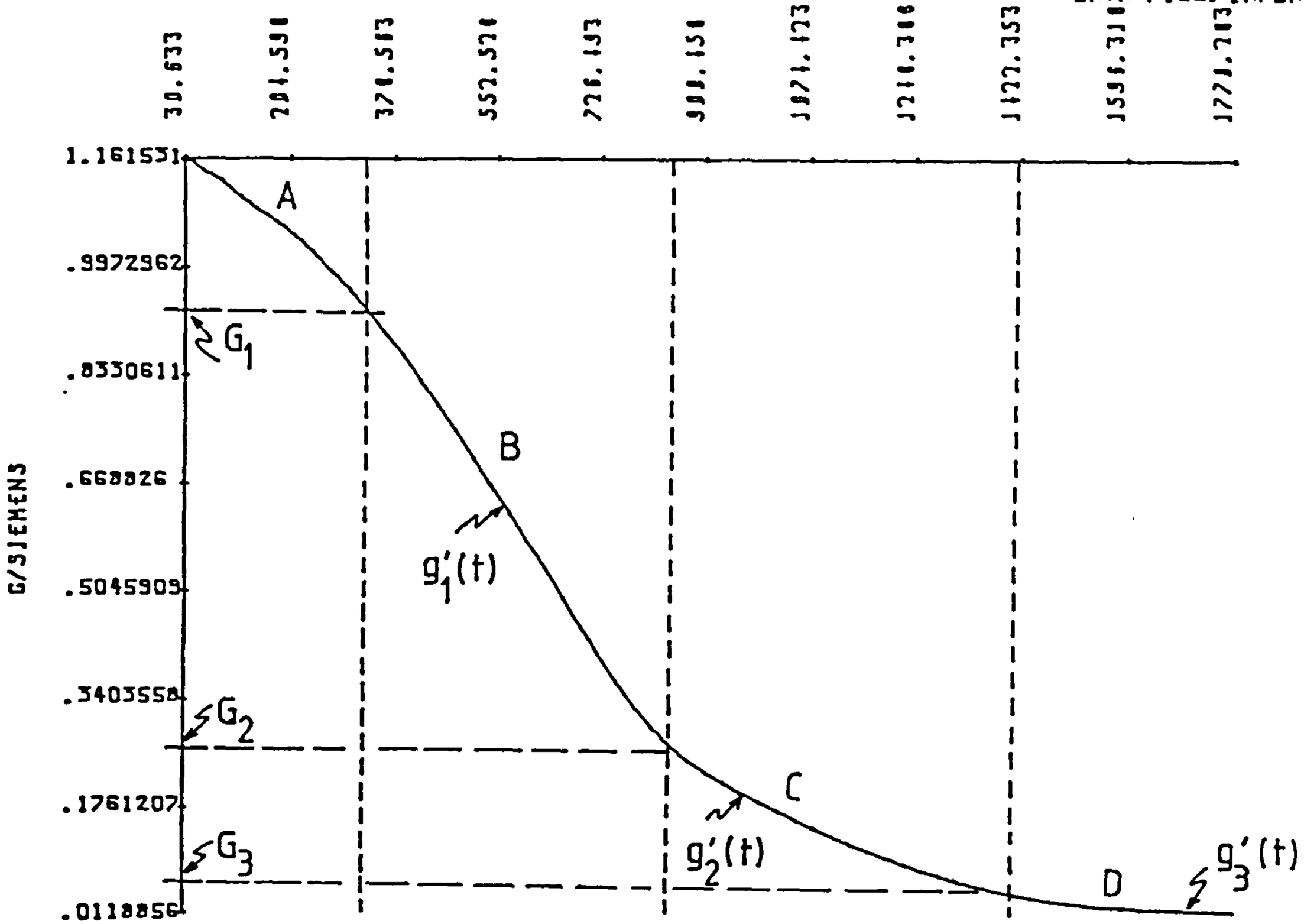

Fig.4.10a

Experimental junction potential, V_j, versus time plot for acetone ("INFDATA23"). The junction resistance, R_j, is approximately given by $R_j \simeq V_j \times 10^3$. (See also caption for Fig.4.8a)

Fig.4.10

The corresponding G-t plot showing regions A to D.

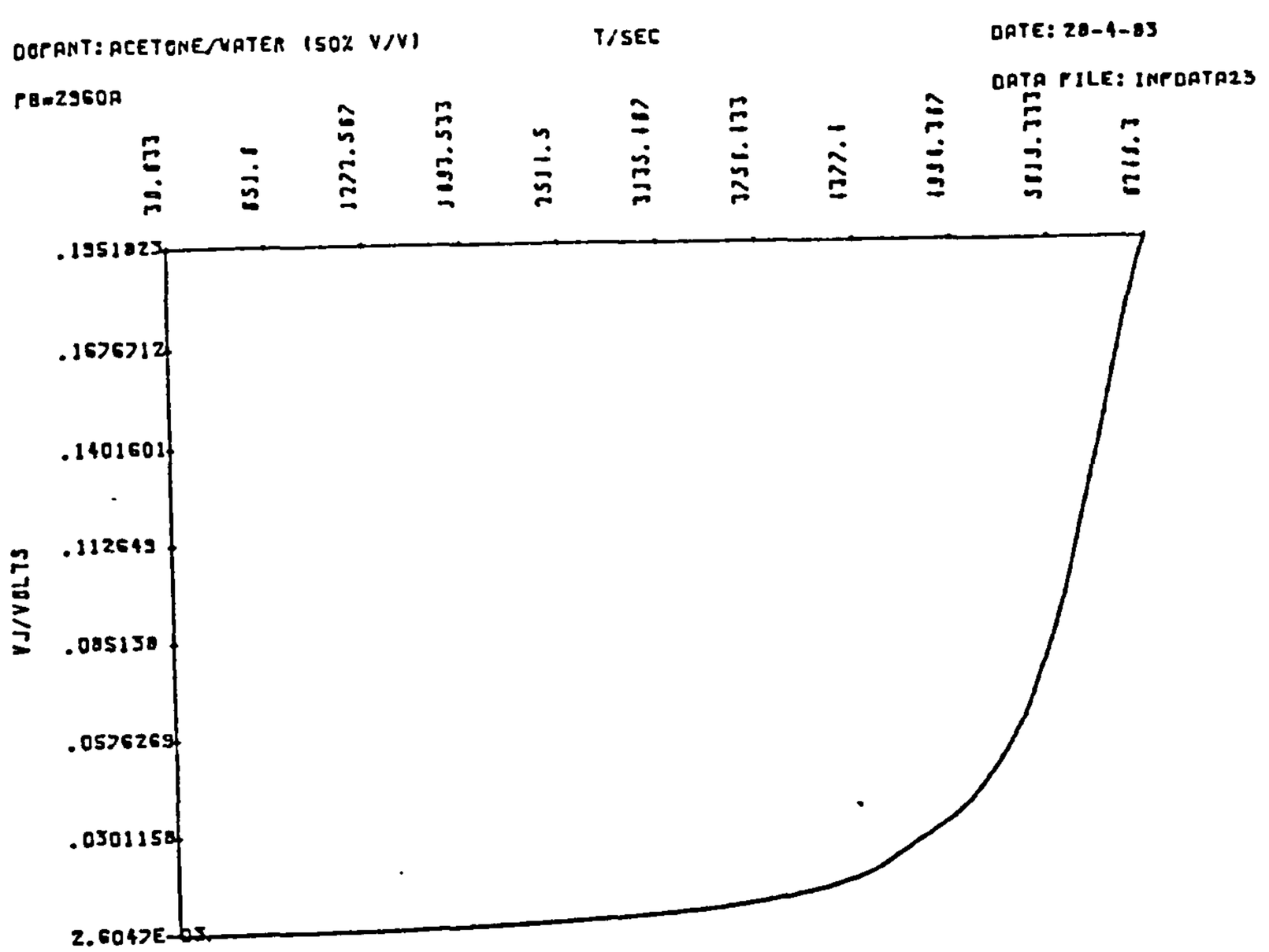
DOPANT: ACETONE/WATER (50% V/V)
T/SEC
DATE: 28-4-83
PB=2960A
DATA FILE: INPDATA23
30.833
651.8
1272.567
1893.533
2511.5
3135.187
3758.133
4377.1
4998.367
5619.333
6238.3
.1951823
.1676712
.1401601
.112649
.085138
.0576269
.0301158
2.6047E-03
VJ/VOLTS

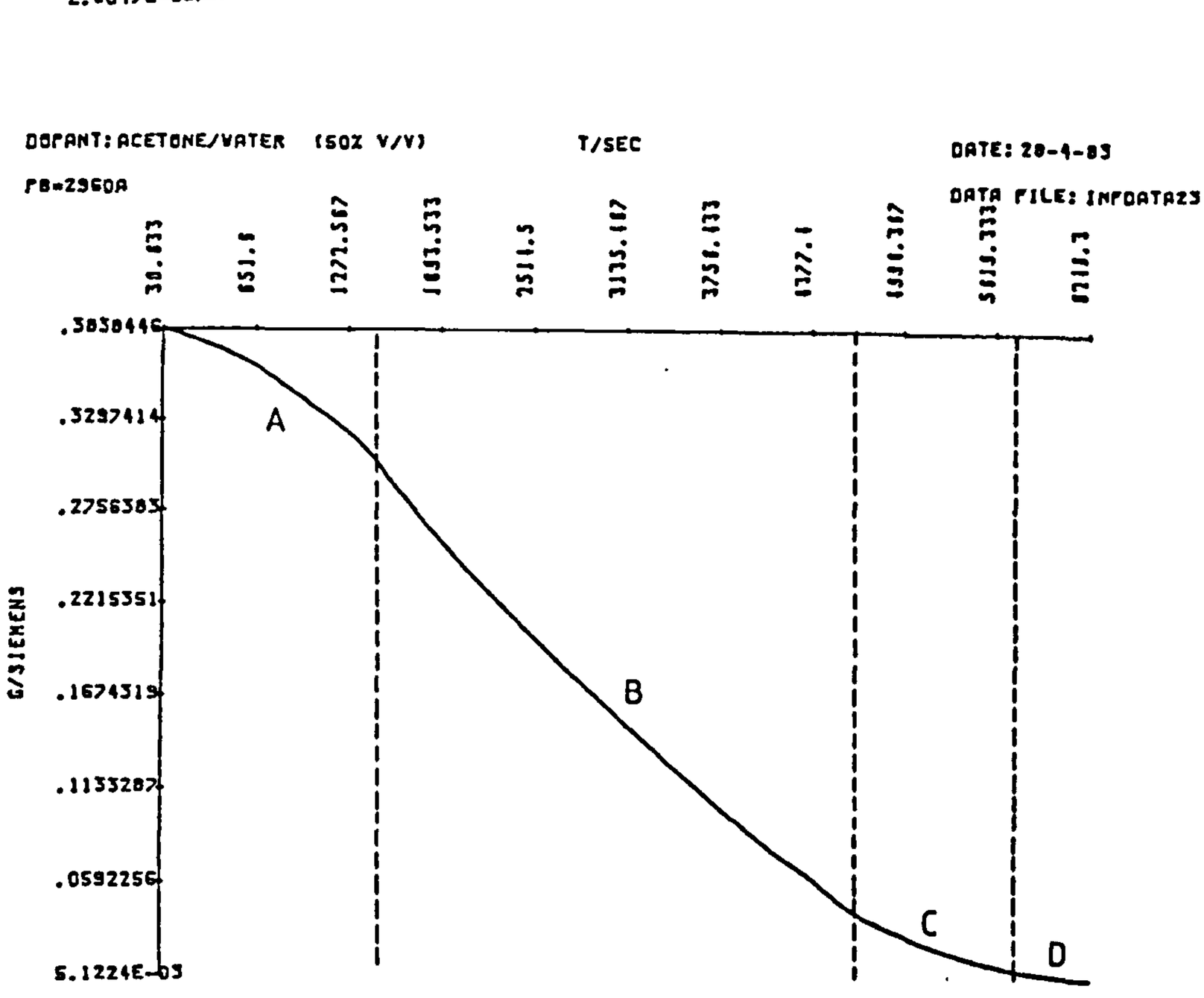
DOPANT: ACETONE/WATER (50% V/V)
T/SEC
DATE: 28-4-83
PB=2960A
DATA FILE: INPDATA23
30.833
651.8
1272.567
1893.533
2511.5
3135.187
3758.133
4377.1
4998.367
5619.333
6238.3
.3838446
.3297414
.2756383
.2215351
.1674319
.1133287
.059225
5.1224E-03
G/SIEMENS
A
B
C
D

Fig.4.10c

Expansion of Fig.4.10 showing regions B to D, and how slopes $g_2'(t)$, $g_3'(t)$, and conductances G_2 and G_3 were estimated. The difficulties associated with making accurate estimates are illustrated by $g_3'(t)$, a shallow and poorly defined slope. Errors incurred in estimating $g_3'(t)$ are reflected in G_3.

Fig.4.10b

Expansion of Fig.4.10 showing regions A and B, and how $g_1'(t)$ and G_1 were estimated. Values of G_1 to G_3, and $g_1'(t)$ to $g_3'(t)$ are given in Tables 4.4 and 4.5 respectively.

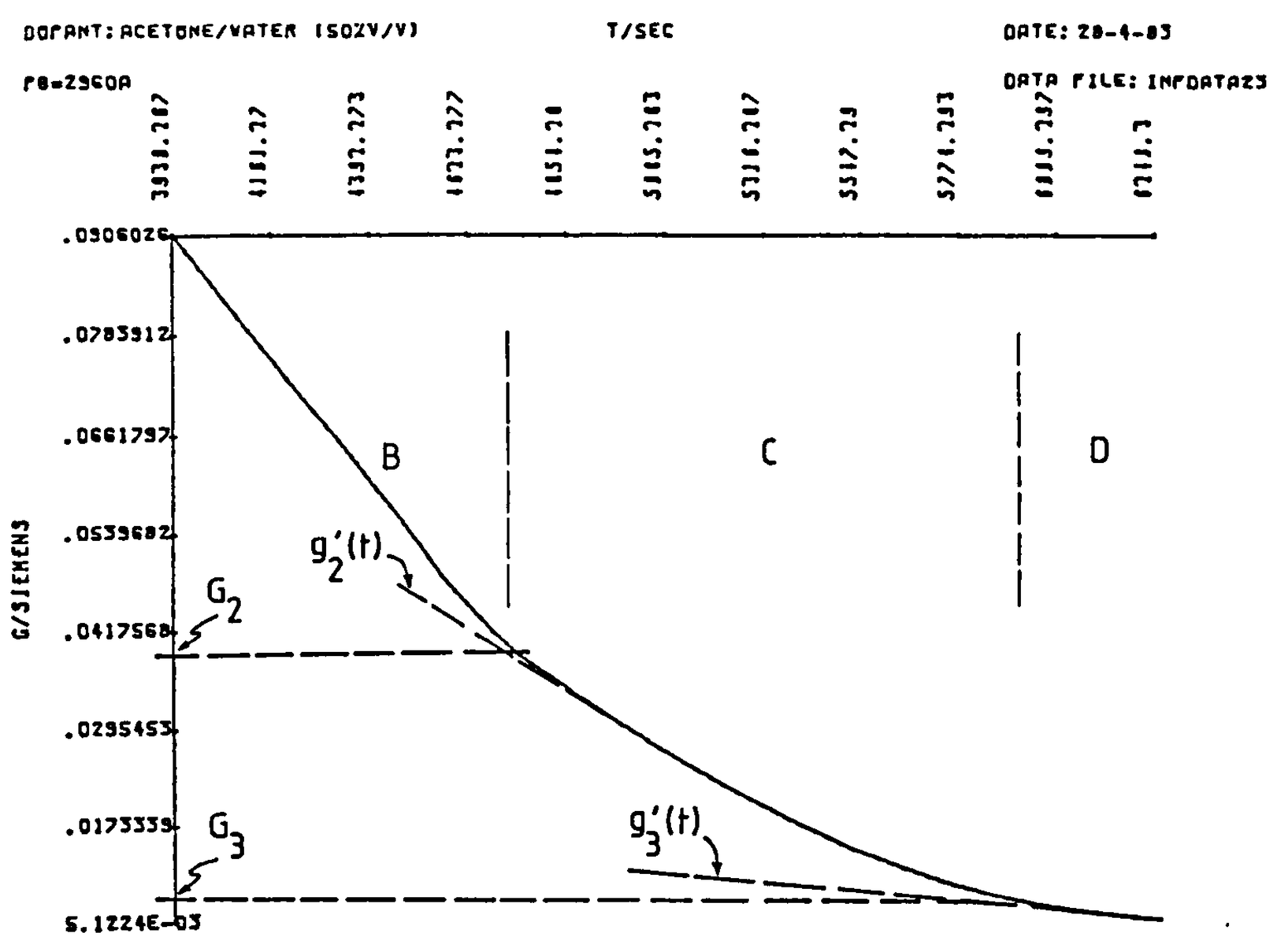
DOPANT: ACETONE/WATER (SOZV/V)
T/SEC
DATE: 28-4-83
PB=2960A
DATA FILE: INPDATA23
3938.287
4181.27
4392.273
4673.277
4851.28
5185.283
5316.287
5512.29
5774.293
6113.297
6211.3
.0906026
.0785912
.0661797
.0539682
.0417568
.0295453
.0173339
5.1224E-03
G/SIEMENS
B
C
D
$g_2'(t)$
G_2
G_3
$g_3'(t)$

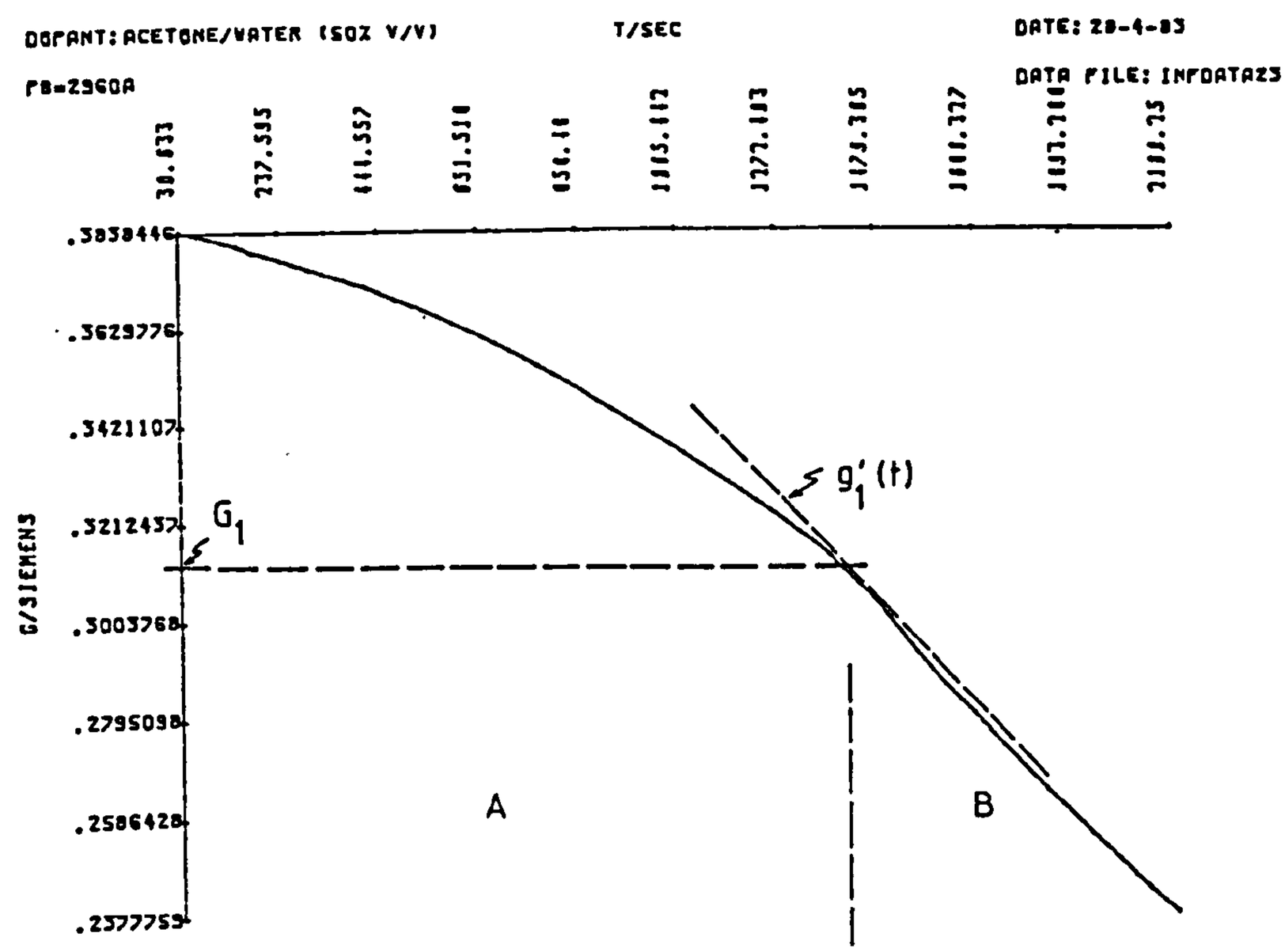
DOPANT: ACETONE/WATER (SOZ V/V)
T/SEC
DATE: 28-4-83
PB=2960A
DATA FILE: INPDATA23
30.833
237.535
411.557
651.518
856.18
1185.112
1327.183
1574.385
1811.727
1937.788
2188.25
.3838446
.3629776
.3421107
.3212437
.3003768
.2795098
.2586428
.2377759
G/SIEMENS
A
B
G_1
$g_1'(t)$

points. (Junction potentials quoted have been measured to the nearest μV using the Keithley 192 DMM.) Measurements taken at 30s intervals were sufficiently frequent to resolve easily any rapid changes in conductance. For both sets of data, it is observed that region A - corresponding to the time taken to penetrate the Pb electrode is relatively short. This may be due to a high mobility of the small water molecules. The conductance then falls rapidly until approximately 2000s have elapsed. From there onwards as a consequence of the progressively thickening insulating layer thus formed, the conductance decreases as an essentially thickness dependent negative exponential. Little information is to be gleaned from these latter regions since experimental error becomes commensurate with the observed changes in conductance.

In order to interpret the data, expanded plots indicating the regions A to E and A to D for the two sets of data are shown in Figs.4.8b and 4.9b; it is asserted that these correspond to the formation of successive monolayers of water. Also indicated are the conductances, G_n, corresponding to the estimated points of inflexion between the regions of slopes $g_n'(t)$. Figure 4.8c illustrates how the G_n's and $g_n'(t)$'s were extracted from the experimental plots (Here $g_n'(t) = \frac{dG_n}{dt}$).

Following the discussion outlined in 4.3.3., Table 4.2 lists the calculated incremental monolayer thicknesses due to analyses of the ratios of conductances towards the ends of successive regions. The corresponding thicknesses calculated from the ratios between slopes of consecutive regions are given in Table 4.3

Experimental error inevitably enters into the analysis with progressing infusion time due to the rapidly diminishing junction conductance. The differences between slopes of successive regions also diminishes as the numerical value of the slopes tends towards zero. It was

Table 4.2 - Analysis of experimental conductance ratios for IET junctions infusion doped with water. Δt is the incremental thickness corresponding to the change in conductance $G_{n+1} - G_n$.

DATAFILE	n	G_n/S	$\ln \frac{G_n}{G_{n+1}}$	$\Delta t/\text{Å}$ Φ = 1 eV	$\Delta t/\text{Å}$ Φ = 2 eV
INFDATA22	1	11.4870			
			0.84	0.84	0.59
	2	4.9652			
			1.15	1.15	0.81
	3	1.5738			
			1.39	1.39	0.98
	4	0.3922			
				average = 1.13	average = 0.79
INFDATA24	1	0.9316			
			1.28	1.28	0.91
	2	0.2852			
			1.44	1.44	1.02
	3	0.0612			
				average = 1.36	average = 0.97

Table 4.3 - Analysis of ratios of the experimental slopes g_n' (t) for IET junctions infusion doped with water. t is the thickness corresponding to the logarithmic conductance ratios shown.

DATAFILE	n	g_n' (t)/S.s^{-1}	ln $\frac{g_n'(t)}{g_{n+1}'(t)}$	t/Å Φ = 1 ev	t/Å Φ = 2 eV
INFDATA22	1	9.15×10^{-3}	0.44	-	-
	2	5.92×10^{-3}	1.56	1.56	1.11
	3	1.24×10^{-3}	2.52	2.52	1.78
	4	0.10×10^{-3}		average = 2.02	average = 1.45
INFDATA 24	1	1.41×10^{-3}	1.31	-	-
	2	0.38×10^{-3}	2.54	2.54	1.80
	3	0.03×10^{-3}			

not possible to estimate accurately the slopes of regions D or E (i.e. $g_3'(t)$, and $g_4'(t)$ respectively) nor the positions of the discontinuities between regions. As mentioned earlier, the observed smoothing effect may well be due to the fact that monolayer growth is not strictly sequential, and new monolayers start to grow prior to the completion of previous layers. Any analysis of the data must therefore be treated on a qualitative basis due to the above considerations and those discussed in 4.2.2.

On the whole, the data in Tables 4.2, and 4.3 show that the incremental monolayer thickness displayed in regions B onwards is fairly constant, and of the order 1 - 2 Å, i.e. what one might expect due to the adsorption of monolayers of water. Clearly, the mean barrier height, Φ, will also have a marked effect on the analysis. It is noted that the thickness values obtained due to the analyses of slope ratios are on average slightly greater than those from the conductance ratios. Again, it cannot be over emphasized that the measurement of the numerical values of the slopes is not straightforward. Consequently, the estimated thicknesses which are of the correct order of magnitude should if possible be considered in conjunction with corresponding junction capacitance data. Having said this, it is interesting to note that the approximate thicknesses here do agree surprisingly well with the predicted values due to the model. This will be discussed further in 4.4.4.

4.4.2.2 Acetone

On first inspection, the G-t plots for acetone in Figs.4.10, and 4.11 would appear incongruous when one considers that the two sets of data were taken from nominally similar experimental arrangements. The rate of infusion in Fig.4.11 is the more rapid of the two, with the conductance quickly attaining a low, and fairly constant value after approximately 2000s.

Fig.4.11a

Experimental junction potential, V_j, versus t plot for acetone ("INFDATA25"). The junction resistances, R_j, are approximately given by $R_j \simeq V_j \times 10^3$. (See caption for Fig.4.8a).

Fig.4.11

The corresponding G-t plot.

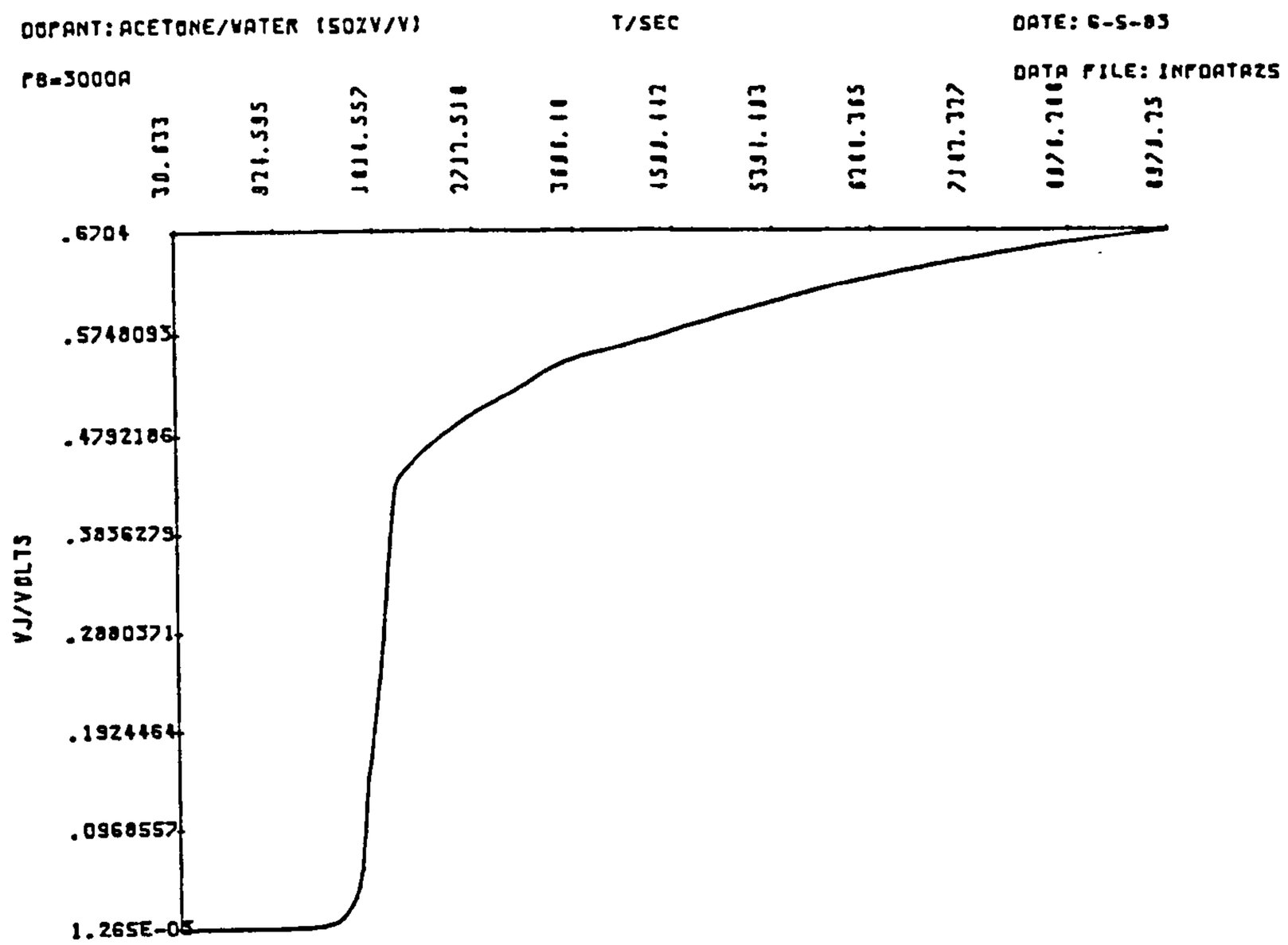
DOPANT: ACETONE/WATER (50ZV/V)
T/SEC
DATE: 6-5-83
PB=3000A
DATA FILE: INFOATAZS
30.633
921.535
1811.557
2712.518
3613.11
4513.112
5331.183
6211.365
7112.727
8076.288
8978.25
.6704
.5748093
.4792186
.3836279
.2880371
.1924464
.0968557
1.265E-05
VJ/VOLTS

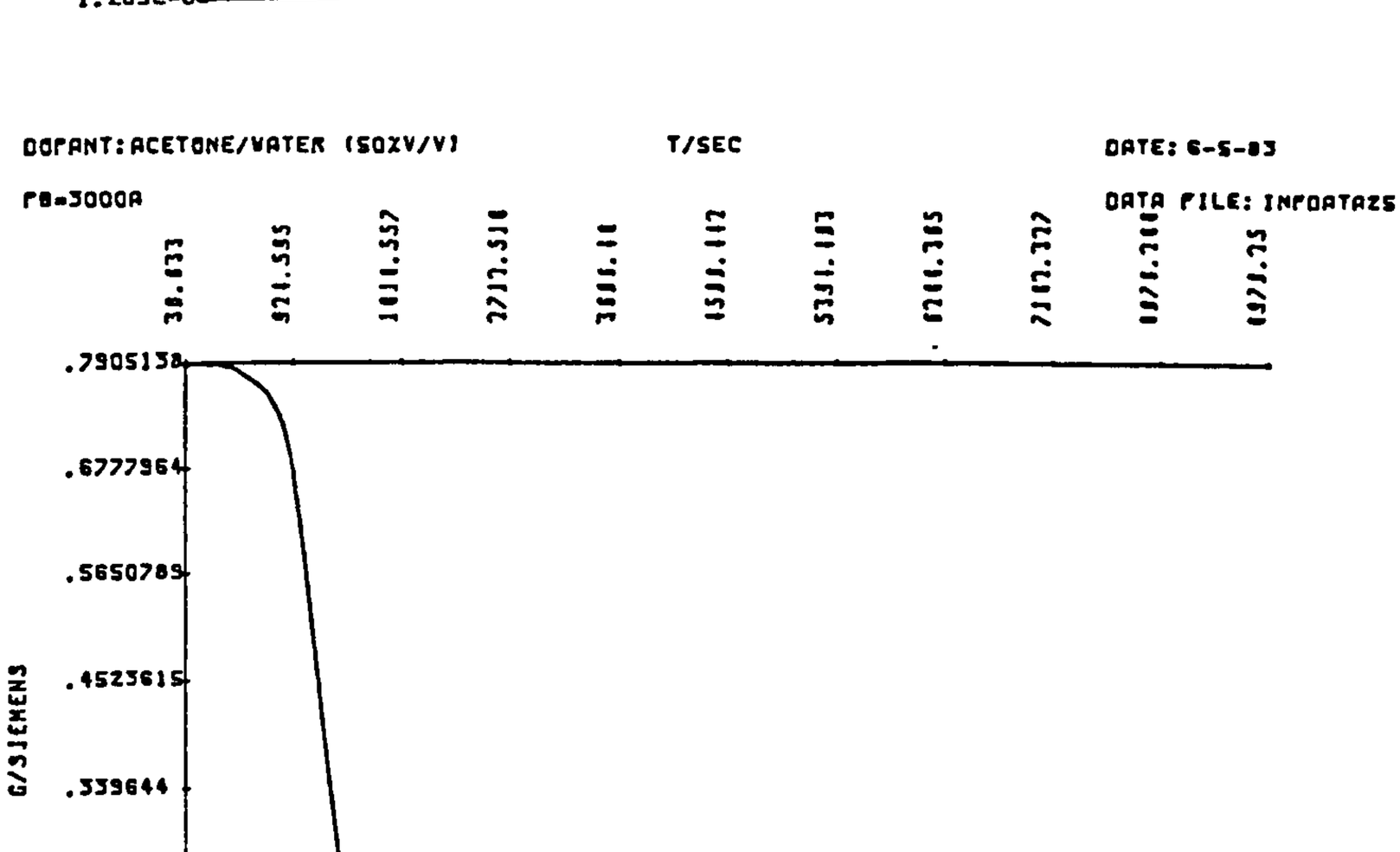
DOPANT: ACETONE/WATER (50ZV/V)
T/SEC
DATE: 6-5-83
PB=3000A
DATA FILE: INFOATAZS
30.633
921.535
1811.557
2712.518
3613.11
4513.112
5331.183
6211.365
7112.727
8076.288
8978.25
.7905138
.6777964
.5650789
.4523615
.339644
.2269266
.1142091
1.491GE-03
G/SIEMENS

Fig.4.11b

Expansion of Fig.4.11 showing regions A to D.

Fig.4.11c

Expansion of Fig.4.11, showing regions A to D and how slopes g_1' (t), to g_3' (t), and conductances G_1 and G_2 were estimated. G_3 was then estimated by further expansion of Fig.4.11. Values of G_1 to G_3, and g_1' (t) to g_3' (t) are given in Tables 4.4, and 4.5 respectively.

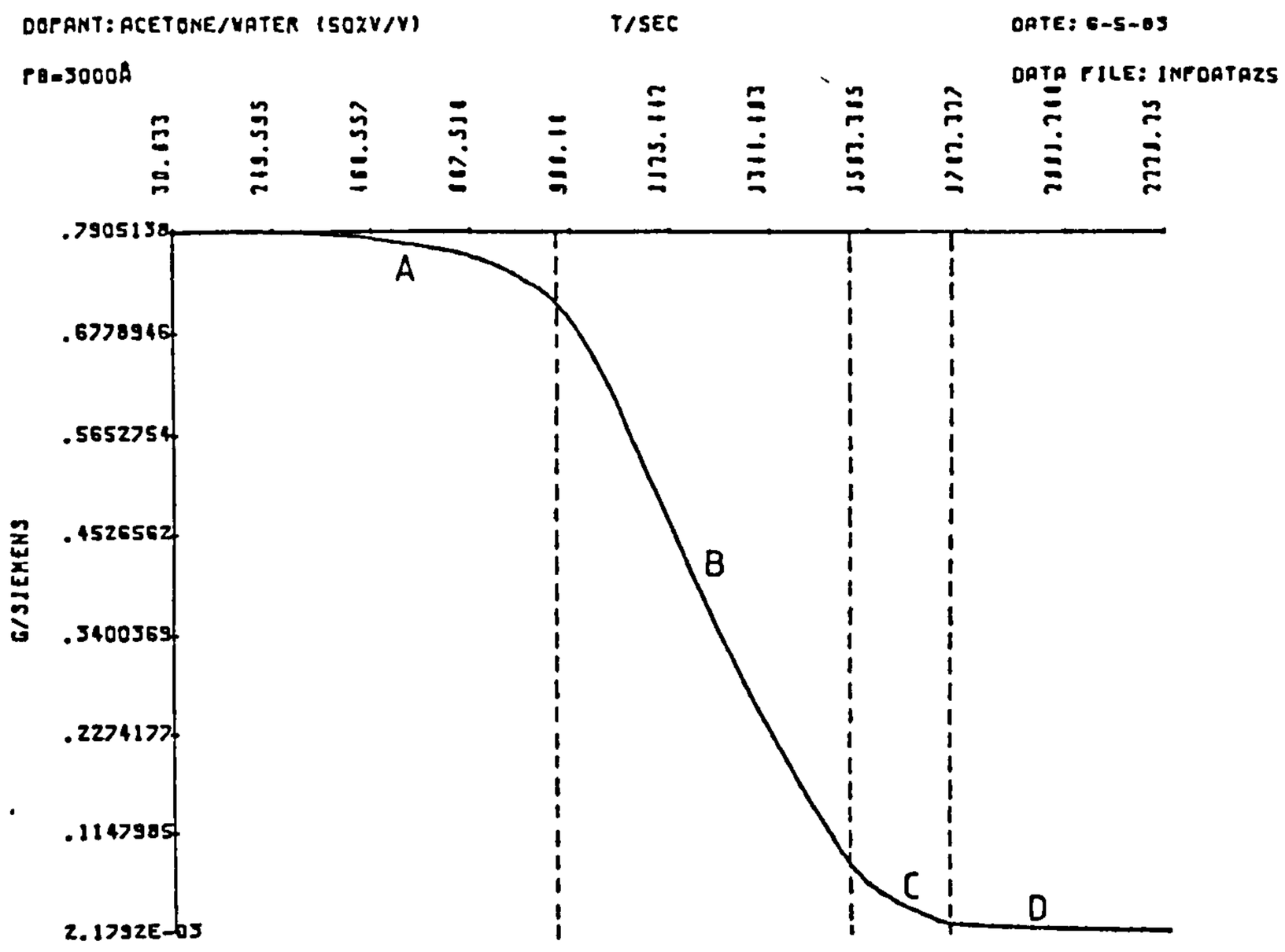
DOPANT: ACETONE/WATER (50ZV/V)
T/SEC
DATE: 6-5-83
FB=3000Å
DATA FILE: INFOATAZS
30.633
219.535
401.557
607.518
788.18
1175.142
1311.183
1567.385
1767.727
2003.268
2221.75
.7905138
.6778946
.5652754
.4526562
.3400369
.2274177
.1147985
2.1792E-03
G/SIEMENS
A
B
C
D

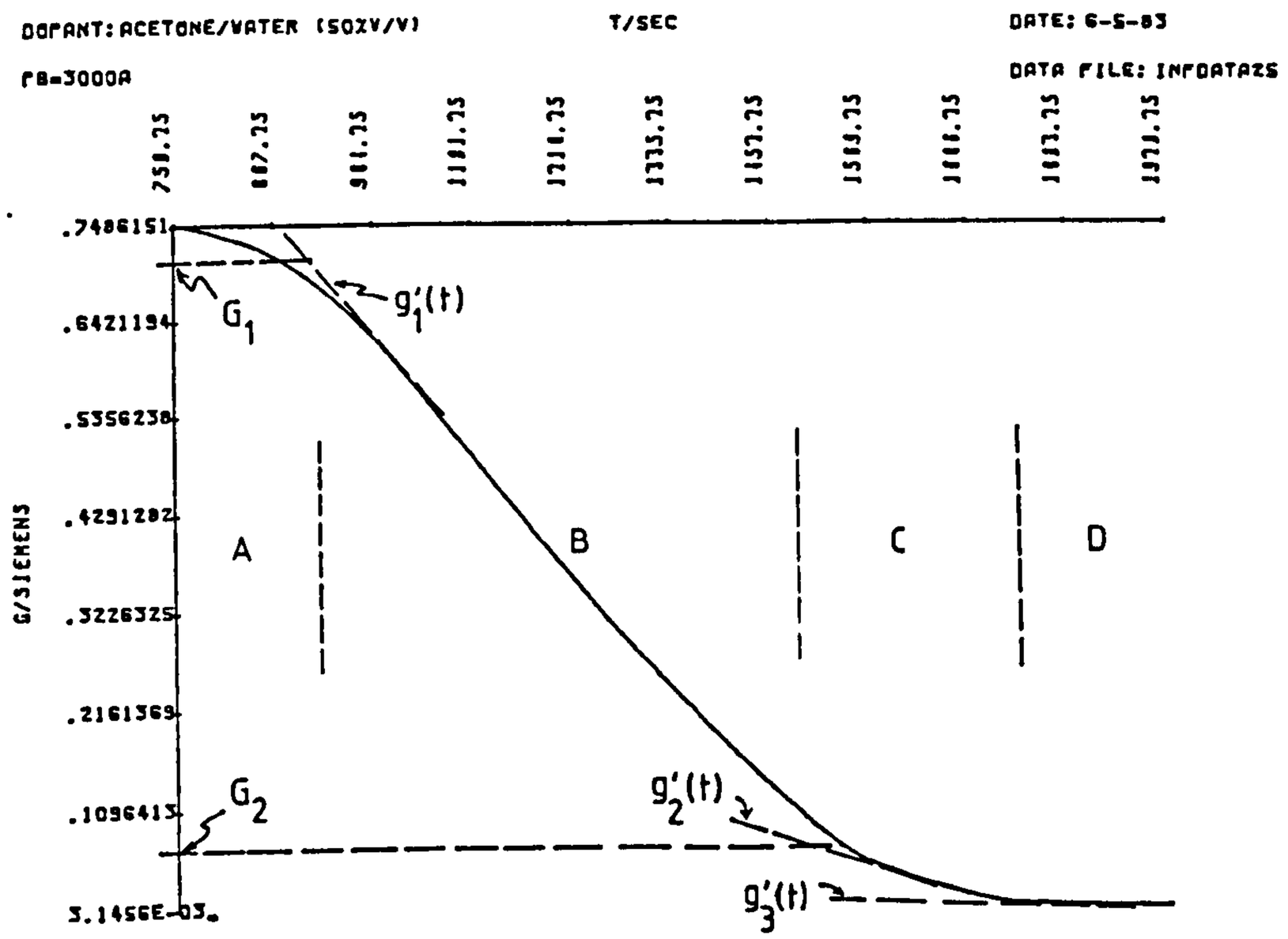
DOPANT: ACETONE/WATER (50ZV/V)
T/SEC
DATE: 6-5-83
FB=3000A
DATA FILE: INFOATAZS
758.25
882.25
981.25
1181.25
1318.25
1335.25
1457.25
1583.25
1681.25
1883.25
1971.25
.7486151
.6421194
.5356238
.4291282
.3226325
.2161369
.1096413
5.1456E-03
G/SIEMENS
G_1
$g_1'(t)$
G_2
$g_2'(t)$
$g_3'(t)$
A
B
C
D

Table 4.4 - Analysis of experimental conductance ratios for IET junctions infusion doped with a 50% v/v solution of acetone/water.

DATAFILE	n	G_n/S	ln $\frac{G_n}{G_{n+1}}$	$\Delta t/\mathring{A}$ Φ = 1 eV	$\Delta t/\mathring{A}$ Φ = 2 eV
INFDATA23	1	0.3129			
			2.07	2.07	1.47
	2	0.0391			
			1.57	1.57	1.11
	3	0.0082			
				average = 1.82	average = 1.29
INFDATA25	1	0.7060			
			2.17	2.17	1.53
	2	0.0810			
			1.60	1.60	1.13
	3	0.0163			
				average = 1.89	average = 1.33

Table 4.5 - Analysis of ratios of the experimental slopes g_n' (t) for IET junctions infusion doped with a 50% v/v solution of acetone/water.

DATAFILE	n	g_n' (t)/S.s^{-1}	ln $\frac{g_n'}{g_{n+1}'}$ (t)	t/Å Φ = 1 eV	t/Å Φ = 2 eV
INFDATA23	1	6.4 x 10^{-5}			
			0.63	-	-
	2	3.4 x 10^{-5}			
			1.92	1.92	1.36
	3	0.5 x 10^{-5}			
INFDATA25	1	1.06 x 10^{-3}			
			1.23	-	-
	2	0.31 x 10^{-3}			
			2.74	2.74	1.94
	3	0.02 x 10^{-3}			

If however the region up to ∿ 2000s is expanded in the time domain, evidence of discontinuities in slope becomes clear, as indicated in Fig.4.11b. Variations in infusion rate of the order illustrated in these figures (where the overall time taken to complete regions A to D being ∿ 100 and ∿ 30 minutes for Fig.4.10 and 4.11 respectively) were quite common. Discrepancies of this order are as yet not satisfactorily explained, but may be due to slight variations in the island structure of the Pb electrode.

Proceeding along the same lines as the previous analysis for water, (and adopting the same symbol nomenclature) the incremental thicknesses calculated due to the ratios of conductances, G_n, and slopes g_n' (t), extracted from the G-t plots are given in Tables 4.4, and 4.5 respectively. The resulting values due to the ratios of slopes are again the less reliable of the two methods mainly due to the associated difficulties of accurately estimating the slopes. Once more, if a qualitative approach is adopted, the thicknesses are of the correct order, and perhaps slightly greater on average than the values obtained for water if more weight is placed on the values derived from the conductance ratios. Bearing in mind the various shortcomings of the model, and the assumptions made along the way, one might reasonably infer from the acetone data that monolayers of approximate thickness ∿ 2 Å were being sequentially formed. These results should be considered after having inspected the corresponding junction capacitance data.

4.4.3 Capacitance Measurements

Measurements were made using a Wayne-Kerr d.c. bridge (Model B224) at a frequency of 1 kHz with an applied peak to peak voltage amplitude of 100 mV. For reasons discussed in 3.1.5., it was not possible to measure the capacitance of IET junctions having d.c. resistances of less than a few

hundred ohms.

Capacitance measurements during the infusion doping of IET junctions with a 50% v/v solution of acetone/water were obtained by pre-infusion doping the junctions until their capacitances were measurable, and then further doping and measuring the ensuing changes in capacitance. After the changes had been measured, attempts were made to reverse the (prolonged) infusion process by "flushing" the infusion chamber with N_2. This had little or no observable effect on the junction resistances or capacitances. Presumably, by that time several monolayers had formed on the oxide which could not easily be removed. Typical junction resistances, a.c. conductances and capacitances obtained for two IET junctions on the same glass slide after prolonged infusion doping are shown in Table 4.6. It is observed that as infusion progresses, the junction conductance and capacitance decrease as one might expect, and that (from equation 4.19) the ratios of final to initial conductances would predict increases in insulating barrier thickness of the order $\sim$ 5-6 Å for a mean barrier height, Φ, of the order 1 eV. It is noted that for such an increase, the corresponding junction capacitance of an undoped IET junction (where the insulating layer is assumed to be only Aℓ-oxide) is given by the well known expression

$$C_o = \frac{\varepsilon_o \varepsilon_{ox} A_j}{d_{ox}}$$

where $\varepsilon_o \simeq 8.85 \times 10^{-6}$, $\varepsilon_{ox} \sim 8$, $A_j \simeq 0.25 \times 10^{-6}$ m², and the oxide thickness d_{ox} is assumed to be $\sim$ 10 Å, then

$$C_o \simeq 17.7 \text{ nF}$$

If monolayers of pure acetone are now incorporated such that their total approximate thickness, d_A, is 5 Å (i.e. of the order predicted by the model just described), then the final capacitance of the junction may

Table 4.6 - IET junction capacitance measurements for two junctions on the same glass slide after prolonged infusion doping with a 50% by volume solution of acetone/water. Junction resistances were measured using a low power ohm-meter. (Large off scale values of resistance are indicated L.O.S.)

JUNCTION 3				JUNCTION 4			
	BRIDGE MEASUREMENTS				BRIDGE MEASUREMENTS		
R_J	G Term/mV	$1/G$ /Ω	C Term/nF	R_J	G Term/mV	$1/G$ /Ω	C Term/nF
350	2.664 (G_o)	375	19.6	200	4.962 (G_o)	202	20.4
400	2.331	429	19.5	300	3.191	313	19.0
500	1.910	524	19.6	-	-	-	-
600	-	-	19.7	-	-	-	-
------DEVICES FURTHER DOPED FOR ~ 15½ HOURS ----------							
L.O.S.	0.026	38.5K	12.0	L.O.S.	0.019	52.6K	12.9
					0.017	58.8K	9.4
------CHAMBER FLUSHED WITH N_2 FOR ~ 20 MIN----------							
L.O.S.	0.023 (G_F)	43.5K	8.9	L.O.S.	0.017 (G_F)	58.8K	9.1

Junction 3 $\ln \frac{G_F}{G_o} \simeq 5$,

Junction 5 $\ln \frac{G_F}{G_o} \simeq 6$.

be considered to be the series sum of capacitances due to the oxide, and the acetone layer, and is given by:

$$C_F = \frac{\varepsilon_o A}{\frac{d_{ox}}{\varepsilon_{ox}} + \frac{d_A}{\varepsilon_A}} \quad \ldots \quad 4.20$$

which gives

$$C_F \simeq 3.5 \text{ nF}$$

where the relative permittivity of acetone ε_A is ~ 1. The above simple analysis gives an approximate decrease in capacitance by a factor of ~ 5, if 5 Å of pure acetone was incorporated. In fact, a more probable situation would be envisaged where monolayers consisted partly of water, which would lead to a slightly larger final capacitance by virtue of the fact that the relative permittivity of water, ε_W, is rather high (~ 80). For example, if instead of 5 Å of pure acetone, 2½ Å of acetone, and 2½ Å water were naively incorporated, and again the final capacitance was considered as a series sum of capacitances due to oxide, water, and acetone, then C_F is given by:

$$C_F = \frac{\varepsilon_o A}{\frac{d_{ox}}{\varepsilon_{ox}} + \frac{d_A}{\varepsilon_A} + \frac{d_W}{\varepsilon_W}} \quad \ldots \quad 4.21$$

where d_W is the thickness of the water layer. This expression gives a final capacitance

$$C_F \simeq 5.9 \text{ nF}$$

which more closely resembles the experimental values of ~ 9 nF. Allowing for the fact that the junction areas are accurate to $\sim \pm 5\%$, and that capacitance measurements on the bridge are at best $\sim \pm 20\%$, then it would appear that the above capacitance data are in fairly good agreement with the predicted incremental thicknesses due to the model.

4.4.4 Model Conductance-time Data, and Comparison with Experimental G-t Plots

In order to illustrate the effect of varying the parameters M (successive monolayer thickness), and Φ (mean barrier height) on the model junction conductance, graphical outputs from the program described in Section 4.2.3 are shown in Figs.4.12, 4.12a, 4.13, and 4.13a.

Figs.4.12 and 4.12a correspond to the infusion of five monolayers of pure water having set L = M = 1 Å, and with Φ = 1, and Φ = 2 eV respectively. Figs. 4.13 and 4.13a represent the infusion of an initial monolayer of water, followed by the infusion of four consecutive monolayers of acetone, i.e. L = 1, M = 2 Å, again with Φ = 1, and Φ = 2 eV respectively. Region A, corresponding to the time taken for molecules to penetrate the Pb electrode has been omitted from all figures.

4.4.4.1 Water

Figures 4.12 and 4.12a illustrate that when Φ is increased from 1 to 2 eV in the model, the net effect is essentially to steepen the initial (negative) slope g_1' (t) of region B. The differences between successive slopes g_2' (t) to g_5' (t) also becomes more difficult to detect visually. It is noticed that for both figures that from the end of the third monolayer (region C) onwards the discontinuities between regions become increasingly less distinct, and hence difficult to localize as a consequence of the magnitudes of the slopes rapidly tending towards a value of zero.

If one compares the above model G-t plots with the experimental data for water (Figs.4.8b, and 4.9b), then to a first approximation, the of Φ = eV rather than Φ = 1 eV would appear to more closely resemble the general form of the G-t plot. A closer inspection of the ratios between successive slopes g_n' (t)/g_{n+1}' (t) for model, and experimental data are

Fig.4.12

Model g-t plot for water. The first monolayer thickness L, and successive monolayer thickness, M, have both been set to 1 Å (the approximate value for adsorbed water). An arbitrary value of 10 units has been chosen for t_m, the time taken to grow each monolayer, and the mean barrier height, Φ , was assumed to be 1 eV. Regions B to F and corresponding slopes g_1' (t), to g_5' (t) are also indicated. Region A corresponding to the time required to penetrate the Pb electrode has been ommitted.

Fig.4.12a

As Fig.4.12, but has been set to 2 eV, which increases the rate at which the values of the slopes g_n' (t) tends towards zero.

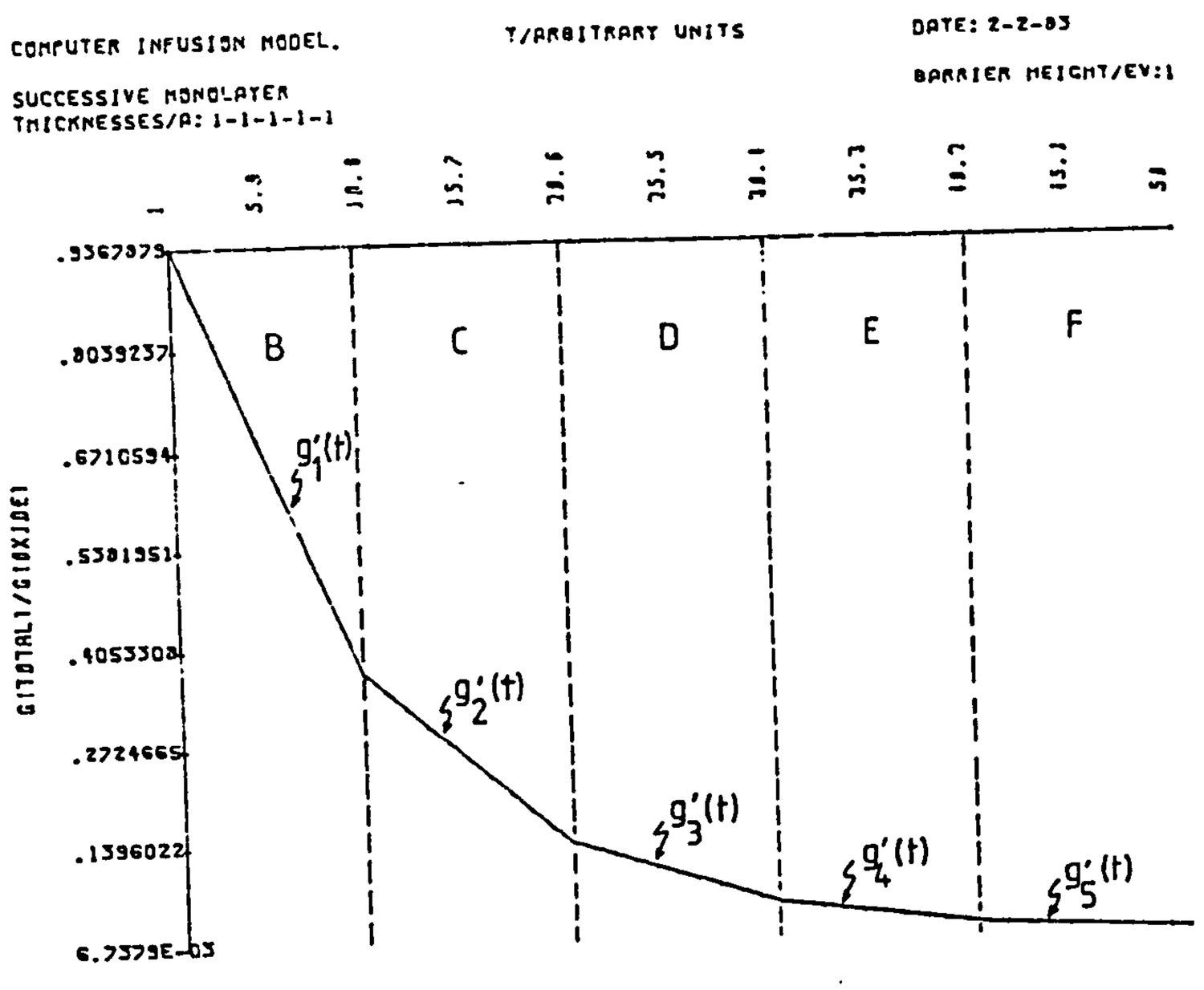
COMPUTER INFUSION MODEL.
SUCCESSIVE MONOLAYER THICKNESSES/A: 1-1-1-1-1
T/ARBITRARY UNITS
DATE: 2-2-83
BARRIER HEIGHT/EV:1
1
5.9
10.8
15.7
20.6
25.5
30.1
35.3
10.2
15.1
50
.9367079
.8039257
.6710594
.5381951
.4053308
.2724665
.1396022
6.7579E-03
G(TOTAL)/G(0)X10E1
B
C
D
E
F
$g_1'(t)$
$g_2'(t)$
$g_3'(t)$
$g_4'(t)$
$g_5'(t)$

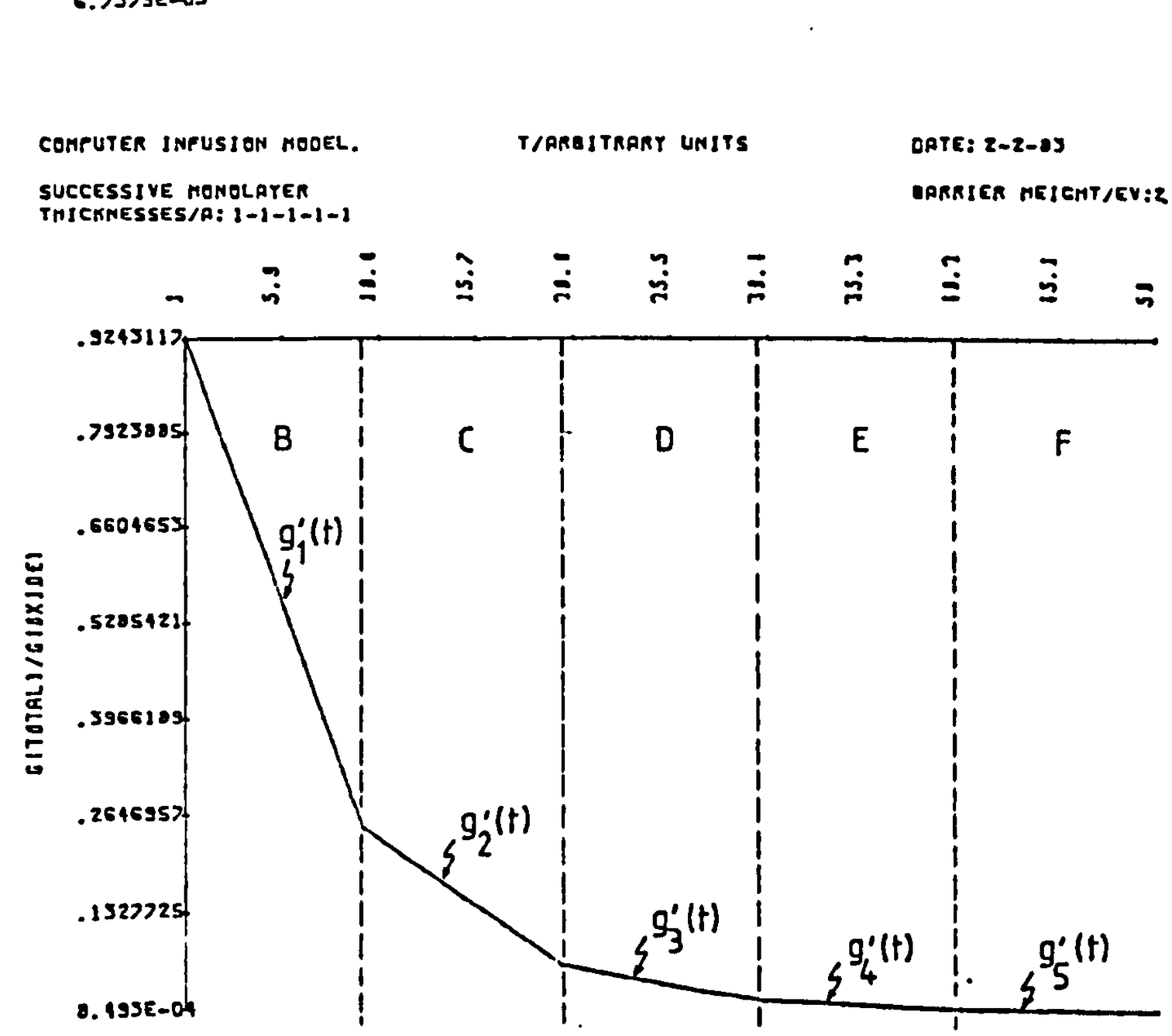
COMPUTER INFUSION MODEL.
SUCCESSIVE MONOLAYER THICKNESSES/A: 1-1-1-1-1
T/ARBITRARY UNITS
DATE: 2-2-83
BARRIER HEIGHT/EV:2
1
5.9
10.8
15.7
20.6
25.5
30.1
35.3
10.2
15.1
50
.9243117
.7923885
.6604653
.5285421
.3966189
.2646957
.1327725
8.495E-04
G(TOTAL)/G(0)X10E1
B
C
D
E
F
$g_1'(t)$
$g_2'(t)$
$g_3'(t)$
$g_4'(t)$
$g_5'(t)$

Table 4.7 - Comparison of the ratios of slopes $g_n'(t)/g_{n+1}'(t)$ for model and experimental conductance-time data for water.

n	$\frac{g_n'(t)}{g_{n+1}'(t)}$			
	Model L = M = 1 Å		Experimental data	
	Φ= 1 eV	Φ= 2 eV	INFDATA22	INFDATA24
1	e(2.718)	$e^{\sqrt{2}} \simeq 4.113$	1.6	3.7
2	2.718	4.113	4.8	12.7
3	2.718	4.113	12.4	-
4				

are given in Table 4.7. These data also suggest that a barrier height of $\Phi \simeq 2$ eV in the model would perhaps give a better fit to the experimental data. Model, and experimental data for the ratios of slopes agree to within an order of magnitude.

4.4.4.2 Acetone

From Figs.4.13, and 4.13a, it becomes apparent that if the successive monolayer thickness, M, is increased to 2 Å, the differences in slope between regions become more pronounced, and the conductance falls more rapidly than for the model values for water, particularly during regions B, and C. As Φ is increased from 1, to 2 eV, this fall in conductance becomes even more exaggerated in these regions. In Fig.4.13a for example, with $\Phi = 2$ eV, it is difficult to locate the discontinuities in slope after the end of the third monolayer growth (region D).

The ratios between successive slopes, $g'_n(t)/g'_{n+i}(t)$ for model, and experimental data are given in Table 4.8. The data would appear to be in better agreement than those for water just discussed. If one considers the experimental G-t plots for acetone it is observed that the regions of different slope do appear to be more well defined as predicted by the mode, and consequently slightly easier to measure (at least for regions B, and C as mentioned above). Generally speaking, as larger molecules are infused, there is a propensity for the differences in slope to become greater, allowing the magnitudes of the slopes, and discontinuities between slopes to be more easily estimated. This phenomenon would partly explain the larger errors experienced when analysing data for water; since the G-t plots are much smoother, discontinuities between regions of different slopes are less well defined, consequently precluding accurate estimates of the magnitudes of the slopes.

Fig.4.13

Model g-t plot for acetone. The first (hydroxyl) monolayer thickness, L, has been set to 1 Å, and successive (acetone) monolayer thickness, M, set to 2 Å. A value of ten arbitrary units has again been chosen for t_m the time taken to grow each monolayer. The mean barrier height, Φ , was assumed to be 1 eV. Regions B to F and corresponding slopes $g_1'(t)$ to $g_5'(t)$ are also indicated. Region A corresponding to the time required to penetrate the Pb electrode has been omitted.

The differences in slope between regions is more pronounced than the corresponding plot for water (Fig.4.12).

Fig.4.13a

As Fig.4.13, but Φ has been set to 2 eV. The values of the slopes $g_n'(t)$ now rapidly tend towards zero, and discontinuities beyond region D therefore become progressively more difficult to detect.

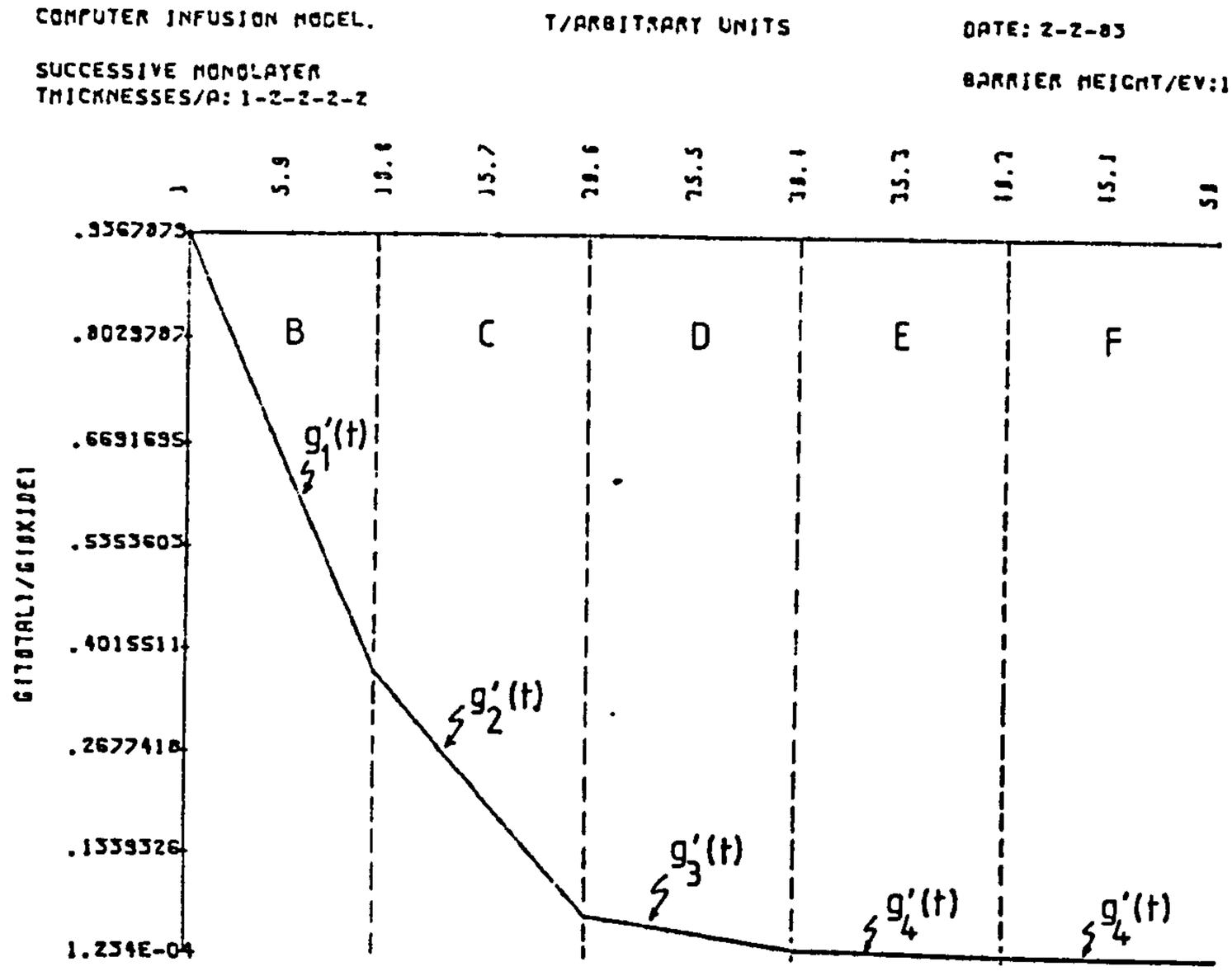
COMPUTER INFUSION MODEL.
T/ARBITRARY UNITS
DATE: 2-2-83
SUCCESSIVE MONOLAYER
THICKNESSES/A: 1-2-2-2-2
BARRIER HEIGHT/EV:1
1
5.9
18.8
15.7
28.8
25.5
38.1
35.3
18.2
15.1
58
.9367875
.8029787
.6691695
.5353603
.4015511
.2677418
.1339326
1.234E-04
GITOTAL1/G18X10E1
B
C
D
E
F
g'1(t)
g'2(t)
g'3(t)
g'4(t)
g'4(t)

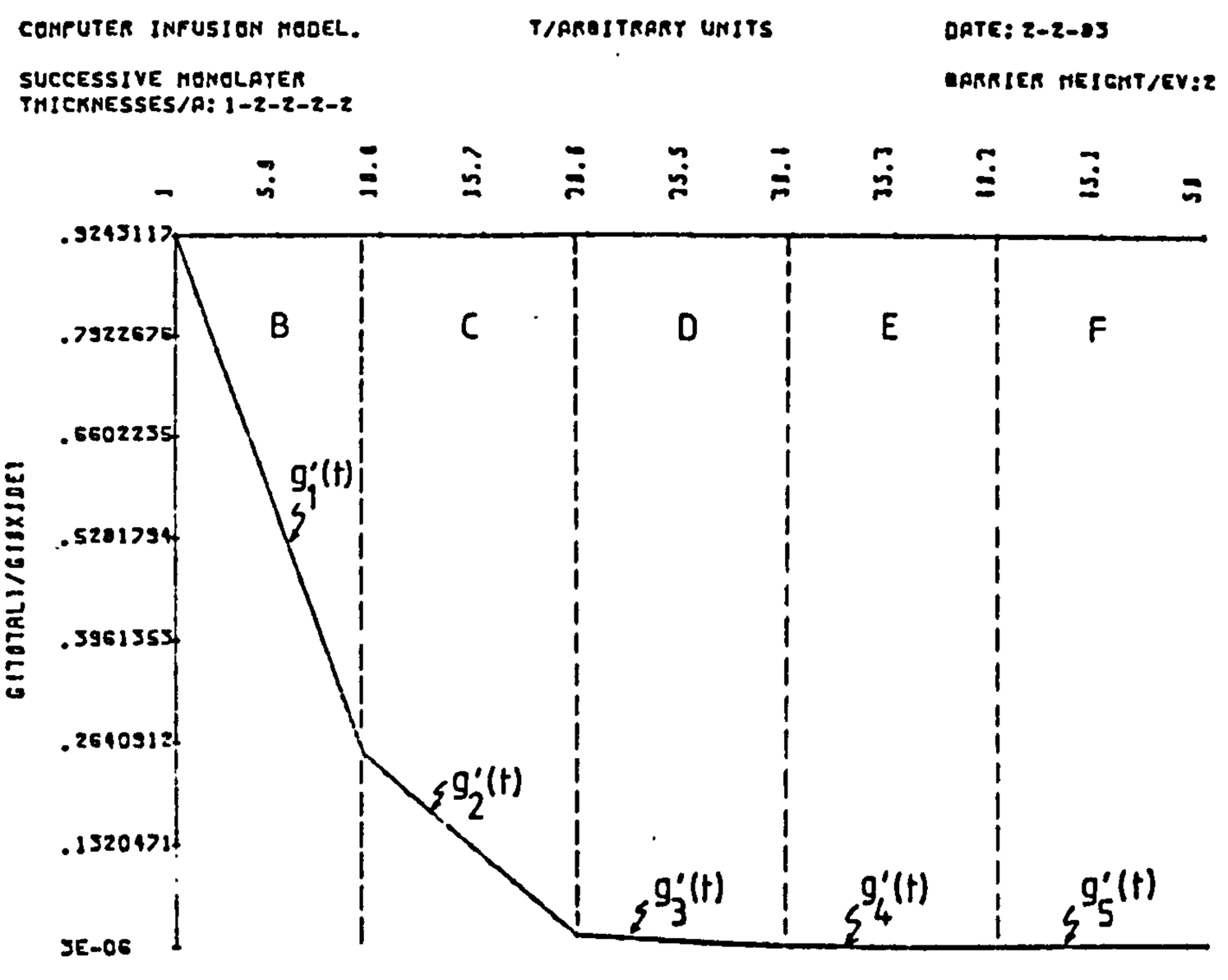
COMPUTER INFUSION MODEL.
T/ARBITRARY UNITS
DATE: 2-2-83
SUCCESSIVE MONOLAYER
THICKNESSES/A: 1-2-2-2-2
BARRIER HEIGHT/EV:2
1
5.9
18.8
15.7
28.8
25.5
38.1
35.3
18.2
15.1
58
.9243117
.7922676
.6602235
.5281794
.3961353
.2640912
.1320471
3E-06
GITOTAL1/G18X10E1
B
C
D
E
F
g'1(t)
g'2(t)
g'3(t)
g'4(t)
g'5(t)

As an example of this phenomenon, Fig.4.3a, and 4.3b show model g-t plots where L = 1 Å, and M = 3 Å (corresponding to a larger molecule) with Φ = 1, and Φ = 2 eV respectively. The difference in slope between regions B and C is now much greater, but the magnitudes of the slopes also tend to zero much more rapidly than for smaller molecules.

4.4.5 IET Spectra

It has been suggested that the first monolayer deposited in an infusion doping experiment corresponds to the formation of a hydroxyl ion coverage of the oxide surface(4). Subsequent monolayers, comprised mainly of dopant molecules are then deposited. In the model thus-far described, region B represents the hydroxyl ion coverage, and regions C onward the formation of dopant monolayers. In order to demonstrate the validity of this model, IET spectra were recorded for a 50% v/v solution of acetone/ water having terminated the infusion process towards the ends of regions B, and C. Termination was achieved by the re-introduction of a controlled flow of N_2 within the doping chamber as described in 4.3.2.

Figure 4.14a shows the resulting IET spectrum when infusion was arrested in region B. The final junction resistance ($\sim$ 20 Ω), and sensitivity on our spectrometer are indicative of fractional monolayer coverage at this stage. Further, it is observed that the spectral features suggest that a limited surface coverage of acetone is present at this stage.

Figure 4.14b shows a strong spectrum of acetone, in this case obtained by arresting infusion towards the end of region C. The junction resistance ($\sim$ 150 Ω), and spectral sensitivity now offer clear evidence for the presence of acetone at near-monolayer coverage.

In further support of the assertion that region C corresponds to

Table 4.8 - Comparison of the ratios of slopes $g_n'(t)/g_{n+1}'(t)$ for model, and experiments conductance-time data for acetone.

n	$\frac{g_n'(t)}{g_{n+1}'(t)}$			
	Model L=1Å, M=2Å		Experimental data	
	Φ = 1 eV	Φ = 2 eV	INFDATA23	INFDATA25
1	1.987	3.309	1.9	3.4
2	7.389	16.919	6.8	15.5
3				

Fig.4.14a

Weak infusion doped IET spectrum of acetone. The spectrum was obtained having terminated infusion towards the end of region B of the corresponding G-t plot (see Figs.4.10 and 4.11b). This was achieved by "flushing" the infusion chamber with N_2.

Fig.4.14b

Strong infusion doped IET spectrum of acetone obtained by termination infusion towards the end of region C. These spectra offer good evidence that region B corresponds to hydroxyl ion coverage of the oxide, and that region C is due to the formation of a predominantly acetone monolayer.

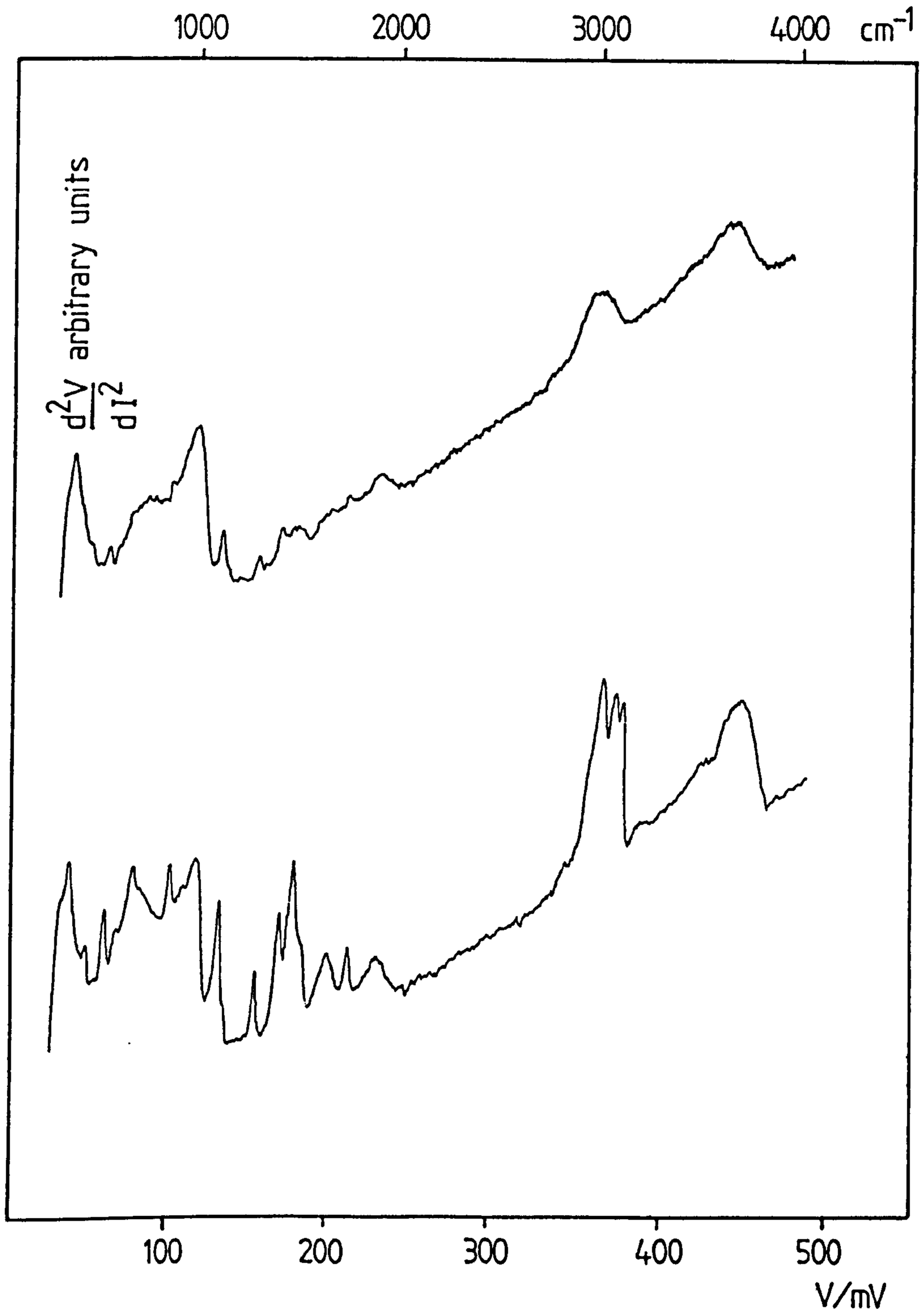
1000
2000
3000
4000
cm^{-1}
$\frac{d^2V}{dI^2}$ arbitrary units
100
200
300
400
500
V/mV

Fig.4.15

Strong IET spectrum of phenol obtained by terminating infusion towards the end of region C on the corresponding G-t plot. Final junction resistance ∿ 200 Ω.

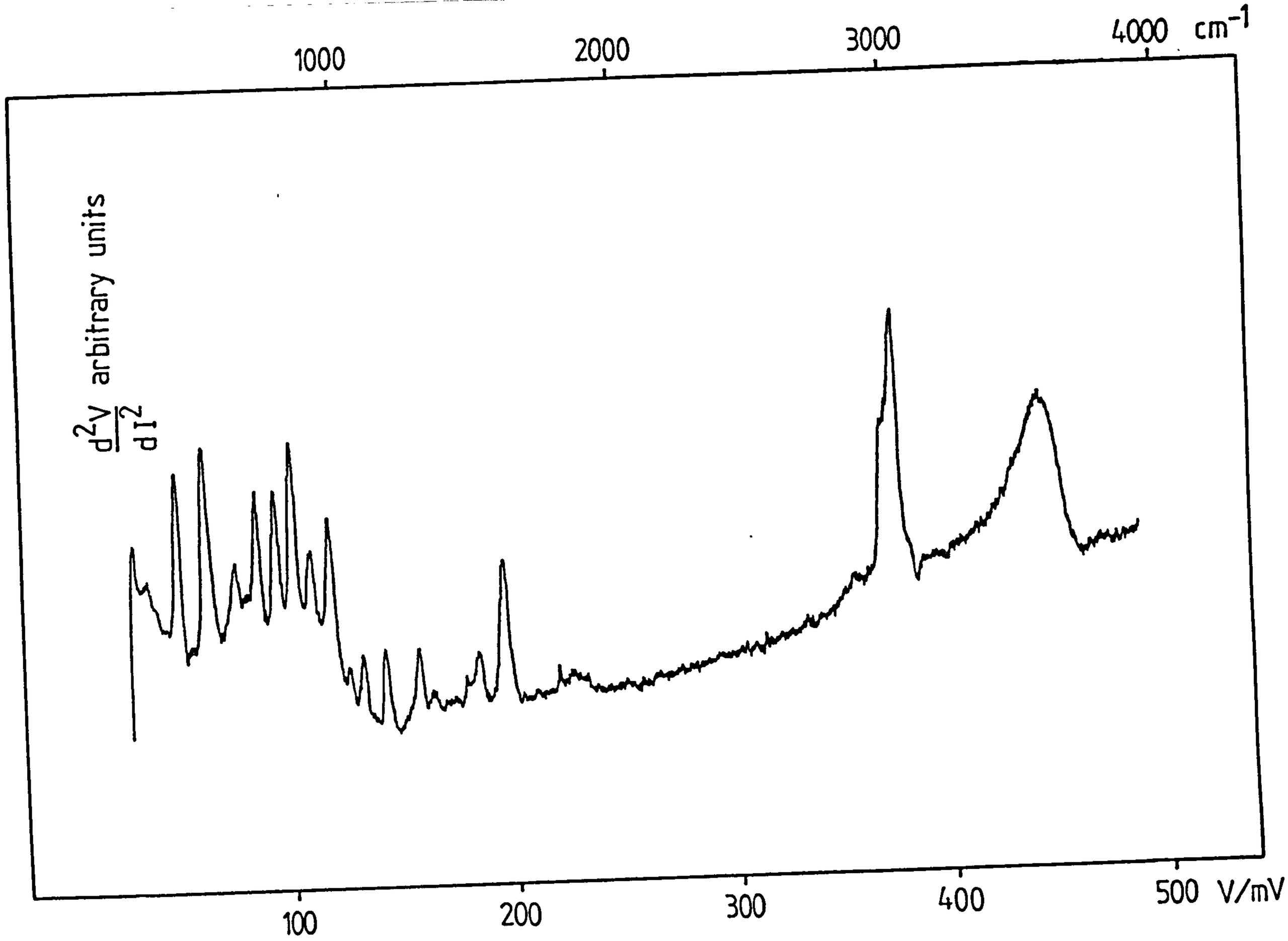
1000
2000
3000
4000 cm⁻¹
d²V/dI² arbitrary units
100
200
300
400
500 V/mV

Fig.4.16

Strong spectrum of propan-2-ol also obtained by terminating infusion towards the end of region C. These spectra offer further evidence to suggest that region C corresponds to the formation of a monolayer comprised mainly of dopant molecules. Final junction resistance ~ 150 Ω.

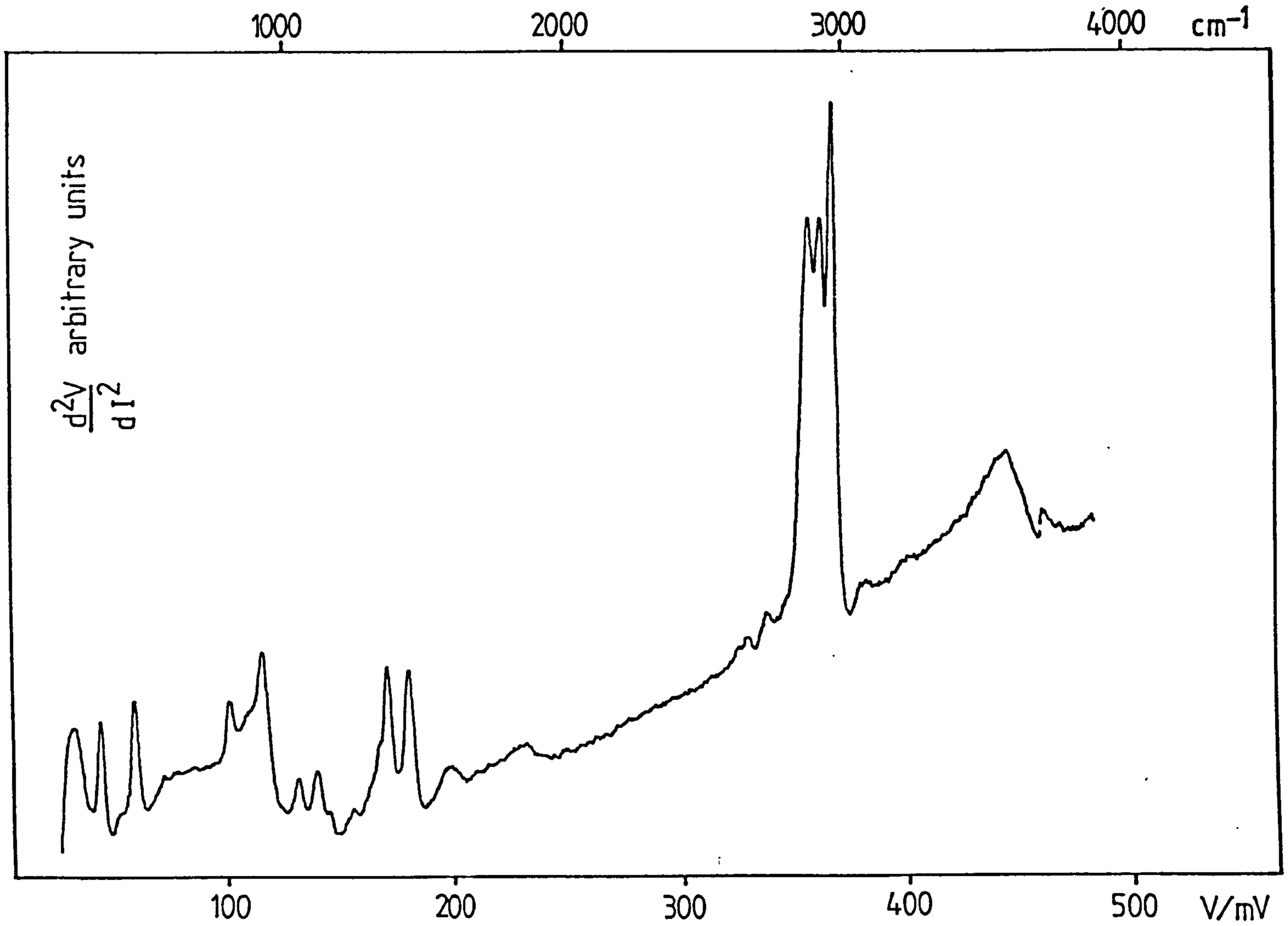
1000
2000
3000
4000
cm⁻¹
$\frac{d^2V}{dI^2}$ arbitrary units
100
200
300
400
500
V/mV

the formation of a predominantly dopant monolayer, Figs.4.15 and 4.16 show strong IET spectra for phenol, and propan-2-ol. Both spectra were obtained by terminating infusion towards the end of region C, and have junction resistances of the order one would expect due to near-monolayer coverage of dopant on the oxide.

It is interesting to note that the resulting IET spectra obtained after proportedly infusion doping with a 50% v/v mixture of 4-methylpentan-2-one in water was very noisy, of poor overall quality, and revealed evidence of adsorbed OH moities only. It would seem that the presence of water does not afford any enhancement in mobility of the fairly large ketone molecules. The observed changes in junction conductance during doping (not presented here) were primarily due to the penetration of the Pb electrode by water vapour, with subsequent formation of hydroxyl monolayers on the Aℓ-oxide surface. Again, this highlights that the role of water in the infusion process is as yet not well understood.

4.5 CONCLUSIONS

A simple apparatus has been developed with which contamination-free infusion doped IET junctions may be obtained routinely. By employing an inert gas (e.g. N_2) to purge the infusion chamber prior to doping, atmospheric CO_2 is excluded; this has effectively minimised formic acid contamination. Another function of the N_2 is to afford some degree of control over the rate of infusion, and additionally it may also be used to reverse the infusion process. Rapid and accurate junction conductance data have been conveniently monitored in situ during infusion by means of a DMM interfaced to a microcomputer. These conductance data in conjunction with junction capacitance measurements have evidenced an increase in thickness of the insulating barrier. The increases are attributed to the formation of successive monolayers of dopant molecules on the Aℓ-oxide surface. IET spectra have been recorded which suggest that the first monolayers consists mainly of mobile hydroxyl ions which have formed a coverage on the oxide, and that subsequent monolayers are comprised primarily of dopant molecules. The full role of water vapour in the infusion process is not yet fully understood, suffice is to say that its presence appears to be essential and has the propensity to increase dopant mobility. It would be interesting to investigate the possibility of utilizing other polar solvents to aid infusion. To date IET spectra have only been obtained for compounds which are miscible in water; this has precluded a variety of compounds (e.g. monomers) from being successfully infused.

A simple model of sequential monolayer growth have been proposed, which to a first approximation is in fairly good agreement with the experimental data. As predicted by this model, some structure was discernible in the experimental G-t plots for water and acetone which is

indicative of sequential growth. Certain refinements to the model might prove useful in a further analysis of infusion doping data. For example, it is believed that dopant molecules diffuse through the Pb electrode grain boundaries and subsequently migrate to free adsorption sites on the Aℓ-oxide surface; a non-linear time dependence (e.g. $t^{\frac{1}{2}}$) may be more appropriate under these circumstances. Also, effects due to the probable variations in barrier parameters during infusion might be considered.

REFERENCES - Chapter 4

1. R.C.Jaklevic and M.R.Gaerttner. Appl. Phys. Lett., 30(12), 646 (1977).

2. R.C.Jaklevic and M.R.Gaerttner. Applications. Surf. Sci., 1, 479 (1978).

3. Tunnelling Spectroscopy, Capabilities, Applications, and New Techniques - Chapter 15. P.K.Hansma (Ed.)., Plenum Press, New York (1982).

4. W.J.Nelson, D.G.Walmsley and J.M.Bell. Thin Solid Films, 79, 229 (1981).

5. R.R.Mallik, R.G.Pritchard, D.P.Oxley, C.C.Horley and J.Comyn. Thin Solid Films, 112, 193 (1984).

6. W.F.Brinkman, R.C.Dynes and J.M.Rowell. J. Appl. Phys., 41(5), 1915 (1970).

7. Tunnelling Phenomena in Solids. E.Burstein and S.Lundqvist (Eds.), Chapter 3, Plenum Press, New York (1969).

8. J.G.Simmons. J. Phys. D., 4, 613 (1971).

9. Inelastic Electron Tunnelling Spectroscopy. Proceedings of the International Conference and Symposium on Electron Tunnelling. T.Wolfram (Ed.), pp.193-201, Springer-Verlag, New York (1978).

CHAPTER 5

A STUDY OF THE ADSORPTION OF SOME POLYMERS ON Aℓ-OXIDE BY LIQUID-PHASE DOPING OF IET JUNCTIONS

5.1 INTRODUCTION

Considerable attention has recently been given to the investigation of the adsorption of compounds used as adhesives or adhesion promoters on Aℓ-oxides by IETS. Interest in this field has arisen largely because aluminium is a widely studied, and commercially important material used for adhesive bonding (1). Other workers have utilized IETS to investigate the adsorption of epoxides and their mixtures with aliphatic amines (2), cyanoacrylates (3), and silane coupling agents (4). However, none of these incorporated polymers directly into IET junctions, although in some cases small molecules were used which then polymerized at the oxide surface. Large biological molecules have been successfully liquid-phase doped and their IET spectra recorded (5,6), but to the best of the author's knowledge little or no work in the literature has been addressed to the incorporation of synthetic polymers into IET junctions. It was therefore considered both timely and appropriate that the adsorption of certain polymers (some of which are of interest in the field of adhesion) should be investigated by IETS. It is now fairly well established that IETS in conjunction with other spectroscopic techniques is a powerful tool for investigating the adsorption of small molecules on Aℓ-oxide. The present work, some of which has been published (7), demonstrates that IETS is also useful for examining the adsorption of much larger molecules. It should be emphasized from the outset that it is impossible to resolve all the vibrational modes of molecules having greater than 100 atoms or so (8); the IET spectra of polymers presented here are believed to reflect the nature of adsorption due to interactions between specific segments of the polymers (e.g. reactive side groups) and adsorption sites on the oxide surface (9).

Comparison between IET and bulk IR spectral data for a few ester based, and water soluble polymers has given valuable insight regarding their adsorption on Aℓ-oxide at a monomolecular level. Both commercially available polymers and those synthesized in the author's laboratory have been studied including:

(1) Polyvinylacetate (PVA)

(2) Polymethylmethacrylate (PMMA)

(3) Polyvinylalcohol (PVOH)

(4) Polyethyleneglycol (PEG)

(5) Polyethylene oxide (PEOX)

(6) Methylcellulose (MeC)

(7) Polyacrylamide (PAAM)

An obvious advantage of synthesizing ones own polymers is that it ensures an ab initio knowledge of their composition and structure. For example, depending upon the polymerization methods adopted, a degree of control may be afforded over the product's molecular weight and tacticity (10,11). It is believed that both of those may influence adsorption on the oxide surface, and their independent and combined effects will be briefly discussed in 5.2.4.1.

An important technological process widely used for the preparation of many commercially available acrylic polymers, and various co-polymers is the emulsion method (10). Two serious drawbacks of this method as far as IETS is concerned are that the possible sources of contamination are numerous, and also that molecular weight control can be difficult. The precautions adopted to avoid contamination in IETS, described in Chapter 3, apply equally during polymer synetheses in the present chapter, and are emphasized again in this content. Polymers were prepared by solution polymerization (10,11), and where possible their molecular weights were

controlled by utilizing chain transfer agents (10,12). Some of the polymers were characterized by IR spectroscopy, and their molecular weights determined by gel-permeation chromatography (GPC) and viscometry.

Polymeric adsorption on the Aℓ-oxide surface may be partly understood by examining IETS data of respective monomers amd/or telomers. These data may then be extrapolated, allowing plausible adsorption mechanisms for the corresponding polymers to be proposed. Of course, the former data may not necessarily reflect the behaviour of the polymer as a whole. For example, theoretical calculations describing the configurational behaviour of adsorbed polymer molecules have been performed in which factors such as chain structure (e.g. branched or straight), polymer-solvent and polymer-surface interactions were taken into account (9). It was suggested that the polymers were adsorbed by interactions between specific segments of the polymers (e.g. reactive side groups) and adsorption sites on the surface. Some of these interactions may be sterically inhibited due to the helical nature of an unperturbed polymer chain. It was also proposed that polymers were adsorbed in a tail-[train-loop]$_n$-tail configuration rather like a piece of spaggetti randomly thrown onto a surface as indicated schematically in Fig.5.1. Adsorption occurs as a result of interactions between the "train" segments of the chain and potential adsorption sites on the surface. Other workers have argued that sub-monolayer ester polymer films deposited on inorganic substrates from solution are adsorbed primarily due to interactions between the basic polymer side groups, and acidic sites in the substrate surface. Dipole-dipole interactions were found to be negligible compared with these acid-base interactions (13). Solvent pH relative to that of the polymer was also found to effect the adsorption process be effectively promoting competition between solvent, and polymer molecules for free adsorption sites.

Fig. 5.1

Schematic representation of a polymer chain adsorbed on a surface in a tail-[train-loop]$_n$-tail configuration after Lal and Stepto (9). Adsorption occurs as a result of interactions between the "train" segments of the chain and potential adsorption sites on the oxide.

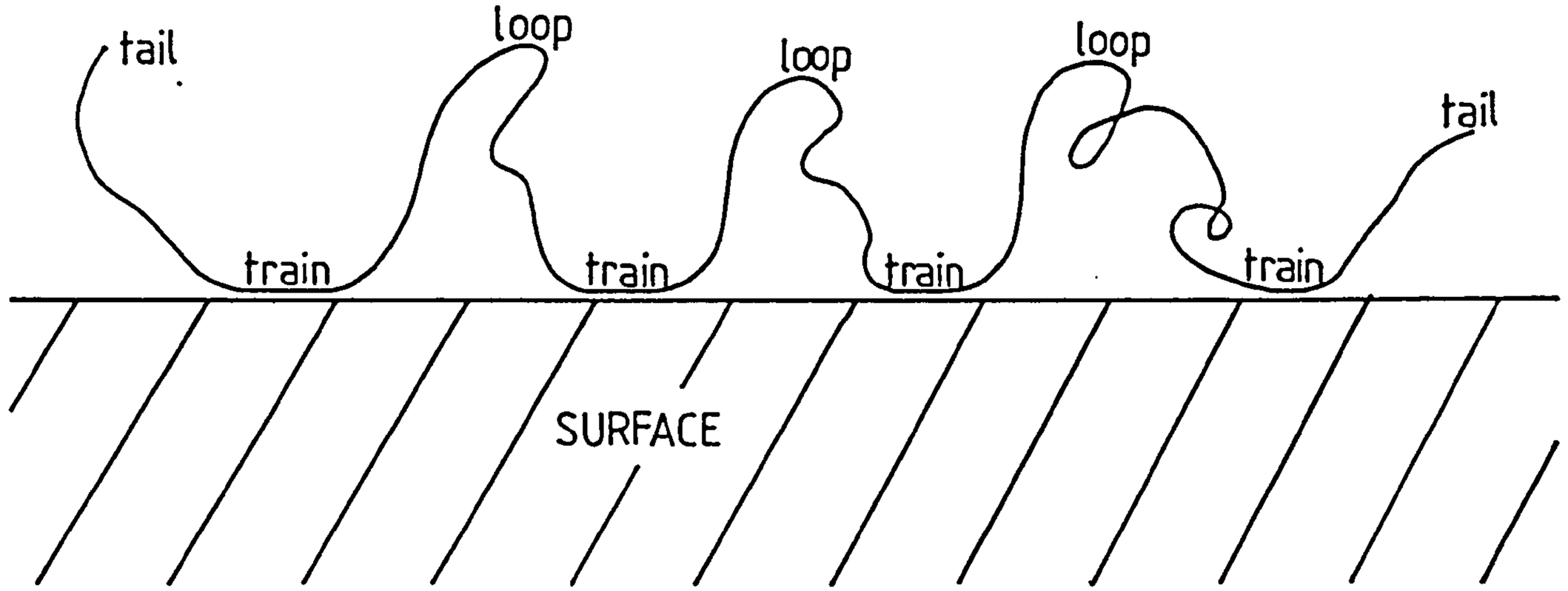
tail
loop
loop
loop
tail
train
train
train
train
SURFACE

An FTIR study of thin (∿ 10 Å) Polyacrylic acid (PAA) films adsorbed on Aℓ-oxide has shown that acid-base reactions of the type mentioned above do indeed prevail at a monomolecular level (14). Clear spectral evidence suggested that the acrylic acid side groups of the polymer interacted with basic sites on the oxide surface; a marked reduction in intensity of the PAA carbonyl peak was observed together with the appearance of two new peaks due to the symmetric, and asymmetric stretching vibrations of the carboxylate anion. These features indicated that the acid side groups dissociated at the surface, leading to the adsorption of the polymer by the formation of a bidentate symmetrical bridging complex between the carboxylate anions of the polymer, and Aℓ cations of the oxide surface. Free water produced as a reaction by-product due to the recombination of protons and hydroxyl groups then desorbs from the surface leading to a slight decrease in intensity of the OH stretching vibration (15). These findings were also in good agreement with previous IETS data for the acrylic acid monomer on Aℓ-oxide (16), although it should be mentioned that the decrease in intensity of the OH mode is difficult to verify quantitatively due to its somewhat variable and broad nature.

The IET and IR spectral data presented in this chapter offer strong evidence to suggest that the polymers with ester bearing side groups also undergo what is essentially acid-, and/or base-catalysed hydrolysis at the Aℓ-oxide surface leading to their subsequent adsorption. The amphoteric oxide surface is believed to play a crucial role in the hydrolysis behaving as a catalyst for the reaction. Data obtained for PVA, and PMMA will be discussed in some detail.

The adsorption of the water-soluble polymers is not well understood, although tentative IET spectral evidence may suggest that PVOH is adsorbed by the formation of an Aℓ-O-C monodentate bridge between the polymer and

the oxide surface, similar to the adsorption of ethanol on Aℓ-oxide at room temperature (17, 18). Another plausible adsorption mechanism for these water soluble polymers is that of hydrogen bonding between polar constituents of their side groups (which are predominantly -OH) and surface hydroxyls on the oxide (19-22). Again it is emphasized that since the OH stretching vibration is generally broad and of variable intensity it is difficult to draw any firm conclusions regarding the nature of such bonding. Hydrogen bonding may also play a minor role in the adsorption of the ester polymers. For example, it will be seen that in addition to the reduced intensity of the IETS ester carbonyl vibrations they also exhibit slight downshifts relative to their bulk IR values. In IETS and reflectance IR studies of the adsorption of ethyl cyanoacrylates on Aℓ-oxide (2,23), other workers have attributed such shifts to hydrogen bonding between the carbonyl group and surface hydroxyls. It is reasonable to infer that a similar mechanism applies for the ester based polymers.

5.2 EXPERIMENTAL DETAILS

Standard experimental procedures adopted for liquid-phase doping of IET junctions have been fully described in Chapter 3. The majority of the present section is devoted to polymer syntheses, and factors affecting the choice of solvents for these polymers for their subsequent IETS analyses.

5.2.1 Synthesis of Atactic PVA

PVA was prepared by free radical addition (FRA) polymerization in solution. It is convenient at this point to outline the generalized 3 stage sequence of events during such polymerization (a more thorough treatment may be found in reference 10).

(1) Initiation. A free radical is generated usually as a result of the homolytic fission of an initiator molecule, e.g. azobisisobutyronitrile (AZBN). The radical is then transferred to a monomer unit thus completing the first step of the polymerization as shown below.

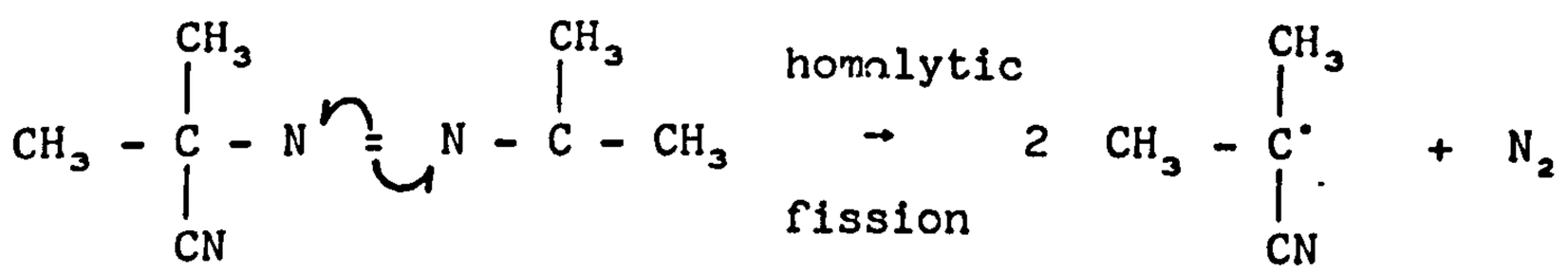

Let 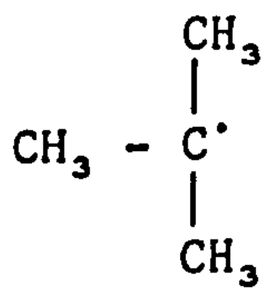 ≡ $I^{\cdot}$

Then $I^{\cdot} + M \xrightarrow[\text{transfer}]{\text{radical}} IM^{\cdot}$

(2) Chain Growth. Subsequent monomer units are added to produce a growing polymer chain.

$$IM^{\cdot} + M \longrightarrow IMM^{\cdot}$$

or in general, the radical is transferred along the growing chain and thus behaves as its active centre in the following manner

$$IM^{\cdot}_{n-1} + M \longrightarrow IM_n^{\cdot}$$

where n is the total number of monomer units.

(3) Termination. One way in which FRA polymerization may terminate is when two active centres collide. Interruption of chain growth may also occur if the active centre is transferred to another species known as a chain transfer agent (CTA). This is shown below:

$$\sim\sim M_n^{\cdot} + XY \rightarrow \sim\sim M_n + Y^{\cdot}$$

Here XY is the CTA.

Several species may behave as CTA's, alkyl thiols are commonly used although other monomers, polymers, solvents and initiators can also act in this manner. Clearly in the present work (solution polymerization) solvents are the most convenient CTA's and the factors affecting the choice of solvents are now briefly discussed.

The effect of chain transfer on the number average degree of polymerization, $\bar{x}_n$, may be estimated by considering all transfer processes leading to an expression known as the Mayo equation (10). If transfer is assumed to be primarily to the solvent molecules then the simplified Mayo equation is given by:

$$\frac{1}{\bar{x}_n} = \frac{1}{(\bar{x}_n)_o} + C_s\frac{[S]}{[M]} \qquad \ldots \quad 5.1$$

where $(\bar{x}_n)_o$ = number average degree of polymerization without CTA

C_s = chain transfer constant (to solvent in this case)

[S] = solvent concnetration

[M] = monomer concentration

$(\bar{x}_n)_o$ is independent of the solvent chosen and approximately constant, therefore $\bar{x}_n$ will be determined by the second term on the RHS of equation 5.1 The first factor in this term, C_s, varies quite considerably from solvent to solvent, and is temperature dependent (10,12). Usually, solvents are chosen whose C_s values are such that the ratio of solvent to monomer concentrations [S]/[M], will be of the order unity for the required $\bar{x}_n$. This is desirable experimentally since it ensures that slight inaccuracies in the measurements of [S], and [M] will not result in large deviations from the required $\bar{x}_n$. Consequently, two suitable solvents, namely acetone and toluene were decided upon for the solution polymerization of vinyl acetate. Now, from equation 5.1, the [S]/[M] ratio is given by:

$$\frac{[S]}{[M]} = \frac{1}{C_s}\left(\frac{1}{\bar{x}_n} - \frac{1}{(\bar{x}_n)_o}\right) \quad \ldots \quad (5.1a)$$

Commercially available PVA samples typically have molecular weights varying from 20,000 to 500,000; for a sample of fairly low molecular weight say 86,000 for convenience, the required $\bar{x}_n$ will be 1000. Inserting this $\bar{x}_n$ into the above expression with an $(\bar{x}_n)_o$ of $7 \times 10^{+3}$, and C_s values of $\sim 1.7 \times 10^{-4}$ and $\sim 34 \times 10^{-4}$ (both at $60^{o}C$) for acetone and toluene respectively (12) yields [S]/[M] ratios of ~ 0.82 and ~ 0.28.

The normal experimental procedure was to place the correct ratio of spectrograde solvent, and redistilled monomer into a quickfit flask with a small amount of initiator. This solution was then maintained at a temperature of $\sim 60\text{-}65^{o}C$ by means of a water bath and under reflux

conditions for approximately 5 hours over which period the polymerization occurs. Typical quantities of reagents used were:

10 cm^3 vinyl acetate monomer

8 cm^3 acetone

$\sim$ 0.13 g initiator (AZBN)*

The final solution was a somewhat viscous clear liquid. The PVA was precipitatated out by adding a non-solvent (e.g. methanol) and shaking vigourously; it was then thoroughly dried on a vacuum line with a liquid N_2 trap containing 13X molecular sieves.

* It is noted that AZBN was chosen as the initiator in preference to the commonly used dibenzoyl peroxide. From the IETS viewpoint the latter is unacceptable since during the initiation process it splits homolytically to give benzoate radicals which may then produce benzoate anions by gaining electrons as indicated below:

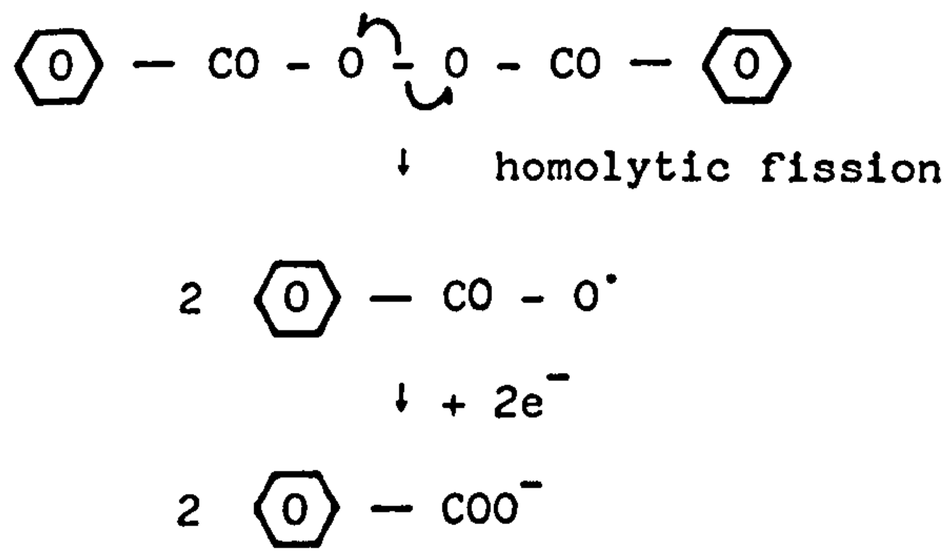

Benzoate anions are known to chemisorb strongly on alumina, (1,24) even at concentrations as low as $\sim$ 0.005% w/v (25) and could mask subsequent IET spectra. Moreover, it will be seen that interpretation of the adsorption of certain polymers in the present work relies upon the presence of spectral features due to the carboxylate anion; clearly this prohibits the use of an initiator which generates such species.

Two method were employed to determine the molecular weight of the product which are summarized below.

(1) Capillary Viscometry

An Ubbelhode (ASTM D.445) viscometer was used to determine the intrinsic viscosity of a PVA/methanol solution at 25°C. For a given polymer-solvent system at a specified temperature, the viscosity-molecular weight relationship is given by the Mark-Houwink equation

$$[\eta] = kM^{\alpha} \quad \ldots \quad (5.2)$$

where $[\eta]$ = intrinsic viscosity of the solution

M = viscosity average molecular weight

k and α are constants for the particular system. The k and α values for PVA in methanol at 25°C are 3.8×10^{-4} cm^3 g^{-1} and 0.59 respectively. An M of 90,000 ± 5,000 was obtained for the PVA sample in fair agreement with the desired 86,000

(2) Gel Permeation Chromatography (GPC)

Chromatograms were run for the author in the School of Chemistry (26) on an Applied Chromatography Systems Ltd., LC750 chromatograph with polystyrene/divinylbenzene spherical particles as the gel packing material. In fact this material is better suited to high molecular weight samples and the GPC results must therefore be viewed as approximate. A solution of PVA in THF of approximate concentration 0.5% w/v was prepared and injected into the sample column of the chromatograph. The resulting spectrum showed the product to have a molecular weight in the range 40-45,000 relative to the polystyrene calibrants, hence this value reasonable agrees with the corresponding viscometry data. It was decided that further molecular weight analyses by viscometry alone would be acceptable.

5.2.1.1 Hydrolysis of Atactic PVA

A simple experiment was performed in an attempt to hydrolyse the PVA to PVOH. Approximately one or two hundred grams of PVA and a KOH pellet (catalyst for the hydrolysis) were placed in a flask and boiled in methanol for several hours. The temperature was maintained at $\sim 85^{o}C$ by means of a water bath, and reflux conditions were employed. A milky solution was obtained from which a polymer was precipitated out in THF, and then vacuum dried. Unfortunately a fairly strong carbonyl peak was present in the IR spectrum of the product, indicating a low degree of hydrolysis. Nevertheless the resulting polymer was examined by IETS.

5.2.2 Synthesis of Atactic PMMA

PMMA was prepared by FRA polymerization from a suspension in water. The suspending agent was 0.4 g of soluble starch dissolved in 160 cm^3 of boiling distilled water. This was placed in a reaction vessel equipped with a stirrer, and to it 50 cm^3 of redistilled MMA monomer and 2 g of AZBN initiator were added. The resulting mixture was maintained at a temperature of 80-85^{o}C for 30 minutes by means of a water bath. As was the case for PVA, the product was precipitated out by washing in methanol, and then thoroughly dried on a vacuum line. The molecular weight of the product was determined by viscometry from solution in acetone at 25^{o}C. With k, and α values of 7.5×10^{-3} cm^3 g^{-1}, and 0.70 respectively (12) a viscosity average molecular weight of 27,000 ± 5,000 was obtained for the product.

5.2.3 Commercially Available Polymers

Several ester - and water soluble-polymers were investigated. IET spectra of the following are presented:

(1) PVA, supplied by BDH, molecular weight ~ 45,000.

(2) 'Resin W', a PVA emulsion used for bonding wood, supplied by Evode Ltd.

(3) PMMA, supplied by Polymer Laboratories Ltd., a GPC calibrant sample of molecular weight 43,000.

(4) PVOH, supplied by Koch-Light, molecular weight 72,000.

(5) PEG, supplied by BDH, molecular weight ~ 370.

(6) PEOX, supplied by BDH, molecular weight ~ 5×10^6.

(7) MeC, supplied by BDH, molecular weight ~ 100,000.

(8) PAAM, supplied by BDH, molecular weight ~ 5×10^6.

These polymers were used as supplied except for the 'Resin W' which was smeared onto a clean glass plate, and dried under vacuum. IR spectroscopy showed it to be PVA. Its viscosity average molecular weight of 40,000 ± 5,000 was determined by capillary viscometry from solution in methanol at 25°C.

The Koch-Light PVOH (presumably obtained by the hydrolysis of PVA) showed no carbonyl absorption in the IR which indicates a high degree of hydrolysis.

Of the above polymers the adsorption of PVA, PMMA, and PVOH will be discussed in some detail in Section 5.3. On the basis of the IET and IR spectral data it is believed that the other related polymers are adsorbed in an analogous manner. A brief account of these polymers is given.

5.2.4 Solvents and Monomers

Spectrograde solvents were used throughout the present work. All monomers were redistilled to remove any inhibitors or retarders, dried over CaH_2, and then de-gassed by evacuation to ~ 10 m Torr. They were then

sealed, and stored in a refrigerator until required. IETS was employed routinely to check the purity of solvents and monomers; vapour-phase, liquid phase-, and infusion-doping methods were utilized.

(i) Solvents

When IET junctions were liquid- and vapour-phase doped with neat solvents, low junction resistances were obtained. Corresponding spectra showed features one would expect from undoped devices. The most widely used solvent in the present work, namely acetone, was infusion doped from a 50% v/v aqueous solution (see Chapter 4, and Fig.4.14). A spectrum of pure acetone was obtained which compared favourably with those of other workers (27).

(ii) Monomers

Liquid phase doping with neat monomers, and monomers in various solutions (e.g. in acetone, benzene, and toluene at concentrations up to a few tens of % v/v) also resulted in IET junctions with low resistances, and gave blank spectra. Vapour-phase doping produced similar results. All the monomers investigated were water-insoluble; infusion doping with such compounds always proved unsuccessful in the author's laboratory. Details of these infusion doping experiments have been discussed in Chapter 4.

From (i) and (ii) above it is clear that no significant residue is left on the surface after liquid- or vapour-phase doping, and that the chemicals are sufficiently pure for IETS purposes.

5.2.4.1 Choice of Solvents for IETS

The behavour of polymers in solution may be quite complex (13,28-32) and will normally require a consideration of the Gibbs free energy of the system and its components. A detailed thermodynamic analysis is beyond

the requirements of this thesis. Suffice it to say that from the IETS viewpoint interactions between polymer molecules and the solvent media in which they are dissolved are of considerable importance. The conformation of a polymer chain may be partly understood in terms of its tacticity (10). Generally speaking, steric hindrance effects due to the polymer side groups will largely dictate the configuration of the unperturbed polymer chain. It is known that isotactic polymers exist in helical structures, as do syndiotactic polymers; the latter can also have an extended zig-zag structure. Atactic polymers have structures that are intermediate between the other two. For IETS work it is essential that the polymers should not be tightly coiled as will be discussed below. Intuitively, syndiotactic polymers might then be considered the most preferable, but since their syntheses are not usually straightforward atactic polymers were used throughout the present work. It is therefore necessary to choose suitable solvents for these polymers, i.e. ones in which polymer-solvent interactions are both favoured, and numerous leading to the expansion of polymer coils from their unperturbed dimensions (10). It is believed that this expansion will result in a more uniform coverage of polymer molecules on the oxide surface when doped from solution. A uniform coverage is desirable since it increases the number of polymer-surface interactions, and therefore increases the probability of adsorption. Such a coverage is also more conducive to a uniform electron tunnelling cross-section over the whole IET junction leading to good quality IET spectra. Conversely, unsuitable solvents may lead to the formation of isolated polymer clumps (comprising of tightly coiled polymer chains) on the surface which in turn may form potential nucleation sites for further polymer deposition; poor adsorption would be anticipated. A similar problem has also been encountered by other workers on an IETS study of some vapour-phase doped

ethylcyanoacrylates (2). Additionally, since the probability of electron tunnelling decreases exponentially with increasing barrier thickness (33,34 35) the majority of electrons would be expected to traverse the regions between the polymer clumps, as illustrated in Fig.5.2; weak IET spectra would be obtained. It is therefore crucial that appropriate solvents are used for liquid phase doping. Good polymer-solvent compatibility is reflected in the viscosity of the resulting polymer solution. Solvents were chosen on the basis of their α values in the Mark-Houwink equation (equation 5.2). These values lie in the range

$$0.5 \lesssim \alpha \lesssim 0.8$$

where $\alpha = 0.5$ corresponds to a "θ" solvent, and $\alpha = 0.8$ a thermodynamically "good" solvent, i.e. one which leads to the uncoiling described above (10). Acetone and benzene were both used in the present work; corresponding α values for the polymers used are given in the results and discussion section. k and α values for a wider range of polymers in solution can be found in reference 12.

Slight shifts in peak position and intensity have been observed by the author when liquid-phase doping with polymers from different solvents. Discrepancies of this nature may well be attributable to polymer-solvent interactions. These findings are discussed in Section 5.3.

5.2.5 IET Spectra of Polymers

Spectra of adsorbed polymers were obtained by the liquid-phase doping technique described in Chapter 3. Doped IET junction resistances, R_J/Ω, in the approximate range $50 \lesssim R_J \lesssim 300$ indicate near-monolayer coverage of dopant molecules on the oxide surface (average junction areas in the author's laboratory were ~ 0.25 mm^2). Solution concentrations required to achieve resistances in the above range varied from ~ 0.01 to $\sim 0.05\%$ w/v,

Fig.5.2

Schematic diagrams of IET junctions doped with polymeric material illustrating the necessity for a uniform insulating layer.

Left. A uniform polymeric adlayer favours a uniform electron tunnelling cross-section. Suitable choice of solvent (see text) may lead to such a conformation.

Right. Unsuitable solvents cause polymer chains to form tightly coiled helices. These may form "clumps" on the oxide surface as shown. The most probable electron tunnelling paths would be through the regions between the clumps.

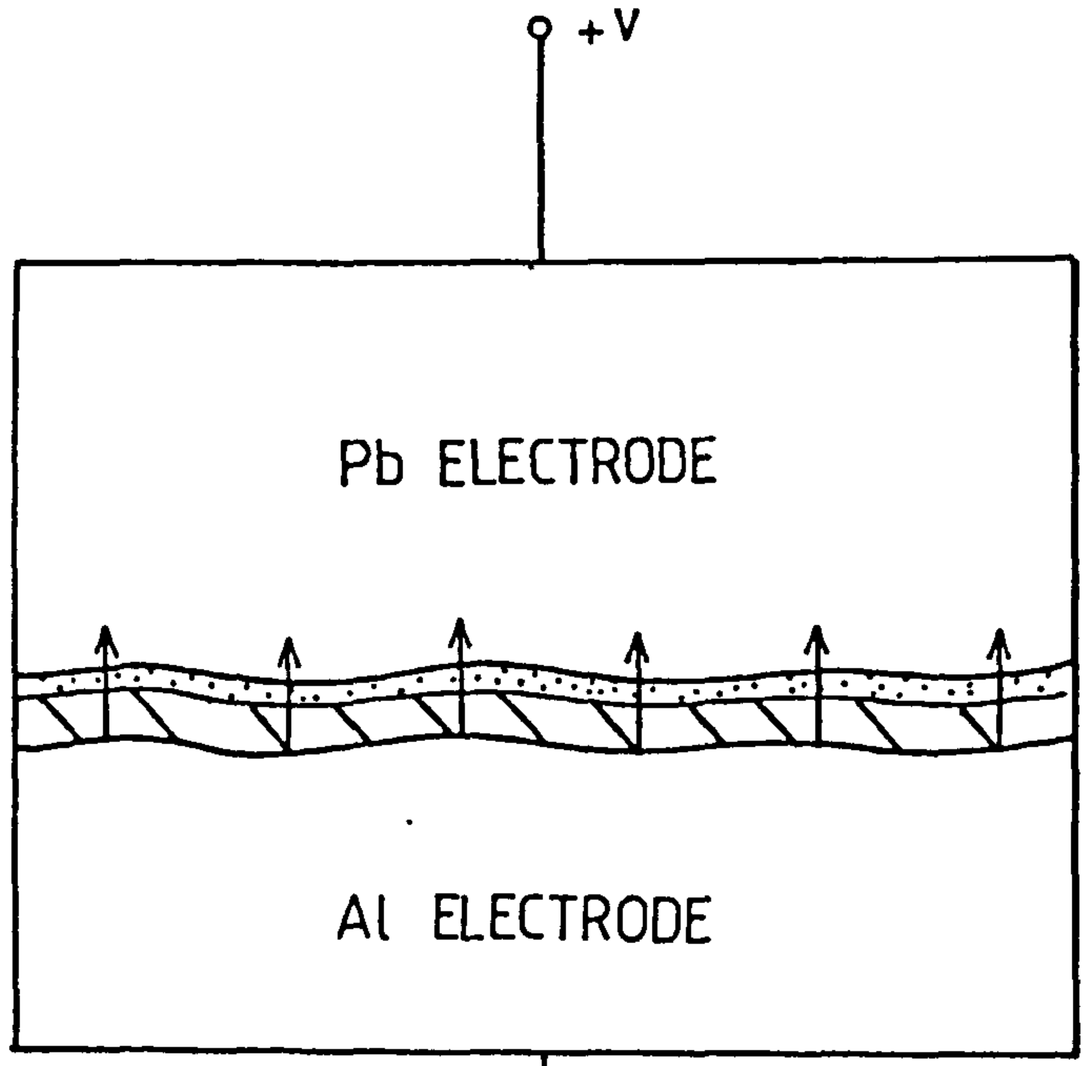

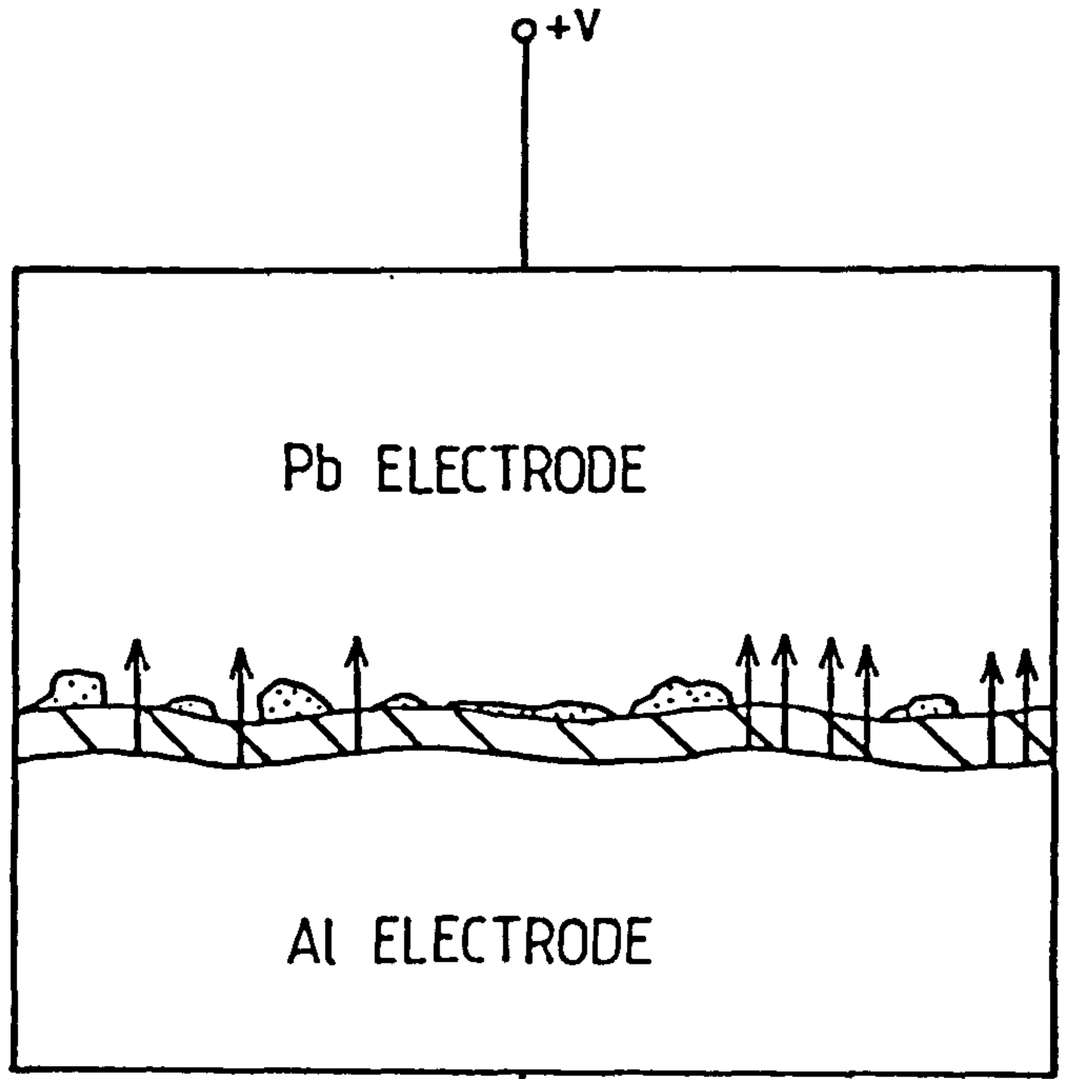

Al OXIDE

POLYMER

ELECTRON TUNNELING PATH

and are similar to those needed for long chain surfactants (36); these concentrations are about an order of magnitude less than those for low molecular weight compounds. Although the reasons for these low concentrations are not yet fully understood, it is surmised that since the large polymer chains are less volatile than smaller dopant molecules they are less likely to desorb from the oxide surface once doped.

5.3 RESULTS AND DISCUSSION

All IET peak energies in cm^{-1} have been corrected for the superconducting energy gap of the lead electrode by subtraction of 8 cm^{-1} (37,38).

5.3.1 PVA

5.3.1.1 PVA Prepared in the Author's Laboratory of Molecular Weight 90,000 ± 5,000

Fig.5.3 shows the IET spectrum of PVA doped from ∿ 0.025% w/v solution in acetone. Peak assignments for this, and the corresponding IR spectrum (not shown) are given in Table 5.1.

Carbonyl groups are known to absorb strongly in the IR (20). It is not surprising that the bulk IR spectrum of PVA has a strong carbonyl peak at 1720 cm^{-1}. In contrast, the intensity of the IET carbonyl peak is noticeably less, and its position has been slightly downshifted to ∿ 1661 cm^{-1}. Surface IR studies have suggested that such a shift is indicative of intermolecular hydrogen bonding between the carbonyl group of the adsorbate and hydroxyl groups on the Aℓ-oxide surface (23). Indeed, this is one plausible mechanism for the adsorption of PVA. As for the reduction in intensity, this may be attributed either to (i) the orientation of the carbonyl groups relative to the plane of the oxide surface or, (ii) a reduction in their number. The former has been dealt with in Chapter 2, but the reader is reminded that, broadly speaking, some correlation exists between peak intensity and bond orientation, viz, polar bonds whose dipole moment axes are aligned perpendicular to the surface couple more strongly with tunnelling electrons than those parallel to it and hence give rise to stronger peaks. Turning to the latter, it is noticed that the IET spectrum exhibits two strong peaks at 1444, and 1596 cm^{-1}. These are widely believed to be due to the symmetric and asymmetric stretching vibrations

Fig.5.3 - IET spectrum of PVA (prepared in the author's laboratory) doped from a ~ 0.025% w/v solution in acetone. Peak assignments are given in Table 5.1 below (corresponding IR data are also presented).

Table 5.1 - Assignments for IET and IR spectra of PVA prepared in the author's laboratory. Spectra were recorded from solutions of PVA in acetone; concentrations for IET and IR were ~ 0.025 and ~ 5% w/v respectively.

Peak No	IETS MeV	IETS cm^{-1}	IR cm^{-1}	Assignment
1	37 (s)	290		Aℓ electrode phonon.
2	56 (w)	444		$r(COO^-)$ in plane
3	78 (w)	621		$\nu(COO^-)$ out of plane and OH bend.
4	98 (wm)	782	785 (w)	$\nu(CO-CH_3)$
5	110 (ms)	879		ν(C-C) skeletal
			905 (w)	
6	118 (ms)	936	950 (w)	Aℓ-O bulk phonon (IETS only) and $\nu(CH_3)$
7	132 (m)	1057		$r(CH_3)$
8	139 (m)	1113	1095 (w)	ν(C-C-O) skeletal
			1220 (vs)	ν(C-O)
9	162 (w)	1299	1360 (s)	$\delta(CH_3)$
10	170 (ms)	1363	1430 (s)	$\delta^s(CH_3)$
11	180 (ms)	1444		$\nu^a(COO^-)$
12	199 (w)	1597		$\nu^s(COO^-)$
13	207 (w)	1661	1720 (vs)	δ^a(C=O)
14	356	2863		
15	362 (vs)	2912	2920	$\nu(CH_2)$ and $\nu(CH_3)$ modes
16	367	2952	2960 (w)	
			3000	
17	448 (m)	3605	3500 (w)	ν(OH)

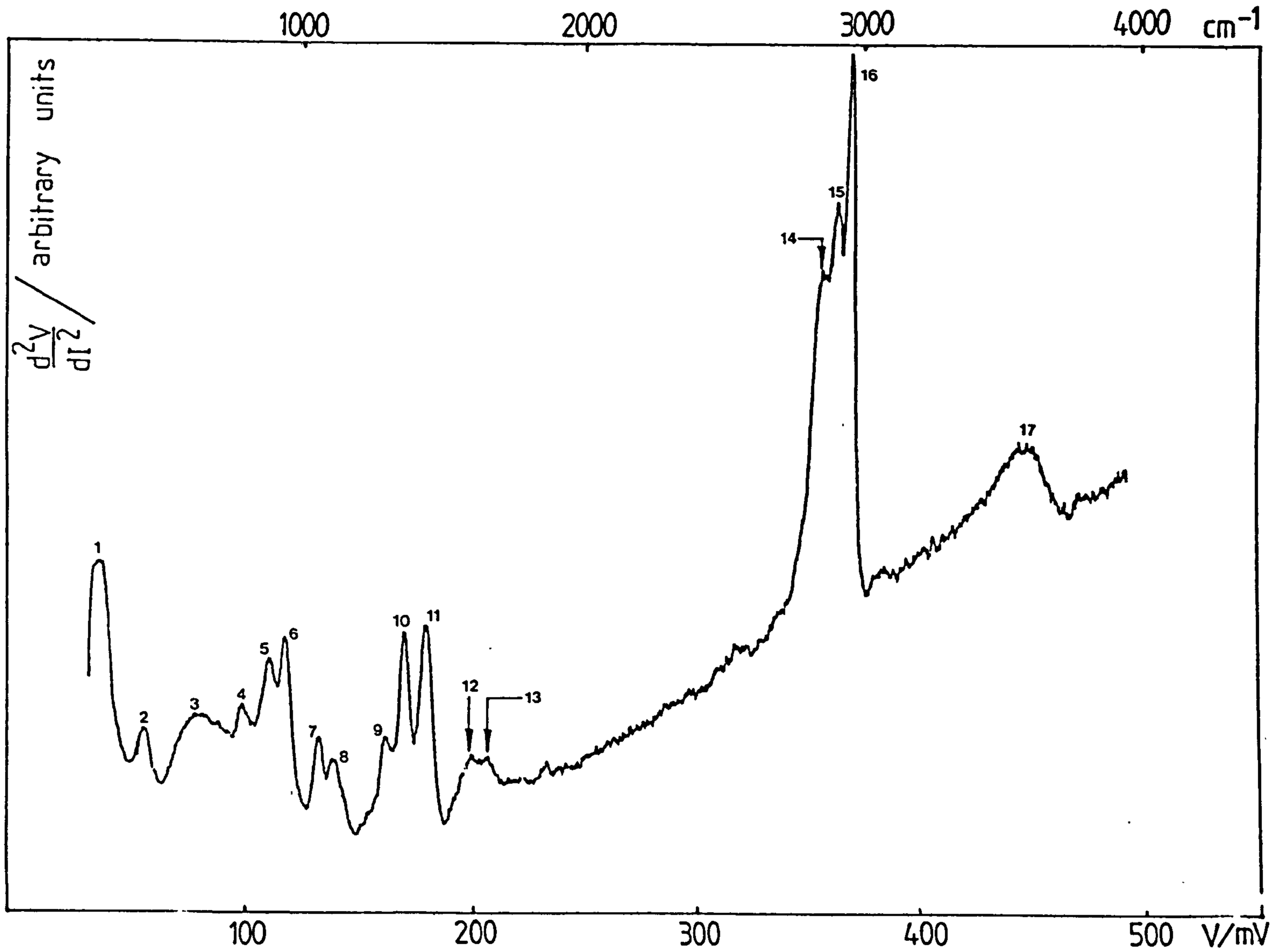
1000
2000
3000
4000
cm⁻¹
d²V/dI² / arbitrary units
1
2
3
4
5
6
7
8
9
10
11
12
13
14
15
16
17
100
200
300
400
500
V/mV

of the carboxylate anion (6,14,15,16). A probable explanation for the presence of these peaks is acid-, or base-catalysed hydrolysis of polymeric ester groups by the hydrated Aℓ-oxide. Hydrolysis usually proceeds as a result of the cleavage of the acyl-oxygen bond (39,40), to give PVOH and acetic acid or acetate anions as indicated below:

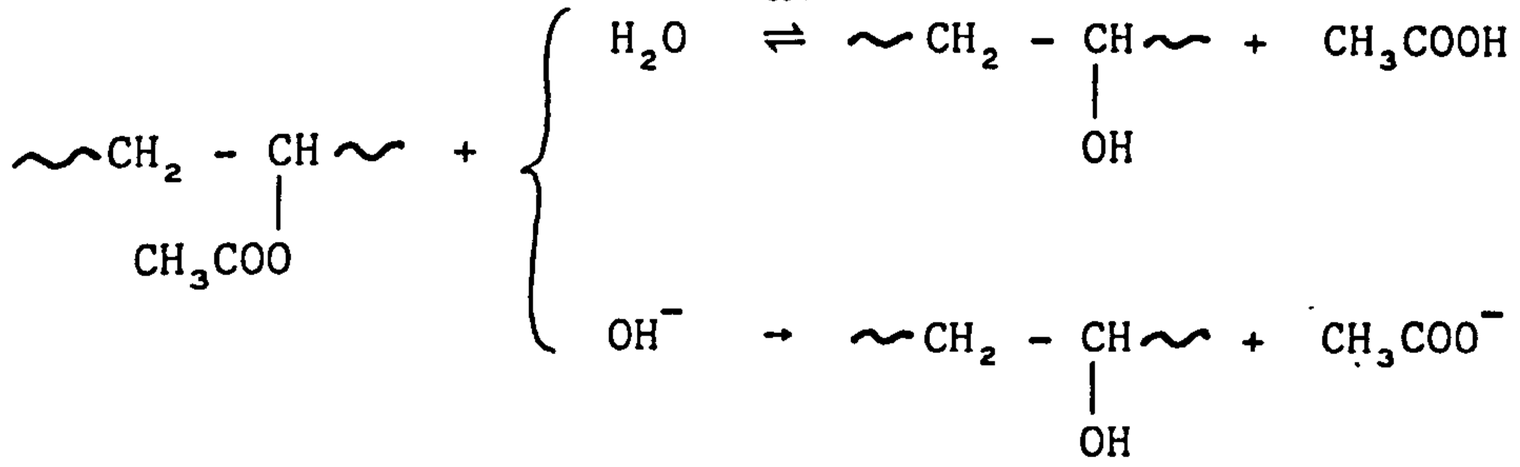

All the species produced would then be adsorbed on the oxide. The above reaction is possible since both acidic, and basic sites on the amphoteric oxide surface may hydrolyse the ester. It is therefore believed that polymeric features observed in the IET spectrum of PVA are due to adsorbed PVOH, while the above carboxylate peaks arise due to adsorbed acetate anions as will now be discussed.

It is known that one of the hydrolysis by-products - acetic acid dissociates on Aℓ-oxide and is then strongly chemisorbed as the acetate anion (15,16) evidenced by the characteristic carboxylate peaks. (Protons removed from the acid groups recombined with surface hydroxyls to liberate water molecules from the surface.) This would explain the reduction in intensity of the carbonyl absorption, and also common features in the IET spectra of adsorbed PVA, and acetic acid. The weak PVA carbonyl peak is presumably due to these acetate side-groups which have not undergone hydrolysis. Formation of the resonance stabilized carboxylate anion as a result of hydrolysis would also serve to reduce the intensity of the PVA C-O stretching vibration which is very strong in the bulk IR spectrum.

Indeed this mode appears to be absent in the IET spectrum of PVA although a very weak skeletal C-C-O stretch does appear at 1113 cm^{-1}.

Very strong aliphatic CH stretching modes appear in the IET spectrum at 2863, 2912 and 2952 cm^{-1}. A semi-empirical study of monobasic aliphatic carboxylic acids adsorbed upon Aℓ-oxide by Walmsley and Nelson (8) has shown that some interdependence exists between increasing chain length, and the intensity of the IET CH stretching vibrations (taken relative to some reliable reference, say the Aℓ-O phonon or carboxylate peaks). A similar trend has also been reported for long chain surfactant molecules (36), and indeed the IET spectra of polymers in the present work exhibit similarly strong CH modes. Although no firm explanations for these observations have yet been offered, it is suggested that the number, and orientation of CH bonds relative to the oxide surface might be considered. For example, De Cheveigné et al have investigated the adsorption of carboxylic acids on Aℓ-oxide at low surface coverages by IETS (15). They proposed that as the fractional surface coverage increases, a crowding effect causes the adsorbed species to adopt what was termed a "more vertical position". Certain IET vibrational mode intensities would be expected to be enhanced. Translating this argument to the present work, since the polymers are present at near-monolayer coverage on the oxide surface (as indicated by corresponding junction resistance and capacitance data) it is reasonable to infer that a large proportion of the CH bonds may be orientated almost perpendicular to the surface; i.e. such that their component of dipole moment normal to the surface is much greater than parallel to it. This would lead to the strong CH stretching peaks observed for polymeric samples.

the IET spectrum of adsorbed PVA also shows evidence of low energy polymeric skeletal vibrations of the carbon backbone (see Table 5.1).

Presumably, these features and the strong CH vibrations are due to the adsorbed PVOH although it should be mentioned that comparison between the IET spectra of adsorbed PVA and PVOH is not straightforward. Inevitable difficulties arise because as will be seen later, PVOH yields weak, poor quality spectra, and in particular, the region from ~ 550 to 1120 cm^{-1} is swamped by the Aℓ-O bulk phonon. The adsorption of PVOH is discussed in 5.3.3.

5.3.1.2 PVA - BDH supplied, Molecular Weight ~ 45,000 doped from different solvents

Spectra obtained from PVA supplied by BDH and from that synthesized in the author's laboratory showed no significant differences. However, slight spectral variations were observed when PVA was doped from different solvents; some of these are now discussed.

Figures 5.4(a) and (b) show typical IET spectra of PVA doped from acetone and benzene at concentrations of ~ 0.04, and ~ 0.01% w/v respectively. Peak assignments are given in Table 5.2. Both acetone and benzene are commonly used solvents in IETS since they are quite unreactive with most compounds under normal doping conditions, and do not leave any significant residue on the Aℓ-oxide surface. Additionally, the α values for PVA in these solvents are about the same (average α values for PVA of the above molecular weight in acetone, and benzene at 30°C are about ~ 0.71, and ~ 0.62 respectively (12)). On the basis of these values one would expect fairly uniform layers of PVA, presumably of similar conformation, to be deposited on the oxide surface as was discussed in 5.2.5.2. Allowing for the slight variations that are normally observed when a set of doped IET junctions are prepared simultaneously on the same glass slide, it was anticipated that the spectra of PVA would be fairly

Fig.5.4 - IET spectra of PVA (BDH supplied, molecular weight ∿ 45,000) doped from:

(a) a ∿ 0.04% w/v solution in acetone

(b) a ∿ 0.01% w/v solution in benzene

Peak assignments for these spectra are given in Table 5.2 below.

Table 5.2 - Liquid-phase doped IET spectra of PVA (BDH supplied, molecular weight ∿ 45,000).

(a) doped from acetone, ∿ 0.04% w/v

(b) doped from benzene, ∿ 0.01% w/v

Peak No	(a) PVA/acetone mV	cm^{-1}	(b) PVA/benzene mV	cm^{-1}	Assignments
1	38 (s)	298	37 (s)	290	Aℓ electrode phonon
2	46 (w.sh)	363			
3	58 (m)	460	62 (m)	492	r(COO^-) in plane
4	78 (w.sh)	621	81 (s)	645	r(COO^-) out of plane
5			107 (m)	855	$\nu(CO-CH_3)$
6	113 (m.sh)	903			ν(C-C)
7	117 (s)	936	115 (m.sh)	919	Aℓ-O bulk phonon
8			123 (s)	984	r(CH_3)
9	133 (m)	1065	135 (s)	1081	r(CH_3)
10	145 (vw)	1161	144 (w.sh)	1153	ν(C-C-O) skeletal
11	160 (w.sh)	1282	163 (s)	1307	$\delta_s(CH_3)$
12	172 (s)	1379	176 (s)	1411	$\delta^s(CH_3)$
13	180 (s)	1444	183 (s)	1468	$\nu^a(COO^-)$
14	201 (m)	1613	205 (w)	1645	$\nu^s(COO^-)$
15	208 (m)	1670	220 (m)	1766	$^a\nu$(C=O)
16	232 (w)	1863	237 (w)	1903	Aℓ-O (2X) overtone
17	343 (vw)	2758			ν(CH) Raman active
18	367 (vs)	2952			$\nu(CH_2)$ and (CH_3)
19	373 (vs)	3000	c.a.372 (vs)	2922	modes
20	458 (m)	3686	463 (w)	3726	ν(OH) surface hydroxyls

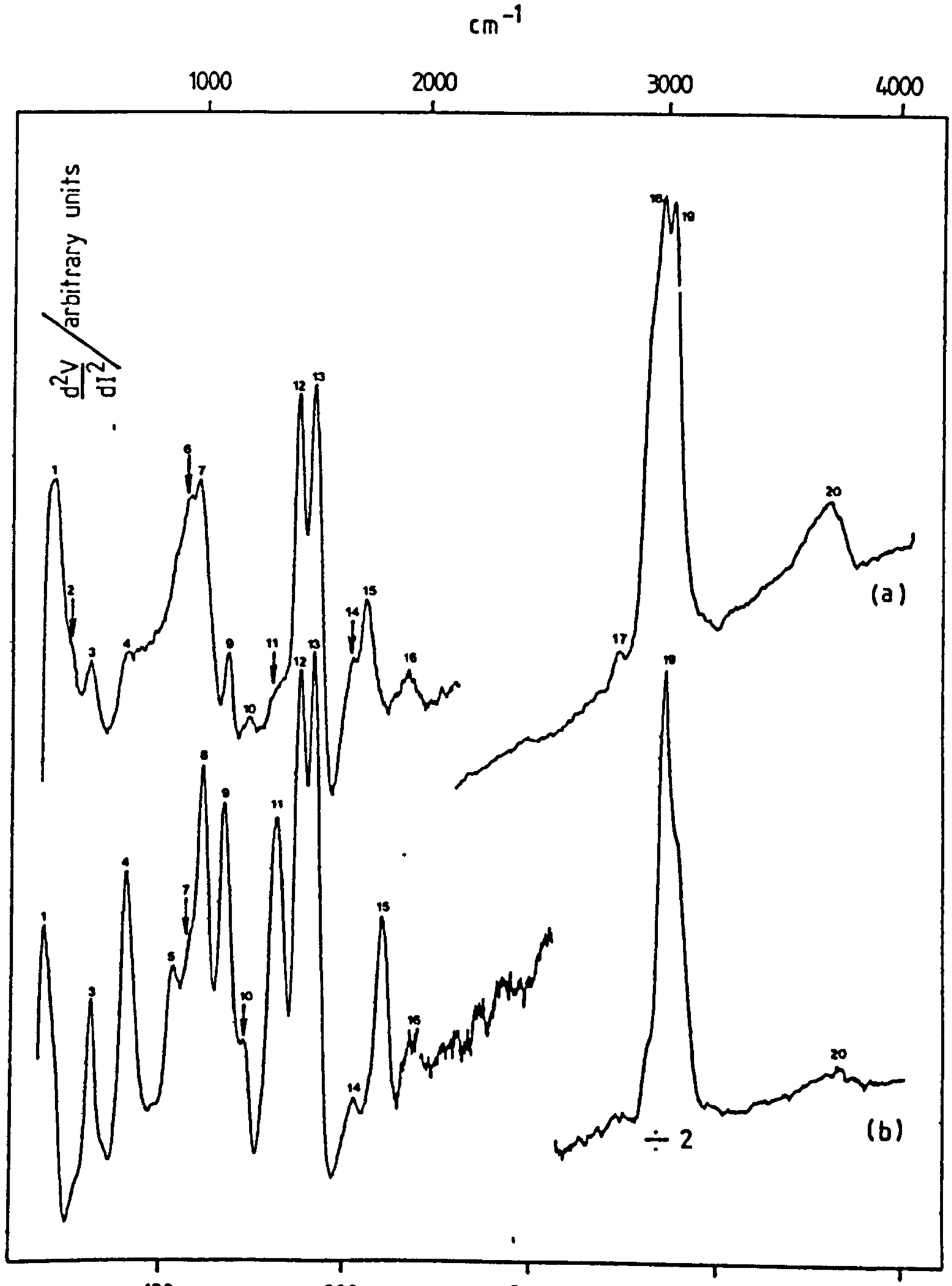
cm-1
1000
2000
3000
4000
d2V/dI2 / arbitrary units
(a)
(b)
÷ 2
100
200
300
400
500
V/mV

similar. As far as peak position is concerned this was found to be largely true. Although the fingerprint region of the spectrum in acetone is somewhat weaker, the two spectra compare quite favourably and most vibrational modes agree to within 4 mV ($\sim$ 32 cm^{-1}) (see Table 5.3). There is however one notable difference; the carbonyl peak for PVA in acetone occurs at 1670 cm^{-1}, while for PVA in benzene it is at 1766 cm^{-1}. The high value for PVA in benzene might suggest that there is little or no interaction between any remaining ester caronyl groups (i.e. those which have not been hydrolysed) and the hydrated oxide surface. As yet the reasons for this are not known. Clearly, further work is necessary to determine whether the position of the carbonyl peak varies in a systematic manner for a range of solvents. For example, it would be interesting to ascertain whether or not it is dependent on the solvents' α values.

Peak intensities for PVA acetone and benzene were found to vary considerably. On the whole the spectrum from benzene is stronger in the fingerprint region. In particular, the low energy rocking and deformation modes of the carboxylate anion at 492, and 645 cm^{-1} respectively are much stronger, as are the methyl rocking and symmetric deformation modes at 1081 and 1307 cm^{-1}. The acetate $CO-CH_3$, and skeletal C-O stretching modes at 855 and 1153 cm^{-1} are also stronger although the latter appears as a shoulder. Modes due to the symmetric, and asymmetric stretching vibrations of the carboxylate anion at 1468, and 1645 cm^{-1} appear with similar intensities.

Overall, the spectrum for PVA in acetone more closely resembles that of the adsorbed acetate anion, with weak polymeric features such as low energy skeletal modes (presumably due to physisorbed PVOH) superimposed. On the other hand, the spectrum from benzene shows strong evidence of polymeric features, and a lower degree of hydrolysis as indicated by the

position of the carbonyl peak as was mentioned above. These findings may suggest that acetone, having a slightly higher α value, tends to "open-up" the coiled PVA chains to a greater extent making interactions between polymer side groups and the oxide surface more favourable. This would lead to a greater degree of hydrolysis and thus partly explain the similarities between the IET spectra of adsorbed PVA and acetic acid (it is recalled that the hydrolysis of PVA to PVOH produces the latter as a by-product).

Since benzene has a slightly lower α value, it is suggested that the PVA coils are not "opened-up" to as great an extent as when doped from acetone. Some interactions between polymer side-groups and the oxide surface would then be sterically hindered resulting in a lower degree of hydrolysis of the PVA. In addition, it is noted that the permittivity of benzene is approximately an order of magnitude less than that of acetone ($\varepsilon_{benzene} \simeq 2.2$, and $\varepsilon_{acetone} \simeq 20$). Any ionic reactions of the polymer in the former would therefore be expected to proceed more slowly, which also suggests a lower degree of hydrolysis.

Clearly, choice of solvent when liquid phase doping with PVA (and presumably other polymers) is of central importance. Contrary to what one might have intuitively expected, a high α value is not necessarily the best criterion for this choice. For PVA at least, too high an α value results in a high degree of hydrolysis, and too low a value will give polymer clumps; benzene would appear to strike middle ground allowing the low energy polymeric vibrations due to the acetate group to be probed.

5.3.1.3 "Resin W" - a PVA Emulsion used for Bonding Wood

Resin W is fairly widely used as an adhesive for wood and paper. Although it is well known that the bonding of such materials is achieved primarily as a result of physical processes such as mechanical interlocking

or keying (41), the chemical aspects of adhesion are not well documented, and may also be of some interest. With this in mind IET spectra of Resin W were recorded; the IET spectrum doped from a ~ 0.05% w/v solution in acetone is shown in Fig.5.5, and peak assignments are given in Table 5.3.

As mentioned in the introduction IR spectroscopy of a dried sample of Resin W showed it to be PVA, and viscometry analysis gave a molecular weight of 40,000 ± 5,000. It is somewhat surprising that the IET spectrum of Resin W is virtually the same as that of the BDH supplied PVA of molecular weight 45,000 also doped from acetone (see Fig.5.5.(a)). It would appear that the dried Resin W is indeed mostly pure PVA. It is suggested that apart from small quantities of certain soaps (which contain CO_2^- groups), a large proportion of any additives to the adhesive was removed during the drying process.

5.3.1.4 Hydrolysed PVA

As was mentioned in 5.2.1.1., the hydrolysis of the PVA synthesized in the author's laboratory was unsuccessful; this was indicated by the fact that the product (which will be referred to as H-PVA for convenience) would not dissolve in water. Nevertheless it is interesting to compare its IET spectrum with that of the PVA starting material (see Fig.5.3, and Table 5.1). The spectrum of H-PVA is shown in Fig.5.6 and peak assignments are given in Table 5.4.

Generally speaking there are no significant differences in peak position between the two spectra. This corroborates that little or no hydrolysis has occurred. Slight variations in relative peak intensity do however exist, particularly in the fingerprint region. Examples of peaks that appear with greater intensities in the IET spectrom of H-PVA are the in- and out-of-plane rocking vibrations of the carbonylate anion

Fig.5.5 - IET spectrum of "Resin W" - a PVA emulsion. The material had previously been dried as described in the text; a ~ 0.05% w/v solution of the dried material was used for junction doping. Peak assignments are given in Table 5.3 below.

Table 5.3 - Assignments for IET spectrum of "Resin W" doped from a 0.05% w/v solution in acetone.

Peak No.	IETS mV	IETS cm^{-1}	Assignment
1	32 (s)	250	Aℓ electrode phonon
2	55 (w)	436	r(COO^-) in plane
3	72 (sh)	573	r(COO^-) out of plane
4	109 (sh)	871	ν(C-C)
5	114 (s)	911	Aℓ-O bulk phonon
6	130 (ms)	1040	r(CH_3)
7	142 (w)	1137	ν(C-C-O) skeletal
8	158 (sh)	1266	ν(C-O) and $\delta_s(CH_3)$
9	168 (s)	1347	$\delta(CH_3)$
10	176 (s)	1411	$\nu^a(COO^-)$
11	197 (m)	1581	$\nu^s(COO^-)$
12	205 (ms)	1645	($\overset{a}{C}$=O)
13	226 (w)	1823	Aℓ-O (2x) phonon overtone
14	337 (vw)	2710	ν(CH_3) Raman active
15	357 (vs)	2871	ν(CH_3) modes
	363 (vs)	2920	
16	447 (m)	3597	ν(OH) surface

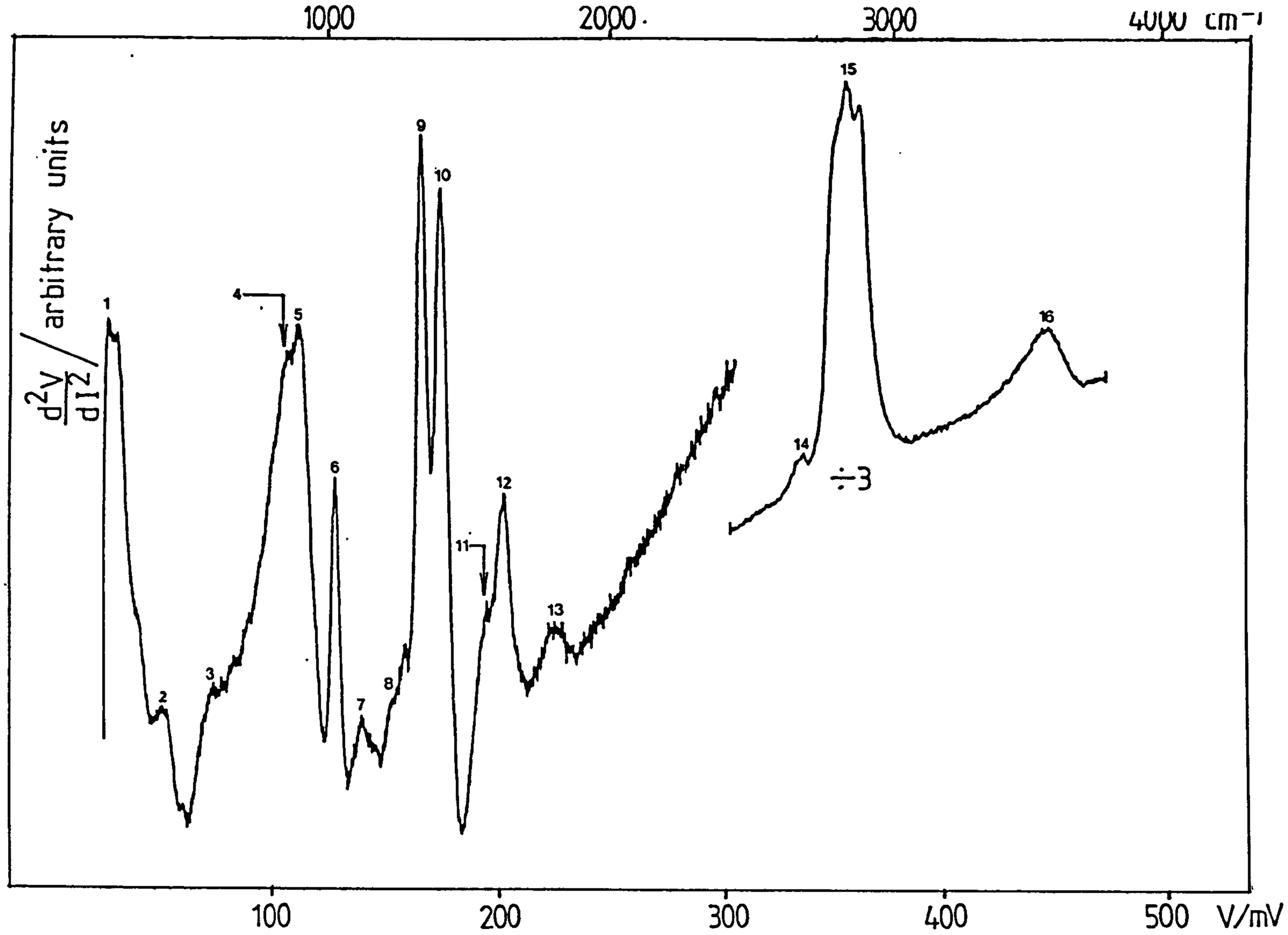
1000
2000
3000
4000 cm⁻¹
$\frac{d^2V}{dI^2}$ / arbitrary units
÷3
100
200
300
400
500 V/mV

Fig.5.6 - IET spectrum of hydrolysed PVA doped from a ~ 0.025% w/v solution in acetone. Peak assignments are given in Table 5.4 below.

Table 5.4 - Assignments for IET spectrum of hydrolysed PVA doped from a 0.01% w/v solution in acetone.

Peak No	IETS mV	IETS cm^{-1}	Assignment
1	34 (s)	266	Al electrode phonon
2	58 (m)	460	$r(COO^-)$ in plane
3	77 (ms)	613	$r(COO^-)$ out of plane
4	100 (wm)	799	$\nu(CO-CH_3)$
5	118 (s)	944	Al-O bulk phonon and $r(CH_3)$
6	130 (ms)	1040	$r(CH_3)$
7	138 (w)	1105	$\nu(C-C-O)$
8	157 (m)	1258	$\delta(CH_3)$
9	170 (s)	1363	$\delta^s(CH_3)$
10	177 (s)	1420	$\nu^a(COO^-)$
11	198 (w)	1589	$\nu^s(COO^-)$
12	211 (m)	1694	$\nu^a(C=O)$
13	227 (w)	1823)	Al-O (2x) overtone
14	340 (vw)	2734	$\nu(CH_3)$ Raman active
15	361 (vs)	2903	$\nu(CH_3)$ modes
16	450 (wm)	3621	$\nu(OH)$ surface

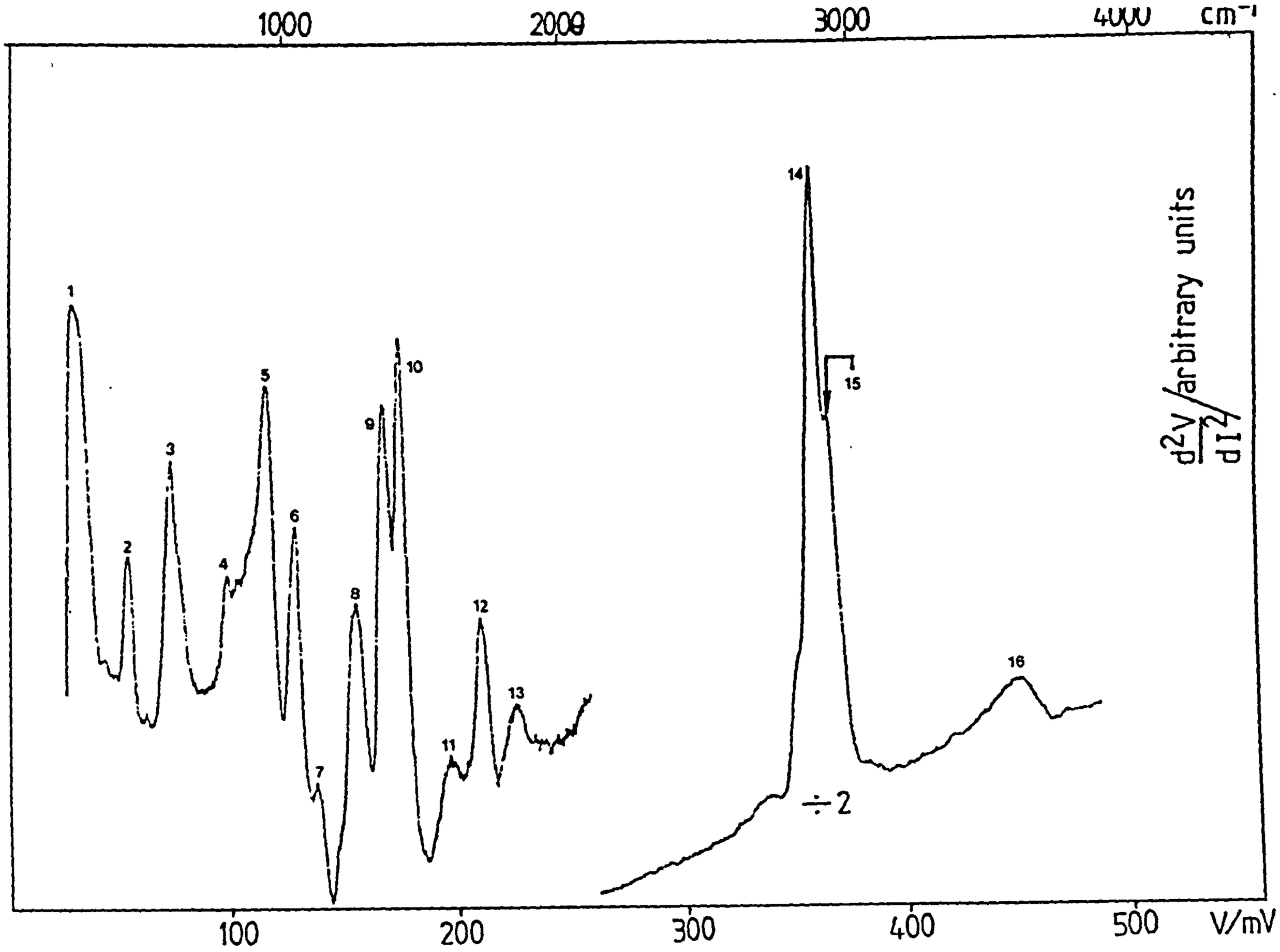
1000
2000
3000
4000
cm⁻¹
$\frac{d^2V}{dI^2}$/arbitrary units
1
2
3
4
5
6
7
8
9
10
11
12
13
14
15
16
÷2
100
200
300
400
500
V/mV

at 460 and 613 cm^{-1} respectively, and the methyl rocking vibrations at 944, and 1040 cm^{-1}. The carbonyl peak is also stronger, and in addition has experienced a slight upshift of $\sim$ 30 cm^{-1} to a value of 1694 cm^{-1}. A few peaks appear with reduced intensities; the C-C-O skeletal stretch at 1105 cm^{-1} for example is considerably weaker while the C-C stretch expected at about 879 cm^{-1} appears to be absent. It is noted that the spectrum of H-PVA strongly resembles that of the BDH supplied PVA doped from benzene (Fig.5.4(b)). This is clear indication that similar adsorbed species are present.

5.3.2 Polymethylmethacrylate (PMMA)

IET spectra were recorded of the low molecular weight (27,000 ± 5,000) PMMA synthesized in the author's laboratory, and PMMA supplied by Polymer Laboratories Ltd., of molecular weight 45,000. The commercially available material was doped from acetone and toluene at a concentration of 0.02% w/v and in both cases weak spectra resembling those of undoped devices were obtained. From these spectra (not shown) it was concluded that the fairly large molecular weight coupled with the choice of solvents available precluded good quality polymeric layers being formed on the oxide surface. (α values for PMMA in acetone and toluene at 30°C are 0.7 and 0.71 respectively).

The low molecular weight sample yielded much better spectra. Fig. 5.7 shows the IET spectrum of PMMA doped from a $\sim$ 0.05% w/v solution in acetone, assignments are given in Table 5.5. Strong peaks due to the symmetric and asymmetric stretching vibrations of the carboxylate anion are clearly present at 1460, and 1621 cm^{-1} respectively. Again, this would suggest acid-, or base-catalysed hydrolysis of ester groups of the polymer by the hydrated Aℓ-oxide to give polymethacrylic acid (or its anionic

Fig.5.7 - IET spectrum of PMMA (prepared in the author's laboratory) doped from a ~ 0.05% w/v solution in acetone. Peak assignments are given in Table 5.5 below.

Table 5.5 - Assignments for IET spectrum of PMMA doped from a 0.05% w/v solution in acetone.

Peak No	IETS meV	IETS cm^{-1}	Assignment
1	35 (s)	274	Aℓ electrode phonon
	45 (sh)	355	
2	57 (m)	452	r(COO^-) in plane
3	77 (ms)	613	r(COO^-) out of plane and OH bend
4	110 (wm)	879	ν(C-C)
5	117 (m)	936	Aℓ-O bulk phonon
6	113 (wm)	1065	r(CH_3)
7	147 (w)	1178	skeletal ν(C-C-O) or ν(C-O)
8	165 (w.sh)	1323	δ (CH_3)
9	173 (s)	1387	δ^s(CH_3)
10	182 (s)	1460	ν^a(COO^-)
11	202 (m)	1621	ν^s(COO^-)
12	209 (m)	1678	ν^a(C=O)
13	231 (w)	1855	Aℓ-O (2x) overtone
	342 (vw)	2750	
14	366 (vs)	2944	ν(CH_2) and ν(CH_3) modes
15	369 (vs)	2968	
16	457 (wm)	3678	ν(OH) surface

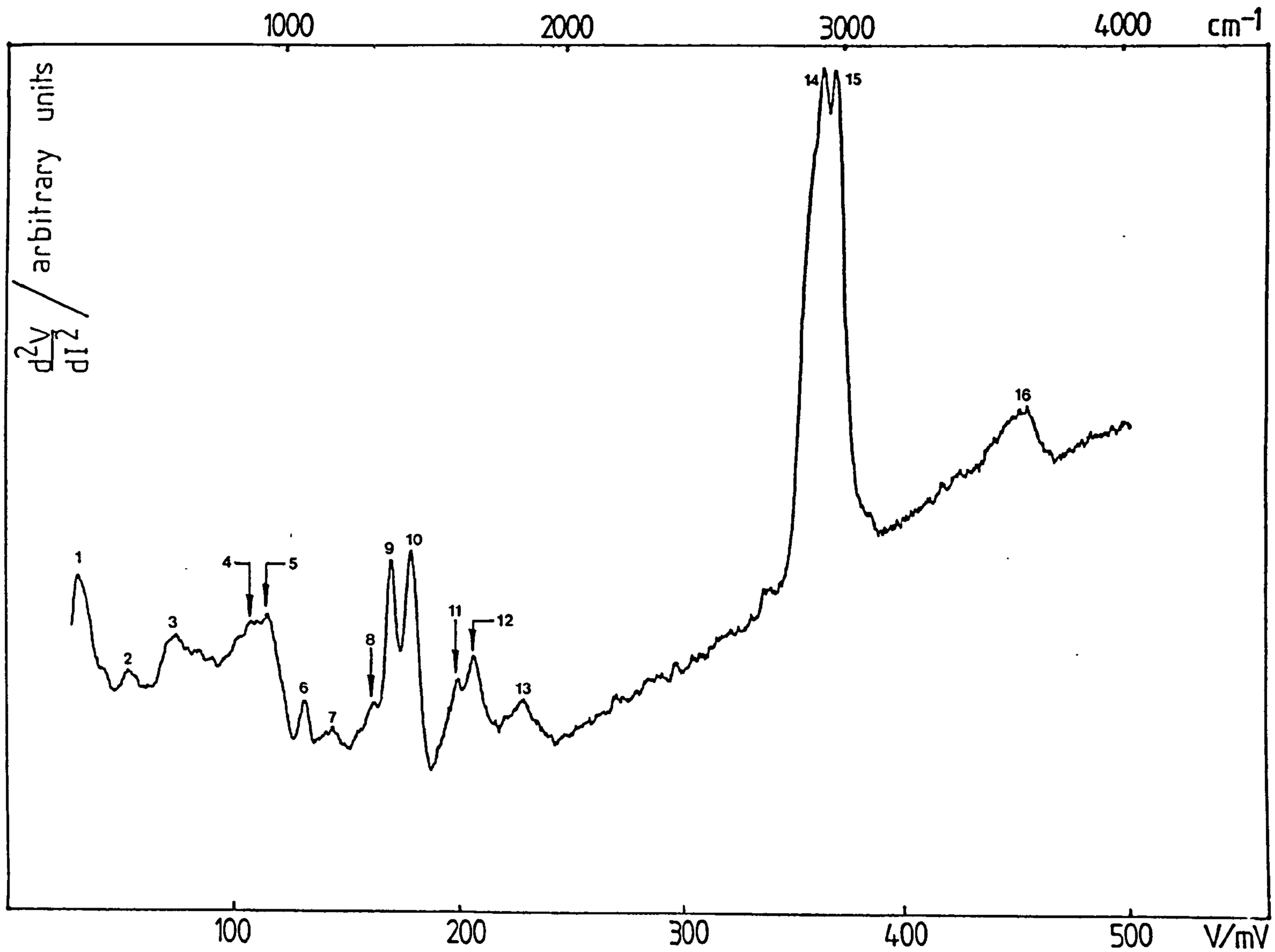
1000
2000
3000
4000
cm⁻¹
d²V/dI² / arbitrary units
1
2
3
4
5
6
7
8
9
10
11
12
13
14
15
16
100
200
300
400
500
V/mV

derivative) and methanol as shown below (36,37).

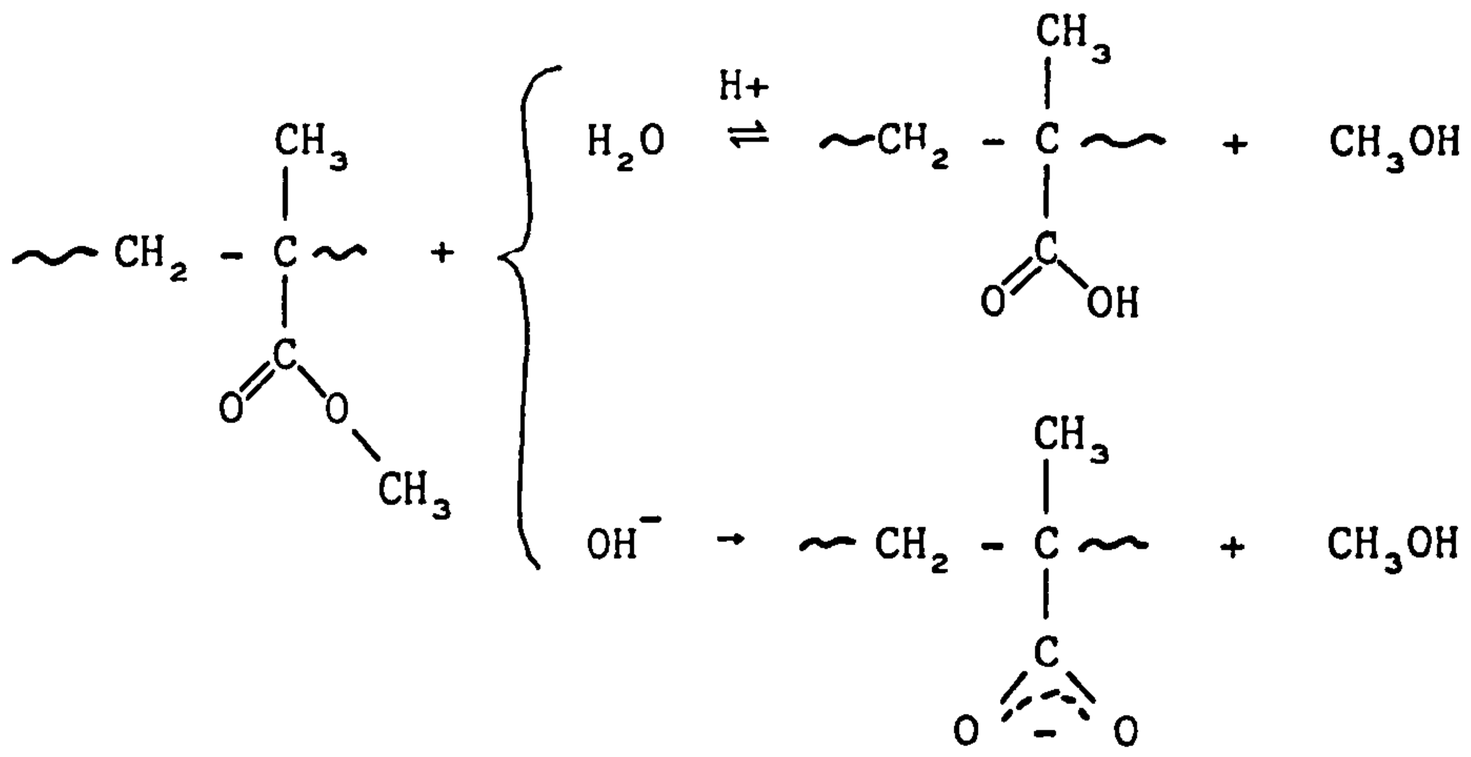

As proposed by Hall and Hansma (16) it is believed that carboxylic acids dissociate on the Aℓ-oxide surface. They are subsequently chemisorbed by the formation of a bidentate symmetrical bridging complex between carboxylate anions and Aℓ ions in the oxide. Consequently, strong carboxylate peaks are observed in the IET spectra. Evidence of these peaks in the spectrum of PMMA would indicate that carboxylate side groups of the hydrolysed PMMA may also be adsorbed in this manner. The spectrum of PMMA also exhibits a weak carbonyl peak at 1678 cm^{-1} presumably due to side groups that have not undergone hydrolysis.

Detection of the methanol by-product would be difficult since it is known that lower aliphatic alcohols are suitable solvents for IETS work in that they are not strongly adsorbed on Aℓ-oxide under normal doping conditions. The methanol would probably evaporate from the oxide, or be pumped away in the vacuum system prior to the evaporation of the Pb counter electrode.

5.3.3 Polyvinylalcohol (PVOH)

Fig.5.8 shows the IET spectrum of PVOH (Koch-Light supplied, molecular weight 72,000) doped from a ~ 0.05% w/v aqueous solution. Peak assignments are given in Table 5.6. The spectrum exhibits strong peaks

Fig.5.8 - IET spectrum of PVOH (Koch-Light supplied) doped from a ∿ 0.05% w/v aqueous solution. Peak assignments are given in Table 5.6 below.

Table 5.6 - Assignments for IET spectrum of PVOH (Koch-Light supplied) doped from a 0.05% w/v aqueous solution.

Peak No	IETS meV	IETS cm^{-1}	Assignment
1	39 (s)	307	Aℓ phonon
2	60 (w)	476	r(COO^-) in plane
3	78 (w)	879	r(COO^-) out of plane
4	90 (sh)	718	CH_2 bend
5	110 (s)	879	Aℓ-O bulk phonon and ν(C-C)
6	131 (m)	1049	CH bend
7	139 (vw)	1113	ν(A -O-C)?
8	157 (w)	1258	skeletal (C-C-O)
9	168 (w.sh)	1347	δ(CH_2)
10	177 (s)	1420	$\nu_s(COO^-)$
11	198 (w)	1589	$\nu^s(COO^-)$
12	230 (w)	1847	[a]Aℓ-O (2x) overtone
13	359 (vs)	2887	ν(CH_2) and ν(CH_3) modes
14	448 (ms)	3605	ν(OH)

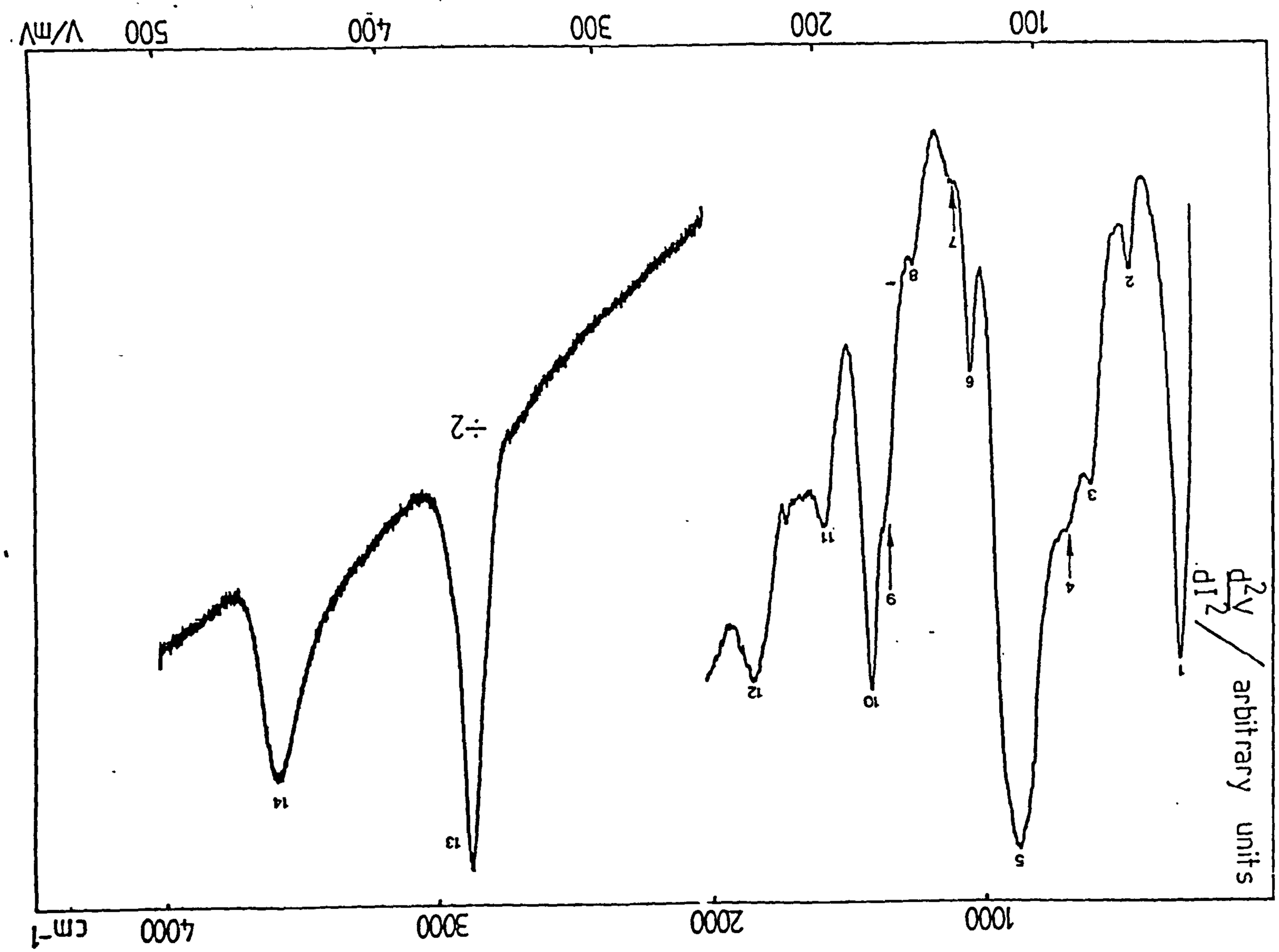
cm⁻¹
4000
3000
2000
1000
arbitrary units
$\frac{d^2y}{dI^2}$
÷2
100
200
300
400
500
V/mV
1
2
3
4
5
6
7
8
9
10
11
12
13
14

due to $-CH_2$ stretching and deformation modes while by comparison modes due to the methyl group are very weak. Clearly this indicates that the PVA starting material from which the PVOH was prepared had been hydrolysed to a large degree.. In support of this view it is noted that the OH stretching mode c.a. 3605 cm^{-1} is considerably stronger than those observed for either undoped IET junctions, or those doped with other polymers; this is in part due to the large number of alcohol side groups of the PVOH. Although the spectra obtained for PVOH were not particularly strong, tentative evidence exists to suggest the formation of a covalently bonded Aℓ-O-C monodentate bridging complex between alcohol side groups and the oxide surface. For example, Evans and Weinberg (17,18), have performed an IETS study of the adsorption of ethanol (and other associated compounds) on alumina over a range of temperatures. At room temperature - as was the case in our work, they attributed the peak at 131 mV (1049 cm^{-1}) to methylene rocking and/or Aℓ-O-C stretching modes, justified by comparison with the bulk IR spectrum of aluminium ethoxide. Although the IET spectral evidence is by no means conclusive, it would seem reasonable to assume that the adsorption of PVOH on alumina may be analogous to that of ethanol.

There is also evidence of carboxylate groups in the IET spectrum, for example, COO^- rocking, deformation, symmetric, and asymmetric stretching modes are present (see Table 5.3). The appearance of both Aℓ-O-C, and acetate-like features may be explained in terms of the degree of hydrolysis of the PVA starting material. Although the side groups of the PVOH samples are predominantly -OH, a small fraction of acetate groups not having undergone hydrolysis may still remain. This is not inconsistant with IR data for the PVOH which showed that the PVA had been hydrolysed to a high degree as was indicated by the absence of carbonyl absorption. It is known that the carboxylate anion is strongly adsorbed on alumina;

hence, even the presence of a small number of carboxylate side groups in a PVOH sample would give rise to fairly strong IET lines while the corresponding IR absorptions may be weak, or absent.

Another possible adsorption mechanism - that of hydrogen bonding between alcohol side groups and surface OH cannot be ruled out. However, firm confirmation of such hydrogen bonding in IETS is generally quite difficult, based upon small shifts in position and changes in intensity of certain molecular modes involved in the adsorption process and the OH stretch. The latter is usually broad and of variable intensity, depending much upon the environment and conditions under which the aluminium oxide layer is formed.

5.3.4 Some Water Soluble Polyers: Polyethyleneglycol (PEG), Polyethleneoxide (PEOX), Methylcellulose (MeC) and Polyacrylamide (PAAM)

The IET spectra of PEG, PEOX, MeC, and PAAM all doped from aqueous solutions are shown in Figures 5.9 to 5.12 respectively. Spectra were recorded using the computer-controlled datalogging facilities described in Chapter 3 (and references therein); quadratic backgrounds have been subtracted to enhance the weaker spectral features. Solution concentrations used to obtain these spectra were 0.01, 0.005, 0.025 and 0.0125% w/v. For convenience sake, peak assignments (in cm^{-1}) have been indicated in the figures.

The molecular weight of the PEG ($HO(CH_2CH_2OO)_nH$ where n = 7 or 8) is $\sim$ 370. A considerably higher value of 5×10^6 is quoted for both PEOX $(OCH_2CH_2)_n$, and polyacrylamide $\{CH_2 - \underset{\underset{\underset{NH_2}{|}}{C=O}}{CH}\}_n$ all of which were supplied by BDH), while that of the MeC is unknown but

Fig.5.9

IET spectrum of PEG doped from a ∿ 0.01% w/v aqueous solution. A Quadratic background slope has been subtracted numerically utilizing the computer techniques described in Chapter 3.

File(c): R2398A-quadratic background

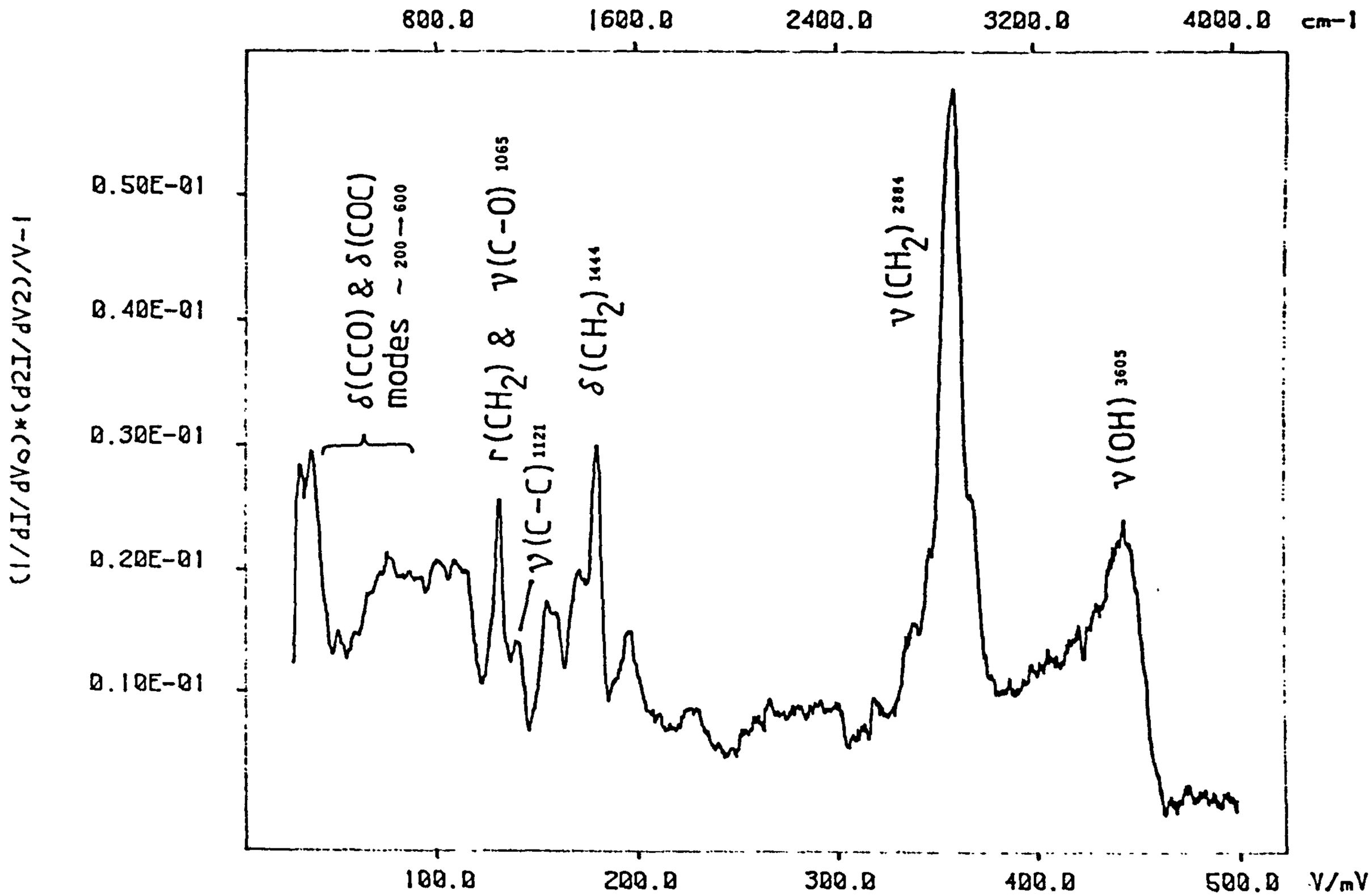

Fig.5.10

IET spectrum of PEOX doped from a ~ 0.005% w/v aqueous solution. A Quadractic background slope has been subtracted numerically utilizing the computer techniques described in Chapter 3.

File(c): R2419A-quadratic background

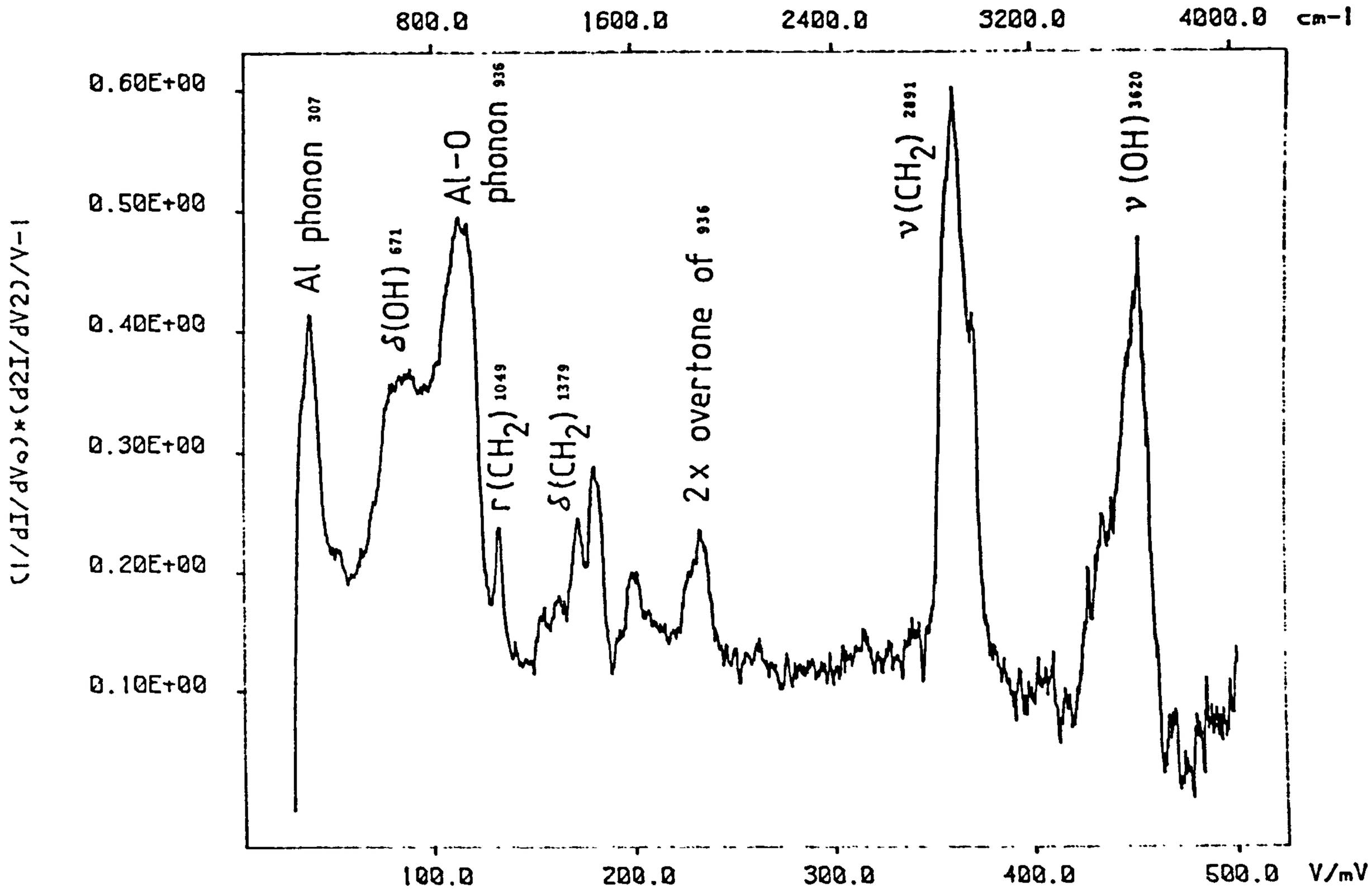

Fig.5.11

IET spectrum of MeC doped from a ∿ 0.025% w/v aqueous solution. A Quadratic background slope has been subtracted numerically utilixing the computer techniques described in Chapter 3.

File(s): R2456A-quadratic background

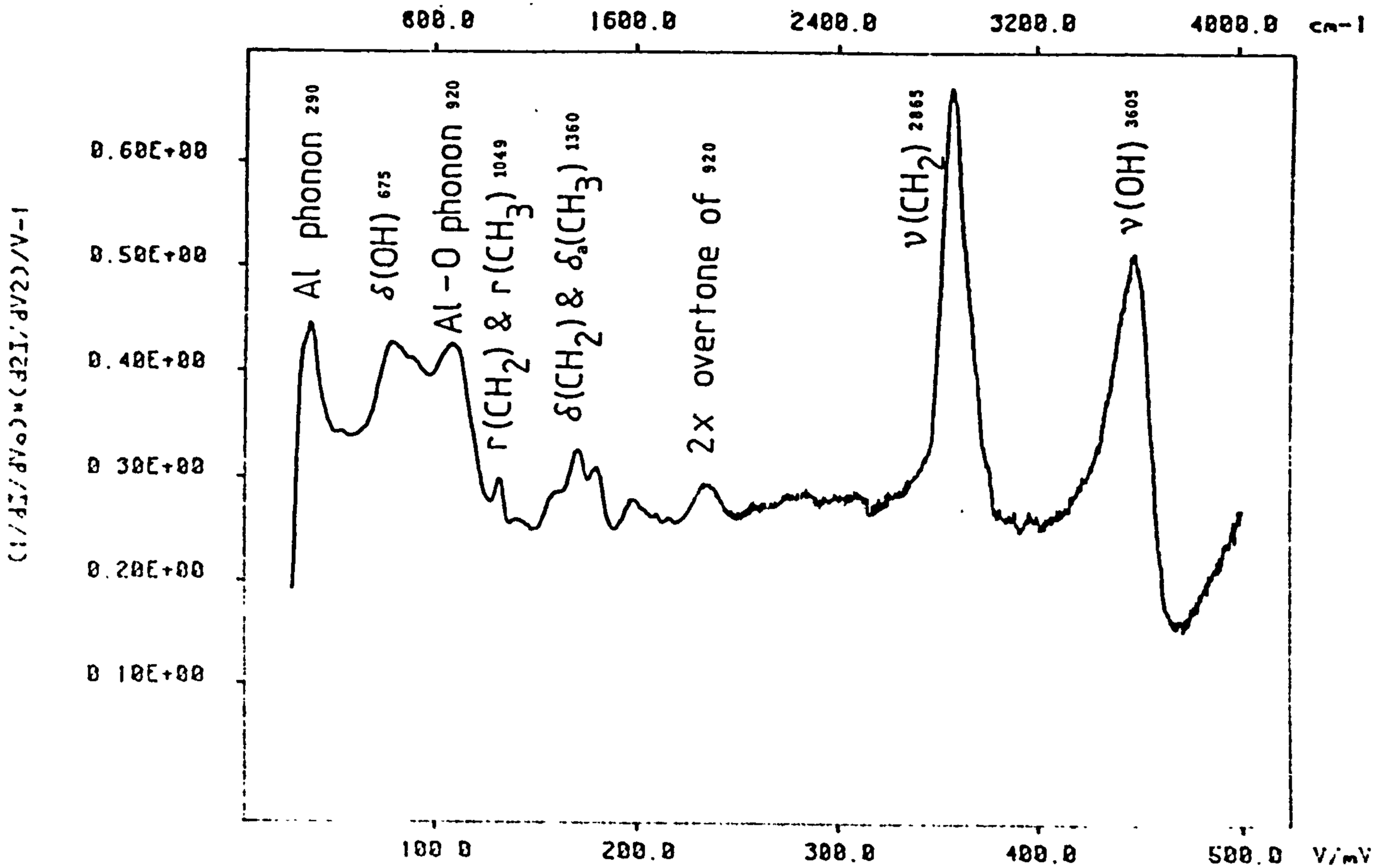

Fig.5.12

IET spectrum of PAAM doped from a ∿ 0.0125% w/v aqueous solution. A Quadratic background slope has been subtracted numerically utilizing the computer techniques described in Chapter 3.

File(c): R2448A-quadratic background

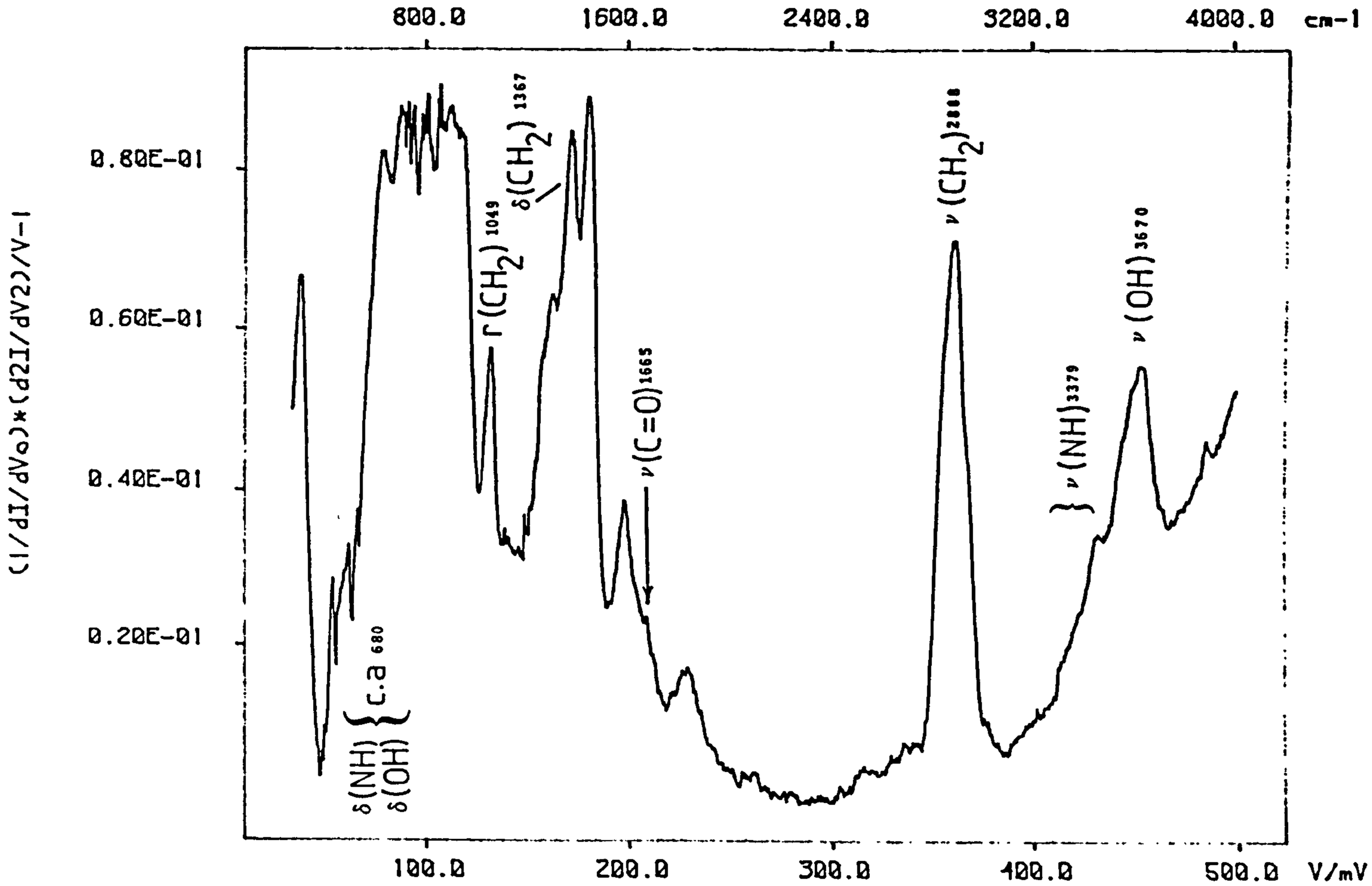

expected to exceed 100,000.

Common features in the spectra of PEG, PEOX, MeC, and adsorbed PVOH are not expected due to their similar structures. The iET spectrum of PEG (essentially a low molecular weight PEOX having two alcohol functional end groups) compares quite favourably with its Raman counterpart (42) and the IET spectrum of ethylenegylcol (8). For the relatively small PEG molecule dissociation of the alcohol groups may lead to its subsequent chemisorption. Protons thus released would recombined with surface hydroxyls on the oxide to produce free-water which would be pumped away in the vacuum system during counter electrode fabrication. By comparison the spectrum of high molecular weight PEOX is quite weak and noisy and more closely resembles the spectrum of adsorbed PVOH. It is possible that interactions between the lone pairs of the oxygen atoms in the PEOX backbone and Aℓ ions in the oxide leads to the physisorption of this polymer. The spectrum of MeC is also very similar to that of adsorbed PVOH, and this compound is expected to adsorb in a similar manner to PEOX.

Although the spectrum of PAAM has an unusual background slope, and is also quite noisy, it is observed that the NH stretching vibration has a very low intensity. This is generally true for most amides investigated by IETS (8) and need not be discussed further. Interestingly, the carbonyl adsorption is also very weak appearing only as a shoulder on the high energy side of the asymmetric stretching vibration of the carboxylate anion. This suggests that the dipole moment axes of majority of the carbonyl groups may be aligned almost parallel to the oxide surface as a consequence of the orientational selection rules. By implication, the NH_2 groups would be orientated towards the oxide surface; it is tentatively suggested that PAAM may then be adsorbed by hydrogen bonding between the amide groups and surface hydroxyls.

This brief account of the water soluble polymers would suggest that similar adsorption mechanisms operate for the polymers studied, i.e. they are primarily hydrogen bonded to the oxide surface through interactions between their side groups (NH, and OH) or lone pairs of oxygen atoms in the polymer-backbone and surface hydroxyls.

5.4 CONCLUSIONS

IETS is a useful technique for the study of the adsorption of certain polymers on an Aℓ-oxide surface. It is not possible to obtain detailed information regarding the configuration of the macromolecules as a whole on the surface. However, it is possible to gain some insight into the nature of their adsorption on the basis of interactions between functional side groups of the polymers and the reactive oxide surface. Interfacial behaviour of the polymers may lead to their adsorption in a tail $\{$train-loop$\}_n$ tail configuration where polymer-surface interactions occur in the train segments. Adsorption is not strongly dependent on chain length although in the case of physisorbed species those with higher molecular weights are less likely to desorb simply due to their lower volatility. Low molecular weight samples are advantageous in that adverse polymer-solvent effects leading to the formation of polymer 'clumps' are less probable. Uniform adsorbed layers are thus formed which result in good quality IET spectra. The effects of polymer tacticity on adsorption have not been fully ascertained; further work to investigate the adsorption of low molecular weight polymers of known tacticities and having small, reactive side groups would be interesting.

For the polymers with ester bearing side groups the most probable adsorption mechanism is believed to be ester cleavage catalysed by the Aℓ oxide and/or surface hydroxyl species present on the oxide. For PMMA, subsequent chemisorption of the carboxylate anions generated on the polymer side groups may occur, whereas PVA may be fully or partially hydrolysed to, and then adsorbed as PVOH. Another plausible mechanism is hydrogen bonding of carbonyl groups of the polymer to surface hydroxyls.

The adsorption of PVOH is not well understood, however, it is possible that covalent Aℓ-O-C monodentate bridges may be formed between alcohol side groups and the oxide surface. This is analogous in nature

to the adsorption of lower aliphatic alcohols on alumina at room temperature. Also hydrogen bonding of alcohol side groups to surface hydroxyls cannot be ruled out.

It is believed that PEG, PEOX, MeC, also adsorbed in a similar manner to PVOH, or possibly physisorbed as a result of interactions between lone pairs of the oxygen atoms of the polymers, and Aℓ ions in the oxide. PAAM may be adsorbed by hydrogen bonding between amide groups and surface hydroxyls.

REFERENCES - Chapter 5

1. See for example "Durability of Structural Adhesives", A.J.Kinloch (Ed.), Applied Science, London and New York (1983).

2. J.Comyn, C.C.Horley, D.P.Oxley, R.G.Pritchard and J.L.Tegg. J.Adhesion, 12, 171-188 (1981).

3. S.Reynolds, D.P.Oxley and R.G.Pritchard. Spectrochim. Acta., 30(A) 103 (1982).

4. D.M.Brewis, J.Comyn, D.P.Oxley, R.G.Pritchard and C.R.Werret. Surf. Int. Anal., 6(1), 40 (1984).

5. R.V.Coleman, J.M.Clark and C.S.Korman. Inelastic Electron Tunnelling Spectroscopy. T.Wolfram (Ed), Springar-Verlag, Heidelberg (1978), pp.34-60.

6. R.V.Coleman. Tunnelling Spectroscopy Capabilities, Applications and New Techniques. P.K.Hansma (Ed)., Plenum Press, New York (1982), pp.201-227.

7. R.R.Mallik, R.G.Pritchard, C.C.Horley and J.Comyn. To appear in Polymer, 26, 551(1985)

8. D.G.Walmsley and W.J.Nelson. Tunnelling Spectroscopy, Capabilities Applications and New Techniques. P.K.Hansma (Ed), Plenum Press, New York (1982), pp.311-357.

9. M.Lal and R.F.T.Stepto. J. Polym. Sci. Polym. Symp., 61, 401-412 (1977).

10. J.M.G.Cowie. Polymers: Chemistry and Physics of Modern Materials. K.Stead Ed., Intertext Textbook Co. Ltd., London (1973).

11. W.R.Sorenson and T.W.Campbell. Preparative methods of Polymer Chemistry (2nd Edn.), Wiley-Interscience, New York (1968).

12. Polymer Handbook (2nd Edn.), Wiley-Interscience, New York (1975).

13. F.M.Fowkes and M.A.Mostafa. Ind. Eng. Chem. Prod. Res. Dev., 17(1), 3 (1978).

14. D.L.Allara. Polym. Sci. Technol., 12(b), 751 (1980).

15. S.DeCheveigné, S.Gauthier, J.Klein, A.Léger, C.Guinet, M.Belin and D.Defourneau. Surf. Sci., 105, 377-385 (1981).

16. J.T.Hall and P.K.Hansma. Surf. Sci., 86, 61 (1978).

17. H.E.Evans and W.H.Weinberg. J.Chem. Phys., 71(4), 1537 (1979).

18. H.E.Evans and W.H.Weinberg. J. Chem. Phys., 71(12), 4789 (1980).

19. L.H.Little. Infrared spectra of Adsorbed Species. Academic Press, London (1966).

20. M.L.Hair. Infrared Spectroscopy in Surface Chemistry, Edward Arnold, Marcel-Dekker Inc., New York (1967).

21. L.H.Little. Chemisorption and reactions on metallic films (Vol.1) J.R.Anderson Ed., Academic Press, London (1971), Chapter 3.

22. L.J.Bellamy. The Infrared Spectra of Complex Molecules (3rd Edn.), Chapman and Hall, London (1975).

23. I.Kusaka and W.Suëtaka. Spectrochim. Acta., 36(A), 647 (1980).

24. D.P.Oxley et al. Surf. Int. Anal., 2(1), 31 (1980).

25. P.K.Hansma and H.G.Hansma. Tunnelling Spectroscopy, Capabilities, Applications and New Techniques. P.K.Hansma (Ed.), Plenum Press New York (1982).

26. Private communication,
Emad Al-Khawam.

27. R.C.Jaklevic and M.R.Gaerttner. Applications. Surf. Sci., 1, 479 - 502 (1978).

28. M.Korn and E.Killmann. J. Coll. Int. Sci., 76(1), 19 (1980).

29. F.T.H.Hesselink. J. Polym. Sci. Polym. Symp., 61, 439 (1977).

30. H.Suzuki, T.Hiyoshi and H.Inagaki. Ibid., 61, 291 (1977).

31. C.A.J.Hoeve. Ibid., 61, 389 (1977).

32. M.Kamachi. Advances in Polym. Sci., 38, 55 (1981).

33. Tunnelling Plenomena in Solids, E.Burstein and S.Lundqvist (Eds.) Plenum Press, New York (1969).

34. J.Kirtley. J. Am. Chem. Soc., 80, 217 (1980).

35. C.B.Duke. Tunnelling in Solids, Solid State Physics (Supplement 10) Plenum Press, New York (1969).

36. A.J.Langley. Ph.D. Thesis, Leicester Polytechnic (1982).

37. R.C.Jaklevic and J.Lamb. Phys. Rev. Lett., 17, 1139 (1966).

38. P.K.Hansma. Phys. Rep., 30(C), 145 (1977).

39. E.S.Gould. Mechanism and Structure in Organic Chemistry, Hold, Rinehart and Winston, New York (1962).

40. P.Sykes. A Guidebook to Mechanism in Organic Chemistry, Longman, London (1962).

41. W.C.Wake. Adhesion and the Formulation of Adhesives (2nd Edn.), Applied Science Publishers, London (1982).

42. J.L.Koenig. Appl. Spectrosc.Revs., 4(2), 233-306 (1971).

CHAPTER 6

A STUDY OF SOME POLYMERS INCORPORATED INTO IET JUNCTIONS BY GLOW-DISCHARGE POLYMERIZATION

6.1 INTRODUCTION

In recent years, several applications for plasma- or glow-discharge-polymerization (GDP) have emerged. Examples include the deposition of thin protective polymeric films on the walls of reaction vessels (1), Si O_2 films for semiconductor device applications (2,3), and substrates for medical purposes (4,5). Metal surfaces have also been treated for the improvement of adhesive joints (6,7,8).

GDP films are deposited by introducing a controlled flow of monomer vapour into a sealed, evacuated chamber within which a radio frequency (RF) glow-discharge may be established. Energy imparted to the monomer molecules by the discharge causes them to dissociate thus generating active centres for polymerization. A GDP film may then be formed on any substrate placed within the discharge. The structure and composition of such films depend mainly on the operating conditions of the RF glow-discharge, the geometry of the chamber and RF electrodes, and to a lesser degree the nature and flow-rate of the monomers in question (9-12). Films deposited for the applications mentioned above, and for IR spectrocopy, are generally of the order of several μm thick, highly crosslinked, and relatively pinhole-free (13). The present work will demonstrate that similar GDP films but of the order of a few Å's thick, may be incorporated as the insulating layer of Aℓ/Aℓ-oxide/insulator/Pb IET junctions. Hence,GDP offers a new and complimentary doping technique for polymers in addition to the liquid-phase method described in Chapter 3. An obvious advantage of the GDP approach is that it precludes the need for solvents. Polymerization may be performed in inert atmospheres, e.g. Argon; subsequent analyses of the

IETS data regarding polymeric adsorption can then be made with greater confidence since any spectral variations due to polymer-solvent effects are effectively eliminated. Additionally, since the commercial applications of Aℓ, and Aℓ bonding are widespread and diverse ranging from the aircraft industry (14,15) to shoe manufacture (16), the deposition of GDP films on Aℓ-oxide for subsequent IETS analyses is of topical interest. As mentioned above, certain constraints concerning the nature of the films are necessarily imposed viz film thickness and continuity. In order to deposit films suitable for IETS a low power RF discharge chamber of appropriate geometry is necessary; full details of the system designed by the author (17) based upon those of other workers (1 - 13 appear in the experimental section.

Several monomers of interest in the field of polymer and adhesion science have been glow-discharge polymerized and investigated by IETS in our laboratory. Of these, results obtained for the following are presented and discussed.

1. Vinylacetate.
2. Ethylacetate.
3. Ethylacrylate.
4. Methylmethacrylate.
5. Acrylic acid.
6. Acrylonitrile.
7. A 50% v/v mixture of styrene/vinyltriethoxysilane.

Polyvinylacetate, and polymethylmethacrylate have also been studied by the author utilizing liquid-phase doping (see Chapter 5). It will be seen that the respective spectraldata for these two polymers obtained by liquid-phase doping, and GDP compare favourably; this suggest that similar adsorbed polymeric layers are formed on the Aℓ-oxide surface in both cases.

IR spectra of thicker GDP films deposited onto KBr discs were recorded on a Perkin-Elmer 683 spectrometer. IR spectra of the respective monomers were obtained using KBr mull plates. The IR data obtained for vinylacetate and methylmethacrylate are presented which clearly indicate that polymerization has occurred and that films of the order several μm thick have been deposited.

Part of the work presented here has is to be summitted for publication (18).

6.2 EXPERIMENTAL

6.2.1 IET Junction Fabrication

Standard shadow masking techniques described in Chapter 5 were used to vacuum deposit the IET junction electrodes onto a clean glass microscope slide. Immediately after the evaporation of the Aℓ base electrodes, the glass slide was removed from the vacuum chamber and positioned in the GDP chamber (described in 6.2.2) where the polymeric films were then introduced onto the Aℓ-oxide surface. The slide was then removed and the Pb counter-electrodes were evaporated in the usual manner thus completing the IET junctions. Junction resistances were measured routinely as a preliminary check to determine whether or not GDP films of suitable thickness had been incorporated (see Chapter 5).

It is preferable for all the above procedures in situ without breaking vacuum. Unfortunately the present geometry of the vacuum chamber does not allow this. Further work to this end would be useful.

6.2.2 The GDP System and Deposition of GDP films for IET Analysis

A 13·56 MHz RF power supply was capacitatively coupled to a parallel plate, flat-bed glow-discharge configuration within the chamber of a modified Nanotech autocoater 300 vacuum plant. A schematic diagram of the system and a more detailed diagram of the chamber is shown in Figures 6.1 and 6.2 respectively. Photographs of the RF electrode geometry are shown in Plates 6.3 and 6.4 respectively. For convenience the individual components comprising the system will be described by considering the typical routine employed for the deposition of the GDP films.

Prior to polymerization the chamber and its contents were glow-discharge cleaned in Ar for several minutes, and then 'gettered' by the evaporation of a few thousand Å's of Pb (19). This procedure reduces the

Fig.6.1 - Schematic diagram of the GDP system.

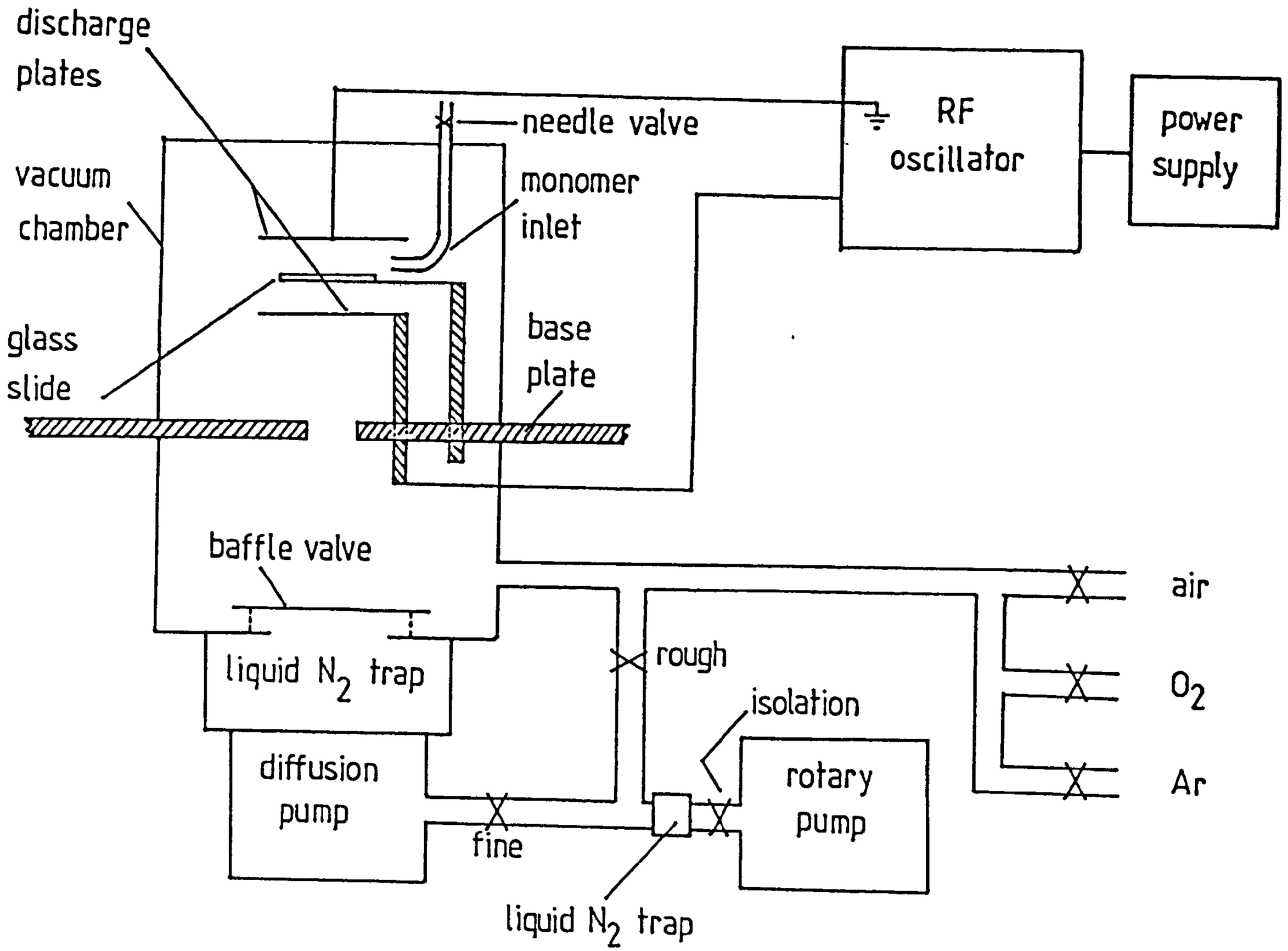
discharge plates
needle valve
RF oscillator
power supply
vacuum chamber
monomer inlet
glass slide
base plate
baffle valve
air
liquid N_2 trap
rough
isolation
O_2
Ar
diffusion pump
rotary pump
fine
liquid N_2 trap

Fig.6.2 - Schematic diagram of the GDP chamber.

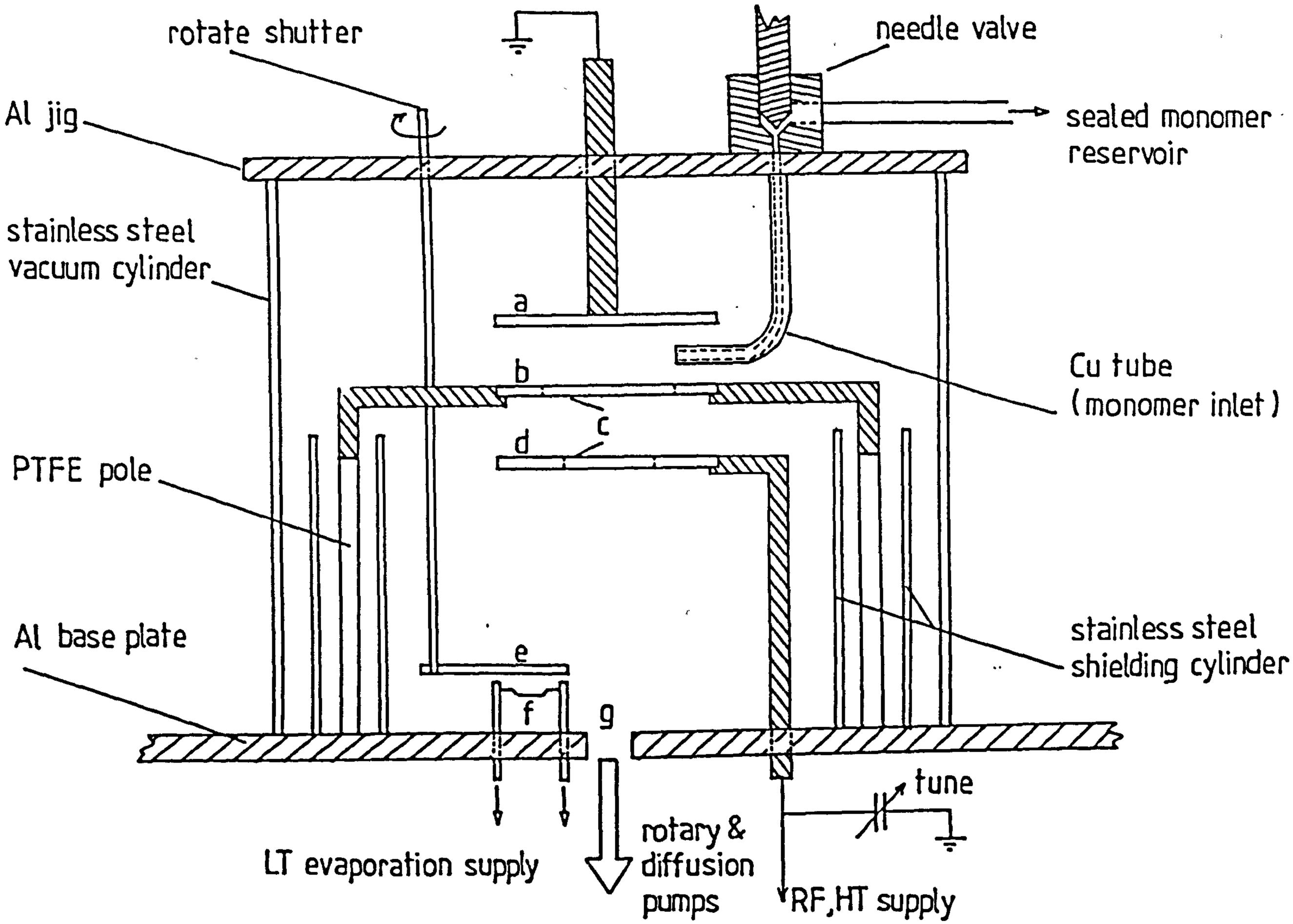
rotate shutter
needle valve
Al jig
sealed monomer
reservoir
stainless steel
vacuum cylinder
a
b
c
d
Cu tube
(monomer inlet)
PTFE pole
Al base plate
e
f
g
stainless steel
shielding cylinder
tune
LT evaporation supply
rotary &
diffusion
pumps
RF, HT supply

amount of water vapour, and atmospheric contamination adsorbed on the internal surfaces of the chambers to an acceptable level. The glass slide was then mounted on a holder mid-way between a pair of circular discharge plates, and held at a floating potential by means of two polytetrafluoroethylene (PTFE) insulating poles (see Fig.6.2). These poles were shielded by stainless steel cylinders to prevent any energy being dissipated to them from the discharge.

Significant factors govening the rate of film deposition are: the geometry of the glow-discharge, (which is to a large extent determined by the plate separation and area (20)) the RF power input to the system, and the monomer flow-rate (9-12). Dealing with these in turn, plates of diameter $\sim$ 145 mm were used whose separation could be varied by means of a sliding jigging arrangement (see plate 6.3). A circular aperture was made in the bottom plate to aid the gettering procedure and also to allow IET junction electrodes to be evaporated in situ if desired. With the above configuration and a plate separation of $\sim$ 60 mm the discharge was restricted to the region adjacent to the glass slide; this configuration was maintained throughout all polymerizations.

A dc power input of 20-30W (200-300 Vdc with a current of $\sim$ 100 mA) to the RF oscillator was found to be optimum for the system and did not produce any excessive heating of the plates. Although the RF power output across the plates is not easily measurable,it may be estimated by measuring the RF potential across a small known resistance, R_s, in series with the plates and that across a large resistance, R_p, in parallel with them as shown in Fig.6.5 below:

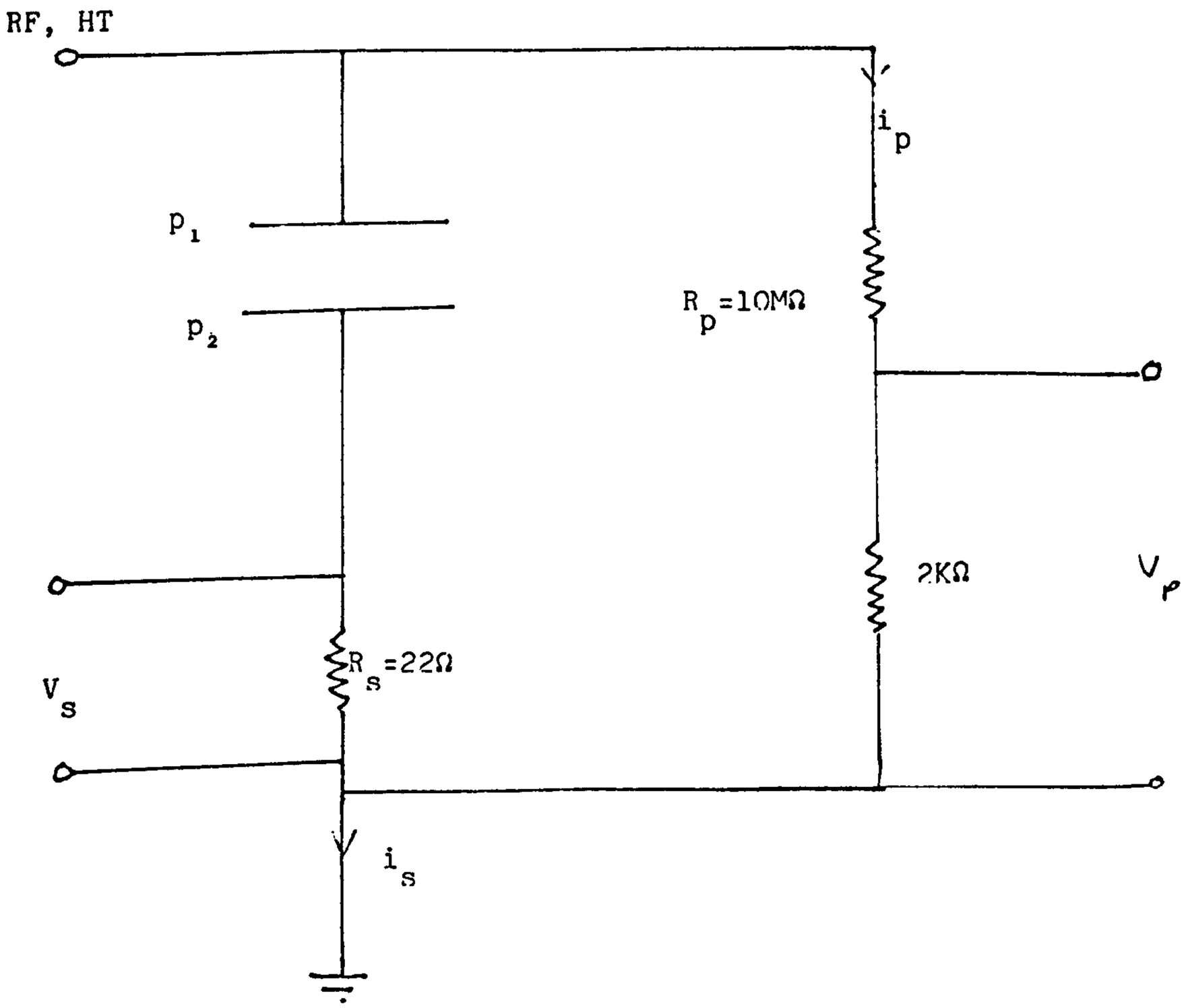

Fig.6.5 - Equivalent circuit for estimating the RF power output across the discharge plates P_1, and P_2. For the values of R_s and R_p shown, the current in series with the plates, i_s, is much greater than that parallel to the plates i_p. A glow-discharge in air was performed at a pressure of ~ 100 m Torr with dc power inputs as described in the text.

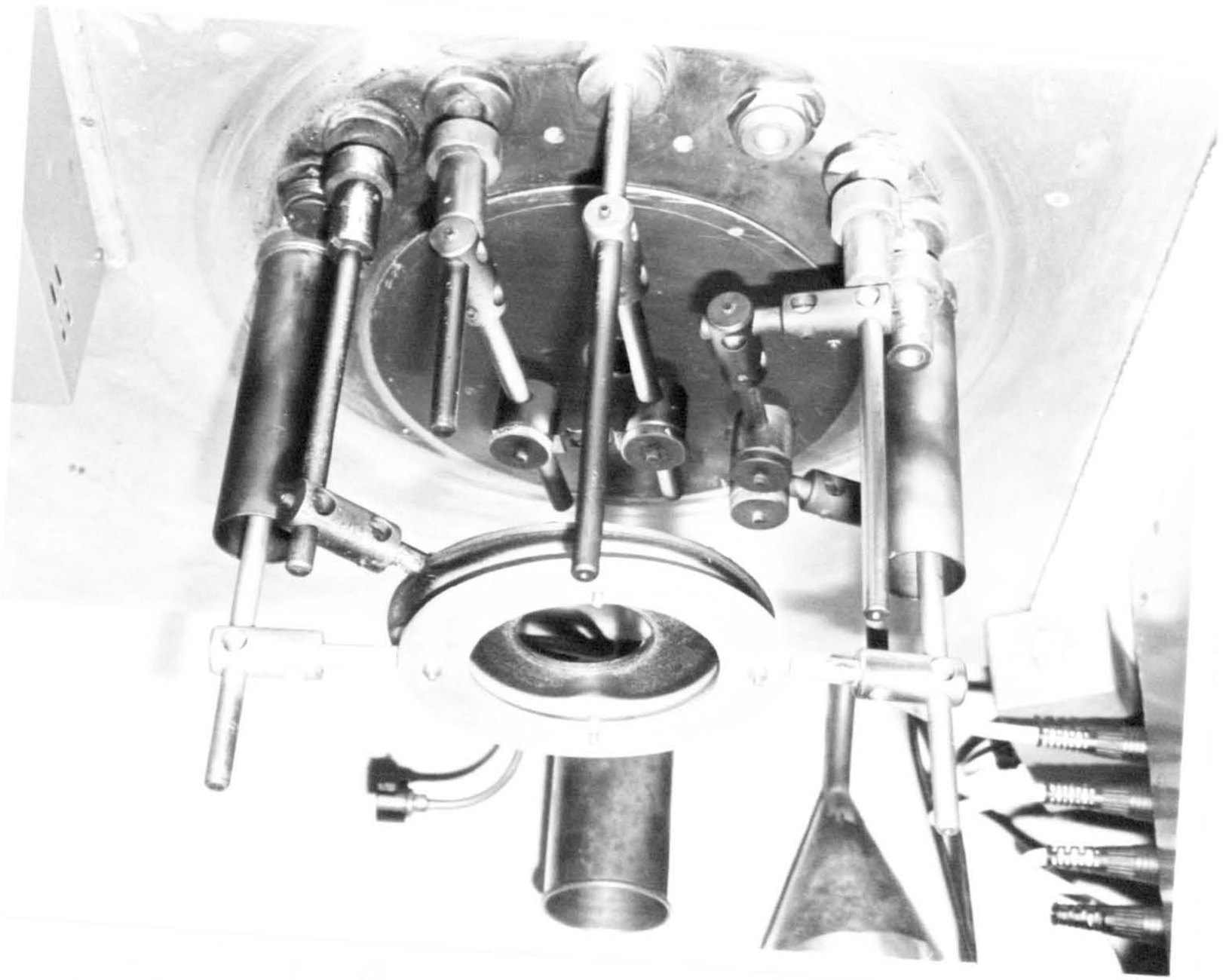

Plate 6.3 - Photograph of RF bottom electrode geometry and substrate holder.

With the above configuration peak to peak values of•4V and 100 mV were measured on an oscilloscope for the potentials V_s and V_p respectively, giving an approximate rms RF power output of ∿10W across the plates.

The dc power input to the RF oscillater was ∿ 20W; losses incurred are expected to be partly due to heating of components in the oscillater circuit. The above level of RF power, i.e. 10W, was maintained throughout all subsequent work.

GDP film thickness was essentially controlled by the monomer flow-rate. However, since GDP exposure times were in general quite short (of the order of a few seconds) the amounts of monomer used were small, so prohibiting any accurate determination of the flow-rates. For this reason it is more convenient to quote the dynamic chamber pressures during GDP, and the exposure times rather than absolute flow-rates. Over a more prolonged period it has been ascertained that the corresponding flow-rates lie in the approximate range 0.1 to 0.3 $cm^3\ min^{-1}$ for the range of chamber pressures used in the present work. Typical values of chamber pressures and exposure times were 50-100 m Torr, and 5-30 s respectively. Actual values for the individual monomers used are given in Table 6.1, and referred to in the Results and Discussion Section.

Immediately prior to polymerization the chamber was purged with Ar to remove any air-bourne contamination which may have entered the chamber while positioning the slide, since this may also be adsorbed on the oxide. The exclusion of such contamination is of paramount importance in IETS (19,21).

Finally, GDP was performed by introducing a monomer into the vacuum chamber via a needle valve, and copper 'J tube' arrangement. The monomer reservoir was coupled to the needle valve by means of a glass-to-metal seal and a lock-nut (see Plate 6.5). All monomers used were redistilled,

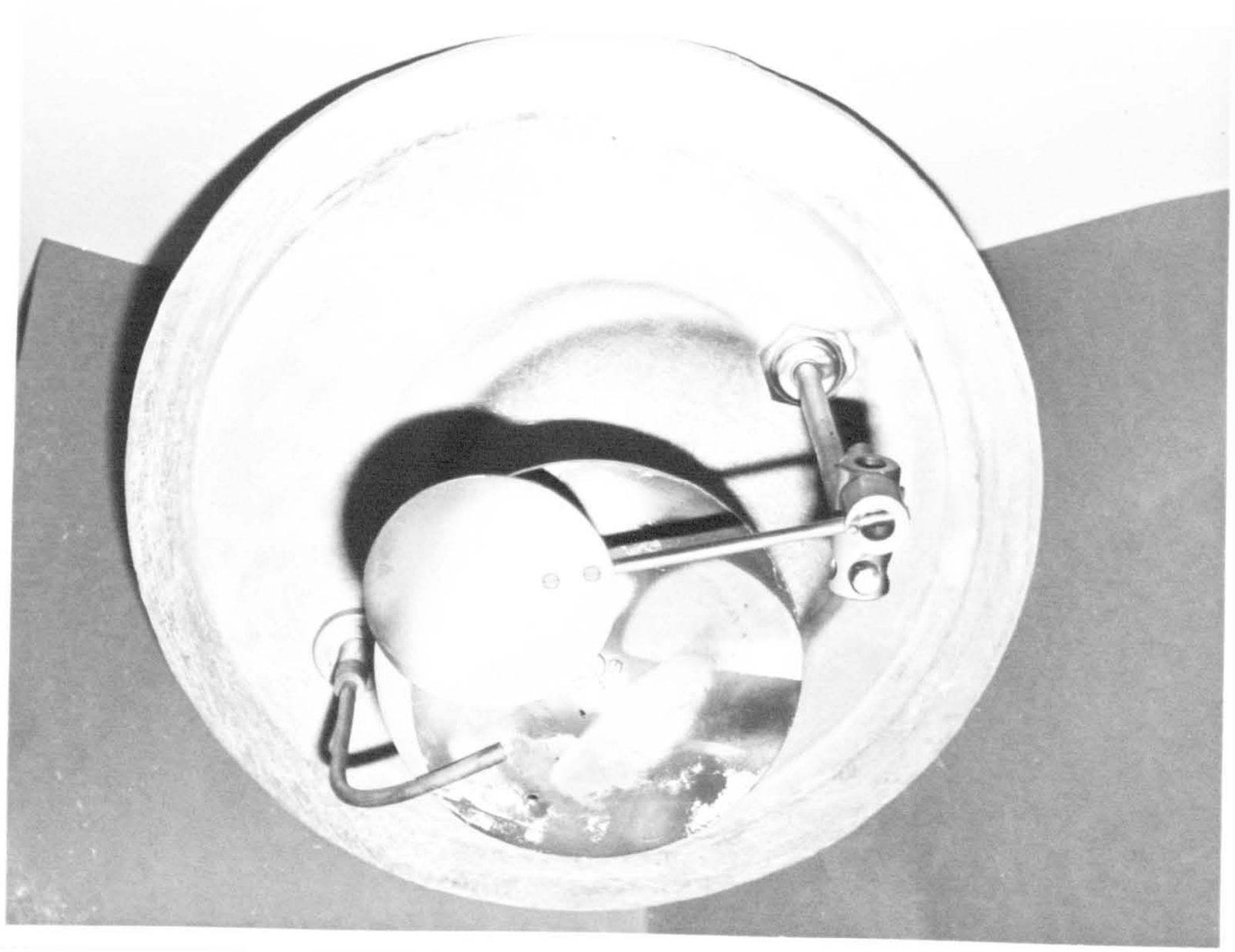

Plate 6.4 - Photograph of Aℓ top plate showing top RF electrode, copper 'J' tube, and shutter arrangement.

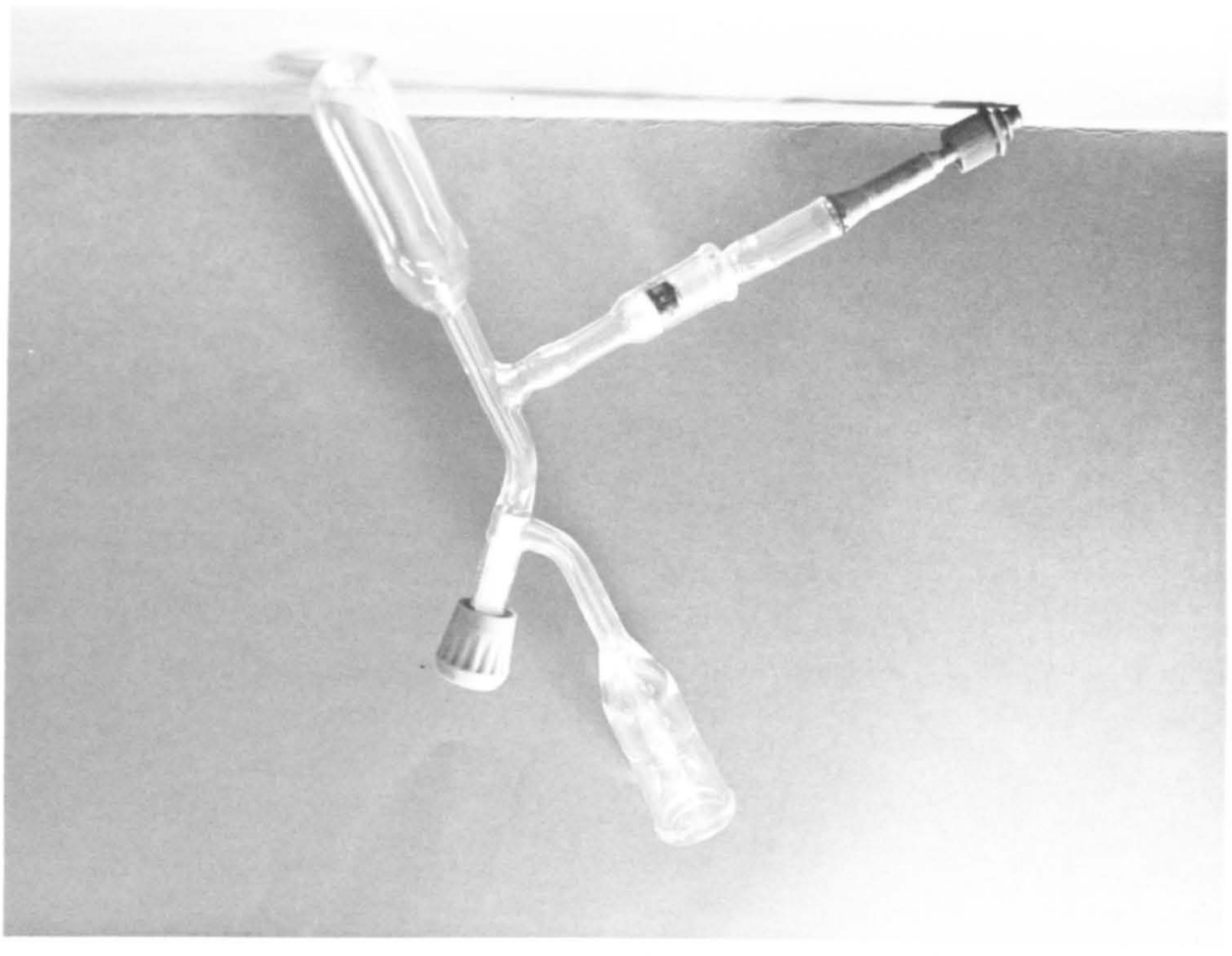

Plate 6.5 - Photograph of monomer reservoir.

Table 6.1 - Operating conditions employed for GDP of the monomers for IETS analysis.

Monomer	Chamber Pressure/m Torr	Exposure Time/s	Approximate IET Junction Resistance/Ω
Vinyl acetate	∿ 100	> 5	70
Ethyl acetate	∿ 100	10	50
Ethyl acrylate	∿ 100	∿ 10	80
Methylmethacrylate	∿ 100	∿ 15	200
Acrylic acid	∿ 50	30	100
Acrylonitrile	∿ 50	∿ 30	50
50% v/v mixture Styrene/vinyl-triethoxysilane	∿ 50	∿ 20	80
None (contamination check, glow-discharge oxidation in air)	∿ 100	30	30 J1 30 J2 30 J3 25 J4 25 J5

Note:

(i) RF power ≤ 10W for all monomers.

(ii) Flow rates in the approximate range 0.1 - 0.3 $cm^3\ min^{-1}$.

(iii) Approximate IET junction area ∿ 0.25 mm^2.

dried over CaH_2 and then de-gassed (while in the reservoir) by evacuation to ∿10 m Torr, and allowing them to freeze and thaw three times in liquid N_2. They were then sealed and stored in a refrigerator until required, or used directly. Once the monomer flow had been instigated and a stable pressure had been attained, the RF glow-discharge was established thus initiating polymerization.

In order to check the level of indigenous contamination in the system, the above procedure was performed intermittently using laboratory air instead of monomer vapour. Chamber pressures and exposure times in excess of those normally employed were chosen to ensure the worst possible case.

It is worth mentioning at this point that the GDP vacuum chamber is capable of attaining a pressure of $\sim 10^{-6}$ Torr. This would allow the Pb counter electrodes to be evaporated directly after the polymerization without breaking vacuum, thus avoiding the possibility of incorporating any atmospheric contaminants into the freshly deposited polymer film. To perform such Pb evaporations with the present system requires that the appropriate shadow mask must be positioned over the glass slide and consequently held there during polymerization. It is also necessary to shield the Pb evaporation source by means of a shutter arrangement which prevents any polymeric material from being deposited on it. After polymerization the shutter is removed, and the Pb electrodes evaporated as usual through the mask. Unfortunately when this method is adopted poor quality, discontinuous films are invariably produced - perhaps due to large electric field build-up at the edges of the mask during polymerization. Evidently for the deposition of films of an acceptable quality the mask must be withdrawn during polymerization. Facilities exist in the author's laboratory which would allow the development of a

moveable masking arrangement incorporating sliding vacuum seals; the whole electrode deposition, and GDP procedure could then be performed in situ. In fact a system has been developed by the author whereby vapour-phase doping may be achieved in a similar manner, and is described in Chapter 7. The time available towards the end of these research project did not allow this apparatus to be suitably modified for GDP, but clearly further work in this area would be interesting.

6.2.3 Deposition of GDP Films for IR Analysis

It must be emphasized from the outset that the present GDP system was designed primarily to meet the requirements of thin film deposition for subsequent IET analyses. The present section is intended merely to demonstrate that the system may be extended if necessary to accommodate the deposition of thicker films (of the order a few μm) suitable for IR analyses. Well established techniques better suited to the latter incorporating smaller chambers, greater flow-rates and RF power levels have been described extensively in the literature (1-13). In order to deposit GDP films suitable for IR analyses, it was necessary to make the following modificstions to the GDP system:

(i) Reduce the plate separation to ∿ 30 mm.

(ii) Increase the RF power level by adjusting the dc input parameters to ∿ 200 mA at 700V.

(iii) Increase the monomer exposure times, and flow-rates; typical values were several tens of minutes, and between ∿ 0.5 and ∿ 0.7 $cm^3\ min^{-1}$ respectively.

Operating conditions employed for the individual monomers during polymerizations are given in Table 6.2 The net effect of the above modifications was to increase the film deposition rate. Typical rates

Table 6.2 - Operating conditions employed for GDP of some monomers for IR analysis.

Monomer	Chamber pressure/m Torr	Exposure Time/min	Flow Rate/cm^3 min^{-1}
Vinylacetate	90	180	0.49
Ethylacrylate	80	154	0.43
Methylmethacrylate	80	145	0.46
Acrylonitrile	100	97	0.68
None (contamination check, glow-discharge in air)	100	140	-

estimated for the IR work were of the order ~ 10 Å s^{-1} while those for the corresponding IET polymerizations were ~ 0.25 Å s^{-1}.

A KBr disc was used as the substrate, and mounted midway between the glow-discharge plates during the polymerization in a similar manner to the glass slide in the previously described IETS work. Once a film of suitable thickness had been deposited the disc was removed, and the IR spectrum was recorded immediately. For control purposes KBr discs were subjected to similar glow-discharge conditions using laboratory air instead of monomer vapour. Subsequent IR analyses of these discs showed no signs of any deposited layers.

IR spectra were recorded of all monomers before, and after GDP; for the sake of brevity only the data for vinylacetate and methylmethacrylate are presented. These data together with IR data for their respective polymers obtained by conventional techniques clearly indicate that polymeric films have been deposited.

6.3 RESULTS AND DISCUSSION

As one would expect, for a particular chamber pressure and flow-rate, an approximately linear dependence of GDP film thickness as a function of exposure time was observed. The RF power was also found to be crucial. In order to deposit thin films suitable for IET analyses when values greater than ∿ 5W were employed with the present GDP system the resulting IET junctions gave noisy and irreproducible spectra. Also, the number of junctions containing shorts was significantly increased. These results would suggest that as the RF power is increased beyond an optimum level, poor quality, discontinuous films are produced. This effect is not so important for the thicker films for IR work in the present context since their structure may be considered to be similar to the bulk polymeric material.

6.3.1 IET Spectra

6.3.1.1 Contamination Check

Fig.6.6 shows a typical set of blank IET spectra obtained from five IET junctions on the same glass slide, the oxidised Aℓ base electrodes having been subjected to an RF glow-discharge in laboratory air as described in Table 6.1.

Generally speaking the spectra are similar to those normally obtained from IET junctions with undoped, thermally grown oxides. Low junction resistances, approximately 30 Ω, and very weak spectral features due to CH, OH and COO^- vibrational modes (see Table 6.3) suggest that traces of atmospheric hydrocarbons, water, and possibly formic acid are adsorbed on the oxide surface. Levels of contamination are commensurate with those normally observed in the author's laboratory.

These data indicate that the Aℓ-oxide layer is not significantly

Table 6.3 - Assignment for blank IET spectra obtained after devices exposed to glow-discharge (see Fig.6.6 and Table 6.1 for spectra, and details of oxidation discharge respectively).

Peak No	IETS mV	IETS cm^{-1}	Assignment
1	36 (m)	282	Aℓ phonon
2	77 (w)	613	r(COO^-) and OH bend
3	115 (m)	919	Aℓ-O bulk phonon
4	131 (wm)	1049	r(CH_3)
5	143 (w)	1145	ν(C-O)?
6	163 (vw)	1307	$\delta_s(CH_3)$
7	171 (w)	1371	$\delta^s(CH_3)$
8	180 (w)	1444	$\nu^a(COO^-)$
9	199 (vw)	1597	$\nu^s(COO^-)$
10	231 (vw)	1855	^{a}Aℓ-O (2x) overtone
11	358 (m)	2879	ν(CH_2), ν(CH_3)
12	450 (m)	3621	ν(OH)- surface hydroxyls

Key to abbreviations and symbols used in assignment tables.

w. weak
m. medium
s. strong
sh. shoulder
v. very
r. rock
ν. stretch, ν_s - symmetric, ν_a - asymmetric
δ. deformation, δ_s - symmetric, δ_a - asymmetric.

n.b. All peak energies in cm^{-1} have been corrected for the superconducting energy gap of the Pb electrode by substraction of 8 cm^{-1} in the assignment tables.

Fig.6.6 - IET spectra of undoped devices after exposure to an RF glow-discharge in laboratory air.

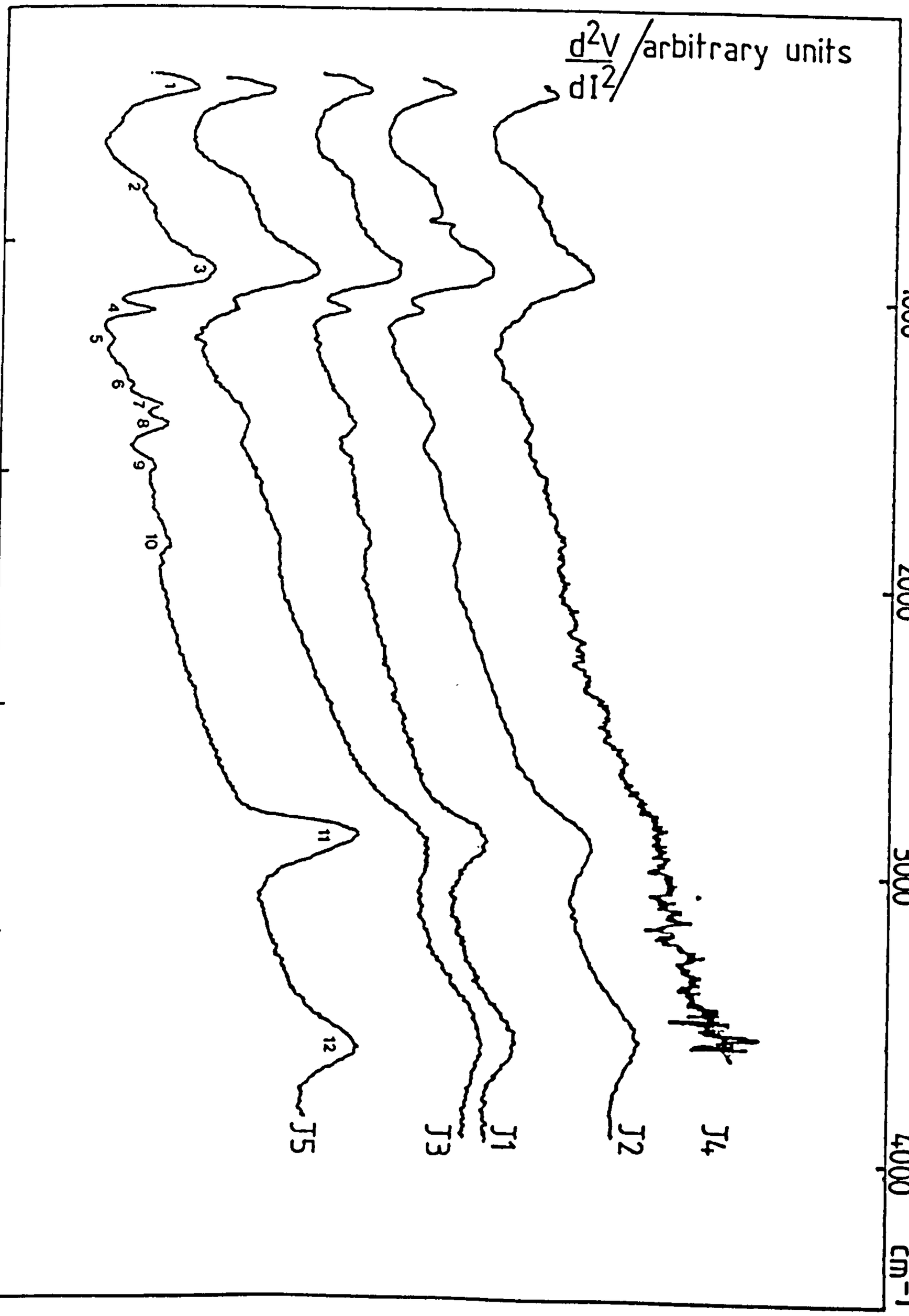

damaged by the RF discharge; it is known that poor oxide films containing defects such as pinholes produce inferior tunnel barriers sometimes resulting in electrical shorts across the junction. Clearly this is not the case here since the IET junction resistances and corresponding spectra are indicative of relatively clean, and uniform oxide layers.

It is noticed that the increases in IET junction resistances that ensue when the Aℓ electrodes are exposed to a glow-discharge in laboratory air are considerably less than those when monomer vapours are used (see Table 6.1). This strongly suggests that the latter are predominantly due to polymeric film formation and <u>not</u> oxide thickening.

6.3.1.2 <u>Glow Discharge Polymerized Vinylacetate (VA), Ethylacetate (EA), Ethylacrylate (EAc), Methylmethacrylate (MMA), Acrylic acid (AA), and Acrylonitrile (AN)</u>

The IET spectra of glow-discharge polymerized VA, EA, EAc, MMA, AA, and An are shown in Figures 6.7 to 6.12 respectively. Assignments for these spectra are given in Tables 6.4 to 6.9 respectively.

Good evidence for polymerization in all these spectra is the marked reduction in intensity the vinyl absorption usually observed and ∿ 1640 cm^{-1} and the presence of polymeric features such as low energy skeletal modes associated with vibrations of the carbon backbone. Strong aliphatic CH stretching, rocking, and deformation modes typical of polymeric samples in IETS are also present (25).

The IET spectrum of glow-discharge polymerized VA compares favourably with that of commercially available PVA (BDH suuplied, molecular weight 45,000) liquid-phase doped from a ∿ 0.04% w/v solution in acetone. These two spectra are shown in Figure 6.7a. Similar adsorbed species are therefore expected to be present on the Aℓ-oxide in both cases; this would

Table 6.4 - Assignment for GDP-IET spectrum of VA (see Fig.6.7)

Peak No	IETS mV	IETS cm^{-1}	Assignment
	33 (w.sh)	258	δ(C-C-O)?
1	37 (m)	290	Aℓ phonon
2	47 (sh)	371	
3	53 (w)	419	$r(COO^-)$ in plane?
4	78 (w)	621	$r(COO^-)$ out of plane
5	87 (w)	694	$\delta_s(COO^-)$
6	97 (w)	774	
7	111 (m)	887	ν(C-C)
8	117 (m.sh)	936	Aℓ-O bulk phonon
9	131 (m)	1049	$r(CH_3)$
10	143 (w)	1145	ν(C-C-O) skeletal
11	155 (w.sh)	1242	
12	162 (w)	1299	$\delta_s(CH_3)$
13	171 (m)	1371	$\delta^s(CH_3)$
14	179 (s)	1436	$\nu^a(COO^-)$
15	198 (m)	1589	$\nu^s(COO^-)$
16	212 (vw)	1702	$^a\nu(C=O)$
17	231 (w)	1855	Aℓ-O (2x) overtone
18	338 (vw)	2718	
19	357 (vs)	2871	$\nu(CH_2)$ and $\nu(CH_3)$ modes
20	368 (vs.sh)	2960	
21	382 (vw)	3073	=CH
22	452 (m)	3637	ν(OH) - surface hydroxyls

Fig.6.7 - GPD IET spectrum of VA.

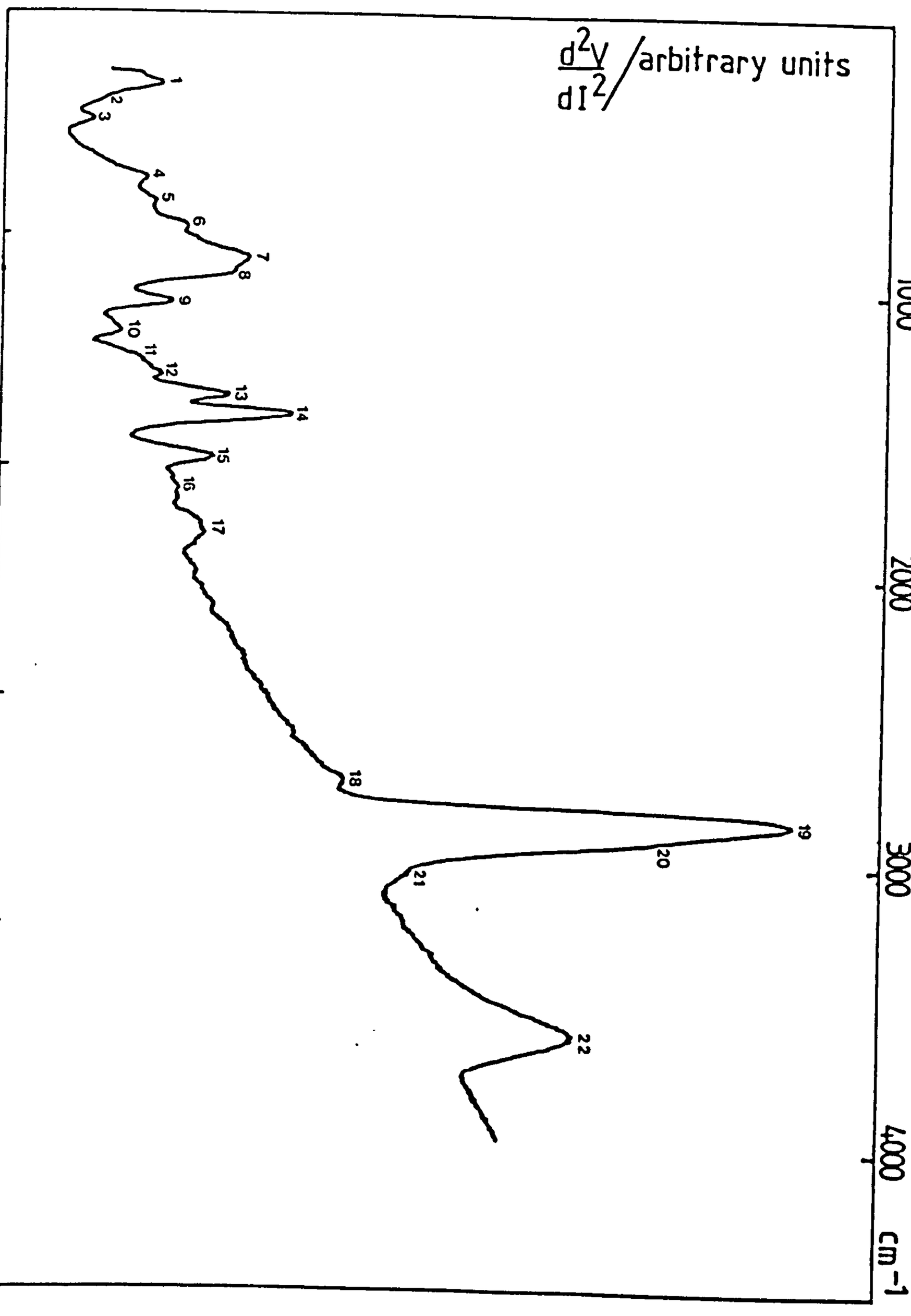

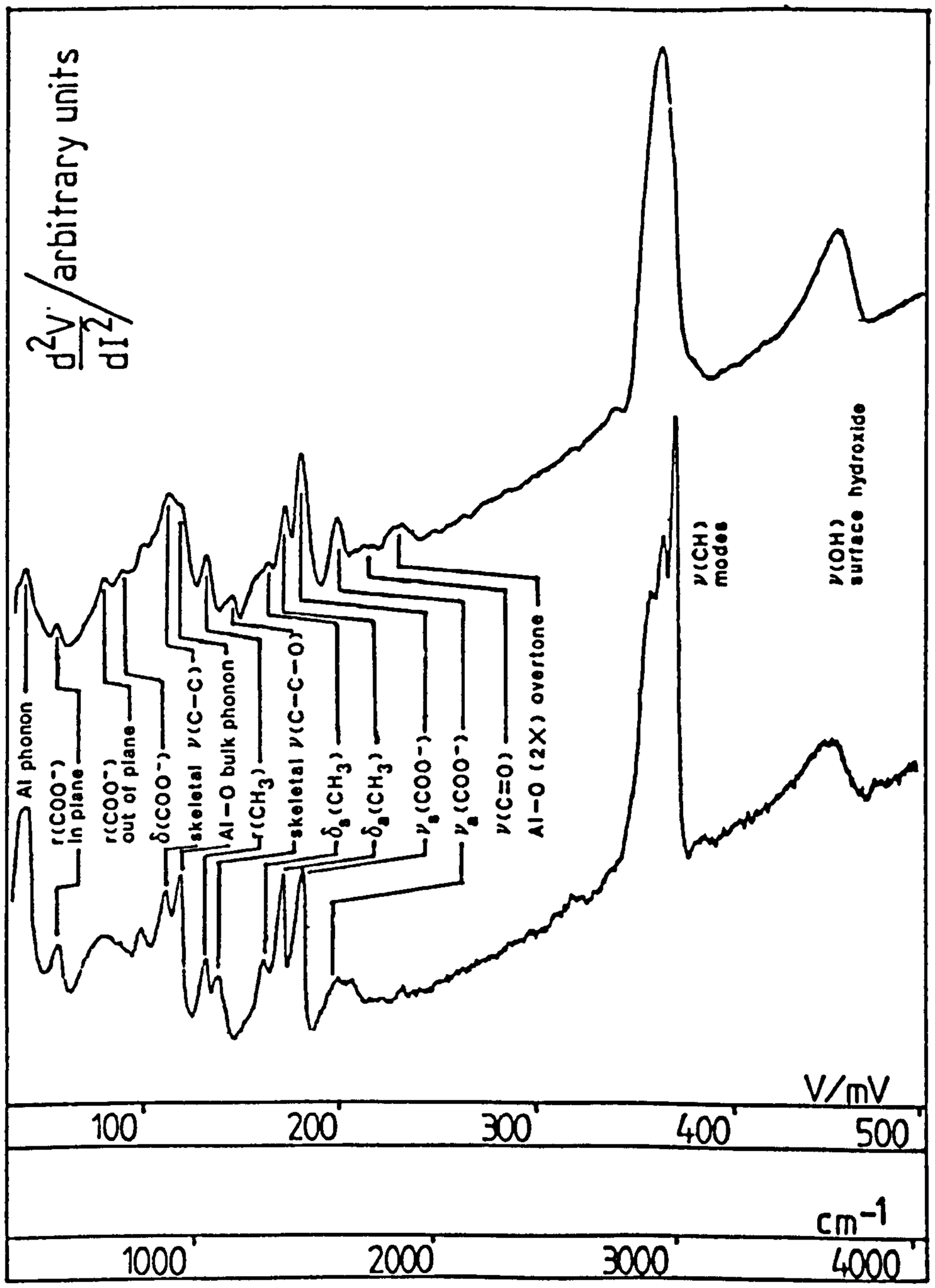

Fig.6.7a - Top GDP IET spectrum of VA.

Bottom IET spectrum of PVA (BDH supplied, molecular weight 45,000) liquid-phase doped from a ∿ 0.04% w/v solution in acetone.

Table 6.5 - Assignments for GDP-IET spectrum of EA (see Fig.6.8)

Peak No	IETS mV	IETS cm^{-1}	Assignment
1	33 (m)	258	
2	37 (m)	290	Aℓ-phonon
3	44 (vw.sh)	347	
4	53 (vw)	410	r(COO^-) in plane
5	76 (w)	605	r(COO^-) out of plane
6	86 (w)	686	δ(COO^-)
7	99 (w.sh)	790	
8	112 (m.sh)	895	ν(C-C)
9	117 (m)	936	Aℓ-O bulk phonon
10	130 (m)	1040	r(CH_3)
11	144 (vw)	1153	ν(C-C-O) skeletal
12	159 (w.sh)	1274	δ_s(CH_3)
13	171 (m)	1371	δ^s(CH_3)
14	179 (s)	1436	ν^a(COO^-)
15	197 (m)	1581	ν^s(COO^-)
16	210 (vw)	1686	ν^a(C=O)
17	230 (w)	1847	Aℓ-O (2x) overtone
18	358 (v.s)	2879	ν(CH_2) and ν(CH_3) modes
20	383 (vw.sh)	3081	ν(=CH)
21	451 (m)	3629	ν(OH) surface hydroxyls

Fig.6.8 - GDP IET spectrum of EA.

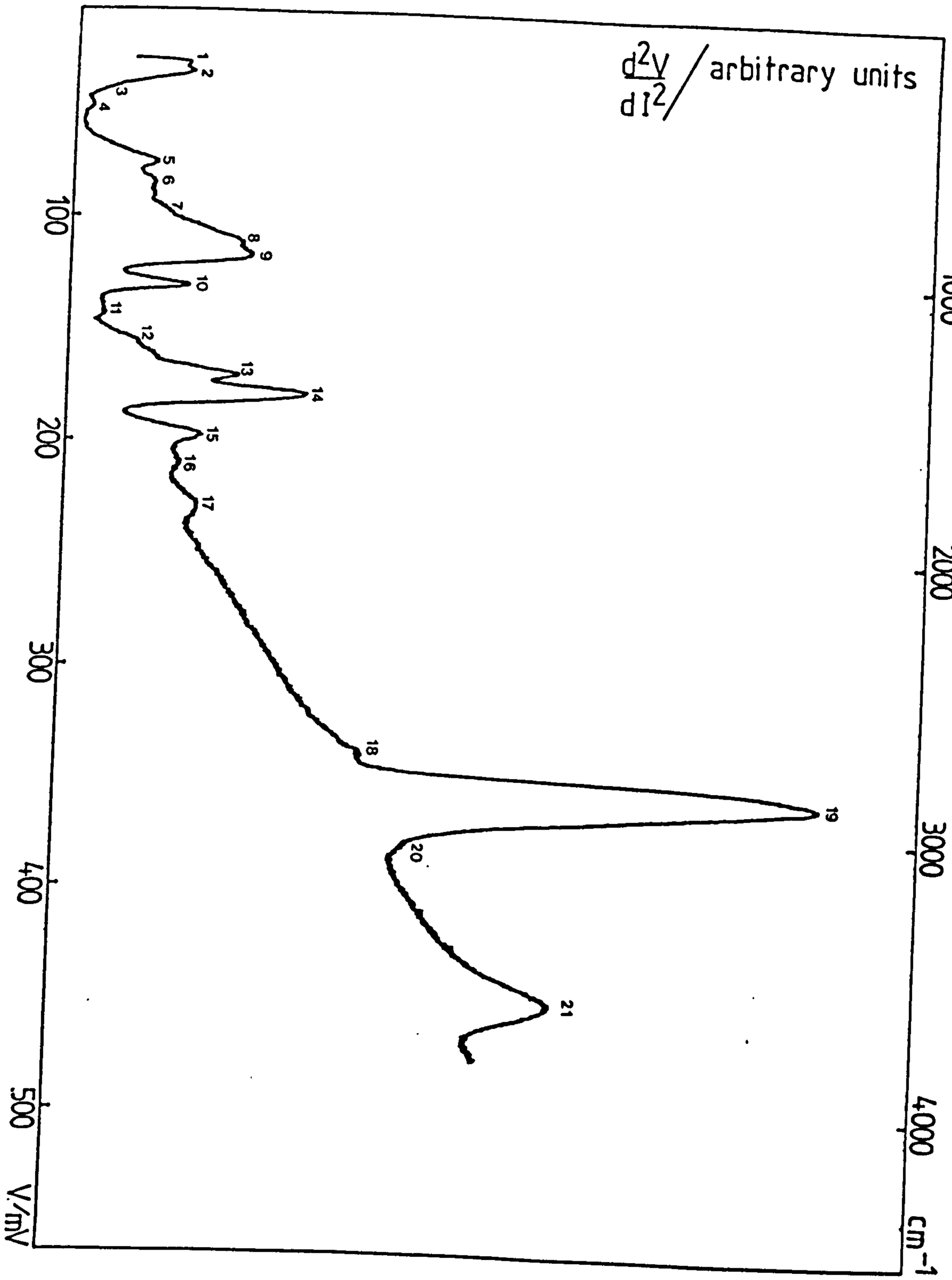

Table 6.6 - Assignments for GDP-IET spectrum of EAc (see Fig.6.9)

Peak No	IETS mV	IETS cm^{-1}	Assignment
1	33 (m)	258	δ(C-C-O)?
2	37 (m.sh)	290	Aℓ phonon
3	52 (w)	411	r(COO^-) in plane?
4	65 (w)	516	
5	77 (w)	613	r(COO^-) out of plane
6	88 (w)	702	$\delta_s(COO^-)$
7	96 (w)	766	
8	105 (w.sh)	839	
9	111 (m)	887	ν(C-C)
10	119 (m)	952	Aℓ-O bulk phonon
11	131 (m)	1049	r(CH_3)
12	144 (w)	1153	ν(C-C-O) skeletal
13	162 (m)	1299	$\delta_s(CH_3)$
14	171 (m.s)	1371	$\delta^s(CH_3)$
15	180 (s)	1444	$\nu^a(COO^-)$
16	199 (m)	1597	$\nu^s(COO^-)$
17	229 (vw)	1839	^{a}Aℓ-O (2x) overtone
18	337 (vw)	2710	ν(CH)
19	360 (vs)	2895	
20	378 (w.sh)	3041	$=CH_2$
21	453 (w.m)	3645	ν(OH) - surface hydroxyls

Fig.6.9 - GDP IET spectrum of EAc.

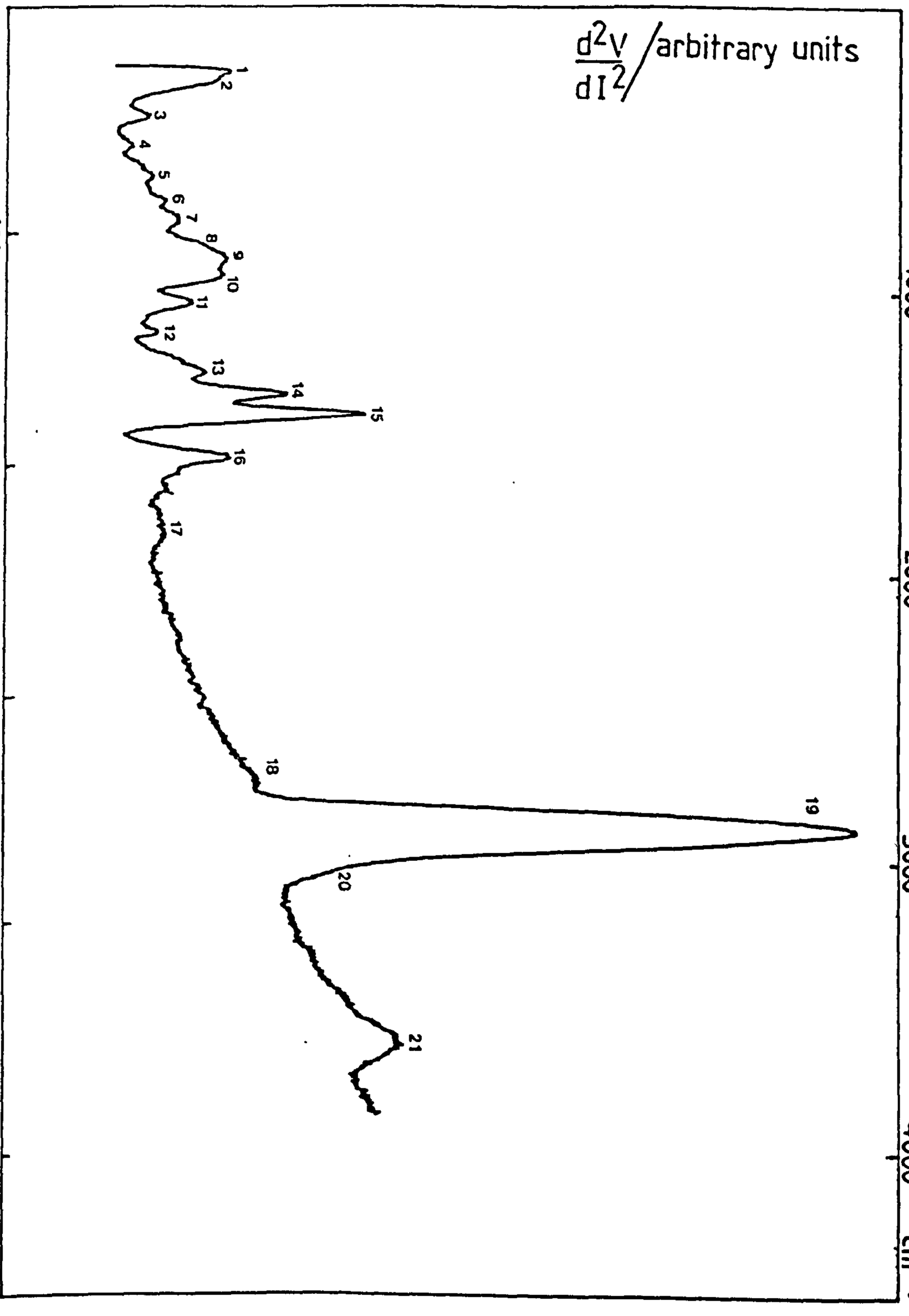

Table 6.7 - Assignments for GPD-IET spectrum of MMA (see Fig.6.10)

Peak No.	IETS mV	IETS cm^{-1}	Assignment
1	33 9m)	258	δ(C-C-O)?
2	38 (m.sh)	298	Aℓ phonon
3	45 (w.sh)	355	
4	53 (vw.sh)	419	$r(COO^-)$ in plane
5	78 (w)	621	$r(COO^-)$ out of plane
6	98 (w.sh)	782	
7	113 (m.sh)	903	
8	117 (m)	936	Aℓ-O bulk phonon
9	131 (w.m)	1049	$r(CH_3)$
10	171 (m)	1371	
11	179 (s)	1436	$\nu_s(COO^-)$
12	200 (w.m)	1605	$\nu^s(COO^-)$
13	229 (vw)	1839	$A\ell^a$-O (2x) overtone
14	361 (vs)	2903	ν(CH) modes
15	369 (vs.sh)	2968	
16	582 (w)	3073	
17	452 (m)	3637	ν(OH) - surface hydroxyls

Fig.6.10 - GDP IET spectrum of MMA.

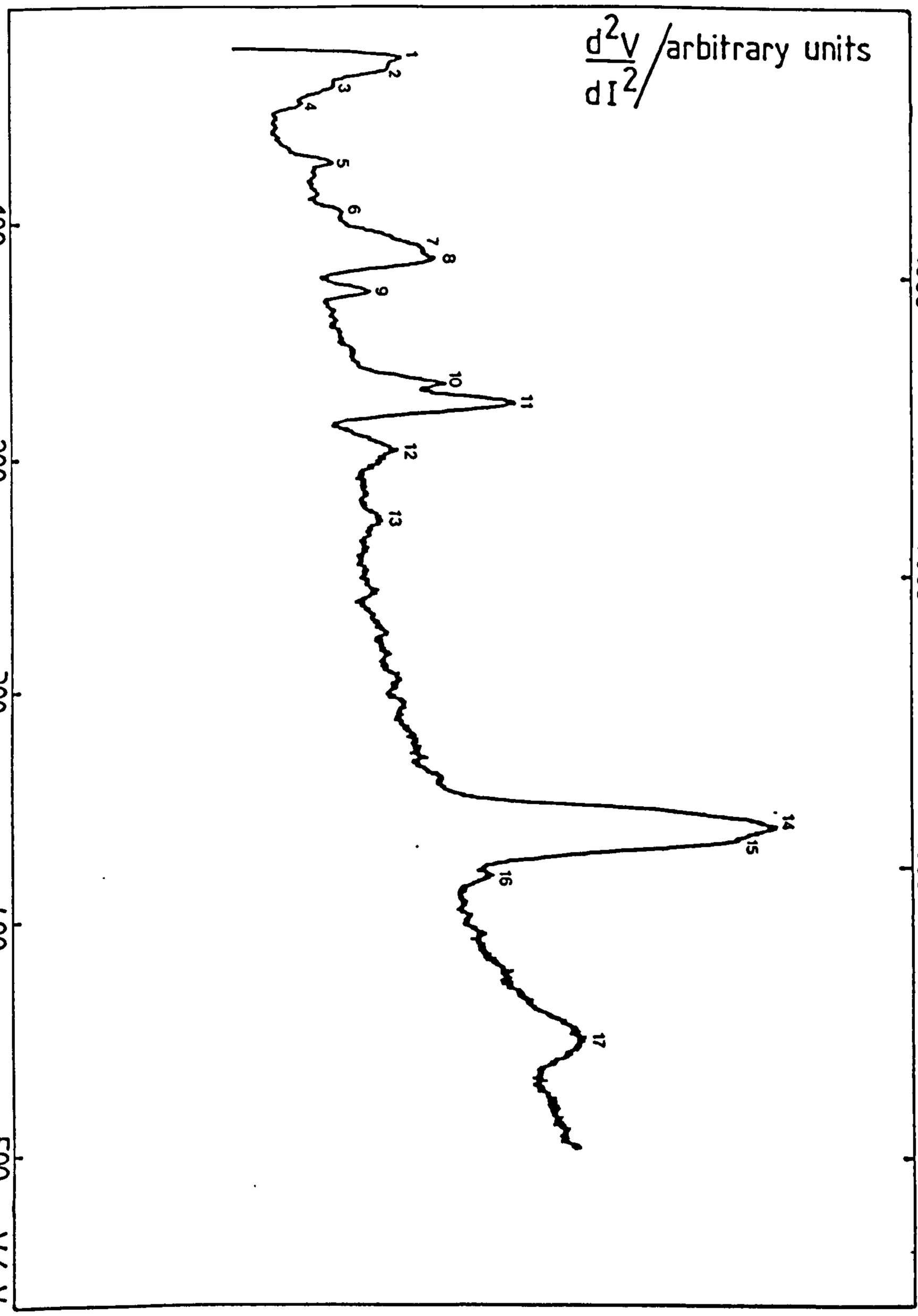

Table 6.8 - Assignments for GDP-IET spectrum of AA (see Fig.6.11)

Peak No	IETS mV	IETS cm^{-1}	Assignment
1	39 (m)	307	Aℓ phonon
2	58 (vw.sh)	460	$r(COO^-)$ in plane
3	63 (w)	500	
4	73 (w)	581	$r(COO^-)$ out of plane
5	82 (vw)	653	$\delta(COO^-)$
6	114 (m)	911	Aℓ-O bulk phonon
7	134 (w)	1073	$r(CH_3)$
8	151 (vw)	1210	
9	159 (w)	1274	
10	166 (w)	1331	$\delta_s(CH_3)$
11	172 (m)	1379	$\delta^s(CH_3)$
12	182 (s)	1460	$\nu^a(COO^-)$
13	199 (m.sh)	1597	$\nu^s(COO^-)$
14	208 (m)	1670	$^a\nu(C=C)$
15	213 (m.sh)	1710	$\nu(C=O)$
16	230 (w)	1847	Aℓ-O (2x) overtone
17	360 (vs)	2895	$\nu(CH)$
18	367 (vs.sh)	2952	
19	379 (w)	3049	$\nu(=CH)$
20	453 (m)	3645	$\nu(OH)$ - surface hydroxyls

Fig.6.11 - GDP IET spectrum of AA.

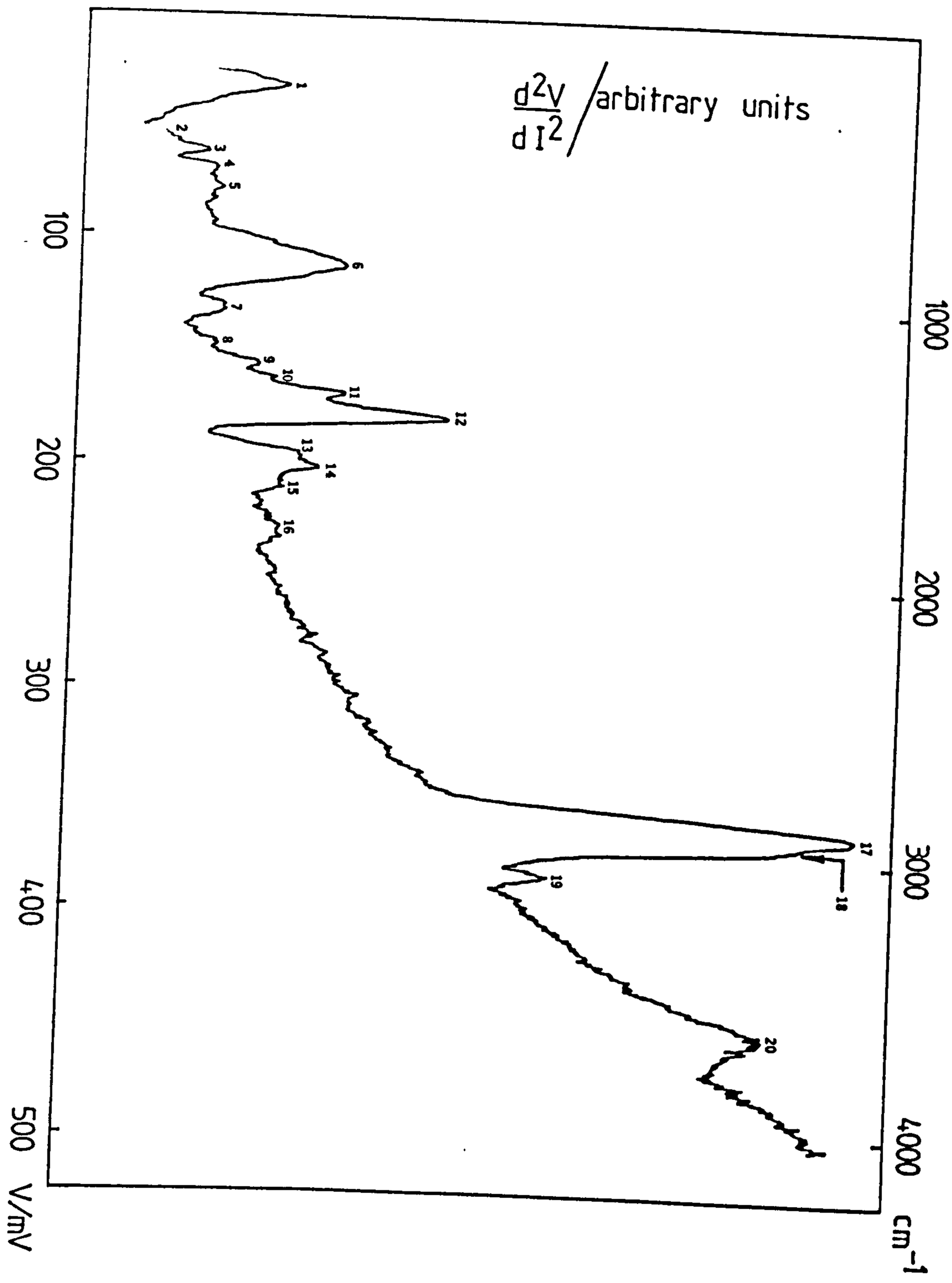

Table 6.9 - Assignments for GDP-IET spectrum of AN (see Fig.6.12)

Peak No	IETS mV	IETS cm^{-1}	Assignment
1	36 (m)	282	Aℓ phonon
2	50 (w.sh)	395	δ(C-C≡N)
3	70 (w.sh)	557	
4	78 (w.sh)	621	and OH bend
5	86 (w.sh)	686	
6	116 (m)	928	Aℓ-O bulk phonon
7	131 (wm)	1049	$r(CH_3)$
8	162 (vw.sh)	1299	$\delta_s(CH_2)$
9	171 (m)	1371	$\delta^s_a(CH_2)$
10	180 (m)	1444	
11	200 (wm)	1605	
12	231 (w)	1855	Aℓ-O (2x) overtone
13	278 (m)	2234	ν(C≡N)
14	358 (s)	2879	ν(CH) modes
15	450 (m)	3621	ν(OH) - surface hydroxyls

Fig.6.12 - GDP IET spectrum of AN.

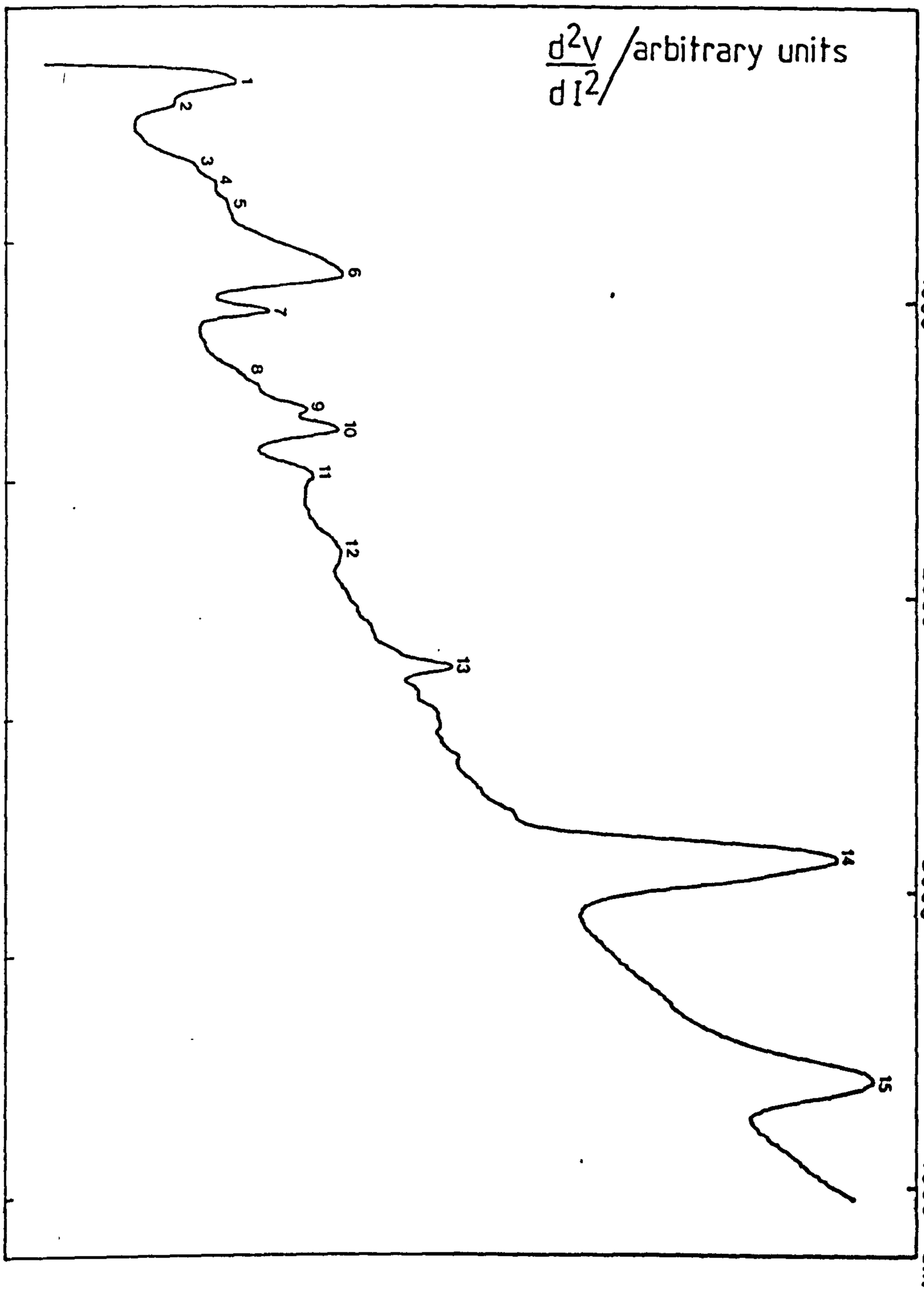

suggest that no significant differences exist between the composition of the adsorbed GDP film and that of liquid-phase doped PVA. A detailed account of the adsorption of PVA has been given in Chapter 5. The reader is reminded that acid-, or base-catalysed hydrolysis of PVA at the hydrated Aℓ-oxide surface lead to its subsequent adosrption as PVOH with acetic acid being produced as a by-product. Glow-discharge polymerized EA is anticipated to adsorb in a manner analogous to PVA. Indeed, its IET spectrum (Fig.6.8) is almost identical to that of glow-discharge polymerized VA.

The adsorption of PMMA on Aℓ-oxide has also been discussed in Chapter 5. Briefly, it was proposed there that hydrolysis of PMMA at the oxide surface generated carboxylate side groups on the polymer. These were then chemisorbed by the formation of bidentate symmetrical bridging complexes with Aℓ ions in the oxide. Methyl groups removed during hydrolysis recombined with surface hydroxyls on the oxide to produce methanol as a by product. Common features in the spectra of glow-discharge polymerized MMA, EAc,AA, and liquid-phase doped PMMA are not surprising, and it is suggested that all are adsorbed in a manner similar to that just described. Hydrolysis by-products for PEAc, and PAA would be ethanol and water respectively. The low energy region of the spectrum of PEAc is somewhat busy due to polymeric skeletal vibrations. It is possible that reactive ethyl fragments produced during hydrolysis may also have polymerized to form long-chained hydrocarbons which may have been adsorbed on the oxide.

Broadly speaking, the adsorption of glow-discharge polymerized AN is not fully understood. From Table 6.1 it is observed that a relatively long glow-discharge exposure time was required in order to obtain acceptable IET junction resistances. Even then, the resulting spectra were quite weak. One might infer that the polymer is not strongly adsorbed on the

oxide. It is possible that a proportion of the highly polar nitrile side groups may be hydrogen bonded to surface hydroxyls on the oxide. The plausibility of this mechanism is qualified in part by a fairly strong OH stretching peak centred at 3621 cm^{-1}, although the characteristic nitrile peak at 2234 cm^{-1} would have been expected to be somewhat stronger due to the orientational selection rules. Additionally, it should be emphasized in this context that the position and intensity of the OH stretching peak is notoriously variable in IETS. Any consideration of surface chemistry based upon observations regarding this mode should be treated with caution.

6.3.1.3 <u>50% v/v Mixture of Styrene/Vinyltriethoxysilane (S/VTES)</u>

Initial attempts to incorporate glow-discharge polymerized films of styrene in IET junctions proved unsuccessful. Prolonged exposure times (several minutes) were required to produce acceptable junction resistances. Resulting spectra were weak, and noisy indicating that the observed increases in resistance were primarily due to oxide thickening, and not film deposition. Furthermore, polymerizations for IR analyses were unfruitful. Consequently it could not be ascertained whether or not the styrene had actually polymerized.

Two simple experiments outlined below were then conducted to see if a known adhesion promoter - VTES could improve the adsorption of styrene.

(i) A set of oxidized Aℓ base electrodes were vapour-phase doped with VTES such that near-monolayer coverage of the surface was achieved; it is known that an exposure time of ∿ 8 minutes is about right for this in our laboratory (23). These doped electrodes were then placed in the GDP chamber, and exposed to a glow-discharge of styrene vapour for ∿ 15 s. The IET junctions were completed in the usual manner by the evaporation of the Pb electrodes.

(ii) A similar set of electrodes were exposed to a glow-discharge of a 50% v/v mixture of S/VTES. The Pb electrodes were then evaporated as usual operating conditions for the discharge are given in Table 6.1.

Perhaps surprisingly, the resulting IET spectra from both of these experiments were for all intents and purposes the same. Figure 6.13 shows a typical spectrum obtained from the latter, assignments are given in Table 6.10. The IET, and IR spectra of VTES are shown in Figure 6.14 (24).

Brewis et al (23) have used IETS to investigate the adsorption of several silane coupling agents on Aℓ-oxide by vapour-phase doping. For VTES they proposed that adsorption was by bonding of the three ethoxy oxygen atoms to the surface, perhaps by hydrogen bonding between their lone pairs and surface hydroxyls. Comparison between the spectra of vapour-phase doped VTES, and glow-discharge polymerized S/VTES indicates that the majority of the strong IET lines in the latter from approximately 1000 cm^{-1} onwards are due to VTES (see Table 6.10). However, several additional modes are present due to low-energy vibrational modes of the aromatic styrene ring. Also; the aliphatic CH stretching modes c.a. 2881 cm^{-1} are much stronger.

It is tentatively suggested that in (i), and (ii) above adducts of styrene and VTES may have been formed. Since styrene does not readily adsorb when glow-discharge polymerized on its own it is anticipated that styrene would not play an active role in the adsorption of such adducts. Presumably they would be adsorbed by bonding of the ethoxy oxygens of VTES as described above. It is tentatively suggested that styrene and VTES may copolymerize.

At this stage it is not certain to what degree, if any, polymerisation has occurred. Further work to investigate the adsorption of other glow-discharge polymerized silane coupling agents would be interesting. Such

Table 6.10 - Assignments for GDP-IET spectrum of glow-discharge polymerized mixture (50% v/v) of styrene/A151. (see Fig.6.13)

Peak No	IETS mV	IETS cm^{-1}	Assignment
1	33 (s)	258	Aℓ phonon
2	44 (m)	353	
3	49 (m.sh)	393	
4	61 (m)	493	
5	70 (m)	564	Styrene aromatic
6	80 (m)	642	ring modes
7	86 (m)	691	
8	93 (m)	751	
9	99 (m)	796	
10	108 (ms)	873	
11	111 (ms)	896	Aℓ-O bulk phonon
	118 (sh)	954	
12	124 (m)	1002	ν (Si-O-C)
13	129 (m)	1038	ν^{s}(Si-O-C)
14	137 (m)	1102	$^{a}\nu$(Si-C)
15	142 (w)	1142	ν(Si-O-CH_2)
16	152 (m)	1228	
17	162 (ms)	1306	δ (CH_3) and =CH_2
18	172 (s)	1385	δ^{s}(CH_3)
19	190 (ms)	1530	ν(C=C)
20	201 (w)	1623	
21	223 (vw)	1797	Aℓ-O (2x) overtone
22	271 (vw)	2184	
23	238 (vw)	2722	
24	357	2881	Aliphatic ν(CH)
25	362 (vs)	2916	modes
26	367	2957	
27	377 (m)	3042	ν(=CH_2)
28	453 (m)	3650	ν(OH) surface hydroxyl

Fig.6.13 - GDP IET spectrum of 50% v/v S/VTES.

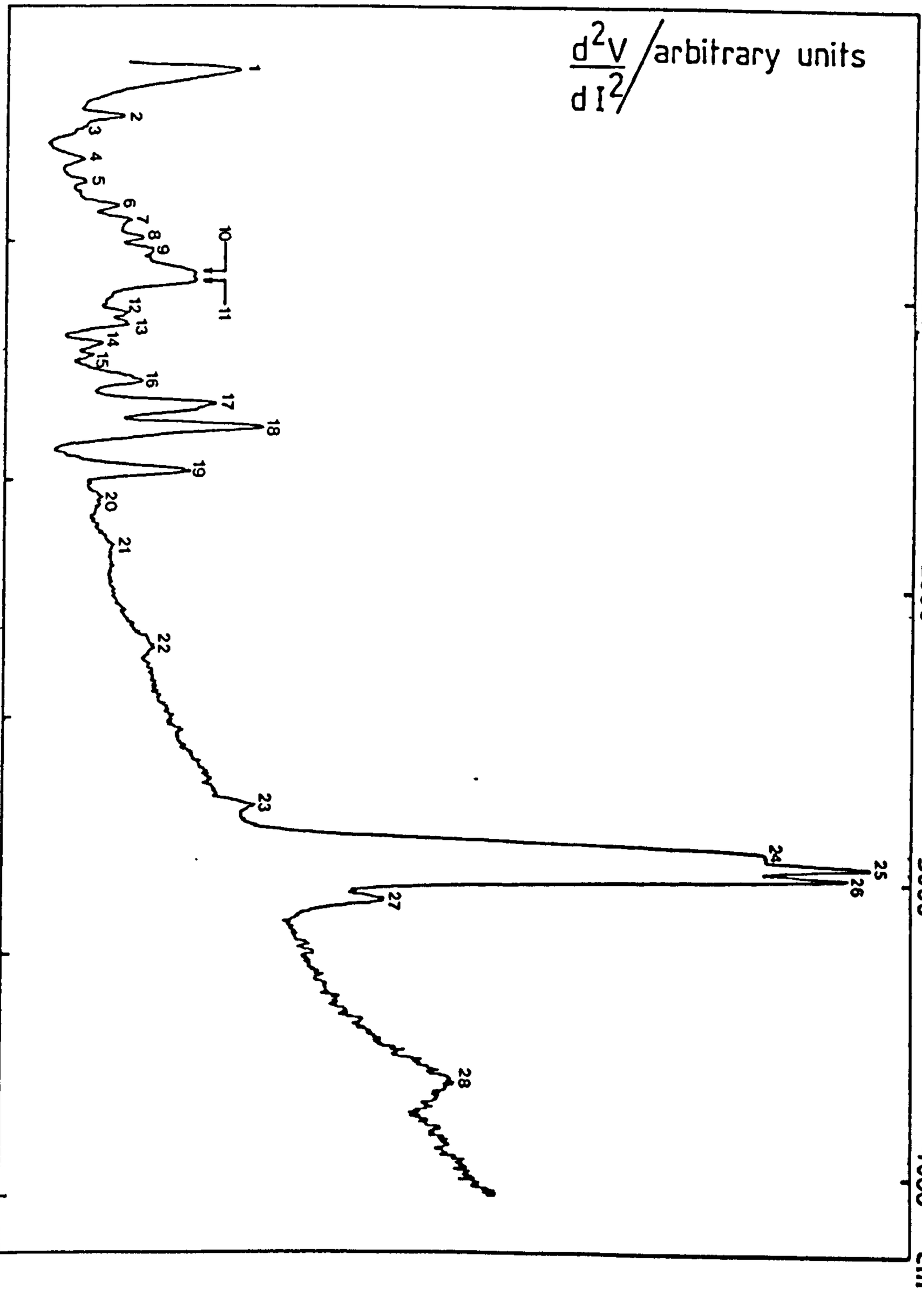

Fig.6.14 - IET and IR spectra of VTES (24).

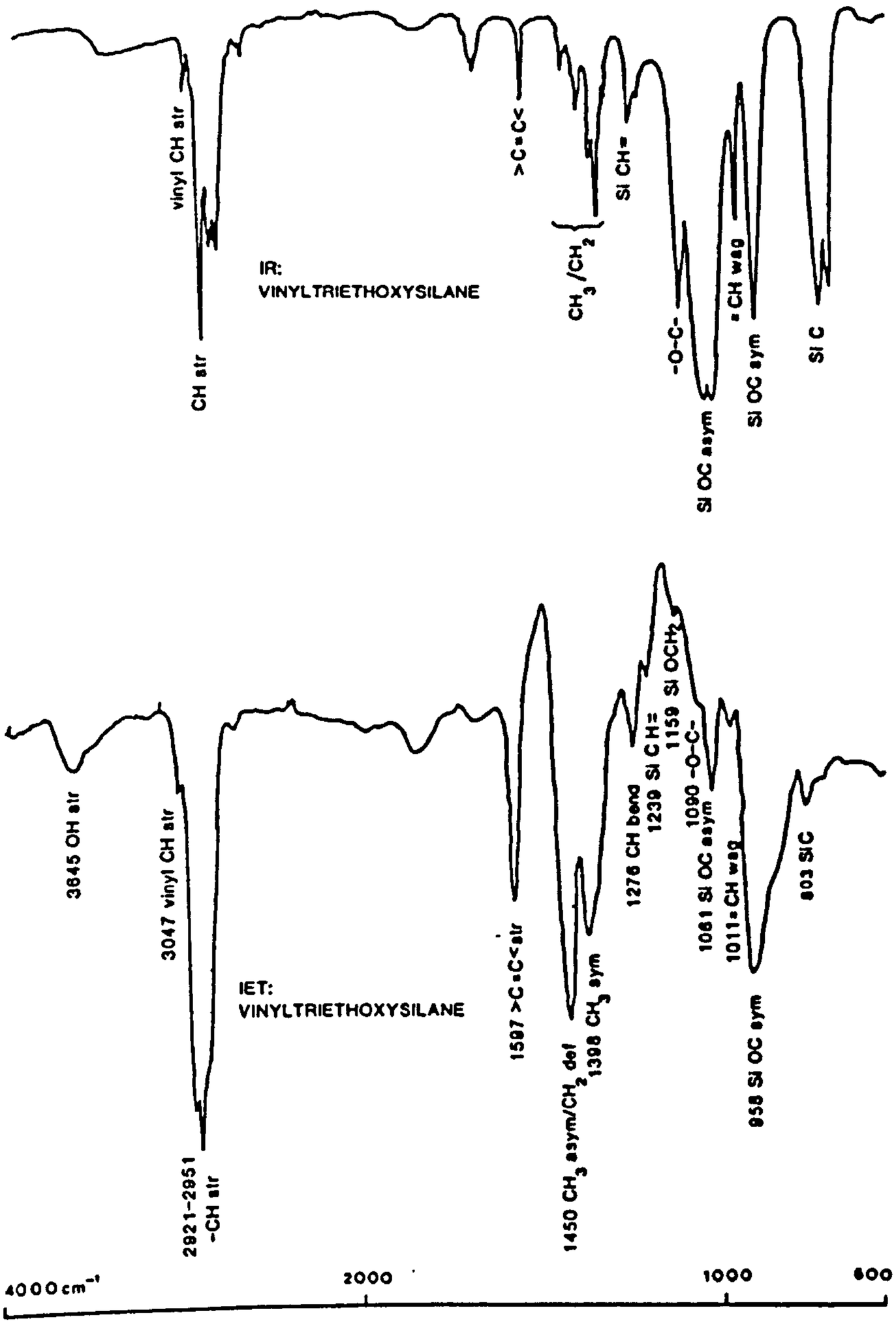

work was deemed beyond the specifications and requirements of the present research programme.

6.3.2 IR Spectra

6.3.2.1 Contamination Check

Spectra were recorded before and after KBr discs were subjected to glow-discharge in laboratory air. Operating conditions are given in Table 6.2. No significant changes were observed and the spectra were typical of blank KBr; i.e. the only features present were weak, broad bands at 1600 and 3400 cm^{-1} due to traces of absorbed water.

6.3.2.2 Glow-discharge Polymerized Vinylacetate (VA)

The spectra of VA, and glow-discharge polymerized VA are shown in Figures 6.15(a) and (b) respectively. Clear evidence for polyermization is the significant reduction in intensity of the monomeric vinyl absorption at 1650 cm^{-1} (indicated in the figure) and also the absence of the =CH stretching vibration at 3100 cm^{-1}. The present of some residual vinyl absorption in the spectrum could be due to a low degree of polymerization, and/or chain termination by disproportionation, i.e.

$$2(\sim\!\!\sim CH_2 - \underset{\displaystyle R}{\overset{\displaystyle |}{C}}\cdot H) \rightarrow \quad \sim\!\!\sim CH_2 - CHR \; + \; CH = CHR$$

Another feature which indicates that polymerization has occurred is that the strong monomeric C-O-C asymmetric stretch at 1220 cm^{-1} has been shifted to the polymeric value of 1240 cm^{-1}; the C-O-C symmetric stretch at 1140 cm^{-1} has been greatly reduced in intensity. Lower energy bands ($\lesssim$ 1000 cm^{-1}) due to the various CH rocking and deformation modes have in general experienced broadening. Overall, the spectrum of glow-discharge polymerized VA strongly resembles that of commercially available PVA (BDH

Fig.6.15 - (a) IR spectrum of VA monomer.

(b) GDP IR spectrum of VA.

(c) IR spectrum of PVA (BDH supplied, molecular weight ~ 45,000) from a 5% solution in methanol.

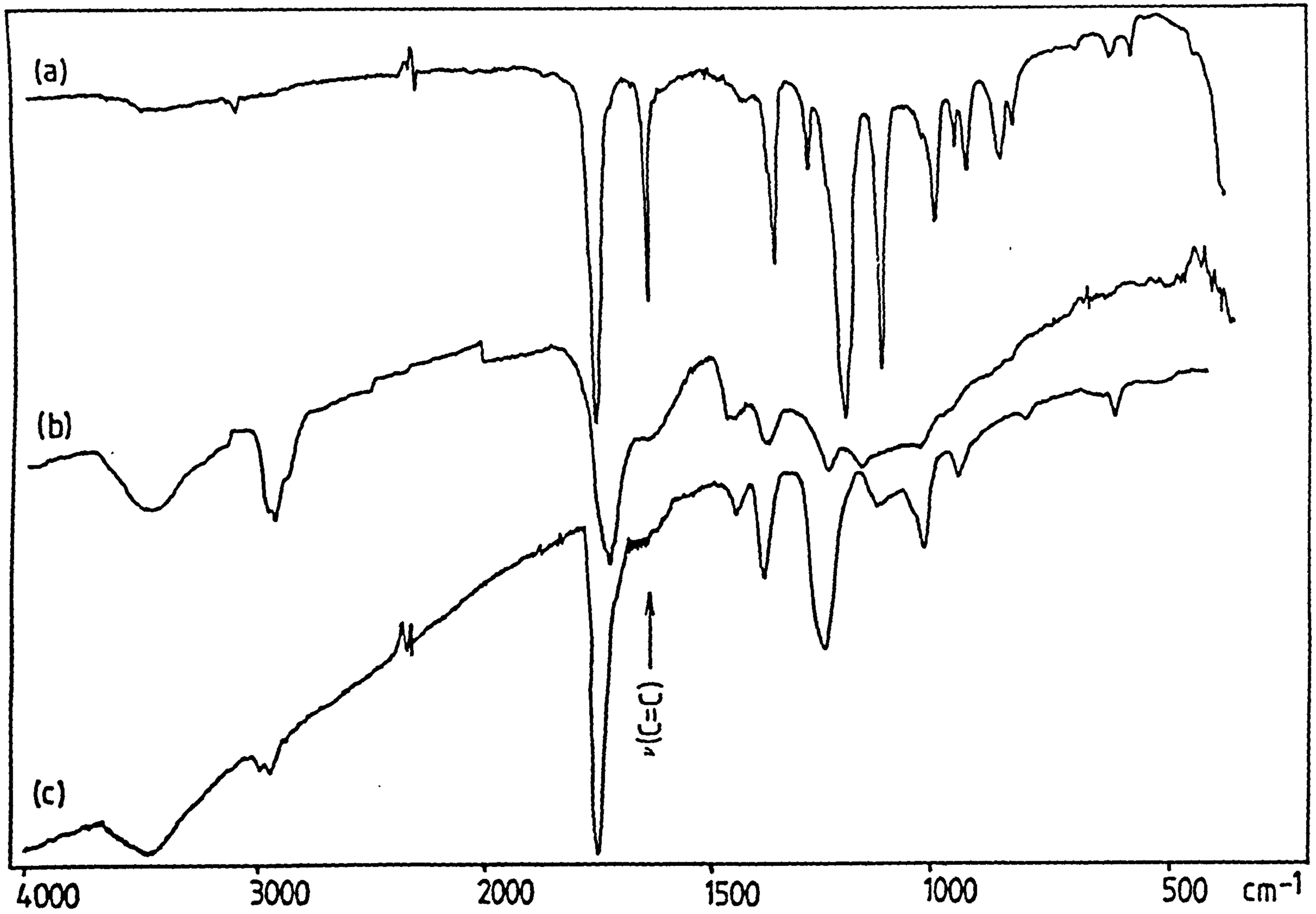
(a)
(b)
(c)
ν(C=C)
4000
3000
2000
1500
1000
500
cm⁻¹

supplied molecular weight 45,000, 5% w/v in methanol) shown in Fig.6.16(c). The spectrum of the former is slightly weaker; this is probably because the adsorbed PVA film is of insufficient thickness.

Assignments for the three spectra above, together with the IETS data for glow-discharge polymerized VA are given in Table 6.11.

6.3.2.3 Glow-discharge Polymerized Methylmethacrylate (MMA)

The spectra of MMA, glow-discharge polymerized MMA, and a ∿ 5% w/v solution of PMMA (supplied by Polymer Laboratories Ltd., molecular weight 45,000) in acetone are shown in Figures 6.17(a), (b) and (c) respectively. These data are not discussed in detail, but a few brief remarks are noted.

As was the case for PVA, reductions in intensity of the vinyl absorbtion, and =CH stretch at 1640 and 3100 cm^{-1} respectively (indicated in the figure) clearly show that polymerization of MMA has occurred. The spectrum of glow-discharge polymerized MMA compares favourably with that of PMMA, although the former is again somewhat weaker for reasons discussed in 6.3.2.2. above.

Table 6.11 - Comparison between IR spectrum of VA monomer, GDP-IR spectrum of VA, IR spectrum of PVA, and GDP-IET spectrum of VA

VA	IR/cm^{-1} GDP-VA	PVA	IET/cm^{-1} GDP-VA	Assignments
			258 (w.sh)	
			290 (m)	
			371 (sh)	
			419 (w)	
595 (w)				acetate out of plane def.
		600 (w)		
			621 (w)	
640 (w)				δ(O-C-O)
			694 (w)	
			774 (w)	
		790 (vw)		
850 (m)				$\delta(CH_2)$ out of plane
880 (m)			887 (m)	
			936 (m.sh)	
	970 (vw)	950 (w)		
965 (m)				
980 (m)				
1020 (m)		1020 (m)		
1050 (w.sh)	1040 (vw)		1049 (m)	
1140 (vs)	1160 (w)	1130 (w)	1145 (w)	ν_s(C-O-C)
1220 (vs)				
1240 (m.sh)	124o (w)	1240 (s)	1242 (w.sh)	ν_a(C-O-C)
1300 (m)				
1375 (s)	1380 (w)	1380 (m)	1299 (w)	$\delta_s(CH_3)$
1440 (w)	1440 (w)	1440 (w)	1371 (m)	$\delta^s(CH_3)$
			1436 (s)	$\nu^a(COO^-)$
			1589 (m)	$\nu^s(COO^-)$ IET
1650 (s)	1630 (w.sh)	1640 (vw.sh)		$^a\nu$(C=C)
1765 (vs)	1720 (s)	1740 (vs)	1702 (vw)	ν(C=O)
			1855 (w)	
			2718 (vw)	
	2880 (m)		2871 (vs)	$\nu(CH_2)$, $\nu(CH_3)$
	2940 (m)	2930 (vw)	2960 (vs.sh)	
	2960 (m)	2980 (vw)		
3100 (vw)			3073 (vw)	=CH
3430 (vw)	3480 (m)	3450 (m)	3637 (m)	ν(OH)

Fig.6.16 - (a) IR spectrum of MMA monomer.

(b) GDP IR spectrum of MMA.

(c) IR spectrum of PMMA (Polymer Laboratories (Ltd., molecular weight ~ 45,000) from a ~ 5% solution in acetone.

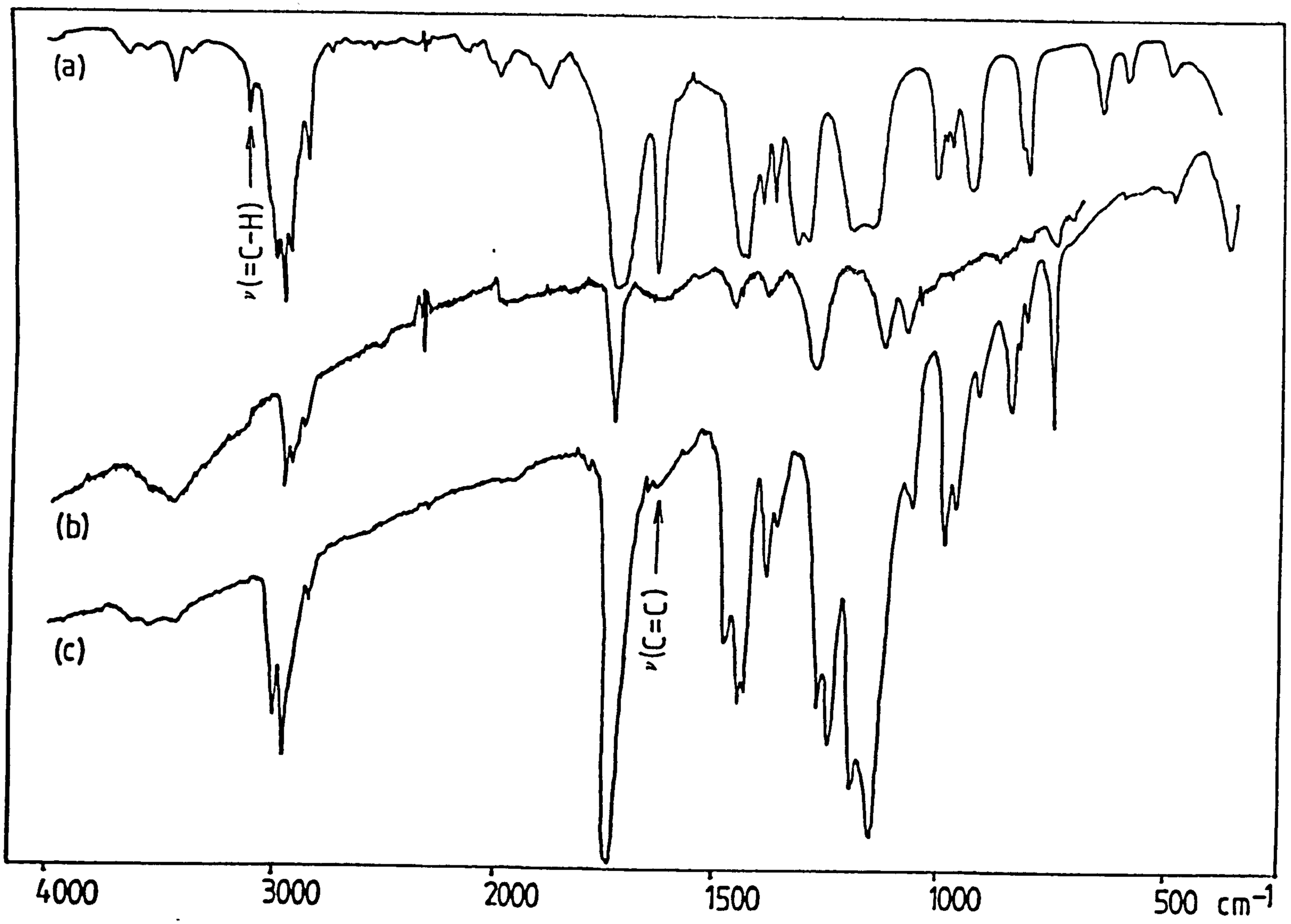
(a)
ν(=C-H)
(b)
(c)
ν(C=C)
4000
3000
2000
1500
1000
500 cm⁻¹

6.4 CONCLUSIONS

It has been demonstrated that continuous, pinhole-free films of the order a few Å's thick can be deposited relatively quickly, and easily by GDP. Such films have been shown to form suitable tunnel barriers for IETS, and thus GDP offers a new doping technique for IET junctions. An immediate advantage of the technique is that polymers may be investigated without the need for solents; polymer-solvent effects observed when liquid-phase doping are therefore eliminated.

Good quality films are difficult to produce if a mask is placed adjacent to the substrate - perhaps due to local electric field build-ups. Critical factors effecting film deposition are those one would expect, i.e. plate separation, power input to the system, chamber pressure, and glow-discharge exposure times. In general low powers (of the order $\sim$ 10W), and chamber pressures (nominally 100 m Torr) are ample for an exposure time of the order of a few seconds.

No significant damage is experienced by the Aℓ-oxide layer of the IET junctions during polymerization and the level of contamination indigenous to the system is acceptable for IETS.

The IET spectra obtained from glow-discharge polymerized VA, and MMA compare favourably with those of their liquid-phase counterparts whose adsorption has been discussed in Chapter 5. This is clear evidence that polymerization has occurred. It is believed that the adsorption of glow-discharge polymerized monomers EA and VA are analogous, while that of EAc and AA is analogous to that of MMA. The adsorption of glow-discharge polymerized AN is not fully understood. Its IET spectrum indicates that the polymer is only weakly adsorbed; this may be by hydrogen bonding of polar nitrile side-groups of the polymer to surface hydroxyls on the oxide. When the mixture of styrene, and VTES was glow-discharge polymerized, it is

anticipated that an adduct of the two may have been formed. The resulting IET spectrum indicates that this was adsorbed on the oxide surface by bonding of the three ethoxy oxygen atoms of the silane constituents as described by Brewis et al (23).

As would be expected in order to deposit thicker GDP films for subsequent IR spectroscopic analyses, proportionally longer glow-discharge exposure times are required. IR spectra of glow-discharge polymerized films of VA, and MMA deposited on KBr discs strongly resemble those of their respective polymers; this corroborates that polymeric films are formed, and provides a useful reference with which the corresponding IET spectra may be compared.

REFERENCES - Chapter 6

1. N.Inagaki, K.Nakazawa and K.Katsuura. J. Polym. Sci. Polym Chem. Lett., 19, 335 (1981).

2. L.L.Alt, S.W.Ing, Jnr., and K.W.Laendle. J. Electrochem.Soc. 110, 465 (1963).

3. D.R.Secrist and J.D.Mackenzie. J. Electrochem. Soc., 113, 914 (1966).

4. H.Yasuda, M.O.Bumgarner and N.Morosoff. Annual Report NIH-NHLI73-2913 (1973).

5. J.R.Hollahan and G.L.Carlson. J. Appl. Polym. Sci., 14, 2499 (1970).

6. A.Moshonov and Y.Avny. J. Appl. Polym. Sci., 25, 771 (1980).

7. N.Inagaki and H.Yasuda. J. Appl. Polym. Sci., 26, 3333 (1981).

8. N.Inagaki, M.Itami and K.Katsuura. Int. J. Adhesion and Adhesives, 2(3), 169 (1982).

9. H.Yasuda. Plasma Polymerization, M.Shen and A.T.Bell Eds., ACS Symp. Ser., 108, Washington D.C., 1979.

10. H.Yasuda and T.Hirotsu. J. Polym. Sci. Polym. Chem. Ed., 16, 743 (1978).

11. N.Inagaki and M.Taki. J. Appl. Polym. Sci., 27, 4337 (1982).

12. D.T.Clark and M.M.Abu-Shbak. J. Polym. Sci. Polym. Chem. Ed., 22, 1 (1984).

13. S.M.Ojha. Physics of Thin Films. G.Hass, M.H.Francombe and J.L.Vossen (Eds.) 12, 237 (1982).

14. P.Poole and J.F.Watts. Lecture 31, Proceedings of the International Adhesion Conference, Nottingham (1984). Organisers: The Plastics and Rubber Institute.

15. E.C.Millard. Lecture 34, IBID.

16. S.G.Abbot. Lecture 16, IBID.

17. The assistance of N.Bevan and D.W.Bazeley in the implementation of the GDP system is gratefully acknowledged.

18. GDP paper to be submitted.

19. P.K.Hansma. Phys. Rep. C(30), 145 (1977).

20.

21. A.J.Langley. Ph.D. Thesis, Leicester Polytechnic (1982).

22. R.R.Mallik, R.G.Pritchard, C.C.Horley and J.Comyn. To appear in Polymer.

(See also Chapter 5, this Thesis).

23. D.M.Brewis, J.Comyn, D.P.Oxley, R.G.Pritchard, S.Reynolds, C.R.Werret and A.J.Kinloch. Surf. Int. Anal., 6(1), 40 (1984).

24. Figure 6.15 appears by kind permission of C.R.Werret.

25. D.G.Walmsley and W.J.Nelson, in Tunnelling Spectroscopy, Capabilities, Applications and New Techniques. Plenum Press, New York (1982). P.K.Hansma (Ed.)

CHAPTER 7

GLOW-DISCHARGE OXIDATION OF Aℓ BASE ELECTRODES UNDER CONTROLLED CONDITIONS

7.1 INTRODUCTION

Aℓ-oxides most commonly used in the authors laboratory are formed by exposure of the freshly evaporated metal electrodes to room air; these are widely referred to as room, or thermal oxides (1,2,3). They are approximately 10-30 Å thick and usually require an exposure of 1 or 2 minutes. During this period, the rate of oxide growth may be considered to be approximately linear although strictly speaking it is in fact parabolic (4,5). Two main types of adsorbed species are present on the oxide surface, these are hydroxyl groups, and low molecular weight hydrocarbon contaminants. The former are known to be of vital importance for the adsorption of many compounds. One of their roles is to behave as potential adsorption sites to which polar compounds (or compounds containing polar constituent groups) may hydrogen bond. In the context of this thesis, several water-soluble polymers including polyvinylalcohol, methylcellulose, polyethyleneglycol, and polyethyleneoxide are thought to adsorb in this manner (see Chapter 5). Other compounds also known to adsorb by hydrogen bonding include lower alcohols and ketones (6,7), and cyanoacrylates (8). Another role of surface hydroxyls is to catalyse reactions of dopant molecules at the oxide surface leading to their subsequent chemisorption. Base-catalysed hydrolysis of certain methoxysilanes (10) are examples of such reactions.

Hydrocarbon contamination is however a nuisance, particularly when investigating weakly adsorbed species whose IET spectra may be easily swamped by the presence of contaminant absorption bands. Several spectra also exhibit peaks due to the symmetric and asymmetric stretching vibrations of the carboxylate anion. It has been proposed that formic acid is a

major contributor to the presence of these peaks and may arise due to reactions between atmospheric CO_2 and water vapour at the Pb electrode during junction fabrication (11). Interpretation of the adsorption of several compounds on Aℓ-oxide hinges on these peaks. For example, carboxylic acids dissociate at the oxide surface and are adsorbed as their carboxylate anion (12,13), and perhaps more importantly, regarding the present work, certain ester polymers are believed to adsorb in a similar manner (9). For example, the adsorption of polyvinylacetate, and polymethylmethacrylate relies upon their hydrolysis at the Aℓ-oxide surface. Evidence of hydrolysis is the presence of carboxylate features in their IET spectra. Clearly, the absence of such features in blank IET spectra is of central importance. It is therefore desirable to investigate the adsorption of various compounds on Aℓ-oxides grown under hydrocarbon-free, and relatively anhydrous conditions, and compare the results with existing data for these compounds on room oxides. In doing so, it may also be possible to establish the source of the anomolous carboxylate peaks, and subsequently eliminate it. With this aim in mind the implementation of a system whereby oxides could be grown and doped under controlled conditions was undertaken. A full description of the system is given in the experimental section; the capabilities of the system are now briefly discussed.

It is possible to remove a large proportion of surface hydroxyls from Aℓ-oxide by heating it to $\sim 850^{o}C$ (14,15) thus producing a relatively "dry" oxide. An incidental consequence is that beyond $\sim 600^{o}C$ a transition occurs, and its structure changes from amorphous Aℓ-oxide to γ-$Aℓ_2O_3$ - this will be discussed later in this section. In itself, this transition does not significantly alter the adsorption mechanisms of most dopants. Unfortunately, at elevated temperatures reactions between the oxide and

dopant molecules are more favoured. Subsequent introduction of dopant molecules at these temperatures may modify their chemical structure such that their adsorbed configurations may not resemble those when doped at room temperature (16,17). The only effective way of ensuring a low surface hydroxyl coverage on the oxide at room temperature is to evaporate the Aℓ electrodes under UHV conditions (18-22), and then form the oxide by bleeding pure O_2 into the system at pressures not exceeding 10^{-7} Torr. UHV facilities were not available in the authors laboratory therefore an alternative approach was adopted whereby as low a level as possible of surface hydroxyls was obtained under normal high vacuum conditions ($\sim 10^{-6}$ Torr).

Another technique widely used to form the oxide layers in IETS is plasma , or glow-discharge oxidation (3,23); this technique was employed for the present work. In glow-discharge oxidation the metal electrodes are exposed to a low energy discharge (usually $\sim$ 25W dc, with a current of $\sim$ 50 mA, at 500V) in air or O_2 at a pressure of $\sim$ 50 m Torr. An exposure of a few minutes is normally required to form an oxide of sufficient thickness. The entire IET junction fabrication procedure in the present work was performed within the vacuum chamber. Oxygen used for growing the glow-discharge oxides was dried by suitable trapping. Hydrocarbon contamination was also minimized in this way. Levels of indigenous water, and hydrocarbons in the system before, and after oxide formation were monitored by mass spectrometry. Where applicable, qualitative assessments were also made of the resulting degrees of contamination by measuring the peak intensities of the aliphatic CH, and surface OH stretching modes (at $\sim$ 360 and 450 mV respectively) relative to a fairly reliable reference - the Aℓ-O bulk phonon peak at $\sim$ 115 mV. It should be emphasized that these anlyses are intended only as a rough

guide to the relative levels of contamination; other considerations such as bond orientation relative to this oxide surface also effect peak intensities in IETS (3). On the whole, the peak intensity ratios reflected the proportions of the respective contaminants present during oxide growth as monitored by mass spectrometry. As will be seen, the mass spectroscopic analyses showed that the major component of the gas occupying the vacuum chamber was water vapour; other gases including N_2 and O_2 were present in amounts approximately one or two orders of magnitude less. A useful empirical relationship between the time, T_m/s, taken to cover 1 cm^2 of a clean metal surface with 10^{15} N_2 molecules at 298K, assuming a sticking probability of $\frac{1}{4}$, and a residual gas pressure P/Torr is given by (24):

$$T_m \simeq \frac{1}{P} \times 10^{-6} \qquad \ldots \quad 7.1$$

In effect this is the expression for the time taken to form a monolayer of N_2 on the surface. If it is assumed that this expression is approximately correct for the adsorption of the gas in the vacuum chamber (i.e. predominantly water vapour) on Aℓ-oxide, then even if a "pure" oxide was formed under UHV conditions a monolayer of adsorbed water would be formed in $\sim$ 10s if the chamber pressure was increased to $\sim 10^{-6}$ Torr. One concludes that adsorbed water will inevitably be present on all Aℓ-oxides grown in the authors laboratory. However, the amounts of adsorbed hydrocarbons will be significantly reduced. Such oxides offer a sound starting point for subsequent adsorption studies. As will be seen, their average surface hydroxyl content is fairly constant and considerably lower than those of thermal or glow-discharge oxides previously obtained in the authors laboratory. Furthermore, it may be varied in a systematic manner by admitting controlled amounts of water vapour into the system immediately prior to oxide growth.

No attempts have been made to characterize the structure of the Aℓ-oxide layers produced clearly, any meaningful structural or surface analytical investigations undertaken using the currently available spectroscopic techniques must be performed in situ. This ensures that no further oxide growth occurs during removal from the vacuum chamber. Coupling of the vacuum system to the sample chambers of the respective spectrometers was not feasible on the joint grounds of cost and availability. It is, however, possible to speculate as to the nature of the oxide by reference to the literature.

Several analytical techniques have been utilized by other workers to investigate the structure of thicker Aℓ-oxide films. Thermal oxides have been studied using (amongst other techniques) Low Energy Electron Diffraction (LEED) (18,25), Electron Energy Loss Spectroscopy (EELS) (19, 22), and Surface-sensitive Extended X-ray Absorption Fine Structure (SEXAFS) (21,26). LEED is sensitive to the geometry of atomic surface sites, EELS can provide information regarding structural symmetry of atomic and molecular surface sites, and SEXAFS allows the interatomic spacing of surface sites to be estimated - it also allows the number of nearest neighbours at a particular distance from the site to be determined thus allowing its co-ordination number to be calculated. Results from these techniques have suggested that below $\sim 450^{\circ}C$ the oxide structure is amorphous. As was mentioned earlier if the temperature is raised beyond $450^{\circ}C$ a gradual transition occurs, until about $\sim 600^{\circ}C$ when there is a change of state to a crystalline γ-$A\ell_2O_3$ structure. In further support of a γ-$A\ell_2O_3$ structure, Peri (27) has reported the surface IR spectrum of Aℓ-oxide at temperatures up to $800^{\circ}C$. At that temperature the hydroxyl bands in the spectra were broadened and their energies slightly downshifted from their room temperature values. However, the bands were still distinct from which he concluded

that the surface hydroxyls were not in random motion but localized on specific surface sites. He went on to propose a model of the alumina surface by considering the dehydration of a 100 crystal face of γ-$A\ell_2O_3$ using computer aided techniques (28). The model predicted vibrational frequencies for the hydroxyl modes which were in good agreement with his experimental data.

Sufficient energy may also be supplied to produce a γ-$A\ell_2O_3$ structure when forming the present glow-discharge oxides (29). It will be seen that the IET spectra obtained from these oxides exhibit much narrower, and more well defined Aℓ-O bulk phonon peaks than those from (amorphous) room oxide spectra; arguably this narrower range of vibrational modes suggests a 'more crystalline' structure. Evans, Bowser, and Weinberg have used XPS (30) in an attempt to characterize the glow-discharge Aℓ-oxides used for IETS in their laboratory (31). No firm conclusions were reached, but it was suggested that their oxides may resemble γ-$A\ell_2O_3$ in structure.

Doping of the present glow-discharge oxides with water, D_2O, and ethylacetate by means of a simple needle valve arrangement has been successful; no adverse effect on the pumping rate or contamination levels of the vacuum system were observed. Results for D_2O, and ethylacetate will be presented in 7.3.4. These incipient results suggest that a range of similar compounds may also be doped in this manner.

Preliminary work has also been undertaken to vapour-phase dope with CO_2. Such work would be of significant importance, particularly in view of the proposed reaction of CO_2 with water vapour to produce formic acid. A cylinder containing CO_2 was coupled to the needle valve on vacuum chamber to facilitate doping. Unfortunately, contamination was evident probably emanating from the connecting pieces which were difficult to clean. This precluded any meaningful analysis of the results.

The adsorption of CO_2 an alumina at room temperature has in fact been a source of some controversy in the literature. Parkyns has argued that it is strongly chemisorbed (32); Little (7,33), and Little and Amberg (34) also suggest a strongly adsorbed species and refer to a surface carbonate and its associated vibrational modes. Peri has proposed that a weakly physisorbed species may co-exist on the surface (35). However, Falconer et al suggest that CO_2 is only weakly bound, but have shown that its rate of adsorption may be significantly enhanced by exposure to an Auger electron beam ($\sim$ 5 μA and 2 keV beam current and voltage) at a temperature of 303-316K. From the above it would appear that the adsorption of CO_2 is not clear, although if surface carbonate species were formed the presence of carboxylate peaks in its IET spectrum could not be ruled out. It should be emphasized that in most IETS doping experiments (atmospheric) CO_2 is present only in small quantities; it is, therefore, unlikely to be adsorbed when liquid or vapour phase doping with the majority of compounds. Possible reactions of CO_2 with water vapour at the Pb electrode are also believed to be of subordinate importance outside the content of infusion doping. As a cursory remark it is mentioned that the adsorption of CO on alumina supported Fe (36) and Rh (37,38) particles has been investigated by IETS. The Fe and Rh particles were evaporated onto the alumina supports at 77-150K in an atmosphere of CO. Linear adsorbed structure of the type Fe=C=O or Rh=C=O were proposed.

7.2 EXPERIMENTAL

7.2.1 Apparatus: The Vacuum System

A standard rotary and diffusion pumped vacuum system of the type described in Chapter 3 was used for the present work. New masks were designed, appropriate modifications were made to the top plate, and a rotatable jig was employed which allowed mask changeover, and therefore complete device fabrication to be performed *in situ*. A schematic diagram of the jig and vacuum chamber is shown in Fig.7.1. Scale diagrams of the masks and slide holder are shown in Fig.7.2.

A trap was incorporated into the gas admittance line (see also Fig.3) to reduce the levels of water vapour, hydrocarbon and other contamination entering the vacuum chamber as mentioned in the introduction. The trap consisted of a copper cylinder (of diameter $\sim$ 10 cm) containing either 13X molecular sieves or $CaCl_2$ chips as a filtering material, and was maintained at a temperature of $\sim -77^{o}C$ by means of a liquid N_2/acetone slush bath. Glow discharge oxidations were performed using gas that had been percolated through the trap as indicated in Fig.7.3. The filtering material effectively removed most of the hydrocarbon contamination and some water vapour from the gas. Cooling the trap to $-77^{o}C$ served to reduce further the water vapour content and also 'freeze out' smaller hydrocarbon gases, e.g. lower alkanes (propane having a boiling point of $-44.5^{o}C$ will be the smallest in the homologous series to be frozen out).

A mass spectrometer head was fitted in the lower vacuum chamber as shown in Fig.7.1. This allowed residual gas analyses to be performed before and after electrode oxidation. Details of the spectrometer's operation are given in 7.2.3.

Fig.7.1

Schematic diagram of the modified jig in position on the top plate. Also shown is the mass spectrometer head. The gas inlet valve admits air or O_2 into the chamber.

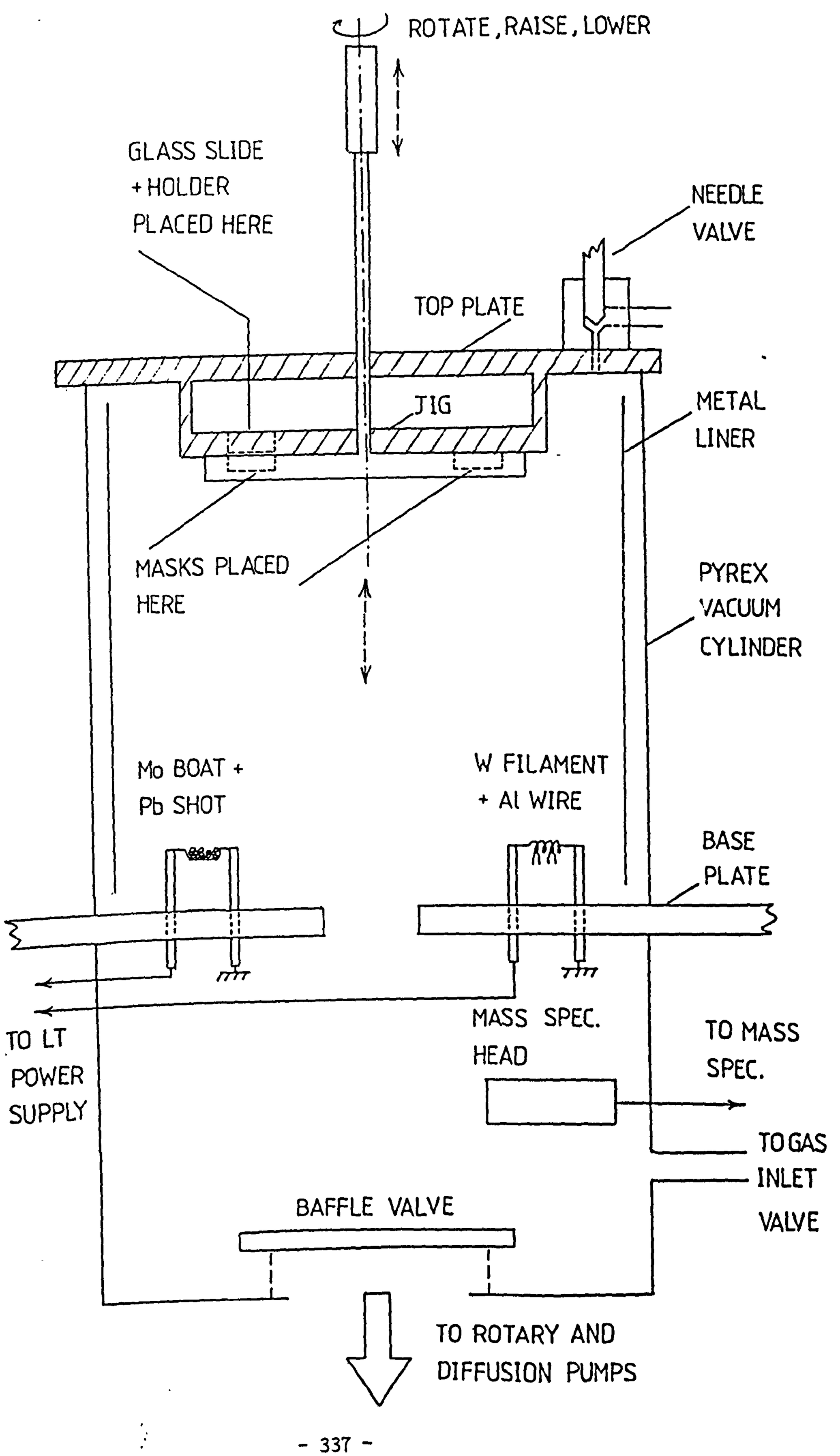
ROTATE, RAISE, LOWER
GLASS SLIDE
+ HOLDER
PLACED HERE
NEEDLE
VALVE
TOP PLATE
JIG
METAL
LINER
MASKS PLACED
HERE
PYREX
VACUUM
CYLINDER
Mo BOAT +
Pb SHOT
W FILAMENT
+ Al WIRE
BASE
PLATE
TO LT
POWER
SUPPLY
MASS SPEC.
HEAD
TO MASS
SPEC.
TO GAS
INLET
VALVE
BAFFLE VALVE
TO ROTARY AND
DIFFUSION PUMPS

Fig.7.2

Scale diagrams of the masks and slide holder. These are positioned in the jig as indicated in Fig.7.1.

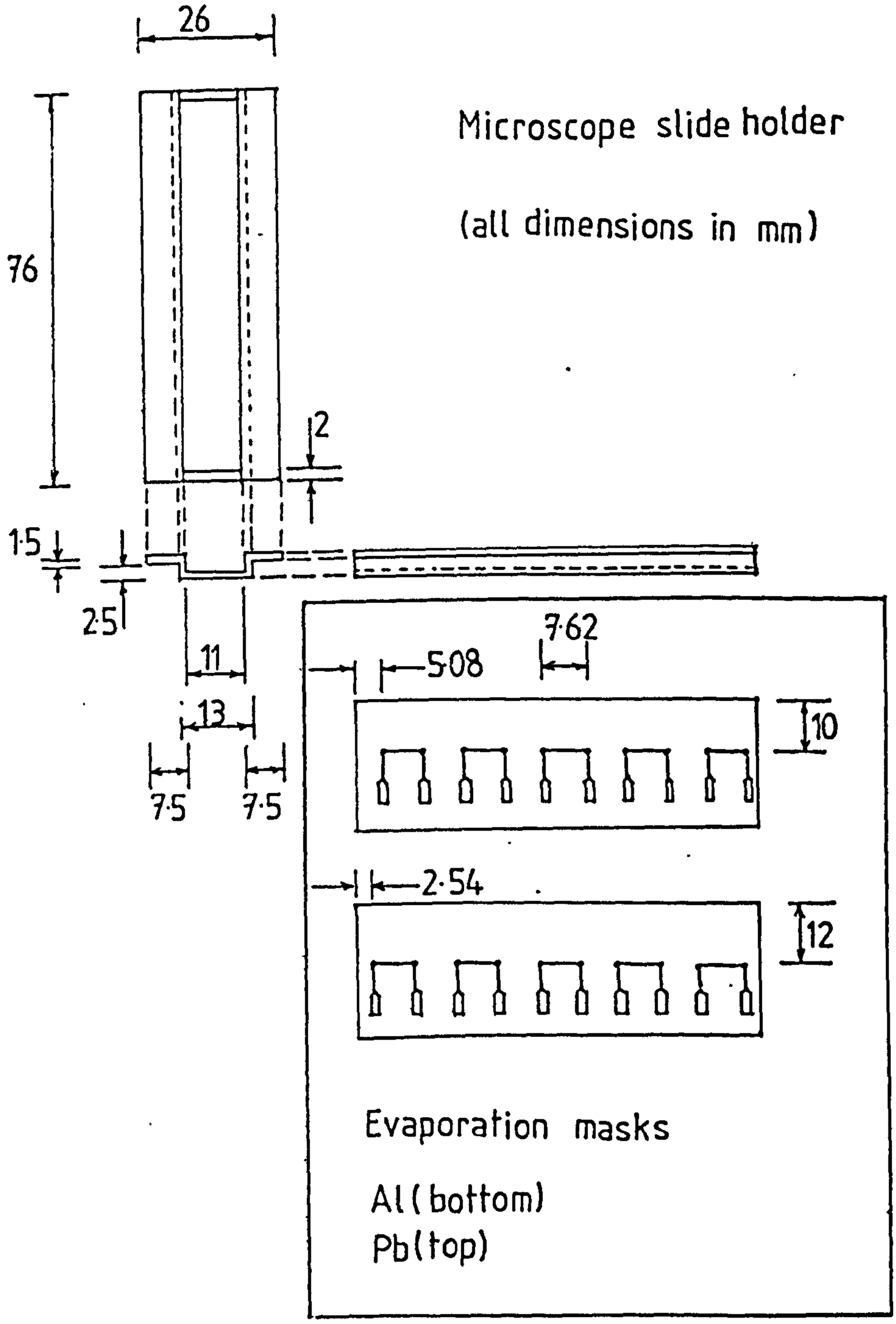
26
76
2
1·5
2·5
11
13
7·5
7·5
Microscope slide holder
(all dimensions in mm)
7·62
5·08
10
2·54
12
Evaporation masks
Al (bottom)
Pb (top)

Fig.7.3

Schematic diagram of the trap incorporated onto the gas admittance line. O_2 is introduced into the trap through the O_2 inlet valve and after leaving the trap enters the vacuum chamber as shown in Fig.7.1.

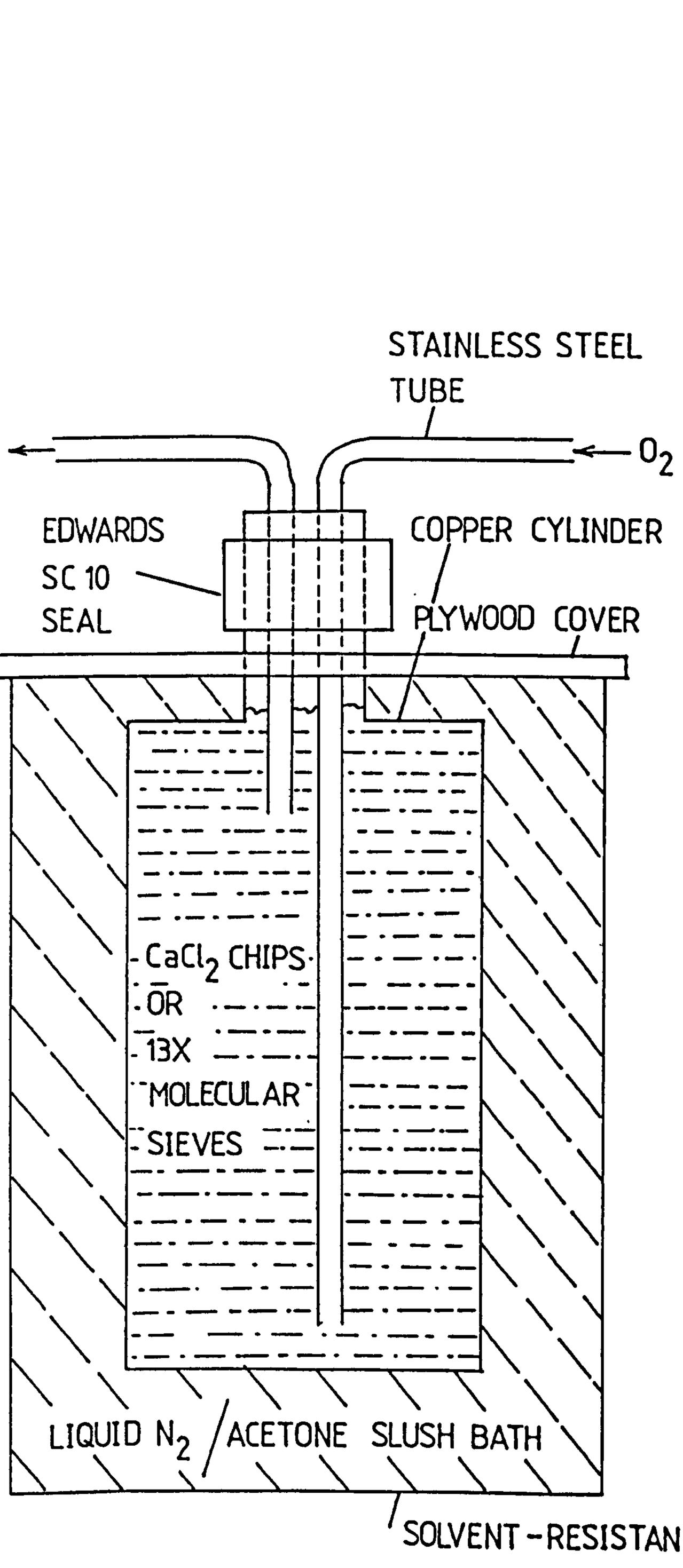
STAINLESS STEEL
TUBE
O_2
EDWARDS
SC 10
SEAL
COPPER CYLINDER
PLYWOOD COVER
$CaCl_2$ CHIPS
OR
13X
MOLECULAR
SIEVES
LIQUID N_2 / ACETONE SLUSH BATH
SOLVENT-RESISTANT
BUCKET

7.2.2 Device Fabrication: in situ Preparation of IET Junctions in the Vacuum Chamber

Before device fabrication the usual gettering, and glow-discharge cleaning procedures were carried out to ensure an acceptably low level of indigenous contamination in the vacuum chamber; these procedures have been described in Chapter 3. A brief summary of junction fabrication with the present system is given below.

(i) Aluminium Electrode Deposition

The appropriate mask was positioned adjacent to the glass slide by rotating the jig (see Fig.7.1). Once a chamber pressure of $\sim 10^{-5}$ to 10^{-6} Torr had been attained the Aℓ electrodes (approximately 1000-2000 Å thick) were vacuum evaporated onto the slide.

(ii) Aluminium Electrode Oxidation

With the mask removed a controlled flow of dry O_2 or air was admitted into the chamber such that a stable equilibrium pressure of $\sim$ 50 to 70 m Torr was maintained. A dc glow-discharge was then struck; a glow-discharge current of 50 mA at a potential of 500 V was used for all oxidations. Glow-discharge exposure times of several minutes were required to produce oxides of suitable thickness for IETS analyses. (Thermal oxides may also be formed in a similar manner by bleeding pure O_2 or air into the vacuum chamber, but are not discussed here.) Levels of contamination on the oxide were monitored by varying the exposure time and then inspecting the intensities of the aliphatic CH, and OH stretching modes relative to that of the Aℓ-O bulk phonon in the corresponding IET spectra. Spectra obtained from glow-discharge oxides grown in O_2 filtered by 13X molecular sieves and $CaCl_2$ chips, both at $-77^{o}C$ are presented and discussed. These are compared with those obtained from glow-discharge oxides grown in O_2 used as supplied.

Quantitative analyses of the levels of contamination based on the

peak height ratio of the Aℓ-O phonon/mode in question (as mentioned above) are presented in the results and discussion section. Peak heights were estimated by constructing a base-line for the peak on the background of the spectrum, and measuring the vertical height, d, from this base-line to the tip of the peak at bias V = hν/e, where ν is the frequency of the oscillator and h, and e have their usual meanings. This is illustrated in Fig.7.4 below.

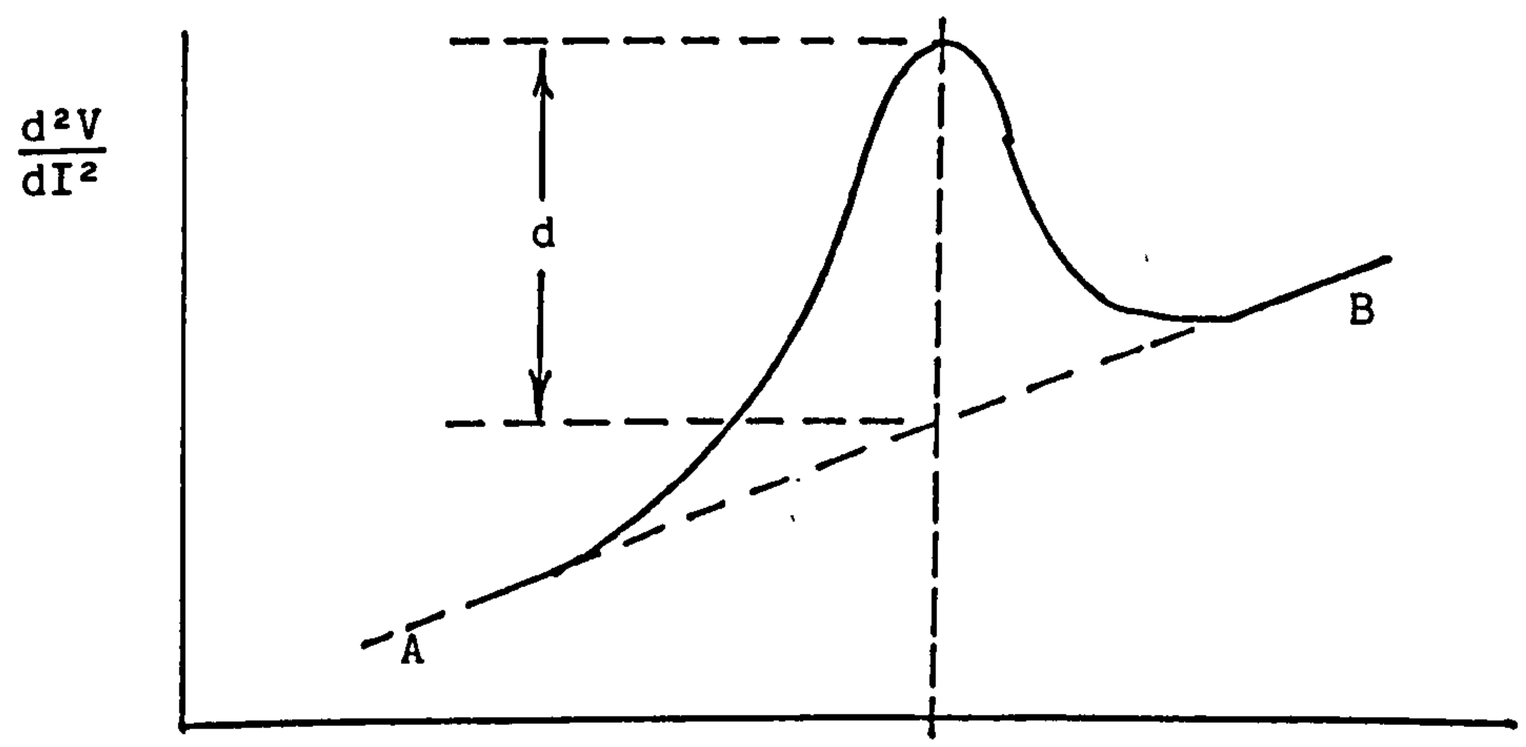

Fig.7.4. Construction employed to estimate IET peak heights, i.e., the vertical distance, d, between the tip of the peak, and base-line AB. (The constants h, and e have their usual meanings, and ν is the frequency of the vibrational mode.)

It must be emphasized that this technique, although commonly used in IR spectroscopy to calculate absorbances (39), is not necessarily an absolute measure of the number of oscillators at frequency ν. Other considerations such as bond orientation relative to the oxide surface will also effect peak intensites in IETS (3). The peak height ratios presented here are intended only as a rough guide to the relative levels of contamination.

(iii) Oxide Doping

Oxides were doped by admitting the dopant vapour into the main vacuum chamber through the needle valve on the top-plate (see Fig.7.1). A chamber pressure of ∿ 100 m Torr was maintained during doping. D_2O (BDH supplied 99.75 % pure) and redistilled ethyl acetate were doped in this manner onto oxides grown in O_2 that had been filtered through $CaCl_2$. Exposure times of 30, and 40 minutes respectively were required to deposit a suitable thick adlayer. After doping, the vapour was removed from the chamber by engaging the diffusion pump.

Routine doping with acrid, volatile compounds such as certain monomers and solvents, is not yet possible. This is largely because the diffusion pump fluid rapidly becomes contaminated by these compounds causing the pumps operation to be impaired severely. In order to avoid this problem an isolated doping chamber (annexed to the main vacuum chamber) has been implemented from which the majority of spent dopant vapour may be removed by means of a dedicated rotary pump. Details of this apparatus - which is still in the development stages, are given in Appendix 2.

(iv) Lead Electrode Deposition

By further rotation of the jig, the correct mask was positioned adjacent to the glass slide. Once a chamber pressure of ∿ 10^{-6} Torr had been attained the Pb electrodes (approximately 2000-3000 Å thick) were evaporated, thus completing the IET junctions.

7.2.3 Mass Spectrometric Analyses of Residual Gases in the Vacuum Chamber

A 20^{th} century electronics AIG50 mass spectrometer was employed for the present work. This instrument has a mass range of 1-50 a.m.u., and operates at pressures $\leq 10^{-4}$ Torr. The spectrometer head was fitted in the vacuum chamber as shown in Fig.7.1. During gas analyses the mass scale

of the spectrometer was traversed manually, and the corresponding output current in mA was monitored. Several current readings were taken for each mass nō in question since gas levels fluctuated slightly during the analyses; the readings presented in the results section are accurate to about ± 5%. These output currents are proportional to the amount of substance ionised in the mass spectrometer head. Readings were taken before, and after the formation of glow-discharge oxides in O_2 filtered through $CaCl_2$, and 13X molecular sieves. Glow-discharge parameters of ∿ 50 mA and 500V dc at a chamber pressure of ∿ 50-70 m Torr were employed in both cases with an exposure time of 25 min. A similar analysis was performed when vapour phase doping with D_2O; readings were taken before the oxide was formed, and after it had been doped. Gas analyses could not be performed during oxide growth or doping since the chamber pressures were prohibitively high.

7.3 RESULTS AND DISCUSSION

7.3.1 Oxides Grown Using Untreated O_2

For control purposes, spectra were recorded for oxides grown in BOC supplied O_2 with no drying agent on the gas inlet line. Spectra obtained after oxidizing for 5, 10, and 20 minutes are shown in Figures 7.5, 7.6 and 7.7 respectively. As one would expect as the exposure time is increased so are the levels of contamination. The strong Aℓ-O bulk phonon peak at ∿ 115 mV dominates these spectra (its second harmonic overtone at ∿ 230 mV is very weak). As mentioned in the introduction, the structure of the Aℓ-O phonon peak is somewhat sharper than those observed for thermally grown oxides. This narrower range of vibrational modes might suggest a greater degree of crystallinity in the former. Aliphatic CH stretching modes at ∿ 360 mV are only apparent after 20 min. exposure. All spectra do, however, exhibit OH bonding and stretching vibrations at ∿ 80 and ∿ 448 mV respectively due to surface hydroxyls.

Broadly speaking, these spectra are typical of undoped, glow-discharge oxidized devices, although the levels of hydrocarbon contamination are slightly lower than those observed for similar oxides formed in air; evidently the oxygen is fairly pure. The ratios of Aℓ-O phonon/OH stretching peak heights for the 20 min. device are 4.2, and 4.6 for junctions 3 and 4 respectively. These values were fairly reproducible, and are relevant when considered with the corresponding mass spectromectric data, and those results obtained from oxides grown in filtered O_2.

Inspection of the mass spectrometric data for Fig.7.7 - the 20 min. device shows that the predominant component of the gas in the vacuum chamber before, and after oxidation is water vapour (see Table 7.2). An output current of ∿ 25 mA was measured prior to oxidation with O_2, and NO (and/or CO) registering only ∿ 1.1 and 0.11 mA respectively. However, after oxidation the H_2O output current fell by about an order of magnitude

Fig.7.5

IET spectra of devices plasma oxidized for 5 min.

in BOC supplied O_2.

Fig.7.6

IET spectra of devices plasma oxidized for 10 min.

in BOC supplied O_2.

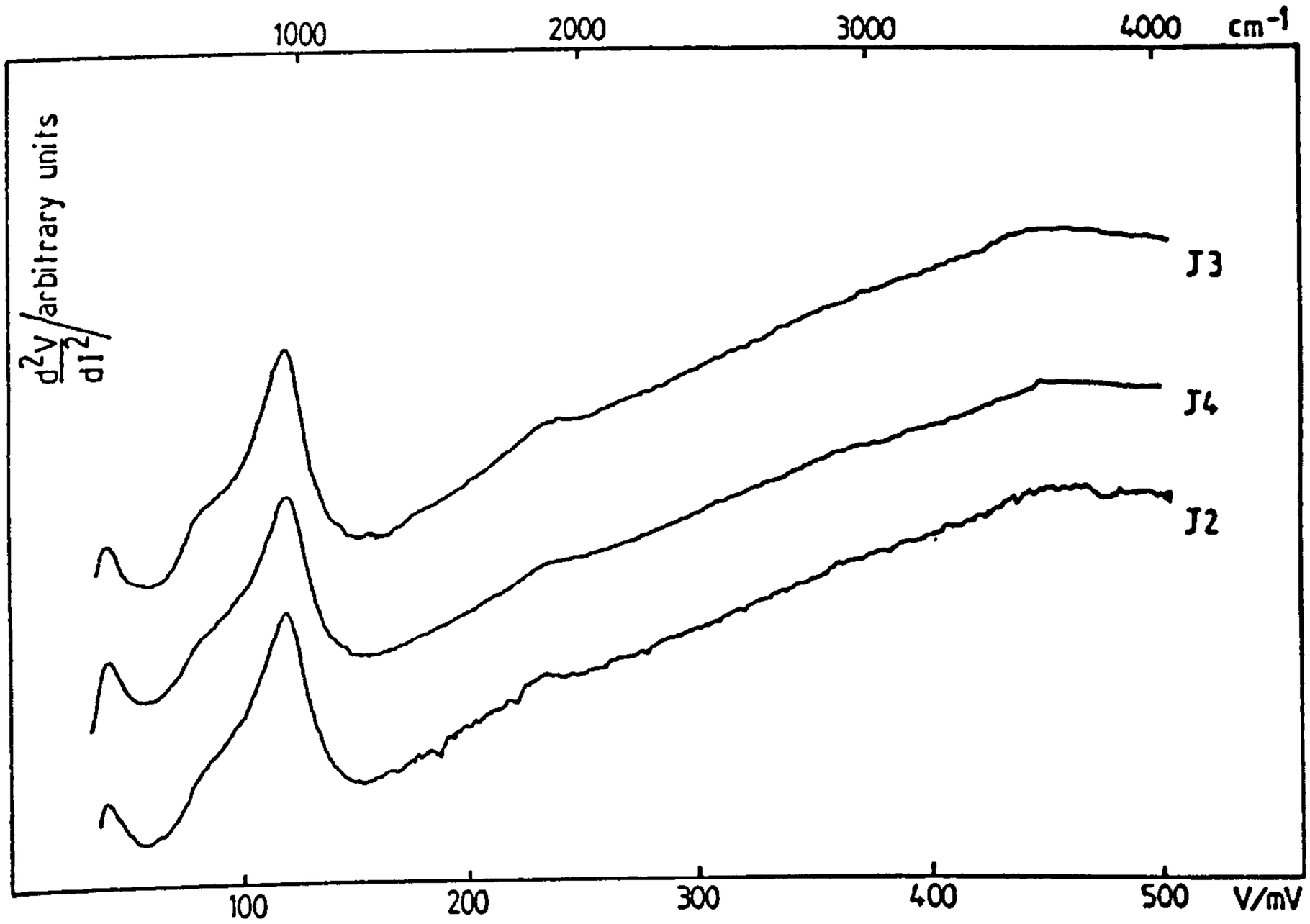
1000
2000
3000
4000
cm⁻¹
d²V/dI² /arbitrary units
J3
J4
J2
100
200
300
400
500
V/mV

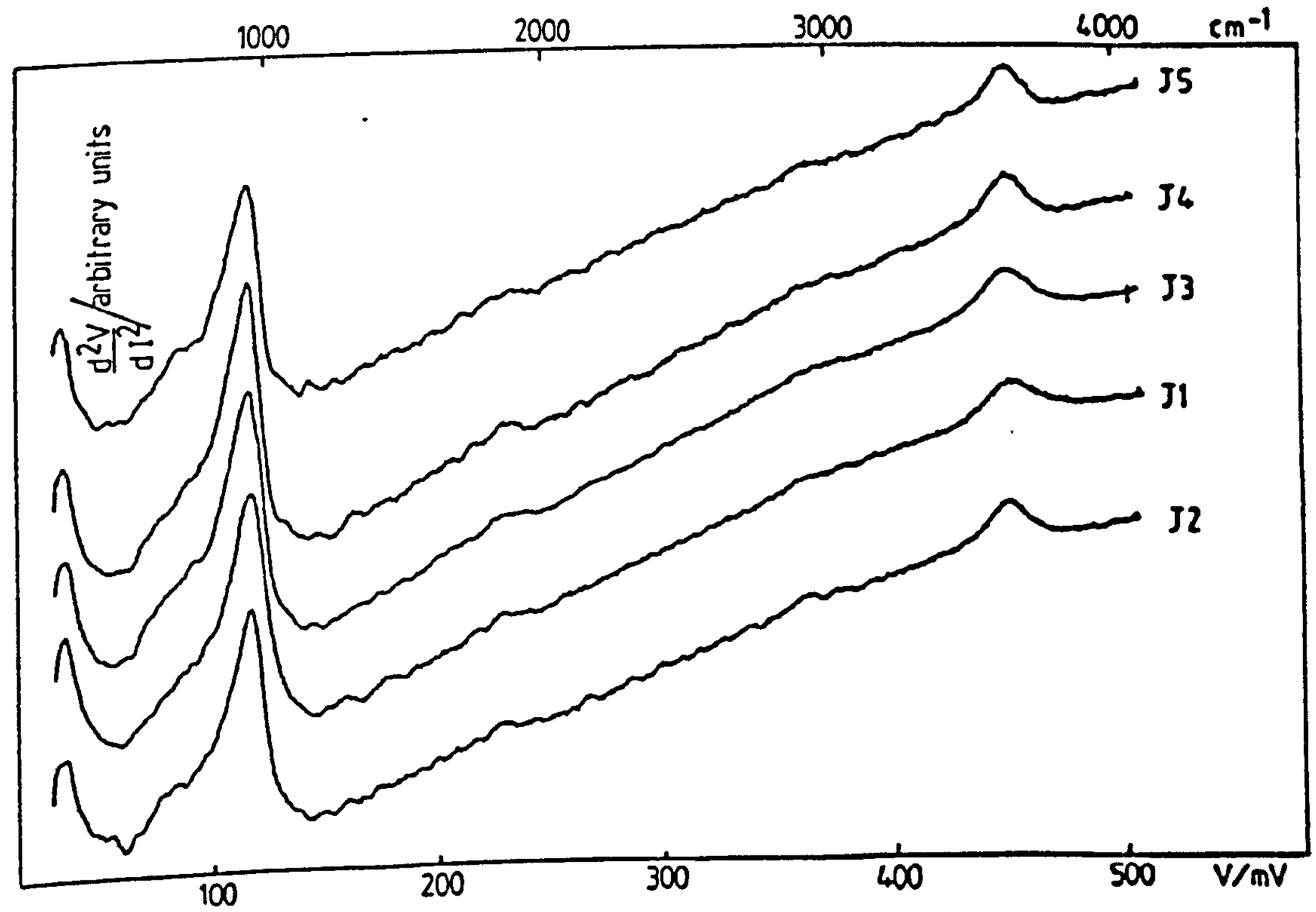
1000
2000
3000
4000
cm⁻¹
d²V/dI² /arbitrary units
J5
J4
J3
J1
J2
100
200
300
400
500
V/mV

Fig.7.7

IET spectra of devices plasma oxidized for 20 min. in BOC supplied O_2.

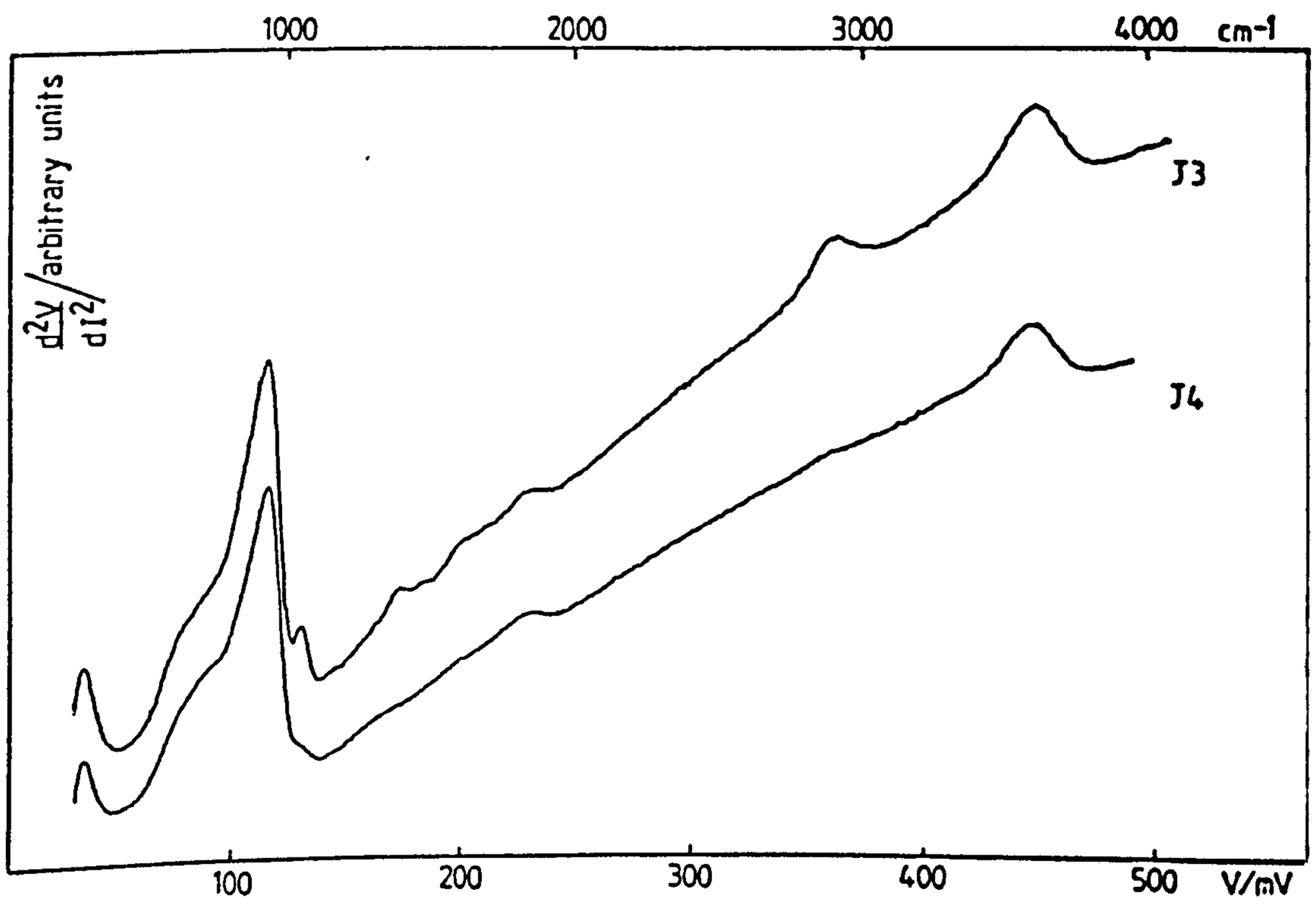
1000
2000
3000
4000
cm-1
$\frac{d^2V}{dI^2}$/arbitrary units
J3
J4
100
200
300
400
500
V/mV

TABLE 7.1 - Approximate peak height ratios of certain vibrational modes relative to the corresponding Aℓ-O bulk phonon for some glow-discharge (gd) oxidixed IET junctions.

Mass Spec. Data Table No	IET Spectrum Fig. No.	Device	Junction No	Junction Resistance	Aℓ-O phonon/peak ratio
7.2	7.7	20 min. gd in untreated BOC supplied O_2	3	50	Aℓ-O/ν(OH) = 4.2
			4	50	Aℓ-O/ν(OH) = 4.6
-	7.8	20 min. gd in BOC supplied O_2 percolated through 13X molecular sieves at -77°C	3	100	Aℓ-O/ν(OH) = 5.3
7.3	7.9	25 min. gd in BOC supplied O_2 percolated through 13X molecular sieves at -77°C	2	30	Aℓ-O/ν(OH) = 14.6
			3	30	Aℓ-O/ν(OH) = 12.0
			4	35	Aℓ-O/ν(OH) = 12.0
7.4	7.11	25 min. gd in BOC supplied O_2 percolated through $CaCl_2$ chips at -77°C	1	90	Aℓ-O/ν(OH) = 6.6 Aℓ-O/ν(CH) = 13.2
			2	40	Aℓ-O/ν(OH) = 9.0 Aℓ-O/ν(CH) = 36.0
			4	25	Aℓ-O/ν(OH) = 20.0
7.5	7.12	20 min. gd in BOC supplied O_2 percolated through $CaCl_2$ chips at -77°C then vpd D_2O for 30 min.	3	40	Aℓ-O/ν(OH) = 10.6 Aℓ-O/ν(OD) = 5.8 Aℓ-O/ν(CH) = 17.3

TABLE 7.2 - Mass spectroscopic analysis of residual gases in vacuum chamber before, and after a 20 min. glow-discharge oxidation in untreated BOC supplied O_2 (see Fig.7.7).

Mass No	output current/mA before	after	element/ compound
1	0.36	0.04	H
12	0.030	0.013	C
18	25.0	6.0	H_2O
28	0.11	0.19	CO, N_2
30	0.014	0.015	NO
31	0.008	0.011	
32	1.1	1.5	O_2
44	0.005	0.005	CO_2

to ~ 6 mA while those currents due to the other components remained approximately constant. It would appear that a large proportion of the water vapour had been incorporated into the Aℓ-oxide layer formed on the internal surfaces of the vacuum chamber. Indeed, the corresponding IET spectra would support this view.

7.3.2 Oxides Grown Using O_2 Treated by Percolation Through 13X Molecular Sieves at -77°C

Spectra obtained after oxidizing for 20, and 25 min. are shown in Figure 7.8, and 7.9 respectively. Comparison of these data with those obtained from devices oxidized in untreated O_2 for 20 min. (see Fig.7.7) shows that the hydrocarbon contamination bonds formerly at ~ 360 mV have now been effectively eliminated. However, OH bending, and stretching vibrations are still present at ~ 80, and 450 mV respectively. Based upon the Aℓ-O phonon/OH stretch peak height ratios (see Table 7.1) the relative intensity of the OH stretch for the 20 min. device is approximately the same as with untreated O_2; the 25 min. device exhibits a reduction in relative intensity by a factor of 3. The fact that the relative intensities of the OH bending and stretching modes have not been significantly reduced is reflected in the corresponding mass spectrometric data. Data for the 25 min. device is given in Table 7.3. Once more water vapour is the predominant component of the gas within the chamber. Corresponding output currents of ~ 24.5, and 3.0 mA were measured before, and after oxidation; these levels are commensurate with those obtained for the 20 min. oxidation in untreated O_2. Molecular sieves with a smaller pore diameter might be substituted for the present 13X grade in order to remove a larger proportion of the water vapour.

Unfortunately larger mass numbers corresponding to fragmented

Fig.7.8

IET spectrum of device plasma oxidized for 20 min.

in O_2 filtered through 13X moleculer sieves at-77^{o}C.

Fig.7.9

IET spectra of devices plasma oxidized for 25 min.

in O_2 filtered through 13X molecular sieves at-77^{o}C.

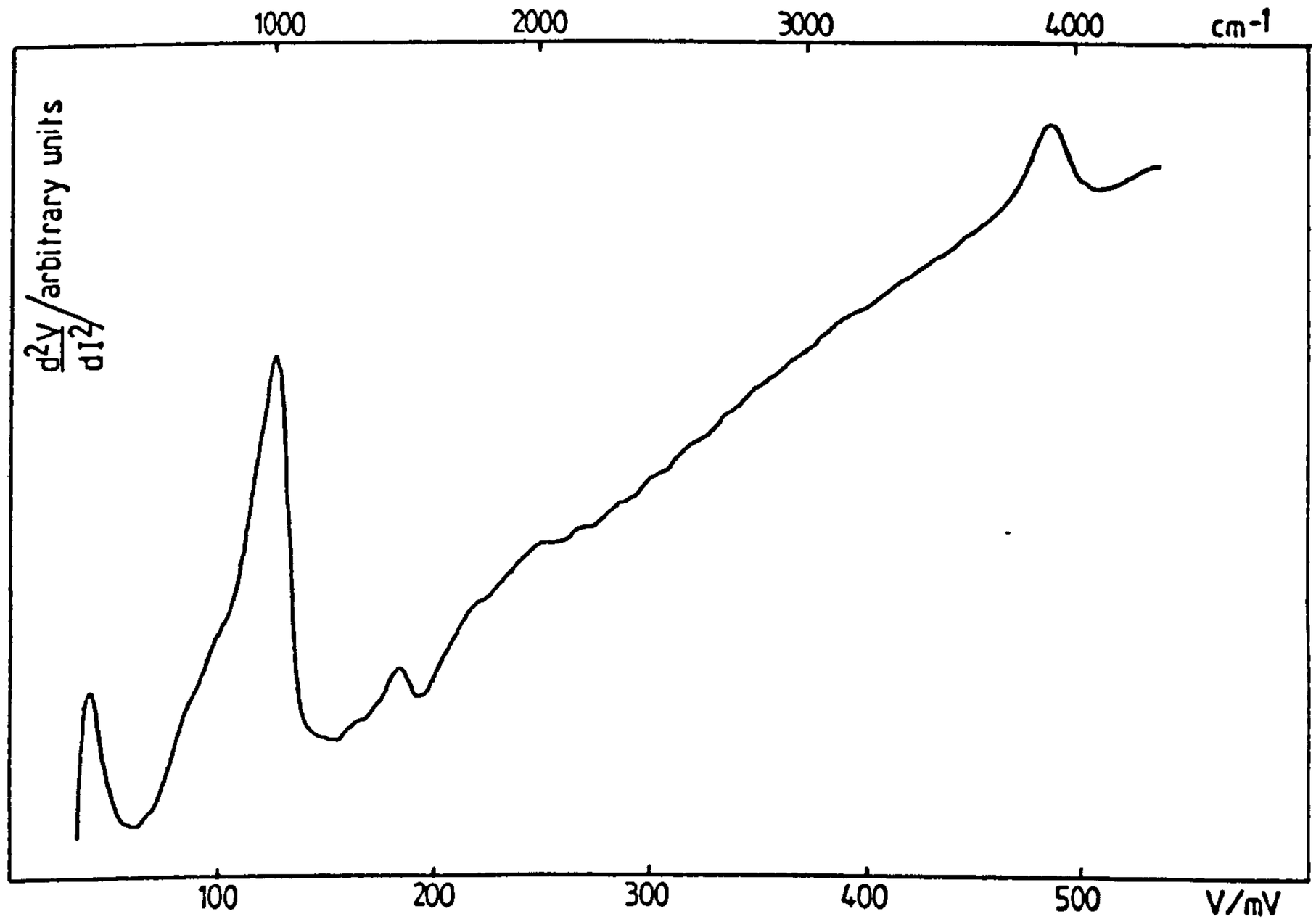
1000
2000
3000
4000
cm-1
d²V/dI²/arbitrary units
100
200
300
400
500
V/mV

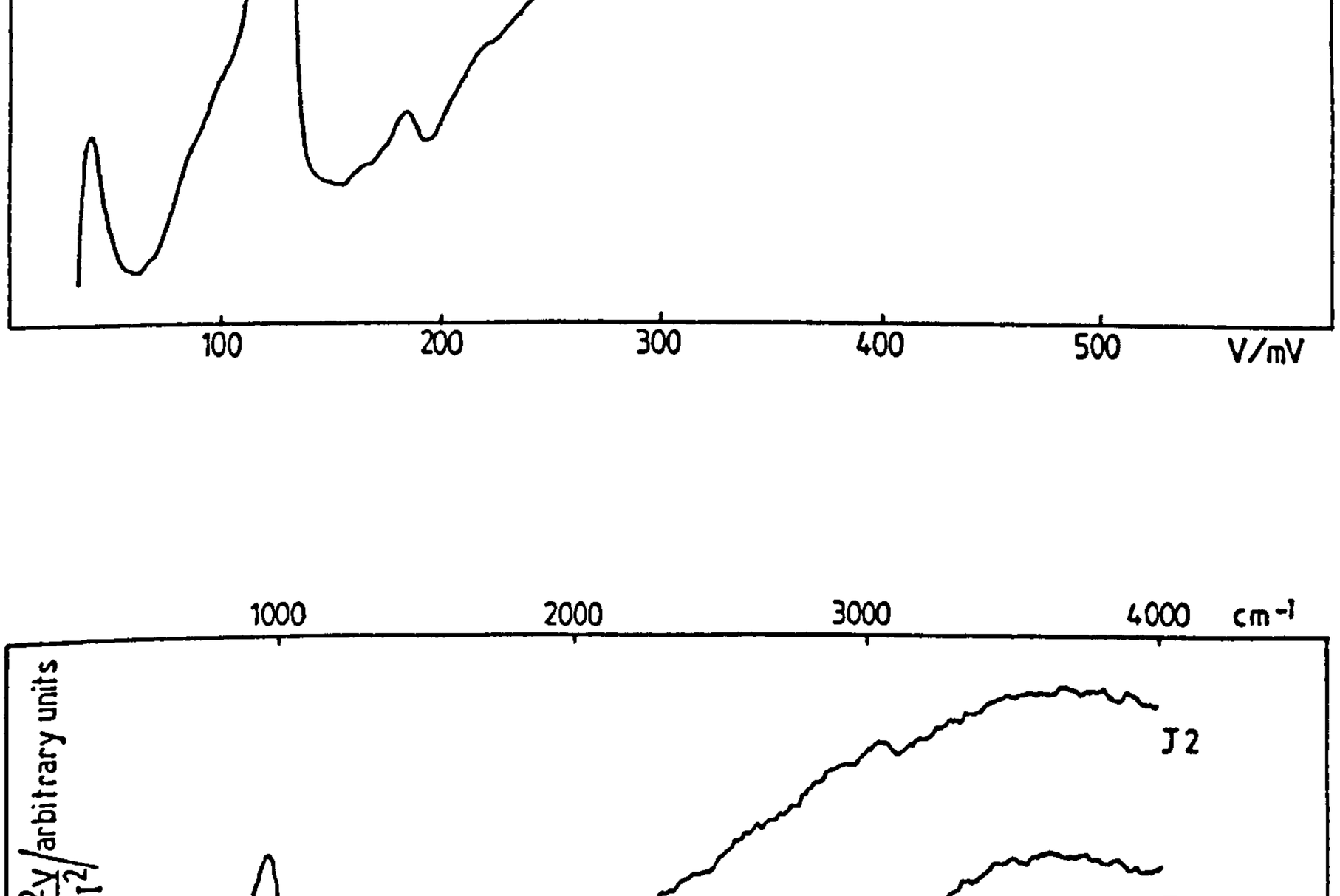
1000
2000
3000
4000
cm-1
d²V/dI²/arbitrary units
J2
J3
J4
100
200
300
400
500
V/mV

TABLE 7.3 - Mass spectroscopic analysis of residual gases in vacuum chamber before and after 25 min. glow-discharge oxidation in O_2 percolated through 13X molecular sieves. (See Fig.7.9).

Mass No	output current/mA				element/ compound
	before	ave	after	ave	
1	0.37, 0.30	0.34	0.04, 0.05	0.045	H
2	0.044, 0.016	0.03	0.009, 0.007	0.008	H_2, He
8	0.001, -	0.001	- -	-	
12	0.026, 0.012	0.019	0.013, 0.010	0.012	C
18	29.0, 20.0	24.5	3.0, 3.0	3.0	H_2O
28	0.11, 0.13	0.12	0.11, 0.11	0.11	CO, N_2
29	- -		0.15, 0.10	0.13	
30	0.016, 0.017	0.016	0.018, 0.010	0.014	NO
31	0.009, 0.014	0.012	0.011, 0.007	0.009	
32	0.8, 1.0	0.9	1.1, 0.9	1.0	O_2
35	0.001, 0.002	0.002	0.003, 0.002	0.003	
40	0.001, 0.001	0.001	0.001, -	0.001	
44	0.005, 0.009	0.007	0.01, 0.004	0.007	CO_2

long-chained hydrocarbons could not be sampled with the present spectrometer. Nevertheless, the resulting IET spectra would suggest that the amounts of these substances present are insignificant. On the whole, it appears that the 13X sieves effectively remove the majority of hydrocarbon contaminants from the O_2, but do not have any noticeable effect on the water vapour content.

7.3.3 Oxides Grown Using O_2 treated by Percolation through $CaCl_2$ chips at-77°C

Spectra obtained after oxidizing for 20, and 25 min. are shown in Figure 7.10, and 7.11 respectively. The Aℓ-O phonon/OH stretch peak height ratios indicate that the relative intensities of the OH modes are slightly less that those for oxides grown in untreated O_2. (See Table 7.1). Levels of OH contamination are commensurate with those just observed for oxides grown in oxygen filtered through 13X molecular sieves.

The mass spectrometric data for the 25 min. device again indicate that the residual gas in the vacuum chamber is mainly comprised of water vapour. Output currents of ∿ 36.0 and 7.0 mA were measured before and after oxidation. Corresponding output currents for O_2 were ∿ 0.025, and ∿ 0.12 mA indicating a slight increase in the amount of O_2 in the chamber after oxidation.

Broadly speaking, the levels of contamination observed for the oxides grown in O_2 using $CaCl_2$ as the drying agent are approximately the same as when using 13X molecular sieves.

7.3.4 Glow-discharge Oxides Vapour Phase Doped *in situ* with D_2O and Ethyl Acetate

Fig.7.12 shows the IET spectrum obtained from a device firstly glow-discharge oxidized for 25 min. in O_2 (percolated through $CaCl_2$ chips)

Fig.7.10

IET spectra of devices plasma oxidized for 20 min. in O_2 filtered through $CaCl_2$ chips at $-77^{\circ}C$.

Fig.7.11

IET spectra of devices plasma oxidized for 25 min. in O_2 filtered through $CaCl_2$ chips at $-77^{\circ}C$.

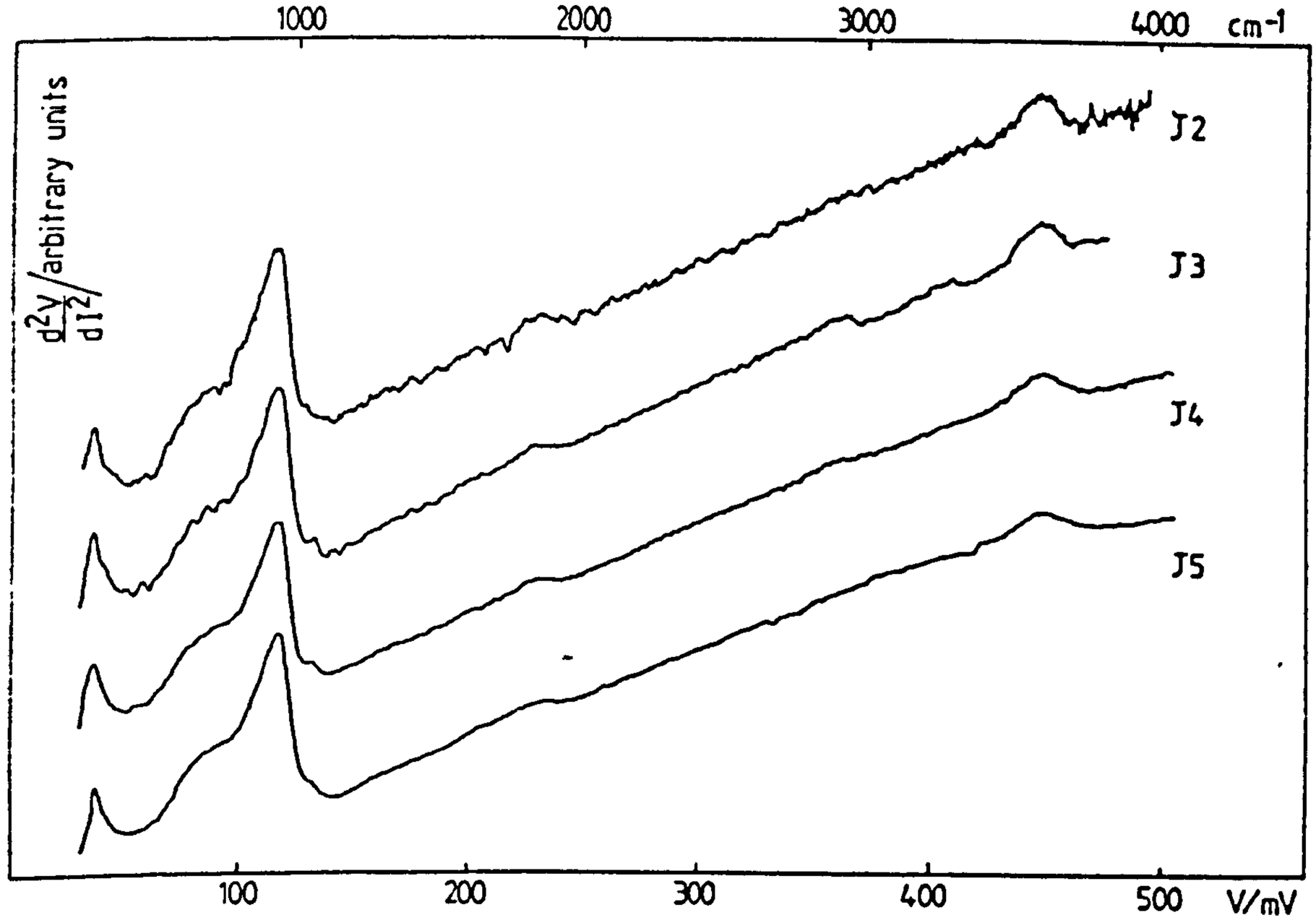
1000
2000
3000
4000 cm-1
$\frac{d^2V}{dI^2}$/arbitrary units
J2
J3
J4
J5
100
200
300
400
500 V/mV

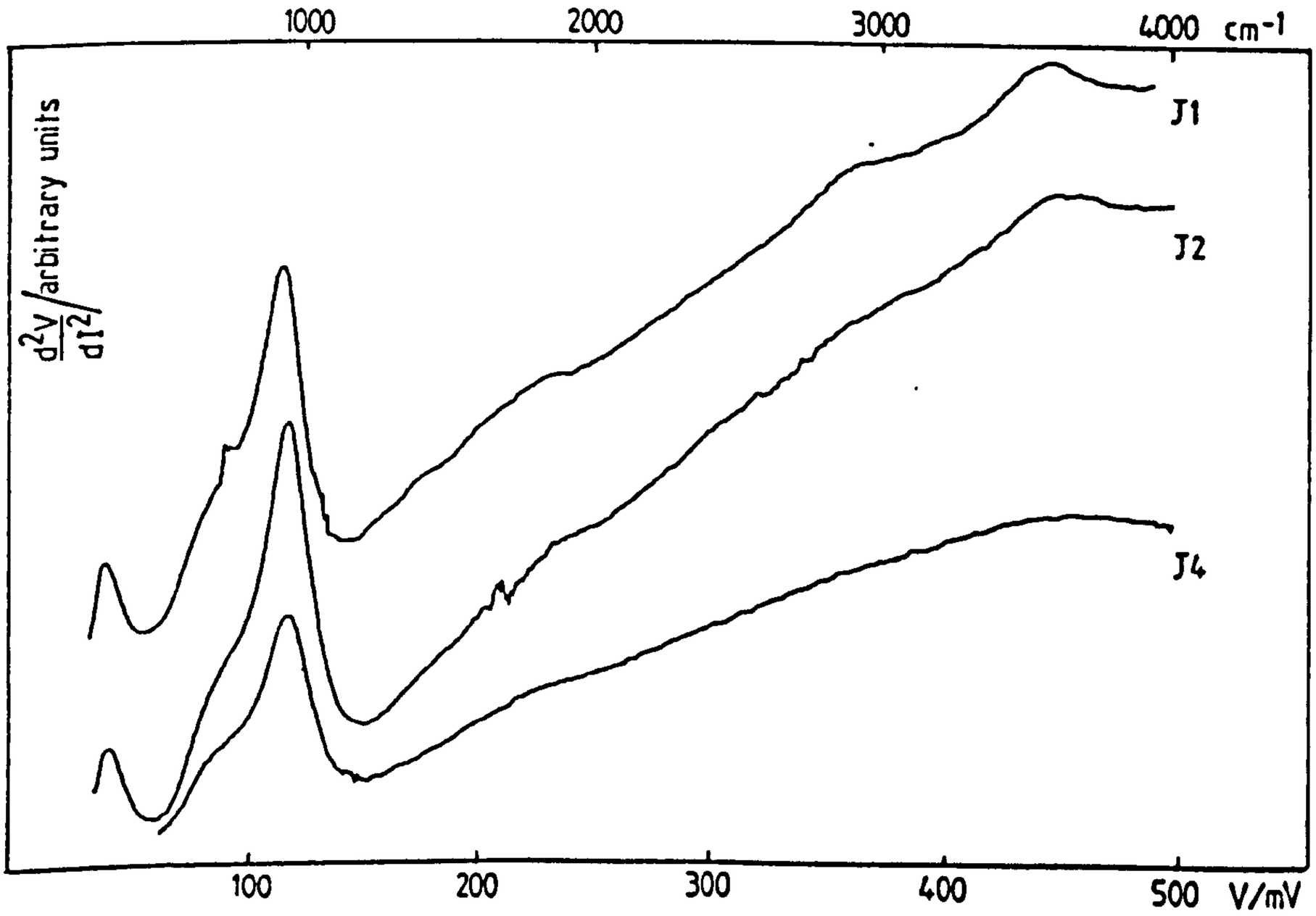
1000
2000
3000
4000 cm-1
$\frac{d^2V}{dI^2}$/arbitrary units
J1
J2
J4
100
200
300
400
500 V/mV

TABLE 7.4 - Mass spectroscopic analysis of residual gases in vacuum chamber before, and after 25 min. glow-discharge oxidation in O_2 percolated through $CaCl_2$ chips. (See Fig.7.11).

Mass No	output current/mA					element/ compound
	before		ave	after	ave	
1	0.43,	0.59	0.51	0.06, 0.11	0.09	H
2	0.052,	0.032	0.042	0.006, 0.009	0.008	H_2, He
8	-	-		- -		
12	0.034,	0.019	0.027	0.020, 0.012	0.016	C
18	36.0,	36.0	36.0	8.0, 6.0	7.0	H_2O
28	0.09,	0.05	0.07	0.21, 0.10	0.16	CO, N_2
30	0.08,	0.003	0.06	0.021, 0.008	0.015	NO
31	0.006,	0.004	0.005	0.019, 0.008	0.014	
32	0.006,	0.044	0.025	0.14, 0.09	0.12	O_2
40	0.001,	0.001	0.001	0.001, -	0.001	
44	0.019,	0.015	0.017	0.014, 0.009	0.012	CO_2

and then vapour phase doped with D_2O for 30 min. The D_2O (BDH supplied 99·75% pure) was introduced into the chamber from a disposable syringe through the needle valve.

The OH stretching vibration at 450 mV is weaker than might have been expected. Its intensity relative to the Aℓ-O phonon is approximately half of those observed so far for undoped oxides; the Aℓ-O phonon/OH stretch peak height ratio is ∿ 10.6 (see Table 7.1). An OD stretching mode is clearly present at ∿ 329 mV, its position isotopically downshifted by a factor of $1/\sqrt{2}$ from the corresponding OH stretching value. Interestingly, the Aℓ-O phonon/OD stretch peak height ratio is about half of that for its OH counterpart indicating that the OD mode is about twice as strong (although its intensity is somewhat disguised by a broad high energy shoulder at 360 mV due to weak CH stretching vibrations). It is known that surface hydroxyl groups exchange with D_2O to produce surface deuteroxyl groups (7). The above IET data would confirm such behaviour for the present Aℓ-oxides.

All previous mass spectrometric data have shown a significant decrease in the H_2O content within the vacuum chamber after glow-discharge oxidation. (See Tables 7.2, 7.3 and 7.4.) However, the data for oxides doped with D_2O (see Table 7.3) indicate that the water vapour content remains approximately constant; output currents of 25.5, and 20.5 mA were measured before oxide growth, and after doping. Corresponding D_2O output currents were zero, and 19.5 mA. These data also suggest a partial exchange of surface hydroxyl and deuteroxyl groups at the Aℓ-oxide. Hydroxyl groups liberated from the oxide surface as a result of such exchange would therefore maintain the water vapour content in the chamber. The net effect would be a dynamic equilibrium between the number of hydroxyl groups being adsorbed at the surface, and those being released due to exchange.

Fig.7.12

IET spectrum of device plasma oxidixed for 25 min. in O_2 filtered through $CaCl_2$ chips at $-77^{o}C$, then vapour phase doped for 30 min. with D_2O.

Fig.7.13

IET spectrum of device plasma oxidized for 25 min. in O_2 filtered through $CaCl_2$ chips at $-77^{o}C$, then vapour phase doped for 40 min. with ethylacrylate.

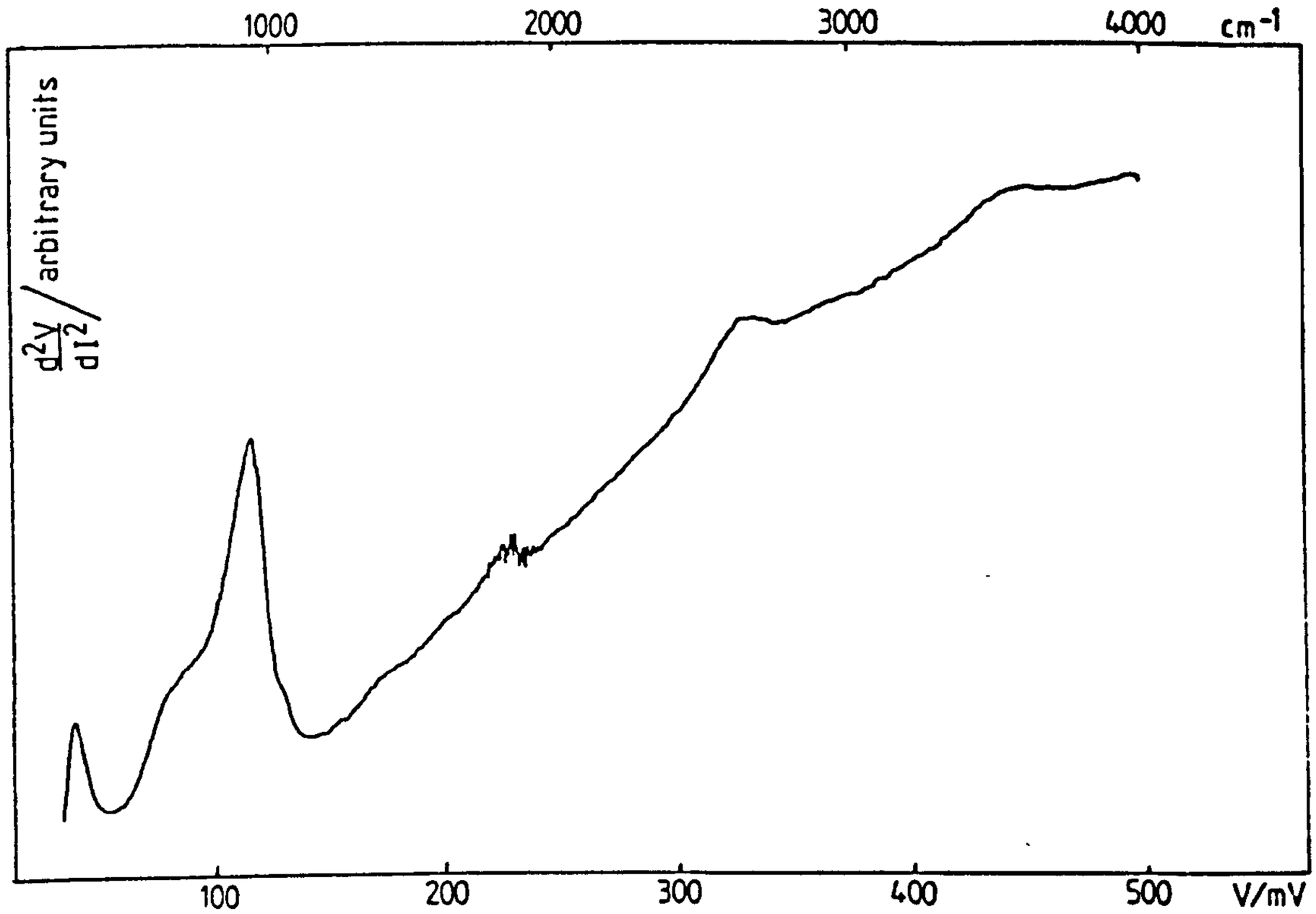
1000
2000
3000
4000
cm⁻¹
$\frac{d^2y}{dI^2}$ / arbitrary units
100
200
300
400
500
V/mV

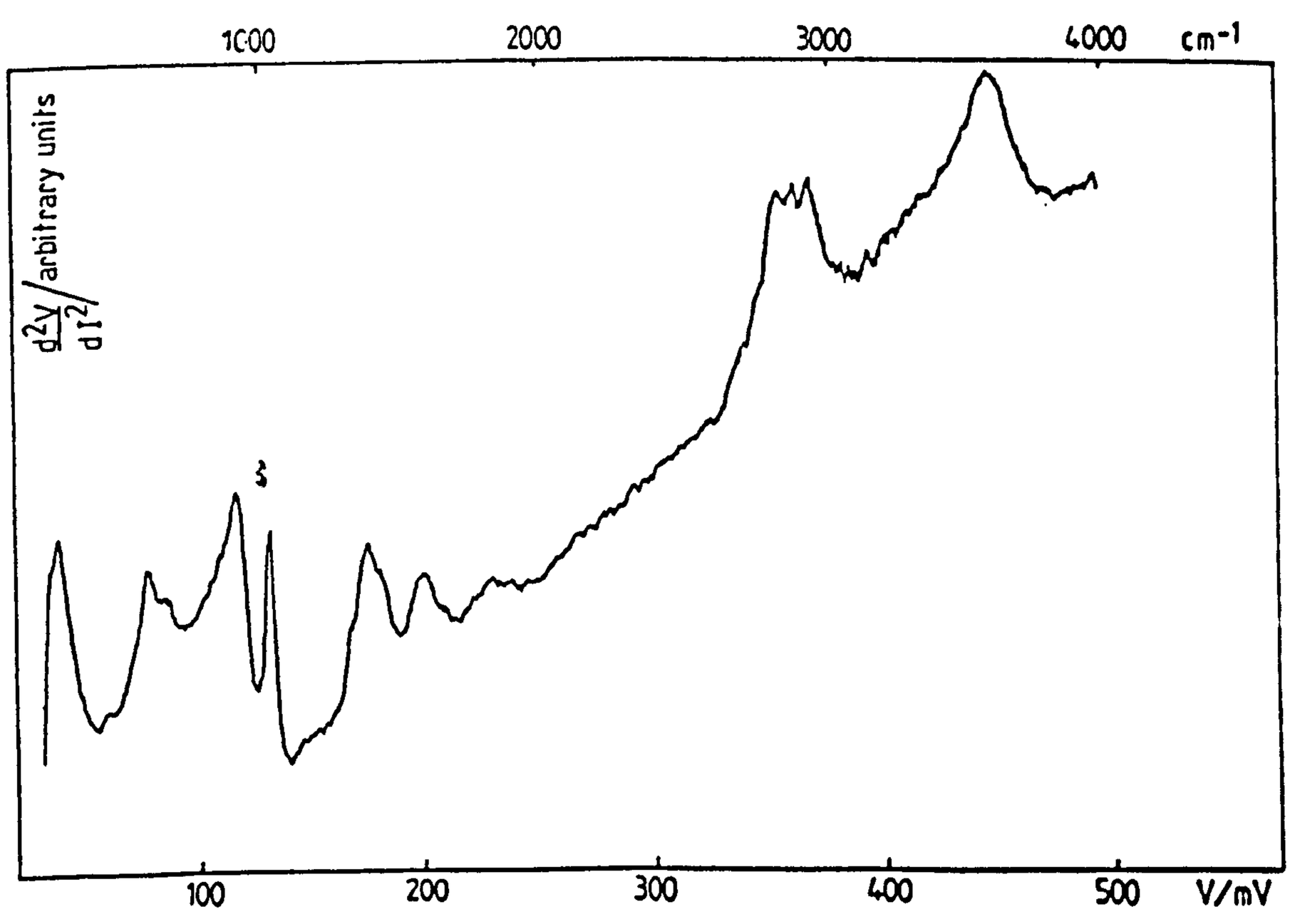
1000
2000
3000
4000
cm⁻¹
$\frac{d^2y}{dI^2}$ / arbitrary units
A
3
100
200
300
400
500
V/mV

TABLE 7.5 - Mass spectroscopic analysis of residual gases in vacuum chamber before a 25 min. glow-discharge oxidation in O_2 (percolated through $CaCl_2$ chips), and after the oxide had been vapour-phase doped in D_2O for 30 min.

Mass $N\bar{o}$	output current/mA						element/ compound
	before		ave	after		ave	
1	0.24,	0.36	0.30	0.17,	0.23	0.2	H
2	0.021,	0.017	0.019	0.63,	0.91	0.77	H_2, He, D
3	-	-	-	-	0.008	0.008	
4	-	-		0.006,	0.004	0.005	D_2
12	0.028,	0.021	0.025	0.020,	0.011	0.016	C
18	21.0,	30.0	25.5	22.0,	19.0	20.5	H_2O
20	-	-	-	20.0,	19.0	19.5	D_2O
28	0.25,	0.05	0.15	0.02,	0.03	0.025	CO, N_2
30	0.027,	0.003	0.015	0.002,	0.001	0.002	NO
31	0.014,	0.006	0.001	0.001,	0.001	0.001	
32	0.14,	0.06	0.10	0.02,	0.03	0.025	O_2
40	0.02,	-	0.02	-	-	-	
44	0.02,	0.01	0.015	0.005,	0.008	0.007	CO_2

Fig.7.13 shows the IET spectrum obtained from a device also glow-discharge oxidized as just described, but then vapour phase doped for ∿ 40 min. with ethyl acetate. The spectrum strongly resembles that of adsorbed acetic acid (12,13,16,17,40). Clearly, ethyl acetate is hydrolysed at the oxide surface and then adsorbed as the acetate anion. Modes due to deformations of the carboxylate anion are present at 78 and 83 mV, while its associated stretching vibrations are observed at 178, and 201 mV. A strong methyl rocking vibration appears at 131 mV, and CH stretching modes at 354, 361, and 368 mV.

The intensity of the OH stretching peak at 449 mV is approximately 2 to 3 times greater than those of the undoped devices, or that doped with D_2O above. This fairly strong OH peak can now be attributed with some confidence mainly to moisture in the dopant - even though it had previously been redistilled.

7.4 CONCLUSIONS

Relatively hydrocarbon-free, glow discharge Aℓ-oxides have been produced routinely in situ, and investigated by IETS. Approximate modifications were made to the vacuum system and suitably filtered O_2 was employed for oxide growth. Percolation of the O_2 through 13X molecular sieves or $CaCl_2$ chips at $-77^{o}C$ is an effective means of removing hydrocarbon contaminants; the latter material is marginally better in absorbing water vapour. Inevitably, the oxides were partially hydrated since they were formed at pressures in the range 50 to 70 m Torr. Mass spectrometric analyses of the residual gases in the vacuum chamber at lower pressures ($\lesssim 10^{-4}$ Torr) have indicated that its predominant component is indeed water vapour. Falls in the water vapour content of the chamber have been observed after oxide growth; these were presumably due to the formation of the surface hydroxyl layer on the oxide. UHV conditions are an essential prerequisite for the reduction of the levels of water vapour leading to the formation of relatively "dry" oxides.

Characterization of the oxides by employing various surface analytical techniques (some of which have been mentioned in the introduction) would provide useful complementary data. This may shed some light on the nature of their growth and structure. At present such analyses are not possible since the freshly grown oxides cannot be investigated in situ.

Ethyl acetate, and D_2O have been successfully vapour phase doped onto these oxides without breaking vacuum. The former yields an IET spectrum strongly resembling that of adsorbed acetic acid; it is believed that ethyl acetate is hydrolysed at the oxide surface and subsequently chemisorbed as the acetate anion. Doping with the latter promotes some degree of exchange between surface hydroxyl, and deuteroxyl groups on the oxide as evidenced in its IET spectrum. Corresponding mass spectrometric

analyses for D_2O have corroborated this observation.

Incipient vapour phase doping with CO_2 has been unsuccessful. This may be partly due to the fact that CO_2 is only weakly adsorbed on Al-oxide at room temperature and the chamber pressures employed.

CHAPTER 7 - REFERENCES

1. R.C.Jacklevic and J.Lambe. Phys. Rev. Lett., 17, 1139 (1966).

2. J.Lambe and R.C.Jaklevic. Phys. Rev., 165, 821 (1968).

3. P.K.Hansma. Phys. Rep., 30(C), 145-206 (1977).

4. N.F.Mott. Transactions of the Faraday Society, 35, 1175-1177 (1939).

5. N.F.Mott. Ibid., 36, 472 (1940).

6. M.L.Hair. Infra-red Spectrocopy in Surface Chemistry, Marcel Dekker Inc., New York (1967).

7. L.H.Little. Infra-red Spectra of Adsorbed Species, Academic Press Inc., London (1966).

8. S.Reynolds, D.P.Oxley and R.G.Pritchard. Spectrochim. Acta., 38A(1), 103-111 (1982).

9. R.R.Mallik, R.G.Pritchard, C.C.Horley and J.Comyn. To appear in Polymer.

10. D.M.Brewis, J.Comyn, D.P.Oxley, R.G.Pritchard, S.Reynolds, C.R.Werrett and A.J.Kinlock. Surf. Int. Anal., 6(1), 40 (1984).

11. W.J.Nelson, D.G.Walmsley and J.M.Bell. Thin Solid Films, 79, 229-234 (1981).

12. J.T.Hall and P.K.Hansma. Surf. Sci., 76, 61 (1978).

13. S.De Chevigne, et al. Surf. Sci., 105, 377-385 (1981).

14. J.B.Peri and R.B.Hannan. J. Phys. Chem., 64, 1526 (1960).

15. J.B.Peri and R.B.Hannan. Spectrochim. Acta., 16, 237 (1960).

16. H.E.Evans and W.H.Weinberg. J. Chem. Phys., 71(4), 1537 (1979).

17. H.E.Evans and W.H.Weinberg. Ibid., 71(12), 4789 (1979).

18. S.M.Bedair, F.Hofmann and H.P.Smith. J. Appl. Phy., 39, 4026C-4028C.

19. C.Benndort, C.Keller, H.Seidel and F.Theime. Surf. Sci., 67(2), 589 (1977).

20. E.E.Huber Jr., and C.T.Kirk Jr. Ibid., 5, 447 (1966).

21. D.Norman, S.Brennan, R.Jaeger and J.Stöhr. Ibid., 105, L297-L306 (1981).

22. F.Pellerim, C. Le Gressus and D.Massignon. Ibid., 103, 510 (1981).

23. R.Magno and J.G.Adler. Phys. Rev., B(13), 2262 (1976).

24. S.J.Thomson and G.Webb. Heterogeneous Catalysis, Oliver and Boyd Ltd., Edinburgh and London (1968).

25. F.Jona. J. Phys. Chem. Solids, 25, 2155 (1967).

26. C.B.Bargeron, B.H.Hall and A.N.Jette. Surf. Sci., 120, L483-L486 (1982).

27. J.B.Peri. J. Phys. Chem., 69, 211 (1965).

28. J.B.Peri. Ibid., 69, 220 (1965).

29. C.R.Werrett. Private communication.

30. H.E.Evans, W.M.Bowser and W.H.Weinberg. Applications of Surf. Sci., 5(3), 258 (1980).

31. W.M.Bowser and W.H.Weinberg. Surf. Sci., 64, 377 (1977).

32. N.D.Parkyns. Proceedings of the Third International Congress on Catalysis, p.914, North-Holland, Amsterdam (1965).

33. L.H.Little. Chemisorption and Reactions on Metallic Films, Volume I, J.R.Anderson (Ed.), Chapter 6, Academic Press, London (1971).

34. L.H.Little and C.H.Amberg. Can. J. Chem., 40, 1977 (1962).

35. J.B.Peri. J. Phys. Chem., 70, 3168 (1966).

36. R.M.Kroeker, P.H.Hansma and W.C.Kaska. J. Chem. Phys., 72(9), 4845 (1980).

37. R.M.Kroeker, W.C.Kaska and P.K.Hansma. J. Catal., 57, 72 (1979).

38. A.Bayman, P.K.Hansma and W.C.Kaska. Phys. Rev. B., 25(5), 2449 (1981).

39. B.W.Cook and K.Jones. A Programmed Introduction to Infra-red Spectroscopy, Heyden and Sons Ltd., London (1972).

40. B.F.Lewis, M.Moseman and W.H.Weinberg. Surf. Sci., 41, 142-164 (1974).

CHAPTER 8

GENERAL CONCLUSIONS, AND SUGGESTIONS FOR FURTHER WORK : A BRIEF SUMMARY

8.1 IET SPECTRA OF POLYMERS ADSORBED ON Aℓ-OXIDE OBTAINED BY LIQUID-PHASE DOPING

Liquid-phase doping has been employed for the first time to obtain IET spectra of synthetic polymers adsorbed on Aℓ-oxide. This work has particular relevence in the field of adhesion where Aℓ is a widely used substrate material. Good quality spectra are obtained when uniform polymeric adlayers are deposited; this may be achieved by suitable choice of solvents based upon their α values in the Mark-Houwink viscosity-molecular weight relationship (equation 5.2). Spectra obtained have shown clear evidence for interactions between side groups of the polymers, and the reactive Aℓ-oxide surface; these interactions are believed to lead to the adsorption of the polymers.

For PVA and PMMA the most probable adsorption mechanism is cleavage of the ester side groups catalysed by acidic and/or basic sites on the oxide surface. PVA is thought to be hydrolysed to PVOH and then physisorbed by hydrogen bonding between -OH side groups and surface hydroxyls on the oxide. Good spectral evidence exists to suggest that PMMA is adsorbed as polymethacrylic acid; chemisorption occurs through the formation of a bidentate symmetrical bridging complex between carboxylate anions on the polymer side groups, and Aℓ cations on the surface. The water soluble polymers (PEG, PEOX, MeC, and PAAM) are believed to adsorb in a manner similar to PVOH above, or through hydrogen bonding between lone pairs of oxygen atoms in the polymer chain and surface hydroxyls.

It is not possible to obtain detailed information regarding the configuration of the polymers as a whole on the surface. Spectral interpretation is complicated by the large number of vibrational modes

of these molecules and possible relaxation of symmetry considerations when adsorbed. Further work might be undertaken to synthesize telomers of known tacticity and investigate their adsorption. Effects due to polymer-solvent interactions could also be investigated further by doping these telomers from different solvents.

8.2 INCORPORATION OF POLYMERS INTO IET JUNCTIONS BY THE TECHNIQUE OF RADIO FREQUENCY (RF) GLOW-DISCHARGE POLYMERIZATION (GDP)

Suitable modifications have been made to existing vacuum systems which have allowed glow-discharge polymerized films to be incorporated into IET junctions. Low RF powers and exposure times (of the order of $\lesssim$ 10W, and a few seconds respectively) are required for the polymerizations which were performed with chamber pressures of nominally 100 m Torr. For the glow-discharge chamber geometry employed for the present work films have been deposited and estimated rates of $\sim$ 0.25 Å s^{-1}. IET spectra obtained for films of PVA and PMMA are in good agreement with their liquid-phase doped counterparts; GDP therefore offers a valuable complementary technique to that of liquid-phase doping.

GDP also offers considerable promise for further work, since polymer films can be deposited relatively quickly and easily in controlled atmospheres without the use of solvents. Several vinyl monomers have already been studied, and preliminary work to deposit a styrene/silane copolymer has proved encouraging. Further progress made in this area might have commercial applications by virtue of the importance of silane coupling agents as adhesion promotors.

With the present system the Aℓ base electrode evaporations and GDP's have been performed in the vacuum chamber without breaking vacuum. However it has not been possible to evaporate the Pb electrodes <u>in situ</u> after the polymerization, and it is necessary to remove the doped electrodes to another vacuum plant. Appropriate modifications to the system to accommodate the entire junction fabrication procedure would be desirable. (See also Section 8.4.)

8.3 INFUSION DOPING OF IET JUNCTIONS

An apparatus has been implemented which allows infusion doped IET spectra to be obtained routinely. Problems associated with formic acid contamination (thought to arise due to reactions between atmospheric CO_2 and water vapour at the Pb overlay electrode) have been effectively eliminated. This has been achieved by excluding CO_2 from the doping chamber simply by purging with N_2 prior to infusion. The presence of water vapour during infusion appears to be essential, but its full role is not yet clear. For example, water-insoluble monomers do not successfully infuse when doped in the presence of water vapour (or various solvents); spectra obtained correspond merely to thickening of the oxide/hydroxyl layer.

Rapid changes in IET junction conductance which occur during infusion have been conveniently monitored in situ and at low bias by the use of a DMM interfaced to a microcomputer. A simple model for sequential monolayer growth has been proposed which to a first approximation predicts the form of experimental conductance versus time graphs for water and water/acetone mixtures.

Further work to infusion dope IET junctions having different overlay electrodes may clarify the dynamics of the infusion process. The intercrystallite gap widths of these electrode metals are believed to influence the infusion rate, and impose a limit for the maximum dimensions of the molecules which may be infused. The effect of temperature on infusion might also be investigated.

8.4 PREPARATION OF GLOW-DISCHARGE Aℓ-OXIDES UNDER CONTROLLED CONDITIONS

Relatively hydrocarbon-free Aℓ-oxides have been formed by DC glow-discharge oxidation in suitably filtered O_2. Percolation of the O_2 through 13X molecular sieves or $CaCl_2$ chips at $-77^{o}C$ effectively removes the majority of hydrocarbon contaminants. Partial hydration of the oxides was inevitable since they were grown at pressures of 50 to 70 m Torr. Development of a mask change-over device has facilitated vapour-phase doping of the oxides, and complete junction fabrication to be performed *in situ*; doping with D_2O, and the monomer ethylacrylate has been successful.

IET spectra of the undoped oxides have indicated some degree of crystallinity (the Aℓ-O bulk phonon peaks are in general less broad, and considerably sharper than those of thermal Aℓ-oxides suggesting a more distinct range of vibrational mode energies). It would be interesting to characterize the oxides by other surface analytical techniques, some of which have been mentioned in Chapter 7 (see Section 7.1).

Further work to incorporate GDP films into the above IET junctions *in situ* is strongly suggested. Such work would offer a systematic approach for investigating the adsorption of polymers on Aℓ-oxides of controlled composition, under known atmospheres, and without the need for solvents. Comparison of these data with those for the corresponding polymers adsorbed on thermal Aℓ-oxides by liquid-phase doping and GDP may give additional insight into the interfacial behaviour of the polymers.

APPENDIX 1

Listing of the program described in Chapter 4, Section 4.2.3. The program calculates the normalized IET junction conductance g_n (t) assuming the growth of an initial monolayer of water, followed by sequential monolayers of dopant molecules, whose thickness may be input into the program. Values for the mean barrier height, and an arbitary time taken to form each monolayer may also be input. Flow charts for the program may be found in Chapter 4 (see Figures 4.2, and 4.2a).

Sample program outputs are also given. The column on the right shows values of g_n (t), and the column on the left shows the corresponding slopes of the g-t plots. Parameters input to calculate these values are given at the bottom of the listing (T'CRIT is the time taken to form each monolayer).

```
READY.

 10 PRINT"■■■■■■■■■■■■■■■■■■■■■■■■■■■■■MONOLAYER GROWTH PROGRAM"
 20 FOR D=0 TO 100 :NEXT D
 30 DIM CS(5,250),T(5,250),GR(5,250)
 40 PRINT"■■■■INPUT NUMBER OF MONOLAYERS (5 MAX)■"
 50 INPUT N
 60 PRINT"■INPUT TIME TAKEN TO GROW ONE MONOLAYER. TCRIT (ARBITRARY) SECONDS
 70 INPUT TC
 80 PRINT"■INPUT FIRST MONOLAYER THICKNESS IN      ANGSTROMS■"
 90 INPUT L
100 PRINT"■INPUT SUCCESSIVE MONOLAYER THICKNESS IN ANGSTROMS■"
110 INPUT M
120 PRINT"■INPUT THE AVERAGE BARRIER HEIGHT IN EV■"
130 INPUT P
140 LET I= 1
150 PRINT"■ I  T  SCALED CONDUCTANCE  ■■■CONDUCTANCE"
160 PRINT"──────────────────────────────────────────"
170 EL=EXP(-L*P^.5)
180 FOR T=0 TO TC
190 TR=(T/TC)
200 CS=1+TR*(EL-1)
210 CS(I,T)=CS:T(I,T)=T
220 IF T=0 THEN 240
230 GR(I,T)=CS(I,T)-CS(I,T-1)
240 IF T<>0 THEN PRINTTAB(23)GR(I,T)
250 PRINTI;T;CS
260 NEXT T
270 PRINT "■■          MONOLAYER"I" COMPLETED":PRINT
280 FOR I= 2TO N
290 PRINT"■ I  T  SCALED CONDUCTANCE  ■■■CONDUCTANCE"
300 PRINT"──────────────────────────────────────────"
310 EM=EXP(-M*P^.5)
320 EL=EXP(-(L+(I-2)*M)*P^.5)
330 FOR T=(I-1)*TC TO I*TC
340 TR=((T-(I-1)*TC)/TC)
350 CS=(TR*(EM-1)*EL)+EL
360 CS(I,T)=CS:T(I,T)=T
370 IF T=0 OR T-1=0 THEN 400
380 IF CS(I,T-1)=0 THEN 410
390 GR(I,T)=CS(I,T)-CS(I,T-1)
400 IF T<>0 THEN PRINTTAB(23)GR(I,T)
410 PRINTI;T;CS
420 NEXT T
430 PRINT "■■          MONOLAYER"I" COMPLETED":PRINT
440 NEXTI
450 PRINT"■■■■/■■■■T          "," T/SEC    ":PRINT
460 FOR I=1 TO N
470 FOR T=((I-1)*TC+1) TO I*TC
480 IF T-1<0 THEN500
490 PRINTGR(I,T), T(I,T)
500 NEXT T
510 PRINTTAB(8)"■MONOLAYER"I"COMPLETED":PRINT
520 NEXT I
530 PRINT
540 PRINT"NUMBER OF MONOLAYERS:"N
550 PRINT"T'CRIT:"TC"/SEC"
560 PRINT"FIRST MONOLAYER THICKNESS:"L"/ANGSTROMS"
570 PRINT"SUCCESSIVE MONOLAYER THICKNESS:          "M"/ANGSTROMS"
580 PRINT"AVERAGE BARRIER HEIGHT:"P"/EV"
590 PRINT"■          ■DIGI-PLOT ROUTINE"
600 FORD=0TO1E3:NEXTD
610 INPUT"■NO: OF DATA POINTS":Z
620 INPUT"■START PLOT":SP
630 INPUT"■END PLOT":EP
640 Z=Z+1
650 DIMR(Z),D(Z),Z(Z,10),M(Z)
```

```
610 INPUT"NO. OF DATA POINTS";Z
620 INPUT"START PLOT";SP
630 INPUT"END PLOT";EP
640 Z=Z+1
650 DIMR(Z),C(Z),Z(Z),GD(Z),TD(Z)
660 DIMTE(Z),F(Z),G(Z),V(Z)
670 DIMV1(25),X1(25)
680 DIMD(Z),E(Z),X(25),Y(25)
690 C=1
700 FORK=1TON
710 FORL=C TO C+TC-1
720 Z(L)=CS(K,L):V(L)=T(K,L)
730 NEXTL
740 C=C+TC
750 NEXTK
760 P=L
770 Q1=2000:Q2=1400:P2=10:P3=7
780 A=V(SP):B=Z(SP):C=V(SP):D=Z(SP)
790 REM FINDS MAX & MIN OF V(J) IN X *
800 REM (I.E. A & C).               *
810 REM AND MAX & MIN OF Z(J) IN Y  *
820 REM (I.E. B & D).               *
830 FOR J=SP TO P-1
840 IF A<=V(J) THEN A=V(J)
850 IF B<=Z(J) THEN B=Z(J)
860 NEXT J
870 FOR J=SP TO P-1
880 IF C>=V(J) THEN C=V(J)
890 IF D>=Z(J) THEN D=Z(J)
900 NEXT J
910 E=A-C:F=B-D
920 REM F(J), & G(J) ARE SCALED V(J) *
930 REM & Z(J) VALUES RESPECTIVELY.  *
940 FOR J=SP TO P-1
950 F(J)=(((V(J)-C)/E)*Q1)+400
960 G(J)=(((Z(J)-D)/F)*Q2)+400
970 NEXT J
980 GOSUB 2020
990 X=F(SP):Y=G(SP):GOSUB 1900
1000 X9$="S":Y=3:GOSUB 1850:REM CHAR        SIZE (1 TO 15)
1010 X9$="N":Y=1:GOSUB 1850:REM CHAR        TYPE (1 TO 6)
1020 FOR J=SP TO P-1:PRINTJ
1030 X=F(J):Y=G(J):GOSUB 1890
1040 NEXT J
1050 GOSUB 1900
1060 X=400:Y=400+Q2:GOSUR 1900
1070 X9$="Q":Y=200:GOSUB 1850
1080 X=1:R=P2:GOSUB 1870
1090 X=400:Y=400:GOSUB 1900
1100 X9$="D":Y=200:GOSUB 1850
1110 X=0:R=P3:GOSUB 1870
1120 REM LABELS AXES. CONVERTS X(I),& *
1130 REM Y(I) INTO STRINGS FOR       *
1140 REM THE DI(I-PLOT).             *
1150 REM*********************MIN IN Y****
1160 Y(0)=INT(D*1E7+.5)/1E7
1170 X$=STR$(Y(0))
1180 X=150:Y=390:GOSUB1900
1190 GOSUB2000
1200 REM*****************************.*
1210 B1=(B-D)/P3
1220 Y1(0)=590
1230 X9$="S":Y=2:GOSUB 1870:REM CHAR        SIZE
1240 FOR I=1 TO P3
1250 Y(I)=(INT((B1*I+D)*1E7+.5)))/1E7
1260 X$=STR$(Y(I))
1270 Y1(I)=Y1(I-1)+200
1280 X=150:Y=Y1(I-1):GOSUB 1900
1290 GOSUB 2000
1300 NEXT I
```

```
1210 B1=(B-D)/P3
1220 Y1(0)=590
1230 X9$="S":Y=2:GOSUB 1870:REM CHAR          SIZE
1240 FOR I=1 TO P3
1250 Y(I)=(INT((((B1*I+D)*1E7+.5)))/1E7
1260 X$=STR$(Y(I))
1270 Y1(I)=Y1(I-1)+200
1280 X=150:Y=Y1(I-1):GOSUB 1900
1290 GOSUB 2000
1300 NEXT I
1310 REM**********************HIN IN X*
1320 X9$="Q":Y=1:GOSUB 1850
1330 X(0)=INT(C*1E3+.5)/1E3
1340 X$=STR$(X(0))
1350 X=390:Y=450+Q2:GOSUB 1900
1360 GOSUB2000
1370 REM*********************************
1380 B2=(A-C)/P2
1390 X1(0)=390
1400 X9$="Q":Y=1:GOSUB 1850:REM CHAR          ORIENTATION (Y=0 TO 3)
1410 FOR I=1 TO P2
1420 X(I)=(INT(((B2*I+C)*1E3+.5)))/1E3
1430 X$=STR$(X(I))
1440 X1(I)=X1(I-1)+200
1450 X=X1(I):Y=450+Q2:GOSUB 1900
1460 GOSUB 2000
1470 NEXT I
1480 REM LABELS AXES,AND PRINTS
1490 REM AND PRINTS COMMENTS*********
1500 X$="G(TOTAL)/G(OXIDE)"
1510 X=100:Y=890:GOSUB1900
1520 GOSUB2000
1530 X9$="Q":Y=0:GOSUB1850
1540 X$="T/ARBITRARY UNITS"
1550 X=1090:Y=Q2+800:GOSUB1900
1560 GOSUB2000
1570 X$="COMPUTER INFUSION MODEL."
1580 X=100:Y=Q2+800:GOSUB1900
1590 GOSUB2000
1600 X$="DATE:"
1610 X=1900:Y=Q2+800:GOSUB1900
1620 GOSUB2000
1630 PRINT"INPUT DATE"
1640 INPUTX$
1650 X=2050:Y=Q2+800:GOSUB1900
1660 GOSUB2000
1670 X$="SUCCESSIVE MONOLAYER"
1680 X=100:Y=Q2+700:GOSUB1900
1690 GOSUB2000
1700 X$="THICKNESSES/A:"
1710 X=100:Y=Q2+650:GOSUB1900
1720 GOSUB2000
1730 PRINT"INPUT SUCCESSIVE MONOLAYER THICKNESSES  IN ANGSTROMS"
1740 INPUTX$
1750 X=500:Y=Q2+650:GOSUB1900
1760 GOSUB2000
1770 X$="BARRIER HEIGHT/EV:"
1780 X=1900:Y=Q2+700:GOSUB1900
1790 GOSUB2000
1800 PRINT"INPUT BARRIER HEIGHT IN EV:"
1810 INPUTX$
1820 X=2400:Y=Q2+700:GOSUB1900
1830 GOSUB2000
1840 END
1850 X8$=X9$+STR$(INT(Y))+CHR$(10)
1860 GOTO 2060
1870 X8$="X"+STR$(INT(X))+","+STR$(INT(Y))+","+STR$(INT(R))+CHR$(10)
1880 GOTO 2060
1890 X8$="D":GOTO 1930
1900 X8$="M":GOTO 1930
```

```
1670 X$="SUCCESSIVE MONOLAYER"
1680 X=100:Y=02+700:GOSUB1900
1690 GOSUB2000
1700 X$="THICKNESSES/H:"
1710 X=100:Y=02+650:GOSUB1900
1720 GOSUB2000
1730 PRINT"□INPUT SUCCESSIVE MONOLAYER THICKNESSES  IN ANGSTROMS"
1740 INPUTX$
1750 X=500:Y=02+650:GOSUB1900
1760 GOSUB2000
1770 X$="BARRIER HEIGHT/EV:"
1780 X=1900:Y=02+700:GOSUB1900
1790 GOSUB2000
1800 PRINT"□INPUT BARRIER HEIGHT IN EV:"
1810 INPUTX$
1820 X=2400:Y=02+700:GOSUB1900
1830 GOSUB2000
1840 END
1850 X8$=X9$+STR$(INT(Y))+CHR$(10)
1860 GOTO 2060
1870 X8$="X"+STR$(INT(X))+","+STR$(INT(Y))+","+STR$(INT(R))+CHR$(10)
1880 GOTO 2060
1890 X8$="O":GOTO 1930
1900 X8$="M":GOTO 1930
1910 X8$="I":GOTO 1930
1920 X8$="R"
1930 X8$=X8$+STR$(INT(X))+","+STR$(INT(Y))+CHR$(10)
1940 GOTO 2060
1950 IF LEFT$(X$,1)="L" THEN 1970
1960 X8$="P"+RIGHT$(X$,LEN(X$)-1)+CHR$(10):GOTO 2060
1970 XX$="":FORX8=2TOLEN(X$):XX$=XX$+CHR$(ASC(MID$(X$,X8,1))+32):NEXTX8
1980 X8$="P"+XX$+CHR$(10)
1990 GOTO 2010
2000 X8$="P"+X$+CHR$(10)
2010 GOTO 2060
2020 POKE 59459,255
2030 POKE 59457,0
2040 POKE 59457,128
2050 X8$="H"+CHR$(10)
2060 FOR X8=1 TO LEN(X8$)
2070 IF PEEK (59469) AND 2 THEN 2090
2080 GOTO 2070
2090 POKE 59457,0
2100 POKE 59457,ASC(MID$(X8$,X8,1))+128
2110 NEXT X8
2120 RETURN
READY.
```

ΔG/ΔT	T/SEC	SCALED COND
-.0316060279	1	.968393972
-.0316060281	2	.936787944
-.0316060279	3	.905181916
-.0316060281	4	.873575888
-.0316060279	5	.84196986
-.0316060279	6	.810363832
-.0316060281	7	.778757804
-.0316060279	8	.747151776
-.0316060279	9	.715545749
-.0316060281	10	.683939721
-.0316060279	11	.652333693
-.0316060281	12	.620727665
-.0316060279	13	.589121637
-.0316060279	14	.557515609
-.0316060281	15	.525909581
-.0316060279	16	.494303553
-.031606028	17	.462697525
-.0316060279	18	.431091497
-.031606028	19	.399485469
-.031606028	20	.367879441
monolayer 1 completed		
-.0116272079	21	.356252233
-.011627208	22	.344625025
-.0116272079	23	.332997817
-.0116272079	24	.32137061
-.011627208	25	.309743402
-.0116272079	26	.298116194
-.0116272079	27	.286488986
-.0116272079	28	.274861778
-.0116272079	29	.26323457
-.011627208	30	.251607362
-.0116272079	31	.239980154
-.0116272079	32	.228352946
-.0116272079	33	.216725738
-.0116272079	34	.205098531
-.0116272079	35	.193471323
-.0116272079	36	.181844115
-.011627208	37	.170216907
-.0116272077	38	.158589699
-.011627208	39	.146962491
-.0116272079	40	.135335283
monolayer 2 completed		
-4.27741074E-03	41	.131057872
-4.27741074E-03	42	.126780462
-4.27741074E-03	43	.122503051
-4.27741074E-03	44	.11822564
-4.27741074E-03	45	.11394823
-4.27741074E-03	46	.109670819
-4.27741074E-03	47	.105393408
-4.27741074E-03	48	.101115997
-4.27741074E-03	49	.0968385866
-4.27741077E-03	50	.0925611758
-4.27741074E-03	51	.088283765
-4.27741074E-03	52	.0840063543
-4.27741071E-03	53	.0797289436
-4.27741074E-03	54	.0754515328
-4.27741077E-03	55	.0711741221
-4.27741074E-03	56	.0668967113
-4.27741077E-03	57	.0626193006
-4.27741068E-03	58	.0583418899
-4.27741077E-03	59	.0540644791
-4.27741077E-03	60	.0497870683
monolayer 3 completed		

NUMBER OF MONOLAYERS: 3
T'CRIT: 20 /SEC
FIRST MONOLAYER THICKNESS: 1 /ANGSTROMS
SUCCESSIVE MONOLAYER THICKNESS: 1 /ANGSTROMS
AVERAGE BARRIER HEIGHT: 1 /EV

▲G/ ▲T	T/SEC	SCALED COND
-.0316060279	1	.968393972
-.0316060281	2	.936787944
-.0316060279	3	.905181916
-.0316060281	4	.873575888
-.0316060279	5	.84196986
-.0316060279	6	.810363832
-.0316060281	7	.778757804
-.0316060279	8	.747151776
-.0316060279	9	.715545749
-.0316060281	10	.683939721
-.0316060279	11	.652333693
-.0316060281	12	.620727665
-.0316060279	13	.589121637
-.0316060279	14	.557515609
-.0316060281	15	.525909581
-.0316060279	16	.494303553
-.031606028	17	.462697525
-.0316060279	18	.431091497
-.031606028	19	.399485469
-.031606028	20	.367879441
monolayer 1 completed		
-.0159046187	21	.351974822
-.0159046187	22	.336070204
-.0159046187	23	.320165585
-.0159046185	24	.304260967
-.0159046187	25	.288356348
-.0159046187	26	.272451729
-.0159046185	27	.256547111
-.0159046187	28	.240642492
-.0159046186	29	.224737873
-.0159046187	30	.208833255
-.0159046186	31	.192928636
-.0159046187	32	.177024017
-.0159046185	33	.161119399
-.0159046186	34	.14521478
-.0159046187	35	.129310162
-.0159046187	36	.113405543
-.0159046187	37	.0975009243
-.0159046185	38	.0815963057
-.0159046187	39	.065691687
-.0159046188	40	.0497870683
monolayer 2 completed		
-2.15245607E-03	41	.0476346123
-2.15245606E-03	42	.0454821563
-2.15245607E-03	43	.0433297002
-2.15245607E-03	44	.0411772441
-2.15245607E-03	45	.039024788
-2.15245607E-03	46	.036872332
-2.15245606E-03	47	.0347190759
-2.15245607E-03	48	.0325674198
-2.15245607E-03	49	.0304149638
-2.15245607E-03	50	.0282625077
-2.15245607E-03	51	.0261100516
-2.15245607E-03	52	.0239575955
-2.15245606E-03	53	.0218051395
-2.15245607E-03	54	.0196526834
-2.15245607E-03	55	.0175002273
-2.15245607E-03	56	.0153477713
-2.15245607E-03	57	.0131953152
-2.15245606E-03	58	.0110428591
-2.15245607E-03	59	8.8904030 7E-03
-2.15245607E-03	60	6.737947E-03
monolayer 3 completed		

NUMBER OF MONOLAYERS: 3
T'CRIT: 20 /SEC
FIRST MONOLAYER THICKNESS: 1 /ANGSTROMS
SUCCESSIVE MONOLAYER THICKNESS: 2 /ANGSTROMS
AVERAGE BARRIER HEIGHT: 1 /EV

▲G/▲T	T/SEC	SCALED COND
-.0316060279	1	.968393972
-.0316060281	2	.936787944
-.0316060279	3	.905181916
-.0316060281	4	.873575888
-.0316060279	5	.84196986
-.0316060279	6	.810363832
-.0316060281	7	.778757804
-.0316060279	8	.747151776
-.0316060279	9	.715545749
-.0316060281	10	.683939721
-.0316060279	11	.652333693
-.0316060281	12	.620727665
-.0316060279	13	.589121637
-.0316060279	14	.557515609
-.0316060281	15	.525909581
-.0316060279	16	.494303553
-.031606028	17	.462697525
-.0316060279	18	.431091497
-.031606028	19	.399485469
-.031606028	20	.367879441
monolayer 1 completed		
-.0174781901	21	.350401251
-.0174781901	22	.332923061
-.0174781901	23	.315444871
-.01747819	24	.297966681
-.0174781901	25	.280488491
-.0174781901	26	.2630103
-.0174781901	27	.24553211
-.0174781901	28	.22805392
-.0174781901	29	.21057573
-.0174781901	30	.19309754
-.0174781901	31	.17561935
-.0174781901	32	.15814116
-.01747819	33	.14066297
-.0174781902	34	.12318478
-.0174781901	35	.105706589
-.0174781901	36	.0882283993
-.0174781901	37	.0707502092
-.01747819	38	.0532720191
-.0174781901	39	.035793829
-.0174781901	40	.0183156389
monolayer 2 completed		
-8.70187847E-04	41	.017445451
-8.70187847E-04	42	.0165752632
-8.70187847E-04	43	.0157050753
-8.70187843E-04	44	.0148348875
-8.70187847E-04	45	.0139646997
-8.70187847E-04	46	.0130945118
-8.70187843E-04	47	.01222424
-8.70187847E-04	48	.0113541361
-8.70187847E-04	49	.0104839483
-8.70187847E-04	50	9.61376043E-03
-8.70187847E-04	51	8.7435725[illegible]E-03
-8.70187847E-04	52	7.8733847[illegible]E-03
-8.70187843E-04	53	7.[illegible]319689[illegible]E-03
-8.70187847E-04	54	6.13300004E-03
-8.70187847E-04	55	5.2628212E-03
-8.70187847E-04	56	4.39263335E-03
-8.70187847E-04	57	3.5[illegible]14[illegible]E-03
-8.70187843E-04	58	2.65225700E-03
-8.70187847E-04	59	1.7020698[illegible]E-03
-8.70187847E-04	60	9.1188197[illegible]E-04
monolayer 3 completed		

NUMBER OF MONOLAYERS: 3
T'CRIT: 20 /SEC
FIRST MONOLAYER THICKNESS: 1 /ANGSTROMS
SUCCESSIVE MONOLAYER THICKNESS: 3 /ANGSTROMS
AVERAGE BARRIER HEIGHT: 1 /EV

APPENDIX 2 - Vapour phase doping of IET junctions *in situ* by means of an isolated doping chamber.

Routine *in situ* doping of the glow-discharge oxides described in Chapter 7 with acrid, volatile compounds such as certain monomers, and solvents is not yet possible. These compounds rapidly contaminate the diffusion pump fluid such that the pumps operation is impaired severely. Chamber pressures acceptable for electrode evaporations ($\leq 10^{-5}$ Torr) are not then readily attainable. At present this problem is overcome by replacing the fluid ('Santovac 5' - a polyphenyl ether with a very low vapour pressure widely used in 'clean' vacuum systems) after a cumulative doping exposure time of a few tens of minutes. This task is both laborious (usually requiring several technician-hours) and cost ineffective (the replacement cost of Santovac 5 is currently £ per litre).

An alternative approach was adopted to avoid this problem: an isolated doping chamber was constructed, annexed to the main vacuum chamber, from which the majority of spent dopant vapour could be removed by means of a dedicated rotary pump. Details of the doping chamber and it's operation will be discussed briefly in Sections A2.1, and A2.2 respectively. Unfortunately, thorough gettering of this chamber has not been possible, and consequently, the levels of contamination are unacceptable. Certain modifications are imperative for the system to be viable - these are also outlined.

A2.1 The Isolated Doping Chamber

An annular stainless steel collar was inserted between the main vacuum cylinder, and top plate in a stacked arrangement to form the doping chamber as shown schematically in Fig.A2.1 (ii). Various devices could be

Fig.A2.1 - Schematic diagrams of the isolated doping chamber.

(i) an ariel view of the collar only showing the moveable baffle valve and evaporation aperture.

(ii) side view of the collar inserted between the top plate and main vacuum chamber. The needle valve and jig on the top-plate have not been labelled (see Fig.7.1).

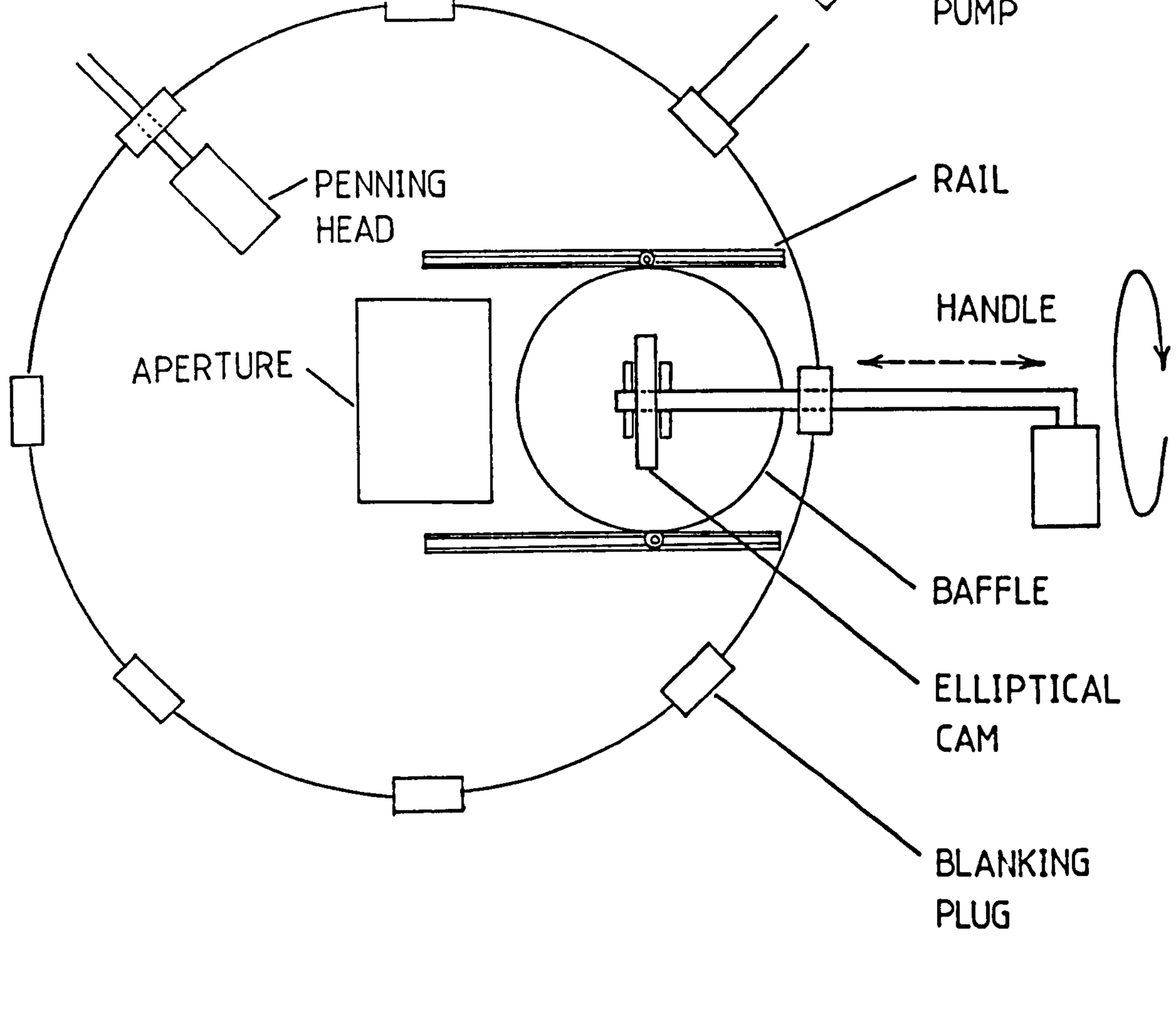
PUMP
PENNING
HEAD
RAIL
HANDLE
APERTURE
BAFFLE
ELLIPTICAL
CAM
BLANKING
PLUG

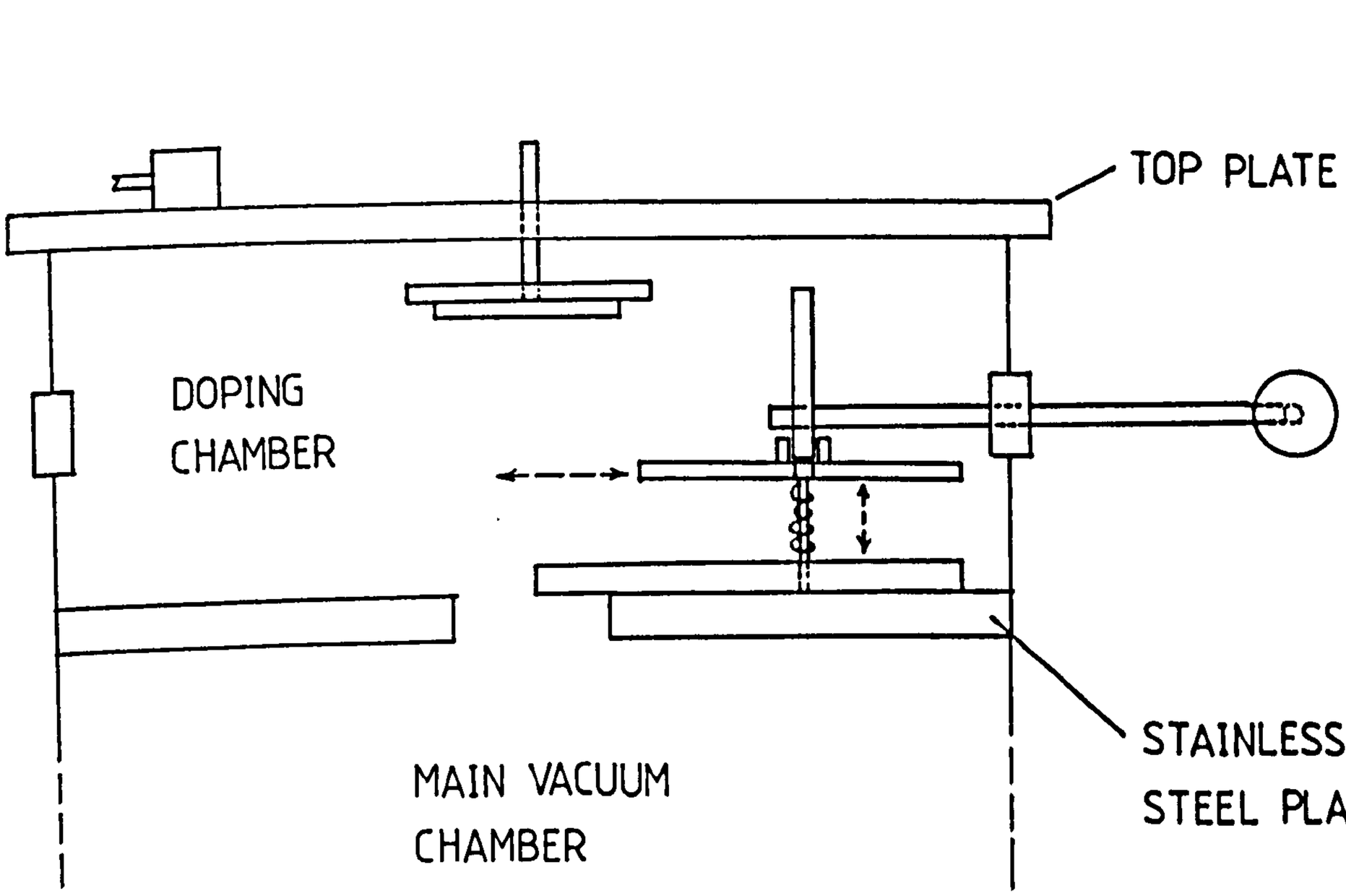
TOP PLATE
DOPING
CHAMBER
MAIN VACUUM
CHAMBER
STAINLESS
STEEL PLATE

fitted into the chamber through a series of removable blanking plugs on the collar. For the present work, the rotary pump, and Penning gauge head were connected as shown in Fig.A2.1 (i). A baffle valve was constructed which could be raised and lowered by means of a spring loaded elliptical cam, and moved horizontally on two parallel rails. This allowed both electrode evaporations, and oxide doping to be performed in the doping chamber without breaking vacuum.

A2.2 Device Fabrication

With the sliding baffle valve open (see Fig.A2.1), both the doping, and main vacuum chambers were evacuated to $\sim 10^{-5} - 10^{-6}$ Torr by engaging the main diffusion pump. Utilizing the glow-discharge supply, and evaporation source of the main vacuum chamber, the system was first glow-discharge cleaned, and then the Aℓ base electrodes were deposited and oxidized as described in Chapter 7. The sliding baffle valve was then closed, and the electrodes were doped by admitting dopant vapour through the needle value. In this way, dopant vapour was effectively excluded from the main chamber. After doping, the majority of spent dopant vapour was removed by the rotary pump; the baffle valve was then re-opened, and the pressure in both chambers was reduced further by the main diffusion pump. Finally, the Pb electrodes were evaporated (in a similar manner to the Aℓ electrodes) thus completing the IET junctions.

Shadowing effects maintained above (leading to poor gettering of the doping chamber) can be readily appreciated when one considers the geometry of the chamber; in particular, the baffle valve aperture is unavoidably small. Development of this chamber to its full operating potential requires the following:

(i) An evaporation source should be incorporated in the doping chamber

itself to facilitate thorough gettering which is known to be of paramount importance in IETS (1).

(ii) A larger baffle aperture is desirable. This would allow a more effective glow-discharge cleaning procedure. Alternatively,

(iii) glow-discharge electrodes (coupled to the main HT power supply) could be installed in the doping chamber.

Further development of the system to this end is necessary if the junction fabrication facilities at Leicester are to be comparable with those of other workers (1-5).

References

1. P.K.Hansma. Phys. Rep., 30(C), 145-206 (1977).

2. R.Magno and J.G.Adler. Phys. Rev., B (13), 2262 (1976).

3. B.F.Lewis, M.Moseman and W.H.Weinberg. Surf. Sci., 41, 142-164 (1974).

4. D.G.Walmsley, W.J.Nelson, N.M.S.Brown and R.B.Floyd. Applications of Surf. Sci., 5, 107 (1980).

5. A.L.Geiger, B.S.Chandrasekhar and J.G.Adler. Phys. Rev., 188 (3), 1130 (1969).

APPENDIX 3

Listing of the software routine used to plot experimental conductance-time data of Chapter 4. Conductance and time values, previously stored as two one dimensional arrays on a cassette file, are read, and then plotted using a digital plotter.

```
READY.

 3000 DATA0,0,0
 3010 DIMR(300),C(300),Z(300),GD(300),TD(300)
 3020 DIMTE(300),F(300),G(300),V(300)
 3030 DIMY1(25),X1(25)
 3040 DIMD(300),E(300),X(25),Y(25)
 3050 PRINT"■"
 3060 PRINT"       ■CRUNCHING NUMBERS NOW!■";PRINT
 3070 P=1
 3080 PRINTP
 3090 IFP=200THENPRINT"■NOT LONG TO GO NOW!!!■"
 3100 READR(P),Z(P),V(P)
 3110 REM V(P)=T=X AXIS                    *
 3120 REM Z(P)=G=Y AXIS                    *
 3130 GOTO 3160
 3140 V(P)=V(P)↑2
 3150 REM IF DATA IN T↑.5 FORM ONLY        *
 3160 IFR(P)=0THEN3190
 3170 P=P+1
 3180 GOTO 3080
 3190 PRINT"DO YOU WANT A4 OR A3 FORMAT";INPUTO$
 3200 IF O$="A3" THEN 3230
 3210 Q1=2000:Q2=1400:P2=10:P3=7
 3220 GOTO 3240
 3230 Q1=2800:Q2=1800:P2=14:P3=9
 3240 A=V(1):B=Z(1):C=V(1):D=Z(1)
 3250 REM FINDS MAX & MIN OF V(J) IN X *
 3260 REM (I.E. A & C),                    *
 3270 REM AND MAX & MIN OF Z(J) IN Y       *
 3280 REM (I.E. B & D).                    *
 3290 FOR J=1 TO P-1
 3300 IF A<=V(J) THEN A=V(J)
 3310 IF B<=Z(J) THEN B=Z(J)
 3320 NEXT J
 3330 FOR J=1 TO P-1
 3340 IF C>=V(J) THEN C=V(J)
 3350 IF D>=Z(J) THEN D=Z(J)
 3360 NEXT J
 3370 E=A-C:F=B-D
 3380 REM F(J), & G(J) ARE SCALED V(J) *
 3390 REM & Z(J) VALUES RESPECTIVELY.  *
 3400 FOR J=1 TO P-1
 3410 F(J)=(((V(J)-C)/E)*Q1)+400
 3420 G(J)=(((Z(J)-D)/F)*Q2)+400
 3430 NEXT J
 3440 GOSUB 4320
 3450 X=F(6):Y=G(6):GOSUB 4200
 3460 X9$="S":Y=3:GOSUB 4150:REM CHAR        SIZE (1 TO 15)
 3470 X9$="N":Y=1:GOSUB 4150:REM CHAR        TYPE (1 TO 6)
 3480 FOR J=1 TO P-1:PRINTJ
 3490 X=F(J):Y=G(J):GOSUB 4190
 3500 NEXT J
 3510 GOSUB 4200
 3520 X=400:Y=400+Q2:GOSUB 4200
 3530 X9$="Q":Y=200:GOSUB 4150
 3540 X=1:R=P2:GOSUB 4170
 3550 X=400:Y=400:GOSUB 4200
 3560 X9$="Q":Y=200:GOSUB 4150
 3570 X=0:R=P3:GOSUB 4170
 3580 REM LABELS AXES, CONVERTS X(I),& *
 3590 REM Y(I) INTO STRINGS FOR            *
 3600 REM THE DIGI-PLOT.                   *
 3610 REM*********************MIN IN Y*****
 3620 Y(0)=INT(D*1E7+.5)/1E7
 3630 X$=STR$(Y(0))
 3640 X=150:Y=390:GOSUB4200
 3650 GOSUB4300
 3660 REM*************************************
 3670 B1=(B-D)/P3
 3680 Y1(0)=590
 3690 X9$="S":Y=2:GOSUB 4170:REM CHAR        SIZE
 3700 FOR I=1 TO P3
 3710 Y(I)=(INT((((B1*I+D)*1E7+.5)))/1E7
 3720 X$=STR$(Y(I))
 3730 Y1(I)=Y1(I-1)+200
 3740 X=150:Y=Y1(I-1):GOSUB 4200
 3750 GOSUB 4300
 3760 NEXT I
 3770 REM************************MIN IN X*
 3780 X9$="W":Y=1:GOSUB 4150
 3790 X(0)=INT(C*1E3+.5)/1E3
 3800 X$=STR$(X(0))
 3810 X=390:Y=450:GOSUB 4200
 3820 GOSUB4300
 3840 REM*************************************
```